Spin-Dependent Tunneling and Heterovalent Heterointerface Effects in Diluted Magnetic II-VI Semiconductor Heterostructures

Dissertation zur Erlangung des naturwissenschaftlichen Doktorgrades der
Bayerischen Julius-Maximilians-Universität Würzburg

vorgelegt von
Alexander Frey
aus Künzelsau

Würzburg, 2011

Eingereicht am:

bei der Fakultät für Physik und Astronomie

Gutachter der Dissertation:

1. Gutachter:
2. Gutachter:
3. Gutachter:

Prüfer im Promotionskolloquium:

1. Prüfer:
2. Prüfer:
3. Prüfer:

Tag des Promotionskolloquiums:

Doktorurkunde ausgehändigt am:

Contents

Nomenclature

Φ_b	Barrier height
e	Elementary charge
m	Effective mass
m_0	Free electron mass
AFM	Atomic force microscopy
BEP	Beam equivalent pressure
DMS	Diluted magnetic semiconductor
ECV	Electrochemical capacitance voltage profiling
FWHM	Full width at half maximum
MBE	Molecular beam epitaxy
ML	Monolayer
MR	Magnetoresistance
PL	Photoluminescence
PVR	Peak-to-valley current ratio
QD	Quantum dot
RHEED	Reflection high energy electron diffraction
XRD	X-ray diffraction

Für meine Eltern
und für Mascha.

Zusammenfassung

Verdünnt magnetische II-VI Halbleiter (DMS) sind seit langem für ihre besonderen magnetischen Eigenschaften bekannt, wie den Giant Zeeman Effekt und die Faraday Rotation [1]. Die Verbreitung der Spintronik, die zur Speicherung oder Verarbeitung von Informationen anstelle der Ladung den Spin von Elektronen ausnutzt, hat neues Forschungsinteresse für magnetische Halbleiter geweckt [2, 3, 4]. Ein Ziel der Spintronik ist es, nichtflüchtige, magnetische Datenspeicherung und Informationsverarbeitung auf einem einzigen Halbleiterchip zu integrieren. Hierfür werden Halbleitermaterialien benötigt, die bei Raumtemperatur ferromagnetisch sind. II-VI Halbleiter sind paramagnetisch und ihre besonderen magnetischen Eigenschaften sind zudem auf tiefe, kryogene Temperaturen beschränkt. Da ein idealer ferromagnetischer Halbleiter noch nicht gefunden wurde, können II-VI DMS jedoch als nützliche Testumgebung für die Erforschung von spintronischen Bauelementkonzepten dienen. Beispiele solcher Konzepte sind Spin-LEDs [5, 6], Spin Superlattices [7, 8], verdünnt magnetische Resonanz-Tunneldioden [9, 10, 11, 12], verdünnt magnetische Einzelbarrieren Tunnelstrukturen [13, 14], sowie die Spin Injektion in Halbleiter-Quantenpunkte [15]. Neben einer potenziellen Verwendung in zukünftigen spintronischen Baulementen trägt die Foschung an solchen Konzepten zu einem besseren Verständnis der magnetischen, elektronischen und optischen Eigenschaften von Festkörpern bei.

Der Beitrag der vorliegenden Arbeit besteht aus drei Teilen. Diese beschäftigen sich mit der Untersuchung bestimmter, für Spininjektion relevanter, Halbleiter Heterogrenzflächen, mit neuartigen, verdünnt magnetischen Einzelbarrieren-Tunnelstrukturen, sowie mit der Weiterentwicklung von verdünnt magnetischen Resonanz-Tunneldioden.

Im ersten Teil werden die elektrischen Eigenschaften der ZnSe / GaAs(001) Heterogrenzfläche untersucht, welche eine wichtige Rolle bei der Spininjektion von II-VI DMS in GaAs spielt [5, 15] und zudem ein Prototyp der sogenannten heterovalenten Heterogrenzflächen ist [16]. Es wird ein neuer Prozess für den Start des MBE Wachstums von ZnSe auf GaAs(001) vorgestellt, welcher zu Grenzflächen mit deutlich reduzierter Potentialbarriere und damit zu verbesserten elektrischen Transporteigenschaften führt [17]. Mittels MBE wurden n-ZnSe / n-GaAs Grenzflächen mit einer systematisch variierten Prädeposition kleiner Mengen von Zn oder Se auf (2×4) rekonstruierten GaAs(001) Startoberflächen hergestellt. Diese wurden untersucht mit temperaturabhängigen, elektrischen Transportmessungen, elektrochemische Kapazitäts-Spannungsmessungen, Raman Spektroskopie und hochauflösender Röntgenbeugung.

An einer Zn-reichen Grenzfläche wird eine bis zu 550 meV hohe Potentialbarriere im Leitungsband gemessen, welche mit zunehmender Se Prädeposition bis etwa 70 meV abnimmt. Gleichzeitig verringert sich der Widerstand der Grenzfläche um mehrere Größenordnungen. Eine breite Verarmungszone an der Heterogrenzfläche von etwa 50 nm wird einer starken Interdiffusion von akzeptorartigen Atomen zugeschrieben. Diese bewirkt ein effektives Elektronendefizit von 1.5×10^{13} cm^{-2}. Sowohl die Weite der Verarmungszone, als auch die Flächendichte von Akzeptoren in der Umgebung der Grenzfläche sind nahezu unabhängig von der Wachstumsstartprozedur. Im Vergleich zur Zn-Prädeposition verschiebt die Se-Prädeposition jedoch die Verarmungszone an der Heterogrenzfläche teilweise vom GaAs ins ZnSe. Die Ergebnisse werden auf Basis eines Bandverbiegungsmodells diskutiert, welches variable Bandoffsets, Grenzflächenzustandsdichten und atomare Interdiffusionsprofile abhängig vom Wachstumsstart beinhaltet. Es wird erwartet, dass solche Grenzflächen mit einer niedrigen Potentialbarriere den Spintransport von ZnSe basierten DMS in III-V Materialien entscheidend verbessern.

Im zweiten Teil wird ein neues Bauelementkonzept zur Spinfilterung von Elektronen durch spinabhängiges Tunneln in einzelnen DMS Tunnelbarrieren experimentell untersucht. Die Barriere besteht aus einer (Zn,Be,Mn)Se DMS Schicht, die zwischen n-dotierten ZnSe Injektor- und Kollektorschichten eingebettet ist. Die Barrierenhöhe im Leitungsband bei B = 0 T wird primär vom Be Gehalt bestimmt und beträgt ca. 50 bis 100 meV. Der Mn Gehalt beträgt etwa 8 %. Durch den Giant Zeeman Effekt in der DMS Barriereschicht wird in einem externen Magnetfeld die Barriere für spin-down (spin-up) Elektronen niedriger (höher) und die Tunnelwahrscheinlichkeit dadurch höher (niedriger). Die Struktur wirkt damit als einstellbarer Spinfilter für tunnelnde Elektronen. Es wurden mehrere Proben mit unterschiedlicher Barrierenhöhe und -dicke hergestellt und ihre Strom-Spannungs-Kennlinien bei Heliumtemperatur als Funktion des Magnetfelds untersucht. Die Strukturen zeigen eine nichtlineare Strom-Spannungscharakteristik, sowie den für spinabhängiges Tunneln erwarteten negativen Magnetowiderstand. Bei B = 6 T beträgt der Widerstand noch etwa ein Drittel des bei B = 0 T gemessenen Wertes. Eine Variation von Barrierenhöhe oder -dicke verursacht die auf Basis eines einfachen Tunnel-Transport-Modells erwartete Änderung der I-V Kennlinien. Der Magnetowiderstand bleibt dabei jedoch nahezu unabhängig von der Barrierenhöhe und -dicke. Mögliche Ursachen hierfür werden diskutiert. Ein direkter Nachweis der Spinpolarisation, z.B. durch optische Methoden, steht noch aus. Einfache Modellrechnungen lassen jedoch erwarten, dass sie, abhängig von den Barriereneigenschaften, deutlich über 90 % liegen kann.

Der dritte Teil der Arbeit konzentriert sich auf verdünnt magnetische II-VI Resonanz-Tunneldioden (RTDs), die es erlauben, die Spinorientierung tunnelnder Elektronen durch einfache Variation einer angelegten Spannung zu steuern [9, 11]. Dies wird mit spinabhängigem Tunneln durch einen DMS Quantentrog oder Quantenpunkt erreicht. Zunächst wird eine Methode beschrieben, die es erlaubt, mittels hochauflösender Röntgenbeugung die Dicke und Zusammensetzung der Doppelbarrierenstruktur solcher II-VI RTDs zu bestimmen [18]. Dies ist nicht trivial, da die normalerweise weniger als

10 nm dünnen Barriereschichten nur ein kleines Streuvolumen im Vergleich zu den umgebenden, ca. 1 μm dicken Kontakt- und Pufferschichten haben und weil Röntgeninterferenz zwischen den Barriereschichten zu einem komplizierten Beugungsmuster führt.

Mithilfe dieser Methode zur Kontrolle des MBE Wachstums wurden mehrere Serien von II-VI DMS RTDs hergestellt und untersucht, mit dem Ziel Strukturen zu entwickeln, die durch laterale Gate-Elektroden einen lateralen Einschluss des resonanten Zustandes von zwei auf null Dimensionen (0D) erlauben. Aufgrund des Coulomb-Blockade Effekts würden Elektronen einzeln und nacheinander durch solche 0D RTDs tunneln, was eine Vielzahl von Experimenten zum spinabhängigen Einzelelektronentransport ermöglicht [19, 20]. Weil der laterale Einschluss durch ein elektrostatisches Gate es erfordert, dass die hauptsächliche Resonanz einer RTD bei sehr niedrigen Spannungen liegt, wurden Möglichkeiten untersucht die Resonanzposition mittels band-gap-engineering zu beeinflussen. Die I-V Kennlinien hergestellter RTDs zeigen bei 4.2 K bis zu fünf Resonanzen im Bereich zwischen 0 V und 0.8 V, sowie ein peak-to-valley Verhältnis bis 2.5. Wenn die Quantentrogbreite systematisch von 5.3 nm auf 15.2 nm erhöht wird, wobei alle weiteren Parameter nominell gleich bleiben, werden alle Resonanzen zu niedrigeren Spannungen verschoben und der Spannungsabstand zwischen ihnen verringert sich. Wenn Cd im Quantentrog einlegiert wird reduziert sich dessen Bandlücke und die Resonanzspannungen werden damit ebenfalls verringert. Mit letzterer Methode konnte die Resonanzspannung von über 150 mV bis auf weniger als 20 mV abgesenkt werden. Lateraler Einschluss des Quantentrog-Zustandes durch ein elektrostatisches Gate sollte mit solchen Strukturen möglich werden.

Eine alternative Möglichkeit, resonantes Tunneln durch einen 0D Zustand zu erreichen, bietet der Einbau selbstorganisierter CdSe Quantenpunkte (QDs) in eine RTD anstelle eines Quantentroges [11, 21]. Um solche QD RTDs gezielt herstellen zu können, wurden die optischen und strukturellen Eigenschaften von CdSe QD Ensembles in ZnSe (Zn,Be)Se und (Zn,Be,Mn)Se Barriereschichten untersucht. In $\mathrm{Zn_{0.8}Be_{0.2}Se}$ eingebettete CdSe QDs zeigen bei kleinen Bedeckungen (etwa 1 ML und weniger) in PL eine Peak Energie, die um etwa den Betrag des Bandlückenunterschieds der Barriereschichten höher ist als die Peak Energie von in ZnSe eingebetteten QDs. Bei höherer Bedeckung ist kein Einfluss des Barrierenmaterials messbar. Nicht überwachsene CdSe Schichten zeigen in AFM unabhängig vom Barrierenmaterial eine hohe Dichte ($10^{10} - 10^{11}$ cm^{-2}) wenige nm hoher, aneinandergrenzender Inseln. Basierend auf diesen Vorarbeiten wurden magnetische und nichtmagnetische QD RTDs mit selbstorganisierten CdSe Quantenpunkten hergestellt. Bei kleinen Spannungen zeigen ihre I-V Kennlinien ausgeprägte Resonanzpeaks aufgrund von Tunneln durch einzelne QDs. Während Resonanzen einer nichtmagnetischen QD RTD von einem äusseren Magnetfeld nahezu unbeeinflusst bleiben, spalten sich solche einer magnetischen QD RTD deutlich auf. Die brillouinartige Aufspaltung deutet auf resonantes Tunneln durch die spinaufgespaltenen Niveaus einzelner QDs hin. Interessanterweise zeigen die Resonanzen magnetischer QD RTDs, wie schon von Gould et al. beobachtet [11], eine kleine Aufspaltung auch ohne Anlegen eines äusseren Feldes.

Summary

II-VI diluted magnetic semiconductors (DMS) have long been known for their extraordinary magnetic properties, such as the giant Zeeman effect and the Faraday rotation [1]. The rise of the field of spintronics, which uses the electron spin instead of its charge to store or process information [2, 3, 4], has led to renewed research interest for magnetic semiconductors. Integrating non-volatile magnetic data storage and information processing within a single semiconductor chip, as envisioned by spintronics, requires ferromagnetic semiconductors that retain their magnetic properties up to room temperature. II-VI DMS are paramagnetic, and their unique magnetic properties are limited to low, cryogenic temperatures. However, since an ideal room temperature ferromagnetic semiconductor has not been found yet, diluted magnetic II-VI semiconductors can serve as a valuable testbed to explore spintronic device concepts. Examples of such concepts include the spin LED [5, 6], spin superlattices [7, 8], diluted magnetic resonant tunneling diodes [9, 10, 11, 12], diluted magnetic single tunnel barrier structures [13, 14], and spin injection into quantum dots [15]. Apart from the application in potential spintronic devices, research on such concepts improves our understanding of the electronic and optical properties of solids.

The contribution of the present thesis consists of three parts. They are centered around investigating certain semiconductor heterointerfaces relevant to spin injection, exploring novel, diluted magnetic single barrier tunneling structures, and further developing diluted magnetic II-VI resonant tunneling diodes.

The first part contains a comprehensive study of the electronic properties of the ZnSe / GaAs(001) heterointerface, which plays a crucial role in spin injection from II-VI DMS into GaAs [5, 15], and which is a prototype of the so-called heterovalent heterointerfaces [16]. We propose a new growth start process for MBE growth of ZnSe on GaAs(001), which leads to ZnSe / GaAs interfaces with a very low interface potential barrier and thereby to significantly improved electronic transport properties [17]. We have prepared n-ZnSe / n-GaAs heterointerfaces by MBE, with a systematically varied predeposition of small amounts of Zn or Se on (2×4) reconstructed GaAs(001) starting surfaces. The samples are characterized by temperature-dependent electric transport across the interface, electrochemical capacitance-voltage profiling, Raman spectroscopy, and high-resolution x-ray diffraction. We find that the potential barrier in the conduction band at a Zn-rich interface is as high as 550 meV, and it gradually decreases with Se predeposition down to about 70 meV. Concomitantly the resistance

of the interface is reduced by several orders of magnitude. A large depletion region at the heterointerface, about 50 nm wide, is assigned to significant intermixing of acceptor-type atoms, resulting in an effective electron deficit of $1.5 \times 10^{13}\,\mathrm{cm}^{-2}$. The depletion width and the acceptor density around the interface are nearly independent from the growth start procedure. Se predeposition, however, partially shifts the depletion region at the heterointerface from GaAs into ZnSe, compared to Zn predeposition. The results are discussed on the basis of a band-bending model accounting for variable band offsets, interface state density and atomic interdiffusion profiles depending on growth start. It is expected that such low-barrier interfaces significantly improve spin-transport from ZnSe based DMS into III-V materials.

The second part experimentally demonstrates a new spin filter concept based on spin-dependent tunneling through a single DMS barrier. An undoped (Zn,Be,Mn)Se barrier layer is embedded between n-type ZnSe injector and collector layers. The barrier in the conduction band at B = 0 T is mainly given by the Be concentration, and is about 50 mV to 100 mV high. The Mn concentration is about 8 %. Due to the giant Zeeman effect in the DMS barrier layer, an external magnetic field decreases (increases) the barrier height and increases (decreases) the tunnel probability for spin-down (spin-up) electrons. Thereby the structure acts as a tunable spin-filter for tunneling electrons. We have fabricated several samples with varied barrier height and thicknesses, and have analyzed their current-voltage characteristics at Helium temperature as a function of the magnetic field up to 6 T. The samples show non-linear current-voltage characteristics and a negative magnetoresistance, as expected for spin-dependent tunneling in such structures. At B = 6 T the resistance is about one third of the value measured at B = 0 T. Changing the barrier height and thickness causes a variation of the I-V characteristics, which is in agreement with a simple tunneling transport model. The magnetoresistance, however, is largely independent of the barrier height and thickness, and possible reasons for this are discussed. A direct measurement of the spin polarization, e.g. by optical methods, remains to be given. Simple model calculations, however, predict possible spin polarizations well above 90%, depending on the barrier properties.

The third part is focused on diluted magnetic II-VI resonant tunneling diodes (RTDs). By spin-dependent resonant tunneling through a DMS quantum well or quantum dot, such RTDs allow to switch the spin orientation of tunneling electrons simply by tuning an applied voltage rather than a magnetic field [9, 11]. A method to determine the thickness and composition of the double-barrier structure of such RTDs using high resolution x-ray diffraction is presented [18]. This is non-trivial, since the usually less than 10 nm thin barrier layers have a low scattering volume compared to the surrounding, about 1 μm thick contact and buffer layers, and since x-ray interference between the barrier layers complicates the diffraction pattern.

Using this technique for MBE growth control, several series of II-VI DMS RTDs are fabricated and characterized, with the aim of developing structures which allow the lateral confinement of the resonant state from two to zero dimensions (0D). Due to the Coulomb-blockade effect, electrons would tunnel through such 0D RTDs one-by-one, allowing a multitude of experiments on spin-dependent, single-electron transport [19, 20]. Since lateral confinement by an electrostatic gate requires the main resonance of an RTD to be at very low bias, ways to influence the resonance position by band-gap engineering are explored. At 4.2 K the I-V characteristics of the fabricated DMS RTDs show up to five resonances between 0 V and 0.8 V bias, and a peak-to-valley current ratio up to 2.5. Systematically increasing the quantum well width from about 5.3 nm to 15.2 nm, all other parameters being nominally constant, moves all resonances to lower bias and decreases the voltage separation between consecutive resonances. Alloying the quantum well with Cd reduces its band gap and thereby also reduces the resonance voltages. Such RTDs with low bias resonances possibly allow for lateral confinement of the quantum well state by the application of an electrostatic gate.

An alternative route towards 0D resonant tunneling is by replacing the DMS quantum well with self-assembled CdSe quantum dots (QDs), as shown in [11, 21]. As a prerequisite for such structures, the optical and structural properties of CdSe QD ensembles embedded in ZnSe, (Zn,Be)Se, and (Zn,Be,Mn)Se barrier layers are studied by PL and AFM. At small coverages (about 1 ML or less), the PL peak energy of CdSe QDs embedded in $Zn_{0.8}Be_{0.2}Se$ barriers is higher than that of QDs embedded in ZnSe. The difference is close to the band-gap difference of the barrier layers. At higher coverages no influence of the barrier layers could be detected. Uncapped CdSe layers show a high density ($10^{10} - 10^{11}$ cm^{-2}) of shallow, abutting islands, independent of the barrier material. Based on these results, magnetic and nonmagnetic QD RTDs with self assembled CdSe QDs are fabricated. At low bias voltages their I-V characteristics show pronounced resonance features due to tunneling through individual QDs. While the resonances of nonmagnetic QD RTDs are hardly affected by an external magnetic field, those of a magnetic QD RTD show a clear splitting when a magnetic field is applied. The Brillouin-like splitting suggests that it is due to resonant tunneling through the spin-split states in single QDs. Interestingly, the resonances of magnetic QD RTDs also show a finite splitting even when no magnetic field is applied, similar to that described in [11].

Chapter 1

Introduction

At the beginning of the 21st century, information technology has pervaded many aspects of life, society and economy in the western world. The ubiquity of computing power, mobile devices, and fast data communication is made possible by the tremendous miniaturization and cost reduction of microelectronic circuits, which has followed Moore's law for nearly 40 years[1]. In 1959 Richard Feynman pointed the way towards nanotechnology with his famous lecture "There is plenty of room at the bottom". For the semiconductor industry this statement will soon no longer be true, since the size of individual transistors on an integrated circuit rapidly approaches the size of individual atoms[2]. At this size the true, quantum mechanical nature of materials and particles dominates, putting a fundamental limit to further miniaturization. Thus a new paradigm for information technology is required, if its progress is to be continued.

One idea is to harness the spin of the electron in addition to or instead of its charge to process and store information [2, 3]. This approach is often termed spintronics, and it is a dynamic area of physics research since the discovery of the giant magnetoresistance (GMR) effect in 1988 [23]. GMR describes a spin-related resistance effect in metals, but its remarkably successful commercial application, e.g. in hard drive read heads and in non-volatile magnetic random access memory (MRAM), has spurred the interest in semiconductor spintronics as well. It has also been encouraged by experiments showing coherent spin transport over long distances [24] and long spin dephasing times [25] in semiconductors.

The numerous possibilities opened up by semiconductor spintronics have been reviewed in [4]. One potential advantage is operation speed. In conventional devices, which are based on manipulating small quantities of electric charge to encode the basic bits of information '1' and '0', speed is limited by the device capacitance and the drive current. In a spintronic device, which instead uses coherent switching of the electron

---

[1] "The number of transistors incorporated in a chip will approximately double every 24 months", Gordon Moore, Intel Corp. (~1975). www.intel.com

[2] By 2011 the physical gate length of an individual transistor in a microprocessor has reached 24 nm, which is less than 50 times the lattice constant of crystalline silicon (0.543 nm) [22].

spin between its two possible orientations ↑ and ↓, the limit is given by the precession frequency of electron spins in a magnetic field, which is in the GHz to THz range.

Adding ferromagnetic properties to semiconductors could also allow to integrate non-volatile, magnetic data storage with logic circuits in the same material system. Magnetic solid-state memory technologies, like MRAM [26] or the "racetrack memory" [27], can combine non-volatility (i.e. they don't loose their memory when they are not powered) with fast write times and a long lifetime, and have the potential to become a universal memory technique. Integrating them into semiconductor logic chips would allow instant-on electronic systems on a single chip.

A long-term goal is the possibility to realize quantum computing using spins in semiconductors [28]. Quantum computing aims to drastically improve the performance of many important computational algorithms, such as prime number factorization [29] or searching [30], by exploiting coherent interactions between quantum mechanical two-level systems. Using the two spin orientations of an electron confined in a semiconductor quantum dot or impurity has several potential advantages over other candidate systems for quantum computing, including scalability, their fixation in space, and being able to address them electrically.

Since the conventional semiconductors like Si, Ge, or GaAs, are diamagnetic and offer little means to influence electron spins, ways to polarize, manipulate, and detect electron spins in semiconductors need to be developed, in order to realize the above possibilities. Optical methods, where circularly polarized photons transfer their angular momentum to electrons, are one possibility, but electric techniques would be preferable for devices.

The currently most promising way is to make semiconductors magnetic by introducing a small quantity of magnetic ions, such as Mn, Cr, Fe, or Eu. This has historically been the realm of II-VI semiconductors, such as CdTe or ZnSe [1]. The resulting diluted magnetic semiconductors (DMS) are known for a strong amplification of magnetic effects due to an interaction of the magnetic ions with sp band electrons, causing a giant Zeeman effect and Faraday rotation. However, these materials are usually paramagnetic, and are limited to low temperatures. III-V semiconductors doped with a few per cent of Mn, such as (Ga,Mn)As, are ferromagnetic, but their Curie temperature is still far below room temperature [31, 32]. Developing ferromagnetic semiconductors that retain their magnetic properties beyond room temperature is the goal of intense research efforts going on world wide. Several candidates have been identified, but an ideal material has yet to be found [33].

Until a viable room temperature ferromagnetic semiconductor is developed, II-VI diluted magnetic semiconductors can serve as a valuable test-bed to explore potential spintronic device concepts and spin related effects. Examples of spintronic device concepts already realized in II-VI DMS include the spin LED [5, 6], spin superlattices [7, 8], spin injection into quantum dots [15], spin-dependent resonant tunneling diodes [9, 10, 11, 12], and other spin-dependent tunneling structures [13, 14].

Compared to (Ga,Mn)As, II-VI DMS have the advantage that divalent magnetic impurities like Mn are incorporated isoelectronically. This allows to control magnetic and electric doping independently, which is important in heterostructure device design. Even though not a mainstream semiconductor, the materials properties and growth techniques for high-quality crystals are relatively well known particularly for ZnSe, in part due to past research activities directed towards developing ZnSe based, blue-green emitting optoelectronic devices. The limitation of II-VI DMS to low temperature may also not be a hindrance for some applications which promise sufficient merit to make an operation at cryogenic temperatures economically viable. The superconducting electromagnets employed in magnetic resonance imaging instruments in hospitals all over the world are just one example of technology that is cooled to liquid helium temperatures for daily operation.

It is the aim of the present thesis to improve existing and to explore new spintronic devices using (Zn,Mn)Se based DMS, and to contribute to a better understanding of the relevant semiconductor interfaces. Special focus is put on a new way to filter electron spins using a single DMS tunnel barrier, and on resonant tunneling diodes, which are further developed in a direction which will allow spin-dependent tunneling through a semiconductor quantum dot.

Chapter 2 begins with a description of the basic structural, electronic, and magnetic properties of the diluted magnetic II-VI semiconductor material system of (Zn,Be,Cd,Mn)Se. The calculation of self-consistent band-diagrams of semiconductor heterostructures is briefly introduced, followed by a detailed discussion of tunneling in semiconductor single- and double barrier structures based on transfer matrix calculations.

Chapter 3 provides an overview over the epitaxial growth of (Zn,Be,Cd,Mn)Se layers by MBE, and over the characterization methods RHEED, XRD, AFM, PL, and ECV. Particular emphasis is put on XRD, since it plays an integral role in the characterization of II-VI RTDs. A short description of lithographic processing of these layers into electronic device structures and their electric characterization is also given.

In **chapter 4,** selected properties of individual ZnSe epilayers, (Zn,Mn)Se DMS layers, (Zn,Cd)Se quantum wells and (Zn,Be)Se tunnel barriers are presented. A systematic analysis of the optical and structural properties of epitaxial CdSe quantum dots embedded in (Zn,Be)Se and (Zn,Be,Mn)Se matrices follows. It is based on the diploma thesis of J. Henke [34]. These layers form the building blocks for more complex heterostructures discussed in the following chapters.

Chapter 5 is a systematic study of the structural and electronic properties of n-ZnSe / n-GaAs heterointerfaces [17]. A new ZnSe growth start process is presented, which markedly improves electron transport across such interfaces and may thereby allow for higher spin-injection efficiency from ZnSe based DMS into GaAs. The results of temperature dependent electric transport, ECV, and Raman measurements for interface potential barrier height, depletion widths, and interface state density are modeled with a 1-d Poisson solver. It is concluded, that the proposed growth start method leads to a reduction of the conduction band offset at the ZnSe / GaAs heterointerface.

Chapter 6 demonstrates a new device concept for electric spin polarization by spin-dependent tunneling through a single DMS tunnel barrier. After theoretical considerations on the basis of a coherent tunneling model, current-voltage and magnetoresistance characteristics of a series of such devices are shown. The experimental results are in good agreement with the model predictions and promise a high degree of spin polarization. Some open questions remain concerning the variation of the magnetoresistance characteristics with barrier height and thickness.

Chapter 7 explores several aspects of II-VI RTDs, which allow voltage controlled spin filtering by spin-dependent resonant tunneling through a DMS quantum well or quantum dot. The complex diffraction pattern of tensile-strained, (Zn,Be)Se based RTDs in HRXRD is analyzed, and it is shown how such measurements can yield precise information about the quantum well and tunnel barrier thickness and composition [18]. Next, the influence of the variation of the quantum well thickness and composition on the position of resonances in the I-V characteristics of such RTDs is investigated. The chapter and the thesis close with the discussion of 0D resonant tunneling in RTDs with self-assembled CdSe quantum dots.

Chapter 2

Theory

This chapter begins by describing the basic structural, electronic, and magnetic properties of the diluted magnetic II-VI semiconductor material system of (Zn,Be,Cd,Mn)Se. The calculation of self-consistent band-diagrams of semiconductor heterostructures is then introduced briefly, followed by a detailed discussion of tunneling in semiconductor single- and double barrier structures based on transfer matrix calculations.

2.1 The (Zn, Be, Cd, Mn)Se Semiconductor Material System

The base material for the semiconductor heterostructures fabricated in this work is the wide-gap II-VI semiconductor ZnSe. Its crystal structure is depicted in figure 2.1 on the left. It has a zincblende crystal structure, in which each Zn-atom is tetrahedrally coordinated by four Se atoms, and vice-versa. Its room temperature lattice constant is $a = 5.6684\,\text{Å}$ [35] and it has only a small mismatch of 0.27 % to GaAs with $a = 5.65325\,\text{Å}$. ZnSe can thus be grown with high quality on readily available GaAs substrates. The electronic band structure of ZnSe is depicted in figure 2.1 on the right. It has been calculated by Chelikowski et al. on the basis of non-local pseudopotential theory [36]. ZnSe has a direct band gap at the Γ point of 2.82 eV at low temperature, and about 2.7 eV at room temperature [35]. The lowest conduction band is the Γ_6 band, which has s-like symmetry and an effective mass of $m = 0.145\,m_0$ [35]. The highest valence band is the Γ_8 band, which has p-like symmetry and is split into a heavy hole band with $m_{hh} = 1.04\,m_0$ and a light hole band with $m_{lh} \approx 0.145\,m_0$ [35].

Figure 2.2 gives an overview over the lattice constant and the band gap of several elemental and compound semiconductors, including the material system of the II-VI "selenides" used in this work. Apart from ZnSe, this material system includes e.g. BeSe, MnSe and CdSe. The latter are not necessarily stable as binary compounds, but they can be alloyed well with ZnSe to vary the band gap and lattice constant.

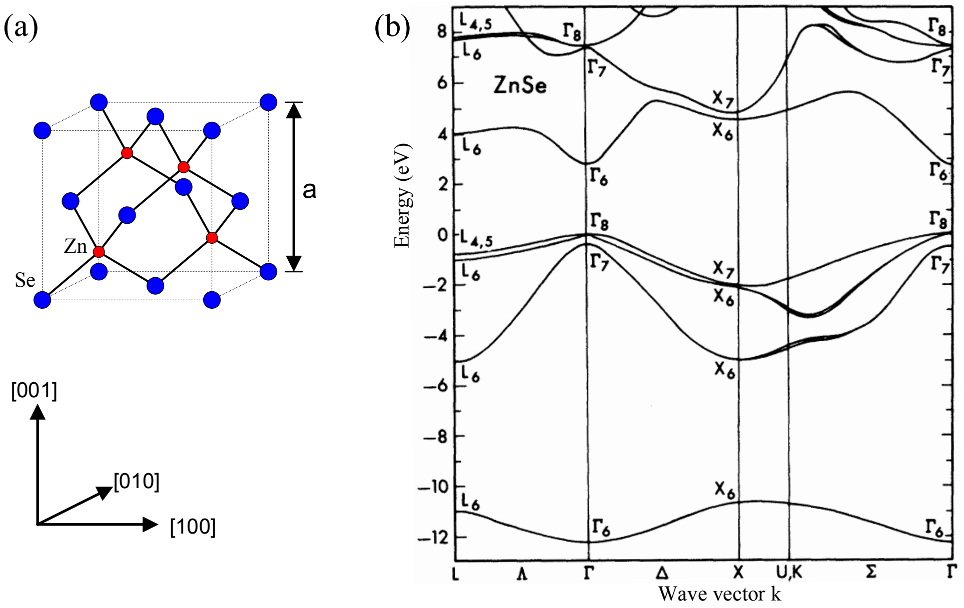

Figure 2.1: (a) Zincblende crystal structure. (b) Energy band structure of ZnSe obtained by nonlocal pseudopotential calculations (adopted from [36]).

Compared to other technologically important semiconductors, such as Si, GaAs, or CdTe, the II-VI selenenides have a relatively large band gap in the blue-green spectral region. For a long time this property has made them the focus of research efforts geared towards developing short-wavelength optoelectronic devices, but the attention has faded somewhat when GaN was established as the material of choice for such applications [37, 38].

The addition of Be to ZnSe increases the band gap and reduces the lattice constant. For Be concentrations higher than 46 % the band gap becomes indirect [40]. Be has also been reported to have a lattice hardening effect on ZnSe, as discussed in [41]. The addition of Cd has roughly the opposite effect on the band gap and the lattice constant. Adding Mn increases the lattice constant, but has a strong bowing effect in the band gap. E_g first decreases for low Mn concentration, reaches a minimum at about 4 %, and then increases rapidly. Above all, the addition of Mn introduces a wealth of magnetic effects due to the coupling of the half-filled Mn d-shell orbitals to conduction and valence band states (see section 2.2).

Literature values for the band gap E_g of the semiconductor alloys mainly used in this work are listed in table 2.2. The lattice constants and Poisson ratios used in the present work are listed in table 2.1. The energy gaps of alloy semiconductors containing more than three constituents (e.g. quaternary $\mathrm{Zn}_{1-x-y}\mathrm{Mn}_x\mathrm{Cd}_y\mathrm{Se}$) are calculated by combining these relationships.

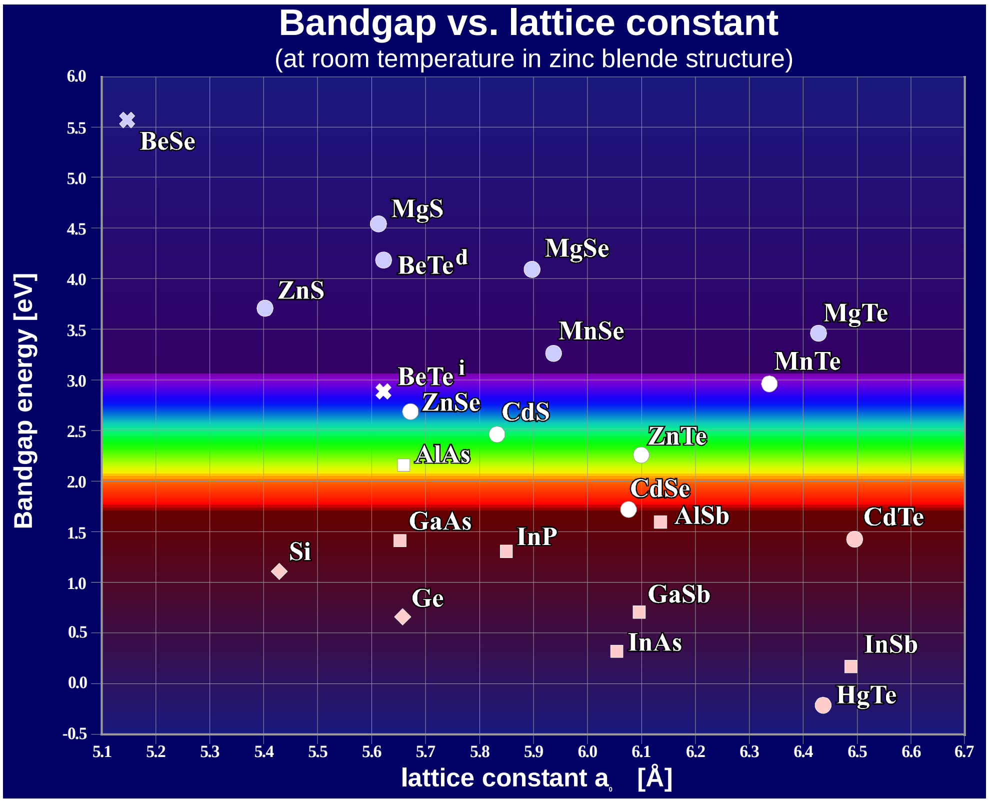

Figure 2.2: Band gap versus lattice constant for a variety of elemental and compound semiconductors [39].

	GaAs	ZnSe	BeSe	CdSe	MnSe
a (Å)	5.65325	5.6684	5.139	6.077	5.93
ν	0.311	0.387	0.297	0.381	0.405

Table 2.1: Room temperature lattice constant a and Poisson ratio ν of several binary semiconductors used in this work.

Material	$E_g(x)$	Reference
$Zn_xBe_{1-x}Se$	$2.82\text{eV} + 1.77\text{eV} \cdot x + 1.1\text{eV} \cdot x^2$	[42, 43]
$Zn_xMn_{1-x}Se$	$2.82\text{eV} - 0.145\text{eV} \cdot x + 4.073\text{eV} \cdot x^2$	[44, 45]
$Zn_xCd_{1-x}Se$	$2.82\text{eV} - 1.42\text{eV} \cdot x + 0.35\text{eV} \cdot x^2$	[35, 46]

Table 2.2: Fundamental band gap E_g at about 4 K as a function of composition for a number of ZnSe based ternary semiconductor alloys used in this work.

When two semiconductor materials with different band gaps are combined in a heterostructure, the question of how the conduction and valence bands are aligned at the interface is important for their electronic properties. A common rule of thumb states that, at interfaces between materials with a common anion (e.g. GaAs / AlGaAs or ZnSe / (Zn,Be)Se) most of the difference in band gaps occurs in the conduction band, while at interfaces between materials with a common cation most of the difference occurs in the valence band [47]. The conduction band offset (CBO) at ZnSe / (Zn,Be)Se heterointerfaces is reported to be 78% of the energy-gap difference [48]. For ZnSe / (Zn,Cd)Se heterointerfaces a CBO of 84 % is reported [46].

Even though p-type doping of ZnSe remains a challenge, it can be easily doped n-type using Chlorine or Iodine. Iodine forms a shallow donor state in ZnSe with an ionization energy of about 26 meV. Carrier densities in the low $10^{19}\,\mathrm{cm}^{-3}$ range can be achieved [35, 49].

2.2 Diluted Magnetic Semiconductors

In diluted magnetic semiconductors (DMS), a small fraction of the cations of the host crystal is replaced by magnetic ions, such as Mn, Fe or Cr. The interaction of these magnetic ions with each other and with states in the conduction and valence bands leads to a wealth of magnetic effects, including a giant Zeeman effect [1].

The most extensively studied magnetic ingredient in semiconductors is Mn. In II-VI semiconductors, the divalent Mn is incorporated isoelectronically and is not automatically accompanied by acceptor states, as e.g. in (Ga,Mn)As . This allows to control the doping density and the magnetic properties of layers independently.

A single Mn atom in the ground state has the electronic configuration $[Ar]4s^2 3d^5$. According to Hunds rules, the five electrons in the Mn 3d shell align their spins in parallel, while the electrons in the other, completely filled shells align their spins anti parallel, resulting in the total spin $S = 5/2$ for the Mn atom. When Mn is incorporated in a II-VI zincblende crystal it contributes its two 4s electrons to the formation of the crystal bonds, while the 3d electrons stay localized. A strong exchange interaction couples the conduction and valence band states to the Mn d orbitals, and causes, among other effects, a very large spin splitting of the bands when the localized Mn spins are aligned by an external magnetic. The interaction is termed s/p-d exchange interaction, referring to the symmetry of the conduction and valence band, and the large spin splitting of the bands in an external field is reffered to as the giant Zeeman effect.

The spin-dependent shift of the conduction band edge due to the s/p-d exchange interaction in a magnetic field is

$$\Delta E_{CB} = \pm \frac{1}{2} N_0 \alpha x \langle S_z \rangle , \tag{2.1}$$

where the factor $\pm{}^{1}\!/_{2}$ is due to the magnetic quantum number $m_j = \pm{}^{1}\!/_{2}$ of spin-up and spin-down electrons in the conduction band, N_0 is the number of cations (e.g. Zn atoms) per unit volume, x is the fraction of Mn ions on cation places, and $\langle S_z \rangle$ is the thermal average of the z-component of the Mn spins [1]. $N_0\alpha$ is the material dependent exchange integral over the Mn d states and the conduction band states. For (Zn,Mn)Se $N_0\alpha = 0.26$ eV has been determined [50]. For the Γ_8 valence band the expression is analogous, with $m_j = \pm{}^{3}\!/_{2}, \pm{}^{1}\!/_{2}$ and with a different exchange integral $N_0\beta = -1.31$ eV [50]. In the following, the absolute value of ΔE_{CB} is referred to as the spin splitting of the conduction band edge. The total separation of the spin-up and spin-down sub level of the conduction band is $2\Delta E_{CB}$. The naming convention for the spin-directions in this thesis is such that the energy of spin-down (spin-up) electrons in the conduction band is reduced (increased) by the giant-Zeeman effect.

II-VI DMS are paramagnetic. The thermal average of the z-component of the Mn spins $\langle S_z \rangle$ in an external magnetic field follows a modified Brillouin function [51]:

$$\langle S_z \rangle = S_{\mathrm{eff}} \mathfrak{B}_{5/2} \left(\frac{\frac{5}{2} g \mu_B B}{k : B(T + T_0)} \right) . \tag{2.2}$$

Here, $\mathfrak{B}_{5/2}$ is the Brillouin-function for a spin of 5/2, g is the Landé factor of Mn (g = 2), μ_B is the Bohr-magneton, k_B is the Boltzmann constant, B is the applied magnetic field, and T is the temperature. The quantities S_{eff} and T_0 are phenomenologic parameters introduced to account for antiferromagnetic coupling between adjacent Mn atoms: S_{eff} represents the effective value of the Mn spins, which may be lower than 5/2, and T_0 is a correction to the temperature. Both depend on the concentration of magnetic impurities. For (Zn,Mn)Se with 8% Mn, $S_{\mathrm{eff}} = 1.13$ and $T_0 = 2.35$ have been determined [44]. The calculated spin splitting of the conduction band edge due to the s/p-d exchange interaction is shown in figure 2.3 for $\mathrm{Zn_{0.92}Mn_{0.08}Se}$ and at three different temperatures. At low temperatures and in a moderate magnetic fields of a few Tesla, this exchange interaction induced spin splitting can easily be on the order of ≈ 10 meV. This is much larger than the normal Zeeman splitting or Landau quantization effects, which are far below 1 meV under the same conditions.

Note that the above model only considers Mn ions situated on cation sites in the zincblende lattice. Mn interstitials or antisites are not included.

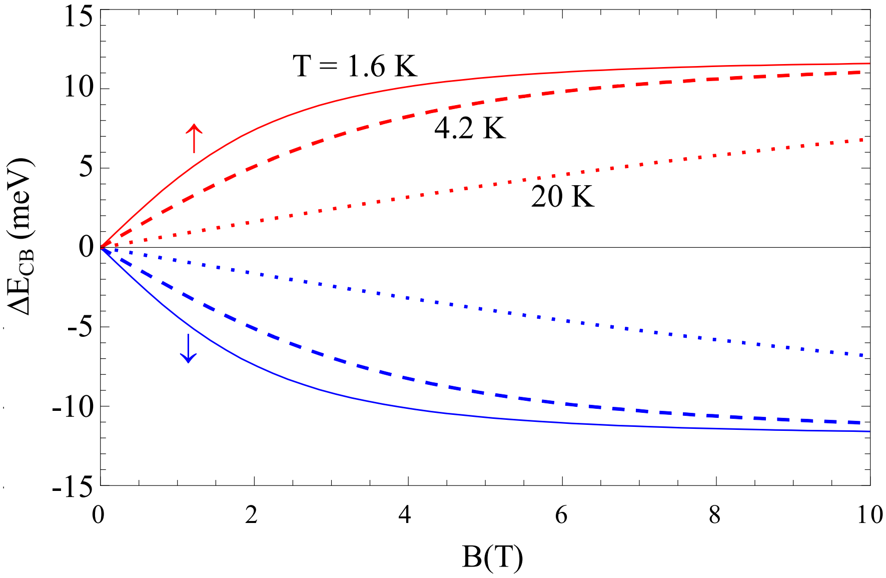

Figure 2.3: Spin splitting of the conduction band ΔE_{CB} due to s/p-d exchange interaction as a function of the magnetic field B, calculated for $Zn_{0.92}Mn_{0.08}Se$ at three different temperatures. By convention, in the rest of this work spin ↓ is defined as the spin direction for which ΔE_{CB} is negative.

2.3 Semiconductor Heterostructures and Calculation of Band Diagrams

Envelope function approximation The electronic properties of semiconductor heterostructures in this thesis are described in terms of the envelope function approximation. It states that “heterojunctions of dissimilar materials, both of which can be well represented by the effective mass approximation, can be described by a material potential, which derives from the band offsets” [52]. In other words, electrons and holes in the conduction and valence bands of a layered semiconductor heterostructure are assumed to obey the 1-d Schrödinger equation

$$-\frac{\hbar^2}{2m}\frac{\partial^2}{\partial z^2}\psi(z) + V(z)\psi(z) = E\psi(z), \tag{2.3}$$

where m is the carrier effective mass, and V(z) includes a material dependent potential given by the band discontinuities at heterointerfaces between layers of different materials. The microscopic details of the crystalline potential given by the individual ionic cores are neglected and are replaced by the long range material potential. Consequently, ψ in equation 2.3 is not the full, microscopic wavefunction, but represents an envelope function which only captures the long-range variation of the probability density.

The term “band-gap engineering” has been coined for the judicious combination of layers of different semiconductor materials and doping profiles [53]. With this approach, artificial potential landscapes for electrons and holes can be created, which allow electronic and optical devices with unique and novel properties. These include quantum well and quantum cascade lasers, high electron mobility transistors, and resonant tunneling diodes.

Calculation of band diagrams and carrier density profiles Band diagrams and carrier density profiles of doped semiconductor heterostructures are calculated in this work either purely classically based on Poisson’s equation, or by taking into account quantization effects by self-consistently solving the Poisson- and Schrödinger equations. Both is done using the numeric semiconductor simulation software *nextnano*. An overview of the calculation scheme and of the numerical methods employed by *nextnano* can be found in [54, 55, 56].

In the following, a brief overview is given over the basic equations as well as the computational procedure to calculate one-dimensional band-diagrams of doped semiconductor heterostructures. The starting point is the envelope function approximation and the assumption that carriers are locally in equilibrium. The latter means, that carrier can be described by a spatially varying Fermi level $E_F(z)$, which is different for electrons and for holes. The Poisson equation in a semiconductor material in 1-d is given by

$$-\frac{1}{e}\frac{\partial}{\partial z}\left[\varepsilon_0\varepsilon_r(z)\frac{\partial\phi}{\partial z}\right] = -n(z) + p(z) + N_D^+(z) - N_A^-(z) \tag{2.4}$$

where e is the elementary charge, $\varepsilon_r(z)$ is the material dependent dielectric constant, $\phi(z)$ is the electrostatic potential, n(z) and p(z) are the densities of electrons and holes, and $N_D^+(z)$ and $N_A^-(z)$ are the densities of ionized donor and acceptor impurities, respectively. The density of ionized donors is related to the total donor density N_D by

$$N_D^+(z) = \frac{N_D(z)}{1 + g_D \exp\left\{\frac{E_F(z)-E_D}{k_B T}\right\}}, \tag{2.5}$$

where $g_D = 2$ is the degeneracy of donor levels (2 for spin), $E_F(z)$ is the local Fermi level of electrons, and E_D is the donor ionization energy. A similar relationship holds for acceptors, with a higher degeneracy $g_A = 4$ (due to heavy hole / light hole band degeneracy at the Γ point) and with the Fermi level of holes. The electron current density due to drift and diffusion current is given by

$$j(z) = -e\mu_n n(z)\frac{\partial\phi}{\partial z} + eD_n\frac{\partial n}{\partial z}, \tag{2.6}$$

where μ_n is the electron mobility, and D_n is the diffusion coefficient. Within the framework of a local Fermi level model this familiar equation is transformed to

$$j(z) = \mu_n n(z) \frac{\partial E_F}{\partial z}. \tag{2.7}$$

In the steady state and in the absence of carrier generation or recombination the current continuity equation is

$$\frac{\partial j}{\partial z} = 0. \tag{2.8}$$

It relates the local Fermi level to the local carrier density.

This system of equations, which is up to now purely classical, is solved iteratively by alternately calculating the carrier density for a fixed Fermi level and then updating the Fermi level for fixed carrier densities. A steady state is reached when consecutive iterations lead to similar results.

The carrier densities are calculated either fully classically, or by using the quantized states obtained from the Schrödinger equation 2.3. In the latter approach the Schrödinger equation with the potential $V(z) = E_{CB}(z) - \phi(z)$ is solved numerically during each iteration. The resulting Eigenstates are then populated with carriers according to the Fermi distribution, and the local carrier density is composed of the wavefunctions of the occupied states.

As an example, figure 2.4 shows the band-diagram of a 10 nm n-type (Ga,In)As quantum well, calculated by self-consistent solution of the Poisson- and Schrödinger equations with *nextnano* [54]. Two bound states are found in the quantum well (thick dots), only the lower one is below the Fermi level E_F and is thus occupied. The band-diagram obtained with *nextnano* is in good agreement with that obtained from more detailed, non-equilibrium Greens function calculations.

The above model is limited to non-degenerate (i.e. low-doped) semiconductors and to a vanishing current density j = 0. For degenerate semiconductors the impurity states are no longer separated from each other and from the band edges, but they form an impurity band which can merge with the conduction or valence band edge. Equation 2.5 is thus no longer valid. As an approximation it is sometimes assumed that all impurities are fully ionized, which corresponds to assuming a large and negative impurity ionization energy. Usually $E_D = -2$ eV works well for *nextnano*.

The present work is focused on uni-polar, n-type heterostructures, where most of the physics happens in the conduction band. For this reason, band mixing as treated in $k{\cdot}p$ theory is neglected, and only the conduction band is considered in Poisson-Schrödinger calculations.

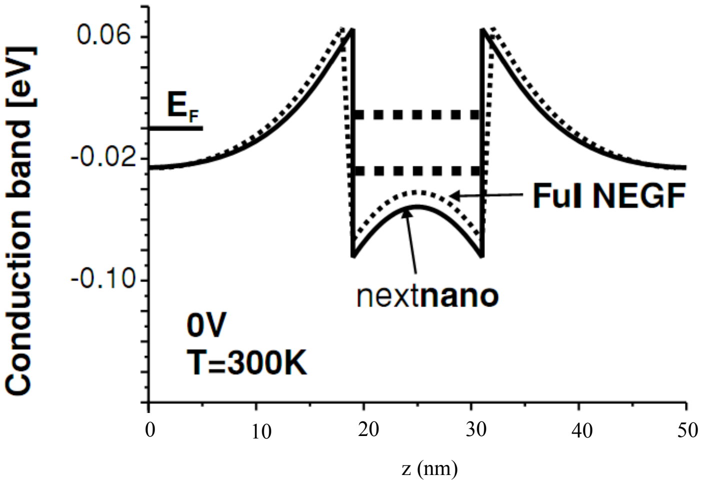

Figure 2.4: Band-diagram of a (Ga,In)As quantum well obtained from self-consistent solution of the Poisson and Schrödinger equations with *nextnano* (solid line) and from non-equilibrium Greens function calculations (dotted line). Adopted from [54].

2.4 Tunneling in Semiconductor Heterostructures

This section lays out a basic model for the description of coherent tunneling conduction in single- and double barrier semiconductor heterostructures.

2.4.1 Transfer Matrix Formalism

The transfer matrix formalism provides a way to analytically calculate the probability of non-interacting electrons to tunnel through potential barriers consisting of an arbitrary number of rectangular blocks, i.e. a piecewise constant potential. The following introduction follows that in [57], but it is given in some detail here to correct a few minor mistakes. For a one-dimensional piecewise constant potential $V(z) = V_n$, the general solution of the stationary Schrödinger equation in each interval $z_n < z < z_{n+1}$ is a plane wave

$$\psi_n(z) = A_n \exp\{ik_n z\} + B_n \exp\{-ik_n z\}. \tag{2.9}$$

The complex wavenumber k_n is given by

$$k_n = \sqrt{2m(E_z - V_n)}/\hbar \tag{2.10}$$

where E_z is the kinetic energy of the movement of the particle in z-direction and m is the effective mass. At the steps z_n the boundary conditions

$$\psi_{n+1}(z_n) = \psi_n(z_n) \tag{2.11}$$

$$\frac{d\psi_{n+1}}{dz}(z_n) = \frac{d\psi_n}{dz}(z_n) \tag{2.12}$$

relate the wavefunction coefficients A_n and B_n in the n-th interval to those in the next interval $n+1$. The (2×2) transfer matrix $\mathfrak{T}_n$ is defined by

$$\begin{pmatrix} A_{n+1} \\ B_{n+1} \end{pmatrix} = \mathfrak{T}_n \begin{pmatrix} A_n \\ B_n \end{pmatrix} \tag{2.13}$$

and after some algebra it is obtained from the boundary conditions

$$\mathfrak{T}_n = \begin{pmatrix} \alpha_n^+ P_n & \alpha_n^- / Q_n \\ \alpha_n^- Q_n & \alpha_n^+ / P_n \end{pmatrix} \tag{2.14}$$

with the coefficients

$$\alpha_n^{\pm} = \frac{1}{2}\left(1 \pm \frac{m_{n+1}k_n}{m_n k_{n+1}}\right) \tag{2.15}$$

$$P_n = \exp\left\{i\left(k_n - k_{n+1}\right) z_{n+1}\right\} \tag{2.16}$$

$$Q_n = \exp\left\{i\left(k_n + k_{n+1}\right) z_{n+1}\right\}. \tag{2.17}$$

The total transfer matrix $\mathfrak{T}$ for a given potential landscape is obtained as the inner product of all individual matrices

$$\mathfrak{T} = \mathfrak{T}_{N-1} \cdot \mathfrak{T}_{N-2} \cdot \ldots \cdot \mathfrak{T}_1. \tag{2.18}$$

It relates the coefficients A_1 and B_1 on one side of the potential landscape to the coefficients A_N and B_N on the other side in an analytical (albeit often complex) expression. For a particle incident from the left (n = 1) the following “scattering boundary conditions” hold

$$A_1 = 1 \qquad\qquad B_N = 0. \tag{2.19}$$

By eliminating the coefficient B_1, the amplitude A_N of the wave traveling to the right in the rightmost interval is obtained

$$A_N = \mathfrak{T}^{11} - \frac{\mathfrak{T}^{12}}{\mathfrak{T}^{22}}, \tag{2.20}$$

where $\mathfrak{T}^{ij}$ denotes the coefficients of the total transfer matrix. The tunnel probability

T for a particle through the whole structure is the square of this amplitude

$$T = \left| \mathfrak{T}^{11} - \frac{\mathfrak{T}^{12}}{\mathfrak{T}^{22}} \right|^2 . \tag{2.21}$$

The right side of equation 2.21 is a complex but analytical expression, which only needs to be calculated once for a certain potential landscape - preferably using computer algebra software. The tunnel probability can be quickly evaluated for different particle energies, barrier heights and thicknesses, effective masses etc. In the following, transfer matrix results are presented for the tunnel probability of two selected potential landscapes, which are of importance for the rest of this work.

2.4.2 Single Tunnel Barrier

Tunnel Probability

Applying the transfer matrix formalism to a single rectangular potential barrier of the height Φ_b and thickness d_b yields the tunnel probability [58]

$$T_{SB}(E_z, \Phi_b, d_b) = \left(1 + \frac{\Phi_b^2}{4E_z(\Phi_b - E_z)} \sinh^2 \left\{ \frac{d_b \sqrt{2m(\Phi_b - E_z)}}{\hbar} \right\} \right)^{-1} . \tag{2.22}$$

A simpler and more intuitive expression can be derived using the WKB approximation[1], which assumes that the potential is slowly varying in space

$$T_{SB}(E_z, \Phi_b, d_b) \approx \exp \left\{ -2 d_b \frac{\sqrt{2m(\Phi_b - E_z)}}{\hbar} \right\} . \tag{2.23}$$

It is a good approximation to the exact transfer matrix solution in the limit of very high and thick barriers, $\Phi_b \to \infty$ and $d_b \to \infty$, and for $E_z \neq 0$.

The tunnel probability according to these two equations is plotted in figure 2.5 as a function of the incident electron energy E_z (a), the barrier thickness d_b (b), and the barrier height Φ_b (c). The free parameters are close to those of the structures discussed in chapter 6. As expected, the tunnel probability increases with the electron energy E_z and it decreases with the barrier height Φ_b and thickness d_b. Over a large range of parameters the agreement between the WKB approximation 2.23 and the transfer matrix result 2.22 is good.

Some important features of the transfer matrix result that are not captured in the approximation are (1) a vanishing tunnel probability for particles with $E_z = 0$, (2)

---

[1] A good introduction can be found at
http://farside.ph.utexas.edu/teaching/qmech/lectures/node48.html

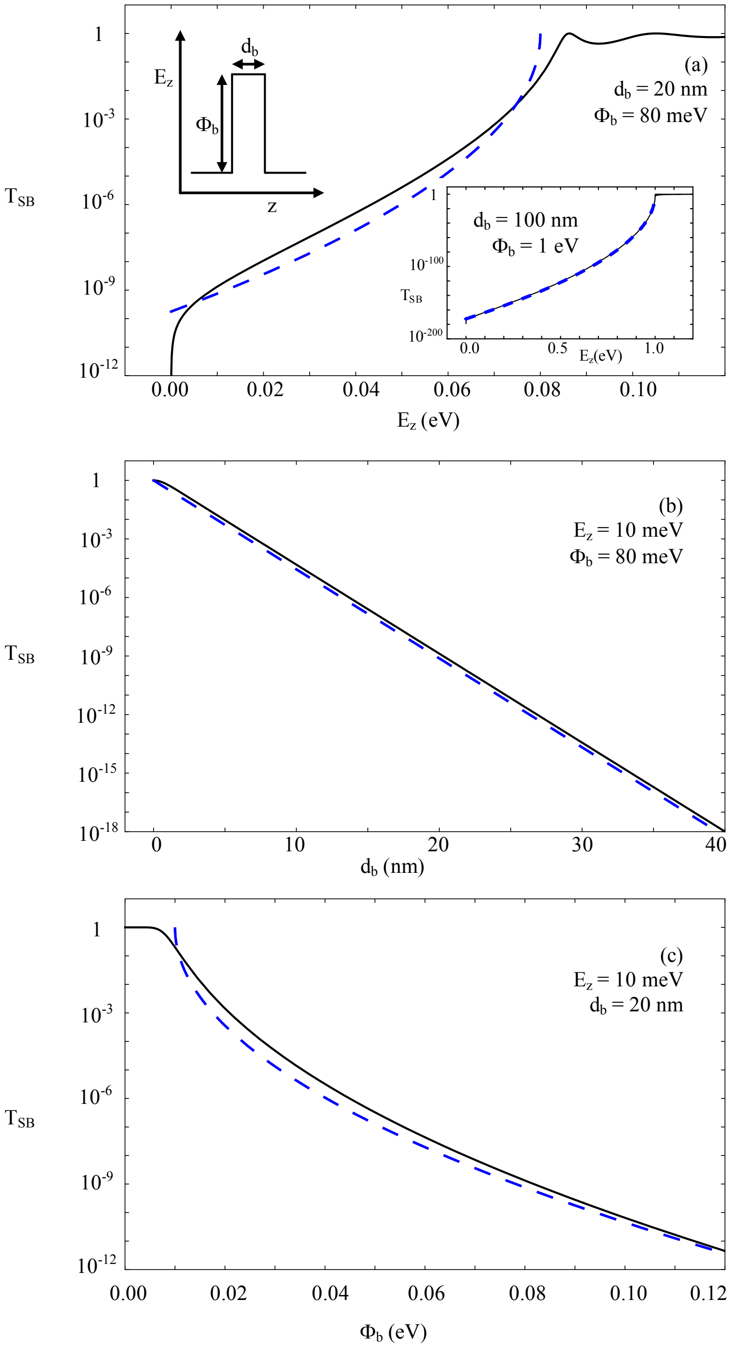

Figure 2.5: Tunnel probability T_{SB} through a single, rectangular potential barrier with the height Φ_b and the thickness d_b, calculated for an electron with kinetic energy E_z perpendicular to the barrier. The black, solid lines correspond to equation 2.22, which results from transfer matrix theory, and the blue, dashed lines correspond to the WKB approximation of equation 2.23. The inset of (a) shows that both models are in very good agreement for very high and thick barriers.

lower than unity tunnel probability for particles with $E_z = \Phi_b$, and (3) oscillations of the tunnel probability as a function of E_z for $E_z > \Phi_b$. For very high and thick barriers the WKB approximation approaches the transfer matrix result, as shown in the inset of panel (a) of figure 2.5.

I-V Characteristics

Electron transport through a single, solid state tunnel barrier has been treated theoretically by C. B. Duke in [59]. His focus is on metal-barrier-metal tunneling, but the calculated relationships are valid to a large extent also for semiconductor tunnel barriers. They are widely used in the literature to describe electron tunneling through semiconductor barriers at low bias voltages [57, 60, 61, 62, 63]. The current density between two electron reservoirs, between which a voltage V is applied and which are separated by an *arbitrarily shaped* tunnel barrier, is given by

$$J = \frac{e\,m}{2\pi^2\hbar^3}\int_0^\infty \mathrm{d}E_z\,T(E_z)\int_0^\infty \mathrm{d}E_{||}\left[f\big(E_z+E_{||}\big)-f\big(E_z+E_{||}+eV\big)\right]. \tag{2.24}$$

Here, $T(E_z)$ is the tunnel probability of particles traveling with a kinetic energy E_z perpendicular to the barrier, and $E_{||}$ is the kinetic energy of in-plane movement. f is the Fermi distribution $f(E) = \left[1+\exp\left\{(E-E_F)/k_BT\right\}\right]^{-1}$ at temperature T and with a Fermi energy E_F. The electron charge is denoted by e, and m is the effective mass. The density of states in the contacts is assumed to be constant. This assumption is valid when the tunneling electrons are emitted from a nearly 2-dimensional emitter, which is the case for the structures described in chapters 6 and 7. Image charge effects are also neglected, but they should only be relevant at very high electron densities, e.g. for metallic contacts. If the tunneling conditions are spin-independent, a factor of two has to be included on the right to account for the two electron spin orientations. Since temperature is included via the Fermi distributions, equation 2.26 describes tunneling conduction as well as thermally activated electron emission over the barrier, and mixtures of both (thermally activated tunneling).

The integral over $\mathrm{d}E_{||}$ in equation 2.24 can be solved analytically, resulting in the electron supply function [59]

$$S(E_z) = k_BT\cdot\ln\left[\frac{1+\exp\left\{-\left(E_z-E_F\right)/k_BT\right\}}{1+\exp\left\{-\left(E_z-E_F+eV\right)/k_BT\right\}}\right]. \tag{2.25}$$

It describes the temperature and bias dependence of the density of electrons available for tunneling between the two reservoirs. The current density without spin through an arbitrarily shaped tunnel barrier is thus

$$J = \frac{e\,m}{2\pi^2\hbar^3}\int_0^\infty \mathrm{d}E_z\,T(E_z)\,S(E_z). \tag{2.26}$$

To calculate the tunneling current through a particular potential barrier landscape, the corresponding tunnel probability has to be inserted. Since the tunnel probability generally depends on the applied bias voltage, it needs to be recalculated for each bias voltage. In the case of a single, rectangular tunnel barrier and for low voltages, the bias dependent tunnel probability can be approximated to first order with a reduced barrier height

$$\Phi_b \to \Phi_b - \frac{eV}{2}. \tag{2.27}$$

For the tunnel probability either equation 2.22 or the approximation in equation 2.23 can be used. The current density without spin through a single, rectangular tunnel barrier at low bias voltage is then

$$J = \frac{e\,m\,k_B T}{2\pi^2\hbar^3}\int_0^\infty \mathrm{d}E_z\, T_{SB}\left(E_z, \Phi_b - \frac{eV}{2}, d_b\right) \\ \ln\left[\frac{1+\exp\left\{-\left(E_z - E_F\right)/k_B T\right\}}{1+\exp\left\{-\left(E_z - E_F + eV\right)/k_B T\right\}}\right]. \tag{2.28}$$

Figure 2.6 shows J-V curves calculated by equation 2.28 for different tunnel barriers, and for $E_F = 20$ meV and $T \ll 1$ K. The curves are ohmic for low bias $V \ll E_F$, where the number of electrons available for tunneling increases linearly with bias voltage, and deformation of the tunnel barrier is still small. For higher bias, $V > E_F$, the number of electrons is approximately constant, but the reduction of the barrier with bias voltage is significant and increases the current exponentially.

Because of the strong dependence of the tunnel probability on the height and width of the tunnel barrier, the current density and the general I-V characteristics also depend critically on these parameters. Additionally, the effective mass of tunneling particles, the Fermi energy in the emitter and collector layers, i.e. the doping density in these layers, as well as voltage drop over these other layers may influence the I-V characteristics. A higher effective mass reduces the tunnel probability and thus the current density. A higher Fermi energy E_F in the emitter increases the number of electrons available for tunneling and reduces their effective barrier height, which both increases the tunnel current density.

If the tunnel probability is not the same for both spin orientations, as it is the case e.g. in the DMS tunneling structures described in chapters 6 and 7, electric transport may be described as parallel conduction through independent spin-channels [64, 65]. The total current density is then

$$J = J_\uparrow + J_\downarrow \tag{2.29}$$

where equation 2.28 describes the individual current densities $J_\uparrow$ and $J_\downarrow$ through the two spin channels by including a spin-dependent tunnel probability.

In realistic tunnel devices, only a fraction of the total voltage applied between two

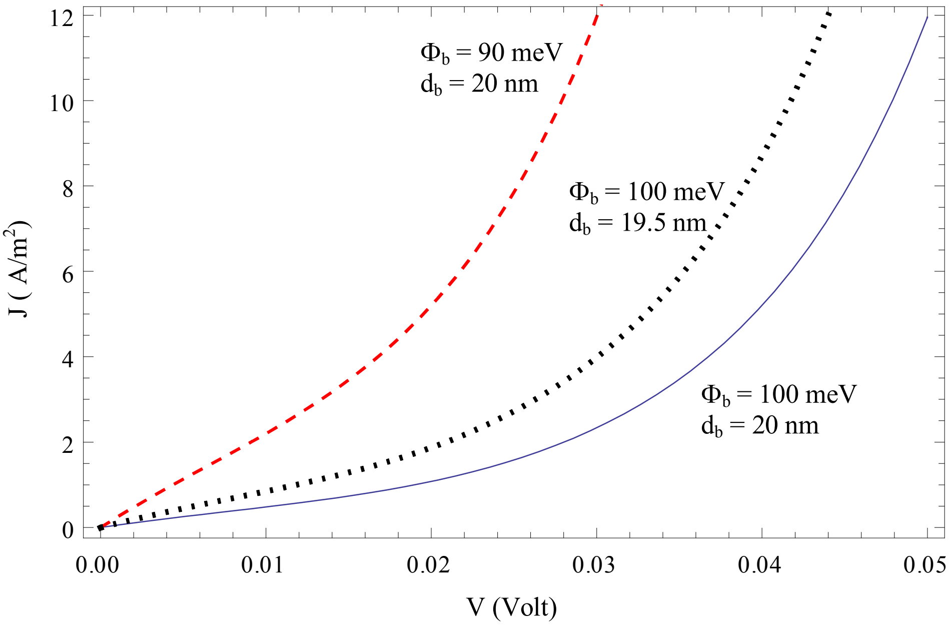

Figure 2.6: Current density J calculated by eq. 2.28 as a function of bias voltage V for single tunnel barriers of different height Φ_b and width d_b. The Fermi energy is $E_F = 20$ meV, the temperature is $T \ll 1\,K$, and the effective mass is $m = 0.15\,m_0$.

contacts drops over the tunnel barrier. To account for this parasitic voltage drop over the contact and emitter/collector layers, the voltage V in equation 2.28 is divided by a lever arm $\alpha > 1$ [66, 67].

This ideal model only describes coherent tunneling conduction through a semiconductor barrier. Other transport channels, such as shortcuts in the barrier (e.g. due to defects), parallel conduction on the sidewalls of vertical tunneling structures, resonant tunneling through impurities in the barrier, or any effects that destroy coherence of tunneling, are not considered.

2.4.3 Symmetric Double Barriers and Resonant Tunneling

When two potential barriers are placed next to each other at a distance comparable to the electron deBroglie wavelength, quantization effects lead to the formation of quasi-bound states between the barriers. Electrons with a kinetic energy equal to the quantization energy of these states have a higher transmission probability up to unity [58, 57]. The effect is similar to the transmission of photons with matching wavelengths through a Fabry-Perrot interferometer [68]. In the following, the tunnel probability of electrons through such double-barrier structures and its dependence on quantum well and barrier properties is discussed, followed by a short description of the corresponding I-V characteristics.

Tunnel Probability

Figure 2.7 depicts the tunnel probability as a function of the incident electron energy in the z-direction E_z, calculated by the transfer matrix method for three different rectangular double-barrier structures. The barrier height is $\Phi_b = 0.2$ eV, the thickness is $d_b = 5$ nm, and the effective mass is $m = 0.15\, m_0$, representing typical nominal values for the structures fabricated in this work (see chapter 7). Calculations are done for three different quantum well widths $d_{\mathrm{QW}} = 0$ nm, 5 nm and 7 nm. While for $d_{\mathrm{QW}} = 0$ nm, corresponding to a single tunnel barrier of width $2d_b$, the tunnel probability increases monotonically with energy (up to $E_z \approx \Phi_b$), sharp resonance peaks occur at energies below the barrier height when $d_{QW} > 0$. The resonances reach $\mathrm{T} = 1$ only for symmetric double barrier structures, and they narrow when the barrier thickness is increased (see below). The tunnel probability in the "valley" between resonances drops approximately to the value of a single tunnel barrier with the width $2d_b$.

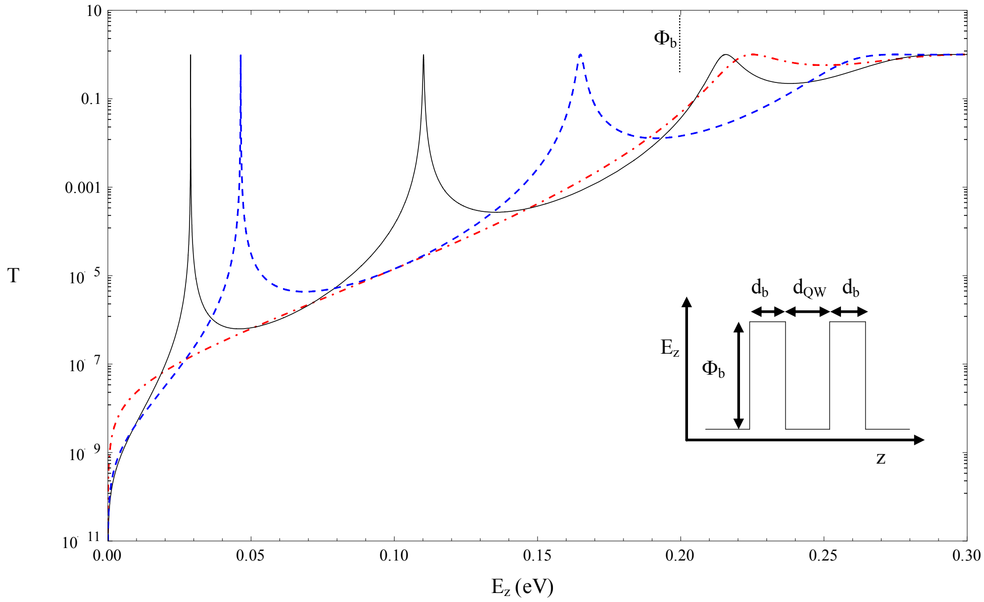

Figure 2.7: Tunnel probability T as a function of electron energy E_z for symmetric RTDs with the same barrier parameters ($d_b = 5$ nm, $\Phi_b = 0.2$ eV) and different quantum well thickness $d_{QW} = 7$ nm (solid black curve), 5 nm (blue dashed curve) and 0 nm (red dot-dashed curve). The latter corresponds to a single tunnel barrier, as described in the previous subsection, of 10 nm width.

The energetic position of the resonances corresponds to the quantization energy of quasi-bound states in the quantum well. Figure 2.8 displays the calculated resonance position as a function of the quantum well width for a double barrier RTD with the above parameters. With increasing quantum well width, the energy of resonances decreases and more resonances appear. For comparison, the blue lines in figure 2.8

represent the energy of bound states in a finite quantum well with the same barrier height and effective mass as the RTD. Both the RTD resonance positions and the finite quantum well states are nearly equivalent over a large energy range. This indicates that, under the selected conditions, the barriers in the RTDs provide sufficient confinement such that leakage of the wavefunction through the barriers may be neglected. Only for resonances at very high energies $E_z \lesssim \Phi_b$ a significant deviation of the resonance positions to even higher energies can be observed, which may be related to leakage of the wavefunction.

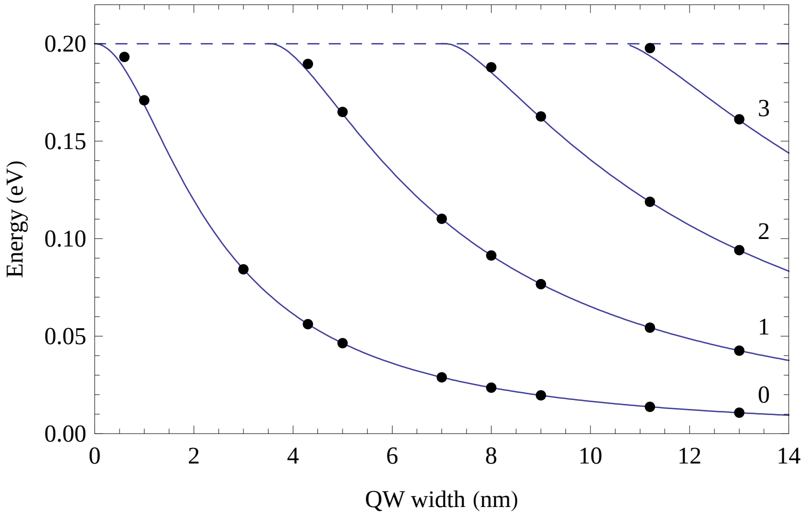

Figure 2.8: The black dots indicate calculated resonance energies as a function of the quantum well width for double barrier RTD structures with $\Phi_b = 0.2$ eV, $d_b = 5$ nm, and $m = 0.15\,m_0$. The blue lines show calculated bound state energies in a finite quantum well with the same barrier height and effective mass.

The effect of varied barrier thickness on the tunneling characteristics is shown in figure 2.9 . Again $\Phi_b = 0.2$ eV and $m = 0.15\,m_0$, and the quantum well width is $d_{QW} = 7$nm. For thick enough barriers $d_b \gtrsim 1$ nm the positions and the height of resonance peaks are independent of d_b. Increasing the barrier thickness leads to sharper resonances, and to a reduced off-resonance tunnel probability. It should be noted that the tunnel probability on resonance of a symmetric double-barrier structure is always equal to 1, even for extremely thick barriers and even though one individual barrier may have a much lower tunnel probability. For asymmetric structures, either due to structural asymmetry or due to inclination by an applied bias voltage, the tunnel probability on resonance is below 1.

Unlike on resonance, the off-resonance tunnel probability depends strongly on the barrier thickness. The tunnel probability at a fixed energy $E_z = 50$ meV in the "valley" after the first resonance is plotted in the inset of figure 2.9 as a function of the barrier thickness. For thick enough barriers $d_b \gtrsim 1$ it can be well approximated by an exponential $T \propto \exp\{-2 \cdot k \cdot 2d_b\}$, with $k = \sqrt{2m(\Phi_b - E_z)/\hbar^2}$. This is similar to the WKB approximation for a single tunnel barrier 2.23, with the noteworthy detail that the total thickness $2d_b$ of both tunnel barriers enters the exponent.

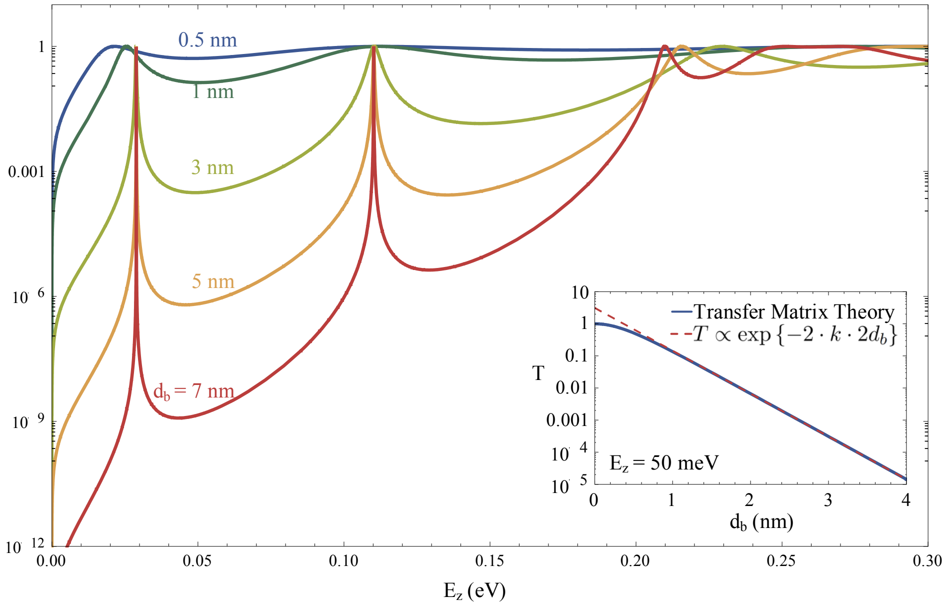

Figure 2.9: Tunnel probability T as a function of the incident electron energy E_z, calculated by the transfer matrix method for symmetric double-barrier structures with different barrier thickness 0.5 nm $\leq d_b \leq$ 7 nm. The quantum well width is $d_{QW} =$ 7 nm, the barrier height is $\Phi_b = 0.2$ eV. The inset shows the off-resonance tunnel probability at $E_z = 50$ meV as a function of d_b (solid blue line). For $d_b \gtrsim 1$ nm the off-resonance tunnel probability decreases exponentially (red dashed line).

I-V characteristics

When such a double-barrier structure is embedded between two doped contact layers, a bias voltage V between the contacts tilts the band diagram and thereby reduces the energy of the quasi-bound states E_n in the quantum well. This is depicted in figure 2.10. At low bias, when the energy of the electrons in the emitter is not enough to tunnel resonantly through a quantum well level, the transmission and thus the electric current is low (a). It starts to increase when the first quantized level is brought into resonance with the Fermi level E_F in the emitter (b), since the transmission probability is then resonantly enhanced for a few electrons. The number of electrons in a 3D emitter, which fulfill the resonant tunneling condition, increases linearly with bias voltage. This causes an about linear increase of the current for ideal RTDs. The maximum current is reached when the quantum well level is aligned with the lowest electron energy in the emitter (c), since then most electrons are available for transport. When the bias is further increased, the quantum well level comes out of resonance and the current decreases abruptly (d), giving rise to the rare feature of negative differential resistance. At higher bias voltages, LO phonon assisted resonant tunneling may cause a replica of the resonance peak, or a higher lying quantized level may come into resonance.

For ideal, symmetric double barrier structures, it may be assumed that the applied voltage drops only over the two barriers. Then only half of the applied voltage is effective in reducing the energy of the quantum well levels by an amount ΔE. In other words, a lever arm $\alpha = qV/\Delta E$ relates the applied voltage to the energy spectrum of the quantum well, with $\alpha = 2$ in the ideal case. In real structures the lever arm may be much higher, since a considerable amount of the voltage drops over the contact layers (compare e.g. α =12.75 in ref. [69]). This is especially true for low-doped contact layers.

In principle, the I-V characteristics of double-barrier RTDs can be calculated with the same model discussed previously for single tunnel barriers, using the relationship 2.26. The reproduction of experimental I-V curves with simulations, however, has turned out to be challenging [57]. Discrepancies are attributed to scattering, to charge accumulation in the quantum well and to band-bending in the quantum well and in the injector and collector layers.

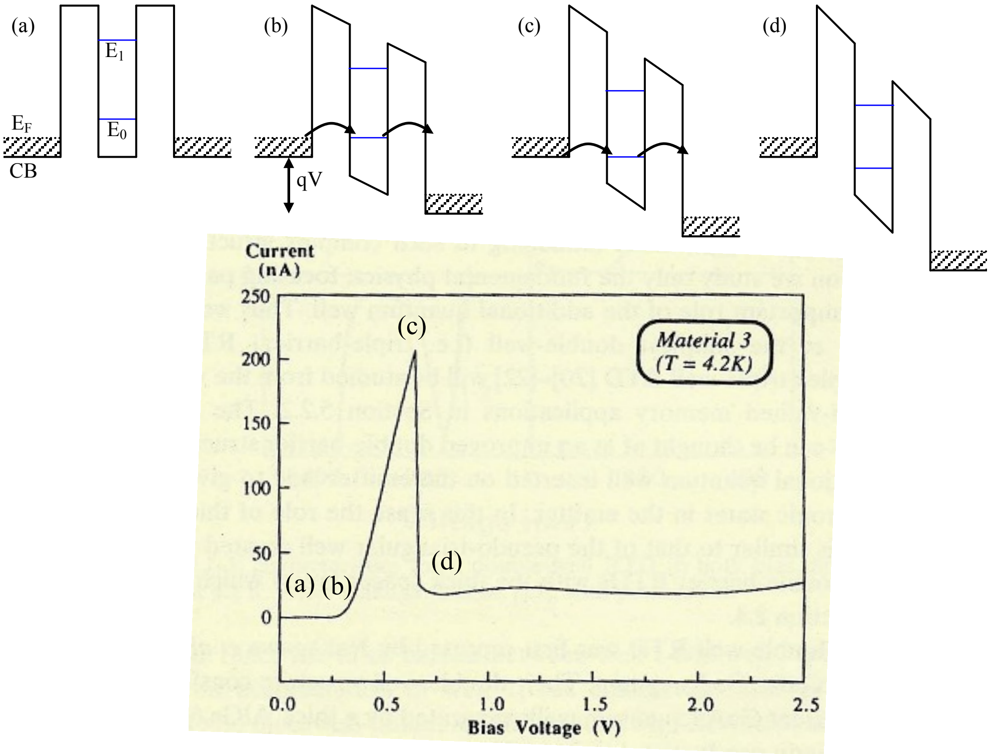

Figure 2.10: Top: Schematic band-diagrams of an RTD with two quasi-bound states under different bias voltages (a)-(d). Bottom: measured current-voltage characteristics of a GaAs / AlAs RTD, adopted from [57].

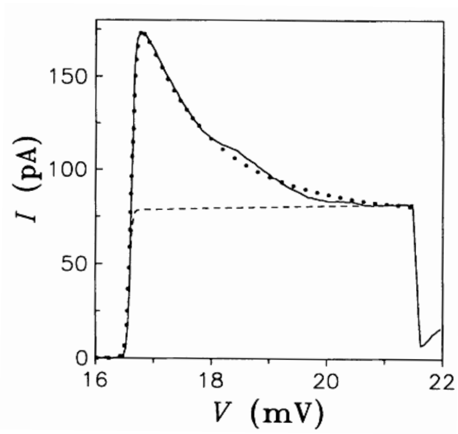

Figure 2.11: I-V characteristics of resonant tunneling through the 0D state associated with a single donor impurity in a III-V RTD, measured at 70 mK (sold line). The theoretically calculated current for single-electron tunneling is shown as the dashed line. The dotted line is calculated including electron-electron interactions, leading to a Fermi-edge-singularity enhanced current at the onset of resonant tunneling. Taken from [67].

Very different behavior and fundamentally new quantum transport effects arise when electrons tunnel through a quantum dot instead of a quantum well [20]. One interesting effect is the observation of atomic-like shell filling and Hund's rules in the electric transport characteristics of such 0D RTDs [19]. Another effect is Coulomb-blockade, which causes a 0D RTD to act as an electron turnstile. It transmits electrons one-by-one and thus allows single-electron transport experiments [70]. Third, the selection and manipulation of electron spins by resonant tunneling through 0D states is also an active area of research [71].

An example of the I-V characteristics associated with resonant tunneling through a 0D state in a double barrier RTD is shown in figure 2.11. The measurement has been done by Geim et al. [67] on a single donor impurity embedded in the quantum well of a III-V quantum well RTD. Electric transport through such a 0D system is limited to one electron at a time due to Coulomb blockade. Therefore it may be expected that a step occurs in the I-V curve when the 0D level comes into resonance with the emitter, followed by a plateau with nearly constant current for higher bias until the level drops out of resonance. This case is depicted by the dashed line in figure 2.11. The measured I-V characteristics in figure 2.11 show that the current at the onset of the resonance is significantly enhanced compared to the step-like increase. This enhancement is attributed to a many particle interaction of tunneling electrons with electrons in the emitter close to the Fermi energy, which is referred to as Fermi edge singularity [67, 21]. It allows electrons of slightly mismatched energy to tunnel through the structure, thus enhancing the current density and leading to a distinct peak in the I-V characteristics of such 0D RTDs. Resonant tunneling through 0D states has, also been studied by Dellow et al. [72] and by Itskevich et al. [73]. Both report distinct peaks in the I-V characteristics in their RTD devices and associate them with a 0D resonant state.

Chapter 3

Experimental Methods

This chapter provides an overview over the epitaxial growth of (Zn,Be,Cd,Mn)Se layers by MBE, and over the characterization methods RHEED, XRD, AFM, PL, and ECV. Particular emphasis is put on XRD, since it plays an integral role in the characterization of II-VI RTDs. A short description of lithographic processing of these layers into electronic device structures and their electric characterization is also given.

3.1 MBE of (Zn,Be,Cd,Mn)Se Heterostructures and RHEED

3.1.1 General notes on MBE

Monocrystalline semiconductor layers of high purity are crucial for electronic and optical applications which require a high mobility, a long quantum mechanical coherence length or a long spin flip length of carriers. Quantum heterostructures, such as the tunneling structures discussed in chapters 6 and 7, additionally require abrupt interfaces on the order of a single monolayer between layers of different composition. These requirements can be met by sophisticated epitaxial crystal growth techniques such as molecular beam epitaxy (MBE), which is widely used in solid state physics and advanced electronics research. In-depth reviews of MBE can be found e.g. in [74, 75, 76, 77].

Figure 3.1 depicts a schematic illustration of a commercial MBE Riber MBE 32 chamber, which is used in this work. It consists of an ultra high-vacuum chamber, several evaporation cells containing very pure source materials (usually 99.9999 % purity), mechanical shutters in front of each cell, a substrate holder including means for temperature measurement and heating of the substrate, a movable vacuum gauge for measuring the beam-equivalent pressure, and an electron gun in combination with a phosphorous screen for in-situ reflection high energy electron diffraction (RHEED)

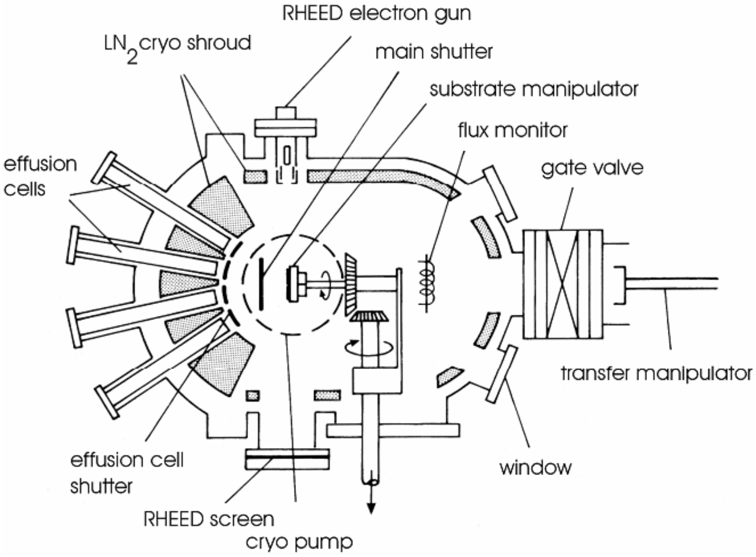

Figure 3.1: Top-view schematic illustration of an MBE chamber of the type Riber MBE 32. Adopted from [78].

characterization of the growing crystal surface. During film growth the constituent materials are evaporated thermally from the effusion cells, and the resulting molecular beams are directed towards the heated, monocrystalline substrate. The impinging atoms diffuse laterally on the substrate until they are incorporated in the crystal, ideally on a crystalline lattice position. The intensity of the molecular flux of individual cells can be controlled by the cell temperature, and it can be shut off completely by the mechanical shutter in front of the cell. By combining molecular beams of different source materials and intensity, the composition and doping density of the growing crystalline layer can be varied. Due to the relatively low growth rate of MBE of about 1 Å/s (compare to a typical monolayer thickness of 2.83 Åfor GaAs) complex layer structures can be grown with precise control of thickness, composition and doping density down to single atomic layers.

In this work, commercial MBE systems of the type Riber MBE 32 (see figure 3.1) and Riber Compact 21 are used to grow ZnSe and GaAs based semiconductor heterostructures. The systems are part of a cluster of six MBE systems dedicated to the growth of different materials including HgCdTe, NiMnSb and GaMnAs, which are interconnected by a UHV transfer system (see e.g. [78, 79]). Most of the ZnSe based samples grown in the course of this work are grown in a Riber MBE 32 chamber [1]. The commissioning of a new Compact 21 MBE chamber for ZnSe growth in the later stages of this work is described in section 3.7. Data presented in this thesis, which

---

[1] Before being turned into a ZnSe MBE chamber in the late 1990s, this Riber 32 chamber had served for CdTe epitaxy for several years, and it was still referred to as "CT chamber" until it was decommissioned in 2010. Samples grown in this chamber are continuously numbered "cb####", and the present work is based on samples numbered cb3107 through cb3543.

is based on samples grown in the new Compact 21 chamber, is specifically labeled as such.

The constituent materials Zn, Cd, Be and Mn, as well as ZnI for n-type doping, are evaporated from thermal effusion cells. Se is evaporated from a valved Se cracker cell, which is operated in the non-cracking mode. Substrates are glued to Mo sample holders with molten indium. The Mo sample holder is radiation heated from a Ta heating filament beneath it, and its temperature is measured by a thermocouple in contact with the back of the Mo block.

The intensity of the molecular beam is measured indirectly by a movable Bayard-Alpert pressure gauge at the position of the sample. The beam-equivalent pressure measured by the gauge is approximately proportional to the molecular flux emanating from the effusion cell, but it also depends on the ionization probability of the evaporated material [80].

3.1.2 RHEED

An important tool to characterize the surface roughness, the crystallinity, and the surface reconstruction of a growing crystal layer during the MBE process is reflection high-energy electron diffraction (RHEED) [81]. A typical RHEED setup consists of an electron source providing a collimated beam of electrons with an energy of about 10-20 keV, the sample, hit by the electrons under a very shallow angle of incidence, and a phosphorous screen facing the electron source on the opposite side of the chamber. Since the electron deBroglie wavelength in that case (about 0.1 Å) is much shorter than the typical semiconductor lattice constant (about 5 Å) and since the electrons interact only with the topmost atomic layers, a streaky electron diffraction pattern can be observed on the screen when the sample surface is atomically flat. When the surface is rough on the atomic scale, which is undesired for most layers, a spotty diffraction pattern is observed. The symmetry of the usually reconstructed crystal surface is also reflected in the RHEED pattern, and oscillations in the specularly reflected electron beam can be used to measure the growth rate in the layer-by-layer growth mode. This renders RHEED one of the most important in-situ characterization methods for MBE growth.

Examples of the RHEED patterns of a (2×4) reconstructed GaAs surface and a (2×1) reconstructed ZnSe surface grown during this work are shown in figure 3.2. The distinct streaks indicate that the surfaces are atomically flat.

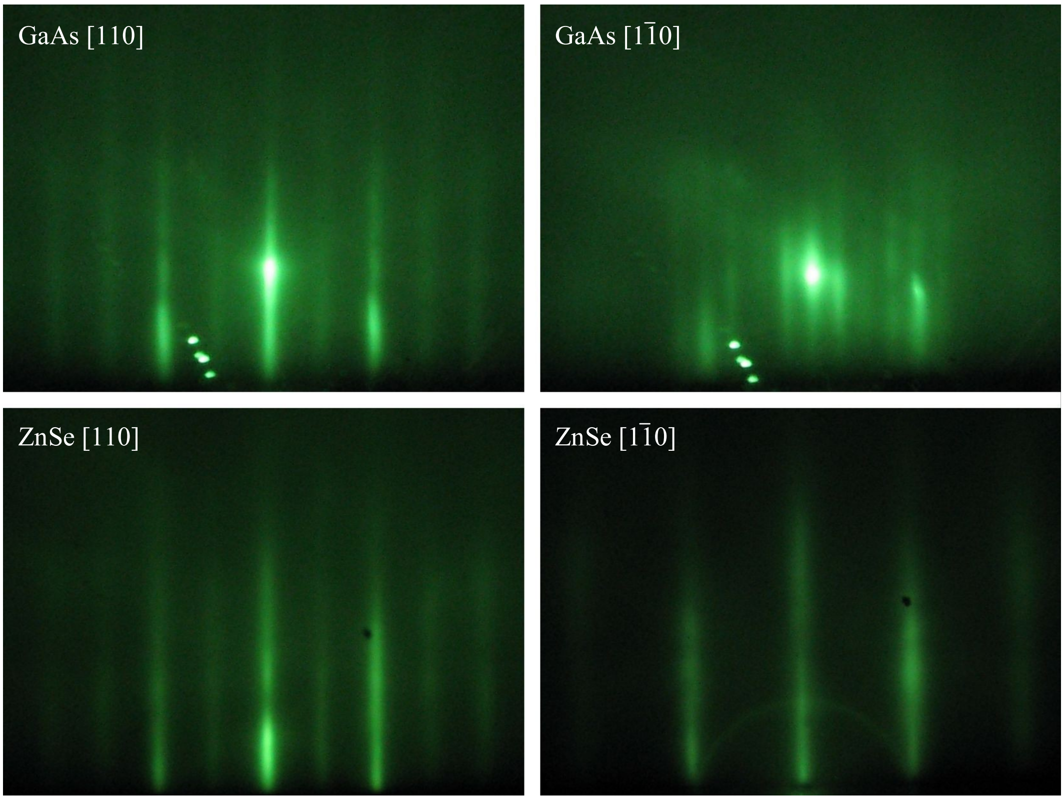

Figure 3.2: RHEED patterns of a (2 × 4) reconstructed GaAs surface (top) and a (2 × 1) reconstructed ZnSe surface (bottom), observed with the electron beam along the two azimuths [1$\bar{1}$0] (upper row) and [110] (lower row).

3.1.3 Typical MBE growth procedure

All II-VI layer structures fabricated in this work are grown on epi-ready [82], Si-doped (n-type) or undoped, (001) oriented GaAs substrates of a diameter of 2 inches. Full wafers or pieces thereof are glued to a Molybdenum sample holder using molten indium. Then the Molybdenum sample holders are introduced to the MBE system via a load lock and are degassed in vacuum at 300 °C for about 10 minutes.

After degassing, the substrates are inserted into a III-V epitaxy chamber, where the oxide layer, which covers the substrate, is thermally removed by heating to 620 °C under an As pressure of about 10^{-5} Torr. Then an about 200 to 300 nm thick GaAs buffer layer is grown at a substrate temperature between 580 °C and 600 °C. The Ga pressure is about 2.5×10^{-7} Torr. During growth the surface shows a 2 x 4 reconstruction and long streaks indicating flat 2D layer growth, as shown in figure 3.2.

The GaAs growth rate is measured using oscillations of the RHEED specular spot intensity, and is typically 1.4 Å/s.

After buffer growth, the substrate is cooled to 200 °C and is transferred to the II-VI MBE chamber under UHV within about 5 - 10 minutes. In the II-VI chamber it is

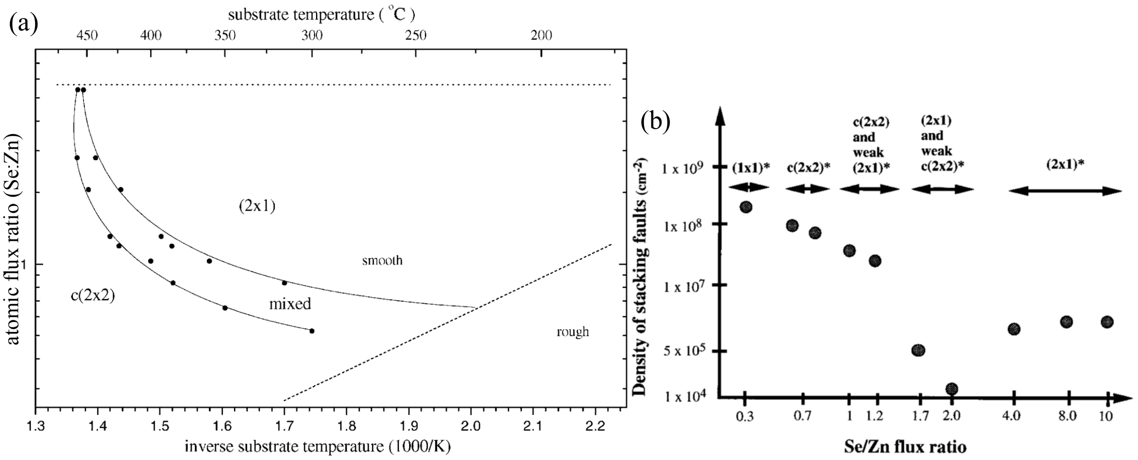

Figure 3.3: (a) Surface phase diagram during MBE growth of ZnSe, showing the surface reconstruction as a function of the substrate temperature and the Se / Zn flux ratio (adopted from [83]). (b) Defect density in ZnSe epilayers on the Se / Zn flux ratio and surface reconstruction (adopted from [84]).

heated to 300 °C in a position which does not directly face the heated cells. To avoid contamination of the GaAs surface, the cell shutters and the Se valve are closed at this point. When the II-VI growth temperature of 300 °C is reached, the substrate is turned to growth position and the surface is inspected shortly by RHEED, which usually shows a clear, streaky 2 x 4 reconstruction of the As-terminated GaAs(001) surface. When the starting surface is deemed to be suitable, II-VI growth is initiated by one of several growth start procedures, which are discussed in detail in chapter 5. Most of the structures discussed in this work are fabricated using a Zn-rich growth start, which is optimal for a low density of defects in the II-VI epilayer. With the exception of certain growth procedures used for the formation of self assembled CdSe quantum dots, the substrate temperature is kept at 300 °C throughout II-VI MBE growth.

The growth conditions for II-VI epilayers in this work are based on previous experience available at the University of Würzburg and on studies such as those by Wolfframm et al. [83] and Kuo et al. [84]. Figure 3.3 (a) shows the dependence of the surface reconstruction and roughness of MBE grown ZnSe on the substrate temperature and on the Se / Zn flux ratio as a phase diagram. For Se-rich growth and for substrate temperatures around 300 °C, the surface has a 2×1 symmetry and is very smooth. Figure 3.3 (b) depicts the defect density in such layers as a function of the flux ratio and the surface reconstruction measured at a substrate temperature of 260 °C. The lowest defect density can be achieved with a flux ratio of 2:1 and a corresponding mixed 2×1 and $c(2 \times 2)$ reconstruction.

For ZnSe growth at 300 °C with a growth rate of typically 1 Å/s the Se BEP in this work is $2 - 4 \times 10^{-6}$ Torr and the Zn BEP is $6 - 8 \times 10^{-7}$ Torr. For pure CdSe growth and for ternary compounds containing a few per cent of Cd, the Cd BEP is on the order of 1×10^{-7} Torr. For the growth of Mn containing DMS layers with a few per cent of Mn, the Mn BEP is typically on the order of 5×10^{-8} Torr.

Except the very short period of the growth start procedure, growth is thus carried out in a Se-rich regime, and the growth rate is limited by the group II fluxes. Unlike in the AlGaAs material system, the sticking coefficient of the cation (group II) atoms depends significantly on the substrate temperature [85]. This affects the II-VI growth rate as well.

Growth interruptions of 30 seconds are inserted before and after tunnel barrier layers in RTD and single-barrier structures. During a growth interruption all group II and doping materials are shut off and the substrate surface is irradiated purely by Se. In [86] it is shown that interruptions of such a duration significantly improve surface flatness, which is attributed to prolonged diffusion and thereby a better incorporation of free adatoms into crystalline positions.

When II-VI growth is finished, all shutters except Se are closed, and the substrate is cooled to 200 °C. Se flux is provided for the first ≈ 20 s of this cooling step, to avoid evaporating Se from the layer when it is hot. After growth the substrate is taken out of the II-VI MBE chamber and either out of the UHV system by a load lock, or it is transferred through UHV to an in-situ metalization chamber.

Many samples need low resistance ohmic contacts to n-ZnSe. Such contacts are reliably formed by growing a very highly n-doped ($N_d \approx 2 \times 10^{19}\text{cm}^{-3}$) ZnSe layer on top of the II-VI layer stack, followed by in-situ deposition of 10 nm Al in the dedicated in-situ metalization chamber. Al is known to form a low Schottky barrier with ZnSe [87]. To avoid oxidation, the Al layer is covered in-situ by a 10 nm Ti layer as a diffusion barrier and a 30 nm Au layer on top.

3.2 High-Resolution X-Ray Diffraction

One of the most important characterization tools of epitaxial semiconductor heterostructures is high-resolution x-ray diffraction (HRXRD), since it allows to measure thickness, composition, structural quality and other quantities in a nondestructive way [88]. The x-ray wavelength of laboratory sources (about 1 Å) is on the order of the inter atomic spacing in crystals (few Å), and thus interference between the elementary waves, scattered from different crystalline planes, can be easily observed.

As depicted in figure 3.4, constructive interference of waves scattered from a set of lattice planes occurs when the diffraction angle Θ satisfies the Bragg condition

$$2d_{\text{hkl}} \sin(\Theta) = \lambda. \tag{3.1}$$

Here, d_{hkl} is the spacing between the diffracting lattice planes which are described by the miller indices {h,k,l}, Θ is the angle between the crystal planes and the incident and emergent x-ray beam, and λ is the x-ray wavelength. For a cubic crystal $d_{\mathrm{hkl}} = a/\sqrt{h^2+k^2+l^2}$, where a is the lattice constant.

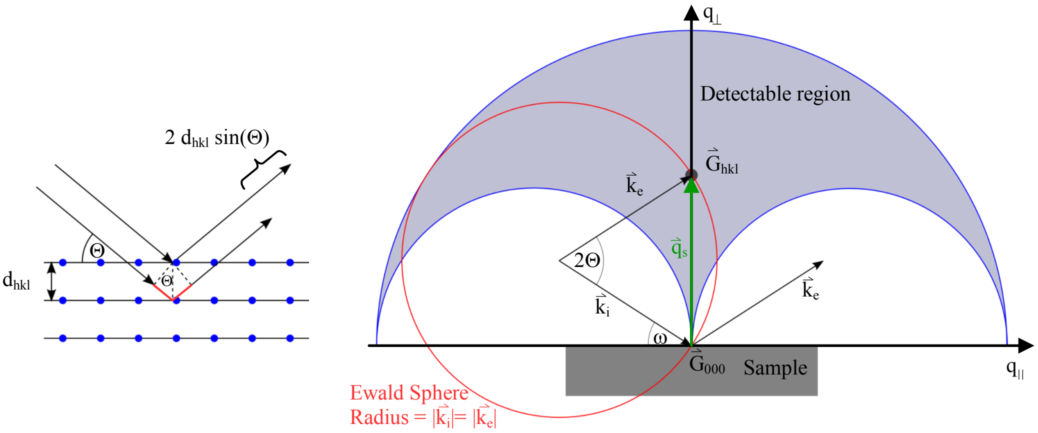

Figure 3.4: Geometry of x-ray diffraction for a symmetric reflection illustrated in real space (left) and as an Ewald construction in reciprocal space (right). Θ is the angle between incident beam and diffracting lattice planes, 2Θ is the angle between the incident and the diffracted beam, and ω is the angle between sample surface and incident beam. For a symmetric reflection $\Theta = \omega$.

An equivalent formulation of the Bragg condition is the Ewald construction shown on the right hand side of figure 3.4. An incident x-ray beam with the wavevector $\vec{k}_i$ hits the sample surface at an angle ω, and the intensity of elastically scattered x-ray light is recorded by a detector placed at an angle 2Θ from the source, defining the emergent wavevector $\vec{k}_e$. When the scattering vector $\vec{q}_s = \vec{k}_e - \vec{k}_i$ ends on a reciprocal lattice point $\vec{G}_{hkl}$ of the sample, x-rays scattered from the corresponding equivalent lattice planes $\{h,k,l\}$ interfere constructively and a peak in the scattered x-ray intensity is observed. The scattering vector is scanned through reciprocal space by varying the angles ω and 2Θ, and different aspects of the reciprocal lattice of the sample can be measured. Since the conversion from a real space lattice to a reciprocal lattice involves a Fourier transform, XRD probes the Fourier transform of the microscopic structure of a sample on the scale of the x-ray wavelength.

A Panalytical X'pert diffractometer equipped with a CuK$_{\alpha 1}$ source ($\lambda = 1.54056$Å) and a Ge 4-crystal monochromator is used for HRXRD measurements in this work. On the detector side either a receiving slit with an aperture of 0.15 ° or a two crystal analyzer is used to limit the angle of acceptance.

Measurements are done in the vicinity of the symmetric 004 reflection and in two principal directions (see figure 3.5): in $\omega - 2\Theta$ scans the scattering vector is varied perpendicularly to the lattice planes and the sample surface, whereas in ω scans it is varied parallel to the surface. Figure 3.5 also shows the effect of different detector acceptance angles on the two scan directions. While scans in ω direction always require a small acceptance angle, since otherwise features offset in the $q_\perp$ direction appear in the scan, $\omega - 2\Theta$ diffractograms of symmetric reflections can be recorded with a larger acceptance angle without distortion as long as the layer peaks are not broadened in $q_{||}$direction.

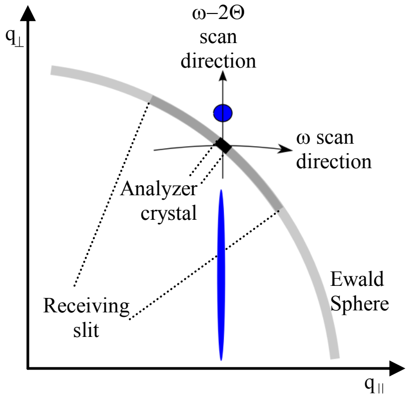

Figure 3.5: Schematic of HRXRD scan directions illustrating the effect of a receiving slit and an analyzer crystal on the acceptance angle. The blue shapes outline a symmetric reflection of a fully pseudomorphic, tensile strained epilayer (bottom) on a monocrystalline substrate (top). The light and dark gray shaded regions sketch the angle of acceptance of a receiving slit and a monochromator crystal on the detector side.

3.2.1 $\omega - 2\Theta$ Scans

If the incidence angle ω and the angle 2Θ between incident and emergent beam are varied symmetrically such that $\vec{q}_s$ is moved perpendicularly to the sample surface, the Fourier transform of the crystalline lattice of the samples in growth direction is probed. Examples of such $\omega - 2\Theta$ scans are shown in figure 3.6 for a pure ZnSe epilayer and a (Zn,Be)Se epilayer on GaAs(001). In the following the analysis of $\omega - 2\Theta$ scans is described based on kinematic scattering theory [88] to obtain information on the thickness and composition of epilayers. A more accurate description of x-ray diffraction is provided by the dynamic diffraction theory, which takes account of multiple scattering effects [88]. The kinematic calculations below, however, are more instructive and often provide a good starting point for dynamic simulations.

Composition Since the lattice constant of most semiconductor alloys is very sensitive to their composition, the composition of epilayers is often determined by measuring the lattice constant by HRXRD. For crystalline alloy materials $A_{1-x}B_x$, consisting of materials A and B with the individual lattice constants a_A and a_B, the alloy lattice constant $a_\mathrm{AB}(x)$ is usually well described by a linear interpolation called Vegards law

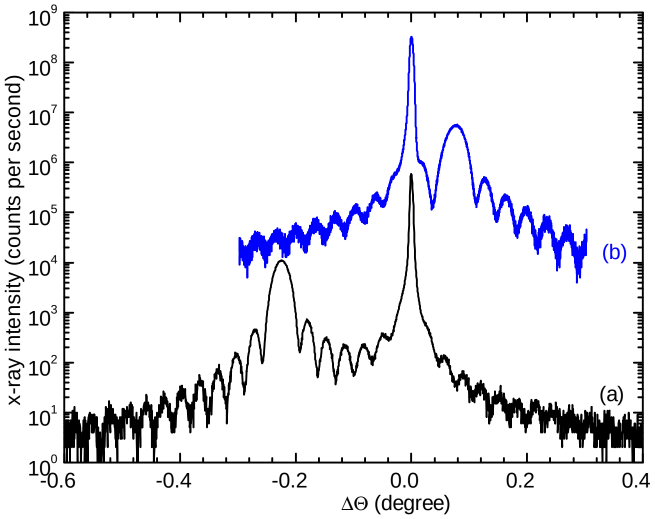

Figure 3.6: $\omega - 2\Theta$ scans in the vicinity of the 004 reflection of (a) a 167 nm thick ZnSe layer and (b) a 152 nm thick $Zn_{0.962}Be_{0.038}Se$ layer, both on GaAs(001). Curve (b) in this figure is vertically offset for clarity. The diffraction angle $\Delta\Theta$ is given relative to the most intense peak in the diffraction patterns, the GaAs 004 reflection.

$$a_{\mathrm{AB}}(x) = (1-x)a_{\mathrm{A}} + x a_{\mathrm{B}}. \tag{3.2}$$

When a thin layer of a material with the relaxed lattice constant a_{rel} is grown epitaxially on a substrate with the same crystal structure, but with a slightly different lattice constant a_s, the layer becomes elastically deformed. This is exemplified in figure 3.7. In the lateral direction it assumes the lattice constant of the substrate $a_{\|} = a_s$, and in the vertical direction the lattice constant $a_{\perp}$ depends on the Poisson ratio ν of the layer and on the relative lattice mismatch to the substrate. The thicker a strained layer gets, the more elastic energy is accumulated. Once a certain critical layer thickness is passed, the layer lowers its total energy by plastic relaxation through the introduction of misfit dislocations.

The relationship between the relaxed lattice constant and the vertical and lateral lattice constants of a tetragonally deformed epilayer obtained from elasticity theory is [89, 90]

$$a_{\mathrm{rel}} = \frac{1-\nu}{1+\nu}\left(a_{\perp} - a_{\mathrm{s}}\right) + \frac{2\nu}{1+\nu}\left(a_{\|} - a_{s}\right) + a_{\mathrm{s}}. \tag{3.3}$$

Assuming $a_{\|} = a_s$ for a fully pseudomorphic epilayer and using $d_{004} = a_{\perp}/4$ for the spacing of 004 lattice planes in Eq. 3.1, a_{rel} can be determined from a measurement of the corresponding Bragg angle

$$a_{\mathrm{rel}} = a_s + \frac{1-\nu}{1+\nu}\left(\frac{2\lambda}{\sin(\Theta_{004})} - a_s\right). \tag{3.4}$$

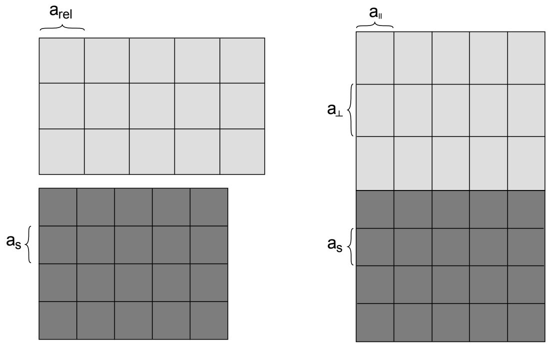

Figure 3.7: Sketch of two relaxed, cubic crystals with the lattice constants a_{rel} and a_s (left), and of a tetragonally deformed, pseudormorphic epilayer under compressive strain, having different vertical $a_\perp$ and lateral $a_{||}$ lattice constants (right).

Since alignment problems make it difficult to measure diffraction angles on an absolute scale, usually the relative angular distance $\Delta\Theta$ between the Bragg reflection of an epilayer and the known Bragg angle of the substrate material $\Theta_{\text{004,sub}}$ ($\Theta_{\text{004,GaAs}} = 33.0259°$) is measured, and $\Theta_{004} = \Theta_{\text{004,sub}} + \Delta\Theta$.

$\omega - 2\Theta$ scans of a pure, 167 nm thick ZnSe layer and a 152 nm thick $\text{Zn}_{0.962}\text{Be}_{0.038}Se$ layer, grown on GaAs(001), are depicted in figure 3.6. The lattice constant of ZnSe is 0.27 % larger than that of GaAs, and the ZnSe 004 reflection is consequentially at a lower angle than the GaAs reflection. By the addition of the small element Be the lattice constant decreases, and the 004 reflection shifts to the opposite side of the GaAs reflection.

The semiconductor alloys mainly used in this work are $\text{Zn}_{1-x}\text{Be}_x\text{Se}$, $\text{Zn}_{1-x}\text{Cd}_x\text{Se}$ and $\text{Zn}_{1-x}\text{Mn}_x\text{Se}$. The lattice constants and the Poisson ratios of the constituent materials used to determine their compositions are listed in table 2.1 in section 2.1. The resulting relationship between the Bragg angle of the 004 reflection and the composition of these alloys is shown in figure 3.8.

Layer thickness The finite thickness of an epilayer manifests itself in several quantities detected by an XRD $\omega - 2\Theta$ scan, such as the peak intensity, the peak width, and interference fringes. The intensity and sharpness of a Bragg reflection increase with increasing layer thickness, as long as the layer is pseudomorphic. Interference fringes due to the finite thickness of a single epilayer can be seen e.g. in figure 3.6 as the regularly spaced, small peaks around the Bragg reflection. The angular separation $\delta\Theta_p$ of two adjacent fringe peaks of a symmetric reflection (such as the 004 reflection) is related to the layer thickness d by the approximate formula

$$\delta\Theta_{\text{p}} = \frac{\lambda}{2d\cos(\Theta)} \tag{3.5}$$

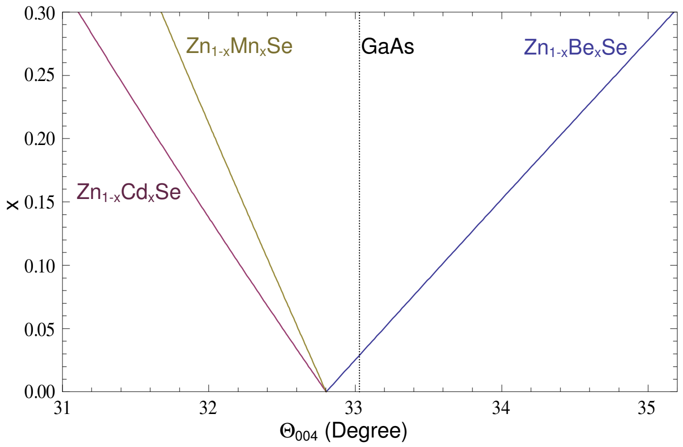

Figure 3.8: Calculated relationship between the composition x of the ternary alloys $Zn_{1-x}Be_xSe$, $Zn_{1-x}Cd_xSe$ and $Zn_{1-x}Mn_xSe$, and the diffraction angle Θ_{004} of the 004 reflection.

where λ is the x-ray wavelength, and Θ is the average diffraction angle of the two fringe peaks [88]. This relationship allows to quickly determine the thickness of an epilayer without any knowledge of material parameters. If more than one epilayer is present, thickness oscillations of all layers superimpose and beat, resulting in complex interference patterns. The thickness fringes can be suppressed by inhomogeneity or by rough interfaces, and the number of fringe peaks observable for layers of identical thickness is thus also a measure of relative layer quality.

Superlattice reflections A periodically repeated sequence of thin epilayers of alternating material composition is commonly referred to as a superlattice. On the one hand, these structures have interesting electronic properties, and on the other hand, they limit the propagation of dislocations and improve the quality of epilayers grown on top of the superlattice. X-ray diffractograms of such superlattices show sharp maxima occurring at regular angular positions, similar to the diffraction orders of optical grids.

If one period consists of two layers with the thickness d_A and d_B and the lattice constants a_A and a_B, the 0th order superlattice maximum associated with the {hkl} lattice planes occurs at an angle $\Theta_{\mathrm{hkl,0}}$ given by the average lattice constant $\bar{a} = (d_A a_A + d_B a_B) / (d_A + d_B)$. From the angular position of the 0th order of a superlattice reflection, the average mismatch can be obtained simply from the Bragg law

$$\bar{a} = \frac{2\lambda}{\sin\left(\Theta_{004,0}\right)}, \tag{3.6}$$

where the lattice plane spacing $\bar{d}_{004} = \bar{a}_{004}/4$ is used. From the angular position of two adjacent superlattice reflections, $\Theta_{\mathrm{hkl,i}}$ and $\Theta_{\mathrm{hkl,i+1}}$, the period $d_{\mathrm{SL}} = d_A + d_B$ of a superlattice with the constituent layers A and B can be calculated

$$d_{\mathrm{SL}} = \frac{\lambda}{2\left(\sin(\Theta_{004,\mathrm{i}+1}) - \sin(\Theta_{004,\mathrm{i}})\right)}. \tag{3.7}$$

X-Ray Interference Very thin epilayers with a thickness on the order of a few ML occur e.g. in the self-organized growth of nanostructures with highly strained material systems, such InAs / GaAs or CdSe / ZnSe quantum dots. Characterizing such layer directly by XRD is difficult due to their very small scattering volume. Intricate microscopy techniques such as transmission electron microscopy or scanning tunneling microscopy can be used, but they often require the destruction of the layer structure and are relatively time-consuming.

An alternative, nondestructive way to characterize the thickness and composition of thin epilayers is the analysis of x-ray interference (XRI) effects in special layer structures, sometimes referred to as “Bragg-case-interferometers” (see inset of figure 3.9). The thin layer of interest is embedded epitaxially between thick cladding layers of a material with a different lattice constant. In an XRD experiment, the interlayer causes a phase shift between the x-ray wave fields diffracted from the upper and lower cladding layers, and the analysis of the resulting interference pattern can yield information on the thickness and lattice constant of the thin interlayer. A treatment of XRI on the basis of the kinematic diffraction theory is presented by Tapfer and Ploog [91] and by Holloway [92]. Prior et al. have applied the technique specifically to the ZnSe / CdSe material system [93].

An example of XRI is depicted in figure 3.9. The blue curve is an $\omega - 2\Theta$ scan of a ZnSe / CdSe / ZnSe Bragg-case-interferometer structure on GaAs, in the vicinity of the 004 reflection. Comparing the diffractogram to that of a single ZnSe epilayer (see e.g. figure 3.6) shows that, due to interference between the two cladding layers, the ZnSe Bragg peak (at $\Delta\Theta \approx -808$ arcsec) and thickness fringes are modulated in intensity. The modulation depends on the phase shift and thus on the thickness and lattice constant of the interlayer. A simulation of the diffractogram of the whole structure, as represented by the red and the black curves in figure 3.9, can yield accurate information on these quantities. Holloway estimates, that in certain III-V semiconductor heterostructures the thickness of interlayers can be determined by XRI with a precision of up to 0.02 Å under optimal conditions [92].

The information obtained from XRI, however, is not necessarily unique. The two simulated diffractograms in figure 3.9 reproduce the experimental data equally well, even though they correspond to structures with interlayers of different thickness and composition. The red curve corresponds to a 4.6 Åthick CdSe interlayer embedded in 44 nm thick ZnSe cladding layers, and the black curve to a 8.5 Åthick $\mathrm{Zn_{0.5}Cd_{0.5}Se}$ interlayer, also with 44 nm thick ZnSe cladding layers. It is possible since the two interlayers lead to the same phase shift. The increased interlayer thickness compensates the reduction of the discrepancy between the lattice constant of the interlayer and that

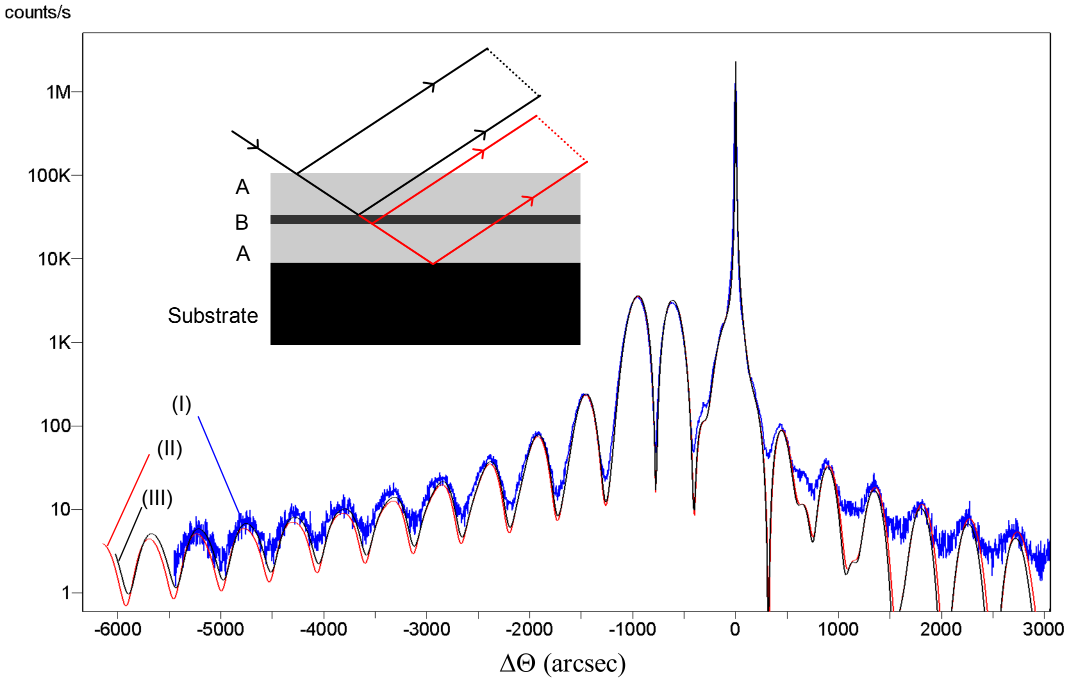

Figure 3.9: XRD $\omega - 2\Theta$ scan (blue curve) showing x-ray interference in a heterostructure consisting of a few ML thin CdSe layer, in between thick ZnSe cladding layers (see inset). The red and black curves represent simulations of the pattern with different interlayers.

of the cladding layers. Additionally, since the phase shift due to the interlayer can only be detected modulo 2π, the same XRI pattern may arise for structures with very different interlayer thickness and composition. A detailed treatment of these issues can be found in [92].

In this work, XRI is mainly used to calibrate the growth rate of CdSe layers for the growth of self-organized CdSe based quantum dots.

3.2.2 ω Scans

If the scattering vector is varied in $q_{||}$ direction over the Bragg reflection of a layer, the lateral lattice constant and homogeneity of the layer is probed and information can be obtained mainly on homogeneity, dislocation content, and degree of relaxation. For a symmetric reflection this is approximated by an ω scan, as depicted in figure 3.10 for a 219 nm thick ZnSe epilayer on GaAs(001). It is recorded with an analyzer crystal in front of the detector (triple axis optics).

ω Peak Width In the vicinity of a symmetric reflection, an ω scan corresponds to a variation of the scattering vector in the lateral $q_{||}$ direction (figure 3.5). Thus the

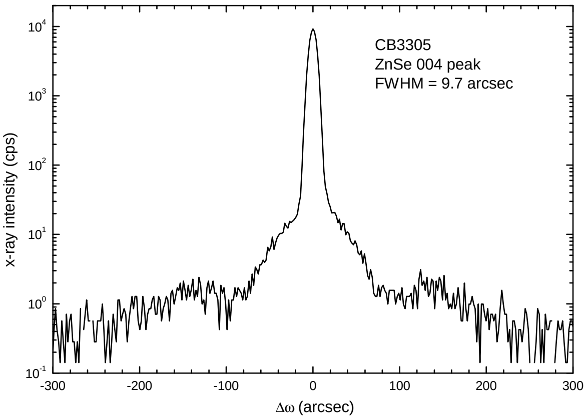

Figure 3.10: HRXRD ω scan of the 004 reflection of a 219 nm thick, pseudomorphic ZnSe layer on GaAs(001).

lateral homogeneity of the lattice is probed, and for an ideal epilayer the peak width is given by the resolution of the diffractometer. Any broadening of the layer peak is an indication of structural imperfection of the crystal, such as dislocations, mosaicity, inhomogeneity or bending of the sample. The ω peak FWHM can thus be used as a measure of crystalline quality of epilayers.

The resolution in ω direction of the Panalytical X'Pert diffractometer used in this work is limited to 6 arcsec. Using a phenomenologic model for the shape and angular distribution of mosaic blocks around dislocations, the minimum detectable dislocation density is estimated to be on the order of $10^6 \mathrm{cm}^{-2}$ [89]. Smaller densities of dislocations can be measured with direct imaging methods, such as etch pit density measurements [94], or with the analysis of the diffuse background described below.

Diffuse Background The shape of the diffraction profile shown in figure 3.10 can not be described by a single Lorentzian or Gaussian peak arising from a perfect heterostructure and a finite detector aperture. A relatively broad, low intensity background peak can be identified in the range $-80\,\mathrm{arcsec} < \Delta\Omega < 80\,\mathrm{arcsec}$, and there are additional small peaks at about $\Delta\Omega = \pm 120\,\mathrm{arcsec}$. The intensity of these features, additionally, is highly anistropic: they are a lot more intense in omega scans taken in the 110 direction, than they are in scans in the 1-10 direction.

Kidd and Fewster [95] have observed such features in omega scans of InGaAs epilayers, and have attributed them to the diffuse scattering of x-rays from the strain field around dislocations. Ress et al. have studied this diffuse background in ZnSe epilayers, and come to similar conclusions [96, 89]. Additionally, they explained the azimuthal anisotropy of this type of diffuse background with the higher glide efficiency of dislocations in one crystalline direction compared to that orthogonal to it, resulting in a linear array of dislocations instead of a crossed one.

The diffusely scattered intensity can thus be used as a measure for the crystalline quality. According to Ress et al. this measure is about one order of magnitude more sensitive than the analysis of the omega FWHM, in the ZnSe / GaAs material system [96, 89].

3.3 Photoluminescence Spectroscopy

Photoluminescence (PL) refers to the emission of light from condensed matter systems after optical excitation. The energy spectrum and the intensity of the emitted light yields information on the band gap, the nature and concentration of impurities, quantum confinement energy in nanostructures, and on the homogeneity of the sample [68].

The basic process of PL is sketched in figure 3.11 for a semiconductor quantum well heterostructure. When a photon of an energy greater than the effective band gap (including e.g. confinement energy) is absorbed in a semiconductor layer, an electron is lifted from the valence to the conduction band, resulting in an electron-hole pair. The pair relaxes to the respective ground state, and can further lower its energy by forming an exciton (X) or other quasi-particles, e.g. biexcitons or charged excitons. It eventually recombines after a certain lifetime, releasing its energy again as a photon or via non-radiative channels. Before recombination, excitons diffuse through the material and are localized at potential minima, such as impurities, quantum wells or quantum dots. PL thus preferentially probes the minima of a potential landscape. In a high-quality barrier / quantum well / barrier heterostructure, such as depicted in figure 3.11, most excitons “fall” into the quantum well, and often no PL from the barrier material is seen. In an inhomogeneous quantum well, excitons are better localized at spots with lower ground state energy, thus giving more spectral weight to these spots in the PL spectrum.

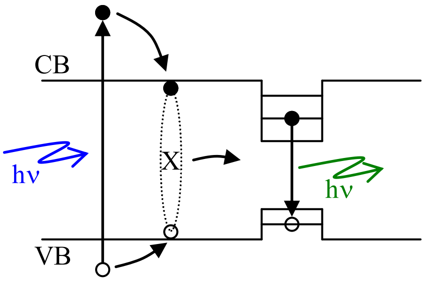

Figure 3.11: Photoluminescence in a semiconductor quantum well structure.

The exciton binding energy in bulk ZnSe is about 20 meV [35]. When excitons are confined in a heterostructure, their binding energy generally increases due to the higher overlap of the electron and the hole wavefunction. It may reach up to about four times the bulk value [97, 98].

A schematic of the setup used for most PL experiments in the present work is depicted in figure 3.12. It consists of a blue laser with $h\nu\; = 3.06$ eV for excitation, a Helium flow cryostat with which temperatures below 10 K can be reached, a spectrometer with an optical path length of 0.55 m, and a Si photo diode with a PC for sequential recording of luminescence spectra. A system of lenses and a prism direct the excitation light onto the sample surface (spot size $\approx 1\,\mathrm{mm}^2$) and collect the emanating luminescence light. The prism also serves the purpose of diverting spurious reflected excitation light from the spectrometer. A longpass filter in front of the spectrometer further represses the remaining, unwanted excitation light.

A more advanced setup is used for magneto-PL and PL excitation measurements by the optics group at EP3. For magneto-PL measurements the sample is placed in a He bath cryostat with a magnetic coil capable of producing magnetic fields up to 6 T.

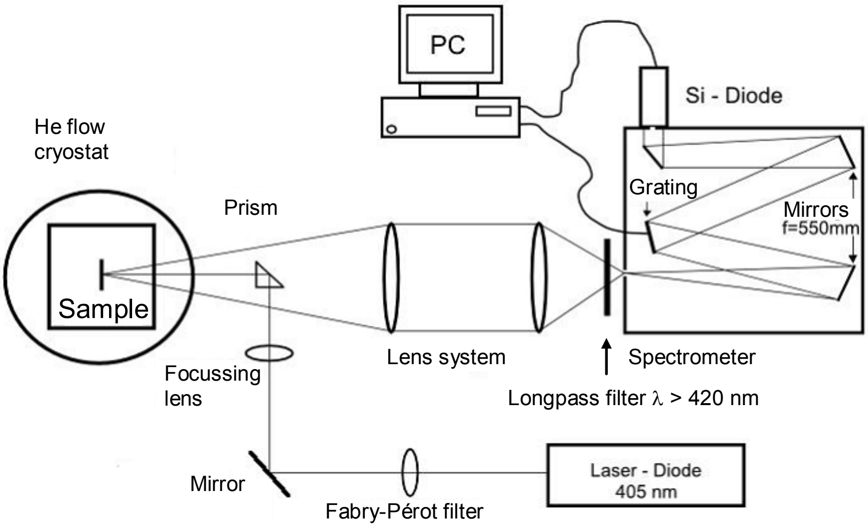

Figure 3.12: Schematic of the optical setup used for photoluminescence experiments. Adopted from [99].

3.4 Electrochemical Capacitance-Voltage Profiling

Electrochemical capacitance-voltage (ECV) profiling allows to quickly measure the doping density in layered semiconductor structures as a function of depth [100]. In the present it is used work for the analysis of the carrier distribution in the vicinity of heterovalent semiconductor heterointerfaces, and for the calibration of the doping density versus doping cell temperature. In the following, the principles of ECV are introduced briefly.

In the depletion approximation, the depletion width at an n-type semiconductor /

metal Schottky contact is given by

$$w_d = \sqrt{\frac{2\varepsilon_0\varepsilon_r\left(\phi_S - V\right)}{eN}}, \tag{3.8}$$

where ε_0 and ε_r are the dielectric constants of vacuum and of the semiconductor material, e is the elementary charge, ϕ_S is the Schottky barrier height, V is a (small) applied voltage which lowers the barrier height in forward bias, and N_d is the donor density in the semiconductor [101]. The diode capacitance is given by $C = \varepsilon_0\varepsilon_r A/w_d$, where A is the contact area. When ϕ_S and ε_r are known, the donor density N_d can be obtained by measuring the capacitance of the Schottky junction. Since ϕ_S is rarely very well known, the donor density is usually determined by additionally measuring the derivative of the capacitance with respect to the bias voltage dC/dV, and is then given by

$$N_d = \frac{C^3}{A^2 e\varepsilon_0\varepsilon_r \frac{dC}{dV}}. \tag{3.9}$$

The application of a reverse bias voltage to the Schottky contact moves the edge of the depletion region deeper into the semiconductor material. Measuring the capacitance and its derivative as a function of bias voltage thus yields a depth profile of the donor density $N_d(z)$, with the maximum depth limited by reverse bias electric breakdown. If the metal is replaced by an appropriate electrolyte, the Schottky contact can be moved into the semiconductor by etching its surface electrochemically. Iteratively etching the surface and measuring the carrier density at a constant bias voltage allows to record very deep carrier density profiles. While the maximum depth for conventional C-V profiling is very limited, especially for highly doped material (e.g. about 20 nm for $N_d \approx 10^{18}\,\mathrm{cm}^{-3}$ [100]), ECV profiling allows maximum depth up to several µm, which is mainly limited by roughening of the etch front.

Eq. 3.9 is based on the assumption that no effects apart from charge carrier transfer from the semiconductor to the metal or electrolyte contribute to the depletion region w_d, and that each impurity atom contributes one mobile charge carrier. In the presence of interface or surface states, which can trap electrons and increase the depletion region, or of compensation of donors by acceptor-type atoms, only the net density of mobile carriers n(z) is probed.

Unlike Hall measurements, ECV neither requires contacts or lithographic structuring of samples, nor a magnetic field. Additionally it allows to perform depth-dependent measurements. However, Hall measurements are usually more precise, since inhomogeneous etching, etch front roughening or re-adsorption of removed material to the etch front can reduce the accuracy of ECV measurements. Also, ECV is limited to about room temperature, since the electrolyte would freeze at cryogenic temperatures.

In this work, ECV profiles are measured using a commercial BioRAD Polaron semiconductor profiler, which is described in detail e.g. in [100]. The general procedures and the electrolyte for ZnSe (a 1:1 mixture of 1 molar $NaOH$ and 1 molar Na_2SO_3)

are described in [102, 103]. Figure 3.13 shows the carrier density profile of an n-ZnSe calibration sample measured by ECV. The sample consists of four, about 200 nm wide n-ZnSe layers with constant doping density, separated by about 60 nm wide, nominally undoped layers. It is grown on n-GaAs. The doping cell temperature is reduced stepwise from 150 °C to 90 °C in steps of 20 °C. The profile in figure 3.13 clearly resolves three plateaus with nearly constant carrier concentration, corresponding to the three highest doping cell temperatures. The topmost plateau, corresponding to the lowest doping cell temperature, is only partially resolved, since the depletion width in the low doped material is very large and since some material may be etched before the actual measurement is started. Also shown in figure 3.13 is a comparison of the carrier density measured by ECV and by low-temperature Hall measurements on separate, homogeneously doped samples. Both techniques yield very similar results, with the largest deviation being about a factor of two at very high doping concentrations.

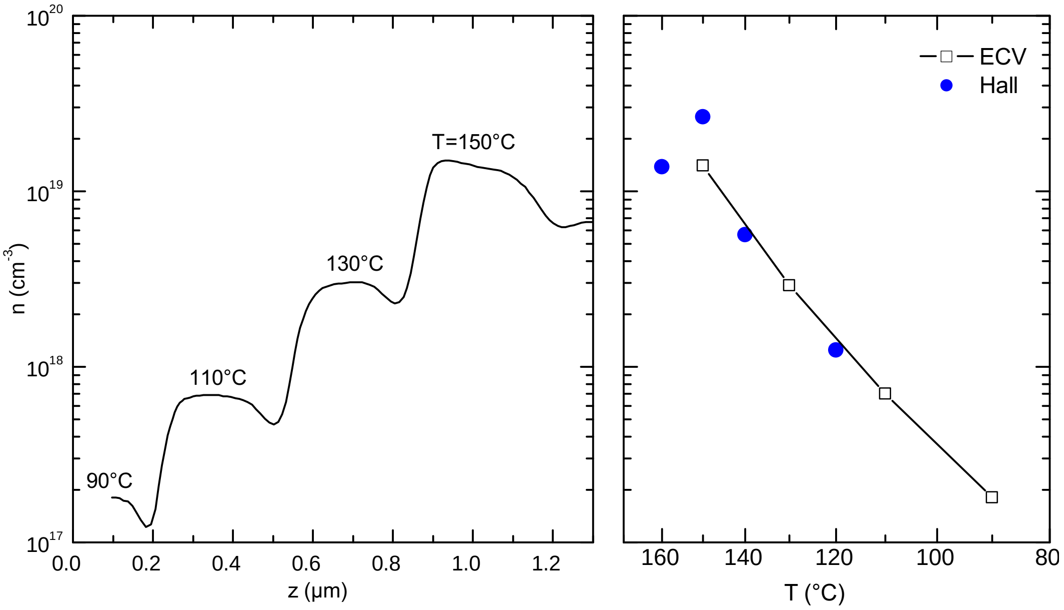

Figure 3.13: Depth profile of the electron density n(z) in an n-ZnSe calibration layer (sample cb3330) measured by ECV (left). Comparison of the carrier density as a function of the doping cell temperature obtained by ECV and by Hall measurements on separate samples (right).

3.5 Atomic Force Microscopy

Atomic force microscopy (AFM) is a scanning probe microscopy technique, which allows to map the surface topography of solids with nm resolution. It has been developed in the 1980s by Binnig et al. [104], after the scanning tunneling microscope (STM). AFM is more flexible than STM, since it can be used on both conducting and insulating samples, and under ambient air conditions. However, it usually has a lower resolution [51].

A schematic of an AFM is shown in figure 3.14. A sharp tip is mounted on a flexible cantilever bar and is brought into close contact with the surface of interest. At a range of a few nm, different attractive and repulsive forces, such as the van-der Waals force, act between the tip and the sample, and deform the cantilever. The tip is scanned over the surface by means of piezo-electric actuators, or alternatively the sample is scanned under the tip, and the topography of the surface is mapped by measuring the deflection of the cantilever. Usually, a low intensity laser beam is reflected from the back of the cantilever, and the position of the specular reflection spot on a photo diode array is detected. Since this detection mechanism is sensitive enough to measure cantilever deformations in the pm range, and since typical spring constants are on the order of 1 N/m, the forces between tip and surface can be in the 10^{-12} N range [51].

There are two modes of operation for AFM: the contact and the non-contact mode. In contact mode, the static deformation of the cantilever is sensed as the tip is dragged over the sample surface. To avoid crashing the tip into the sample, usually the tip-surface distance is kept constant by a feedback controller. The surface topography is mapped by recording the z-movement of the tip (or sample). In non-contact mode the cantilever oscillates close to its resonance frequency. The distance between tip and sample is slightly higher than in contact mode. The resonance frequency and the quality factor are influenced by distance-dependent forces between tip and sample, and the change of oscillation characteristics is used to construct an image of the sample surface topography. The non-contact mode is usually less invasive than the contact mode, since the tip-surface distance is higher and the involved forces are lower [51].

The resolution of AFM depends critically on the effective radius of curvature of the tip. In the present work tips with a curvature of about 10 nm are used. Features on the surface with a lateral separation lower than this tip diameter can not be resolved.

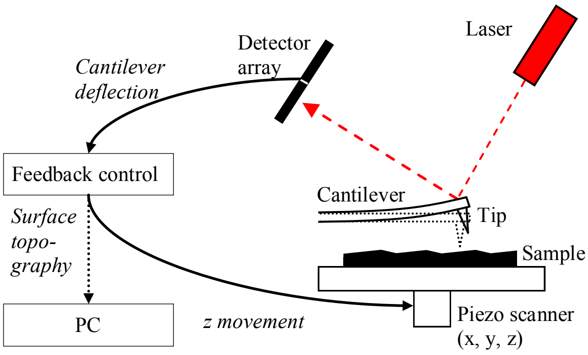

Figure 3.14: Schematic of an atomic force microscope.

3.6 Microstructuring and Electric Transport Measurements

The heterostructures fabricated in this work are processed into device structures for electric transport experiments using optical lithography, wet chemical or dry chemical etching, and electron beam evaporation of metallic contact layers. Typical structure sizes used in this work are on the order of 100 µm, which is well within the resolution limit of optical lithography. Etching of ZnSe based materials is done either wet chemically, using chromo sulphuric acid ($H_2SO_4 + CrO_3$), or dry chemically with reactive ion etching (RIE) or chemically assisted ion beam etching (CAIBE). Metal contacts are evaporated either in-situ after growth in a metalization chamber, which is connected to the MBE system via UHV, or ex-situ in a separate metalization chamber. With in-situ evaporated Al / Ti / Au contacts, the contact resistance on highly doped ZnSe ($N_d \approx 2 \times 10^{19}\,\mathrm{cm}^{-3}$) is usually on the order of $10^{-3}\,\Omega \cdot cm$, while the ex-situ evaporated contact resistance is usually one to three orders of magnitude higher [66].

A typical structure used for vertical transport experiments on tunneling heterostructures (chapters 6 and 7) is depicted in figure 3.15. It consists of an about $100\,\mu m$ wide quadratic pillar, which contains the active region and has an in-situ evaporated metal contact layer on top, and a ring-shaped bottom contact around the pillar, which is about $500\,\mu m$ wide. The bottom contact is evaporated ex-situ after etching the pillar, and has a low resistance due to its relatively large size. A current is sent vertically through the pillar by applying a voltage between the top and the bottom contacts. For transport experiments through n-ZnSe / n-GaAs heterointerfaces, about $500\,\mu m$ wide pillars are used, which contain the heterointerface. Indium, diffused into the n-GaAs substrate, is used as a backside contact. For more details refer to chapter 5.

The structured sample is glued into a chip-carrier. The on-chip contacts are bonded to contact pads on the chip carrier by using ultrasound bonding with Au wires. The chip carrier with the sample is then inserted into a cryostat for low temperature electric transport experiments. Transport experiments at varied temperatures between 300 K and about 10 K are performed using an Oxford He flow cryostat with active temperature regulation. Low temperature magneto-transport experiments are done in a He bath cryostat equipped with a superconducting electromagnet.

Electric transport measurements are done either with a HP4145B semiconductor parameter analyzer (those discussed in chapter 5), or by using dedicated, low noise voltage sources and meters (chapters 6 and 7). Single and double barrier tunneling diodes are characterized electrically by putting them in series with a resistor of well known resistance, which is on the same order of magnitude as that of the device under study. A stabilized voltage source is used to apply bias to this circuit, and two voltage meters are used to measure the voltage drop over the series resistor (i.e. the current) and over the studied device. For RTD structures, often additional precautions are taken to prevent problems associated with oscillations due to negative differential resistance. For I-V measurements of RTDs see also [66, 9].

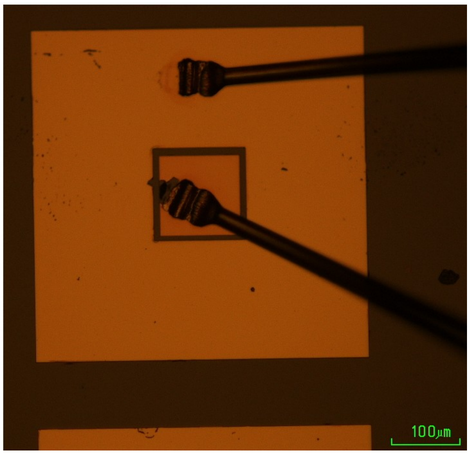

Figure 3.15: Optical micrograph of a typical mesa diode structure used for vertical transport experiments in single- and double barrier tunneling heterostructures. The about 100×100 μm^2 inner square is the pillar containing the heterostructure of interest. It has an in-situ metal contact on top, to which a bonding wire is attached. The outer square ring is the backside contact, also with a bonding wire attached.

3.7 Transition To New MBE Chamber and Calibration

Towards the end of this work, a new MBE chamber of the type RIBER Compact 21 was acquired as a replacement for the RIBER MBE 32 chamber ("CT chamber") used for ZnSe growth until then. This section compares these two growth chambers and describes the commissioning and calibration of the Compact 21 chamber for the growth of high quality, II-VI heterostructures. Aspects of the composition calibration of (Zn,Mn)Se and of the elimination of certain kinds of defects in the early layers grown in this chamber are detailed in the diploma thesis of M. Endress [105].

The general layout of a RIBER Compact 21 MBE chamber is illustrated in figure 3.16. Similar to the MBE 32 chamber (depicted schematically in figure 3.1), it is equipped with a cryo-, ion-getter, and Ti sublimation pump for achieving UHV, with means for manipulation and heating of substrates (up to 2-inch wafers), for the thermal evaporation of source materials, and for in-situ characterization by RHEED. Substrates are glued with indium onto solid Mo blocks, which serve as sample holders in the MBE system. The main difference is, that effusion cells in the new chamber are arranged in a circle at the bottom of the chamber instead of on a sidewall. This vertical geometry allows that more cells can be installed (10 ports instead of 8), and it ensures that all cell ports are equal in their position relative to the substrate.

Even though the layout of the new chamber is quite different, the cell and substrate temperatures and the general process steps for II-VI growth are very similar to those used in the old MBE 32 chamber. Figure 3.17 shows the beam equivalent pressure

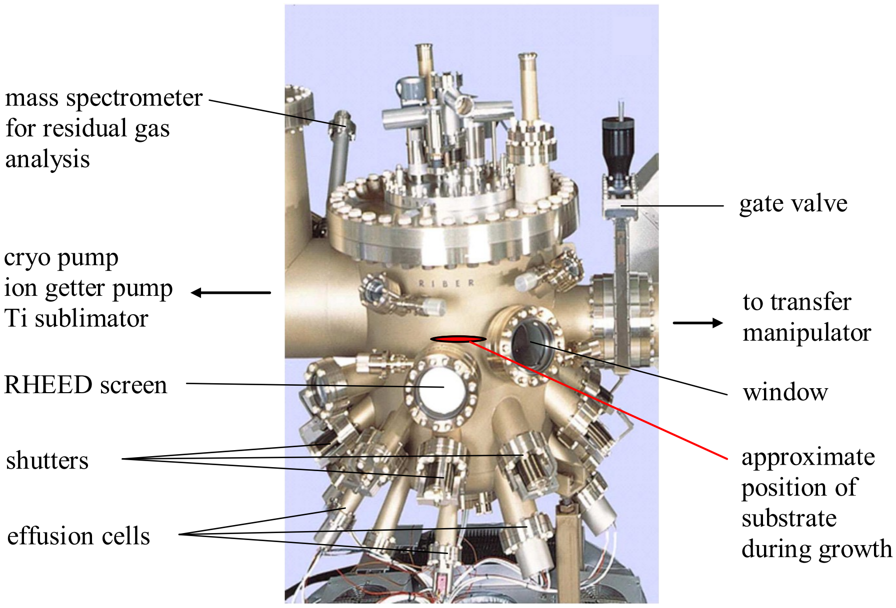

Figure 3.16: Photograph of an MBE chamber of the type RIBER Compact 21. Image adopted from www.riber.com.

(BEP) of several materials as a function of the cell temperature, recorded in the MBE 32 and the Compact 21 chamber. The background pressure measured by the flux gauge at closed cell shutter has been subtracted. The exponential decay of the BEP with 1/T indicates that it is a thermally activated process, as expected for thermal evaporation. For the Zn and Cd cells, the BEP in the old and in the new chamber are very similar. For the higher temperature materials, Be and Mn, the BEP in the new chamber is slightly lower, which may be related to the different geometry of the cells or to their position the chamber. For ZnI no BEP could be measured in the old MBE 32 chamber.

In the following the commissioning of the new chamber and its preparation for the growth of high-quality, ZnSe based heterostructures are described. After the chamber is installed, baked out, and the cells are filled with source materials, the temperature controls of the individual cells and the substrates are optimized. The PID controllers used for regulating the cell and substrate temperatures are tuned either automatically or by hand ("Ziegler-Nichols" method) at their respective operating temperature. Several pure ZnSe layers and "dirt samples" (all source materials deposited simultaneously) are grown, in order to passivate all internal surfaces and to stabilize the growth conditions. The Zn cell is heated close to the melting point of Zn, in order to remove an oxide layer on the material. Plain ZnSe layers are grown with a Zn and Se BEPs of about 8×10^{-7} Torr and 2×10^{-6} Torr, respectively, and their layer thickness and quality are determined by XRD. The ZnSe growth rate is adjusted if necessary to about 1 Å/s by changing the BEPs.

When the ZnSe growth rate is stable, the composition and growth rate of (Zn,Be)Se,

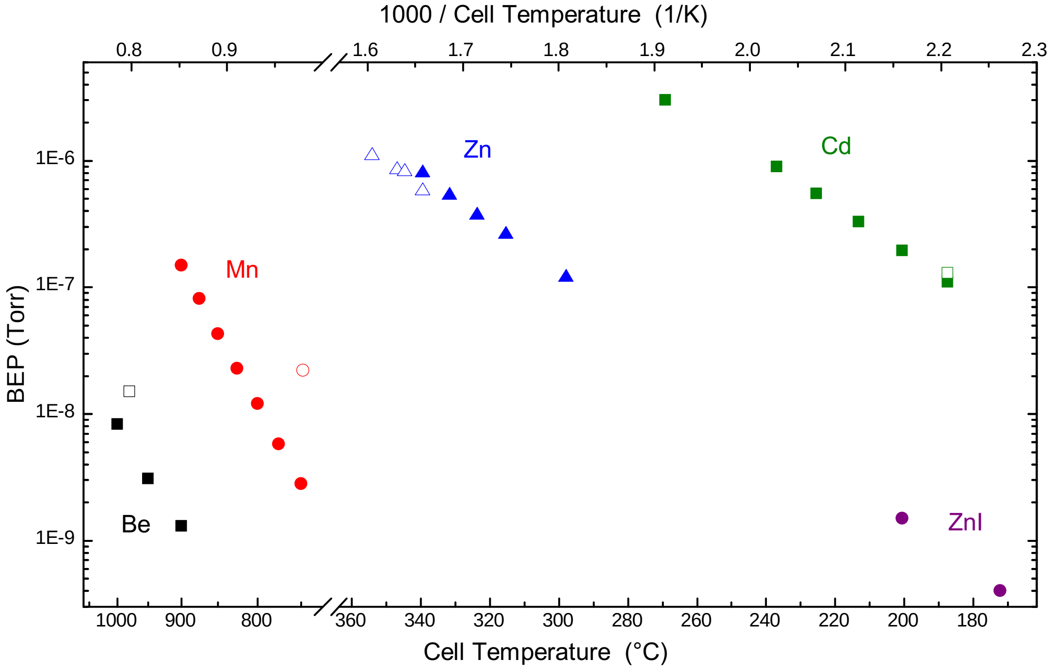

Figure 3.17: Beam equivalent pressure as a function of the effusion cell temperature, measured for different source materials. Solid symbols correspond to measurements in the new Compact 21 MBE chamber, open symbols to the older MBE 32 chamber ("CT chamber").

(Zn,Mn)Se and (Zn,Cd)Se, as well as the carrier density in iodine-doped ZnSe, are calibrated. Since the heterostructures discussed in this work typically need several different Be concentrations in the range from 3 % to 30 % in different layers, a relatively wide range of concentrations is covered in the calibration. Three or more (Zn,Be)Se layers with a projected Be concentration in the range between 1 % and 10 % are grown, and the thickness and composition are determined by XRD, using the materials parameters described in section 2.1. Since the addition of Be can lead to a high tensile strain, the thickness of these calibration layers is reduced for higher Be concentrations to avoid relaxation. For about 10 % Be the calibration layers are typically about 40 nm thick. For higher Be concentrations in the range of 20 % - 30 %, ZnSe / (Zn,Be)Se / ZnSe triple layer structures are grown and analyzed by XRD, with the (Zn,Be)Se layer being only a few nm thin. Making use of the x-ray-interference effect described in sections 3.2.1 and 4.3 the thickness and composition of such thin layers is determined by XRD. The (Zn,Be)Se growth rate usually increases proportionally to the added amount of Be. As an example, the composition of (Zn,Be)Se layers as a function of the Be cell temperature for both, the MBE 32 and the Compact 21 MBE chamber, is depicted in figure 3.18. For both chambers the Be content shows a similar variation with the Be cell temperature, but in the Compact 21 chamber about 20° C higher cell temperatures are required for a certain Be concentration.

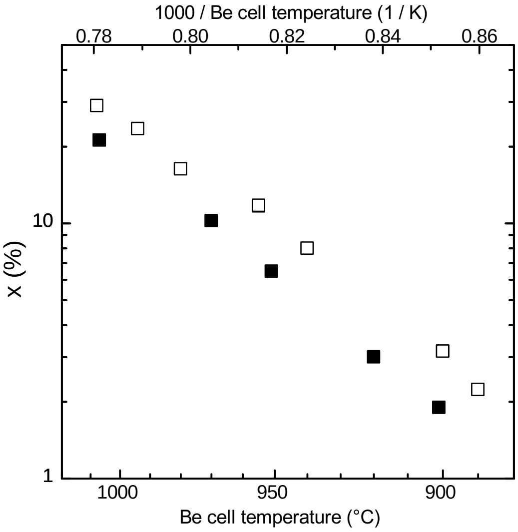

Figure 3.18: Composition of (Zn,Be)Se layers as a function of the Be effusion cell temperature. Solid symbols correspond to measurements in the new Compact 21 MBE chamber, open symbols to the older MBE 32 chamber. The growth rate of the basic material ZnSe in both cases is about 1.1 Å/s.

For (Zn,Mn)Se and (Zn,Cd)Se, two to three calibration samples are grown and analyzed by XRD. To calibrate the composition of (Zn,Mn)Se layers, M. Endress has compared several analytical methods to determine the Mn concentration, including XRD, magneto-PL, SIMS and XPS [105]. In principle, the Mn content can be determined directly and uniquely by measuring the shift of the near-band-edge PL line of a (Zn,Mn)Se epilayer in a magnetic field [44]. However, this method is only sensitive to Mn incorporated on cation lattice sites (Mn antisites or interstitials are not detected), and some ambiguities are found when the Mn concentrations is higher than about 6 % [105]. In the present work, the composition of (Zn,Mn)Se layers is calibrated using the lattice constant determined by XRD on thick epilayers as a measure for the Mn content. When all compositions, growth rates, and doping densities are calibrated, the more complex heterostructures of interest are fabricated. They are continuously characterized by XRD whenever possible, to detect any drift or accidental deviation of the growth conditions from the calibration.

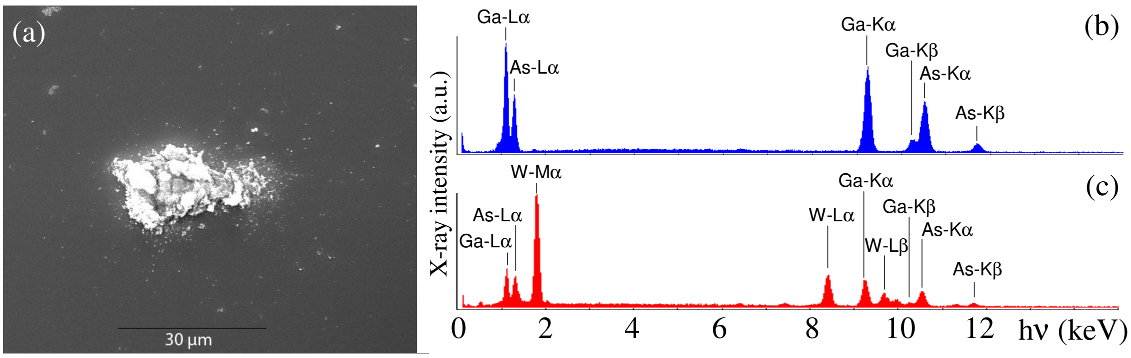

Figure 3.19: SEM image (a) and energy-dispersive x-ray spectra (b, c) of a wafer with macroscopic particle contamination, as found in early samples grown in the Compact 21 ZnSe chamber. Spectrum in (b) is taken on a clean spot of the wafer, spectrum (c) is taken on the contaminated part. Additionally to the characteristic x-ray lines of Ga and As, seen in spectrum (b), spectrum (c) also shows several lines indicating that the particle consists mainly of W.

The first II-VI layers grown in the Compact 21 chamber had a high density of irregularly shaped, macroscopic defects, in the range $10^4 - 10^7$ cm^{-2}. An SEM image of such a defect on a GaAs wafer is shown in figure 3.19 (a). Analyzing a number of them by energy-dispersive x-ray spectroscopy (EDX) revealed a high content of tungsten in the defects. Example spectra of a clean part of the wafer and of the defect in (a) are shown in figure 3.19 (b) and (c), respectively. With this information, a defective vacuum ion gauge in the load lock of the MBE system could be identified as the source of contamination. After its removal and after thorough cleaning of the load lock, most of the subsequently grown samples were contamination free.

Chapter 4

Building Blocks for ZnSe Based Spintronic Heterostructures

In this chapter selected properties of individual ZnSe epilayers, (Zn,Mn)Se DMS layers, (Zn,Cd)Se quantum wells and (Zn,Be)Se tunnel barriers are presented, followed by a systematic analysis of the optical and structural properties of epitaxial CdSe quantum dots embedded in (Zn,Be)Se and (Zn,Be,Mn)Se matrices. The latter is based on the diploma thesis of J. Henke [34]. These layers form the building blocks for more complex heterostructures discussed in the following chapters.

4.1 Pure and n-Type ZnSe Layers

This section describes basic structural, optical, and electric properties of ZnSe epilayers grown in the course of the present work.

4.1.1 Surface Morphology

Figure 4.1 shows a typical AFM image of a 40 nm thick ZnSe layer on GaAs(001), taken ex-situ in ambient air. The main features of this surface are long-range mounds with up to 10 nm height and about 200 $nm \times 1\mu m$ lateral extension, and large islands of up to 80 nm height and up to 100 nm diameter.

The islands can usually be removed without trace by repeated scanning of are same spot by AFM, and are thus attributed to post-growth contamination of the sample before or during the ex-situ AFM measurement. One possible source of such a contamination is a defective vacuum ion gauge in the load-lock of the MBE system, which occasionally emitted small particles of tungsten. This is verified by energy-dispersive X-ray spectroscopy on different samples (see end of section 3.7).

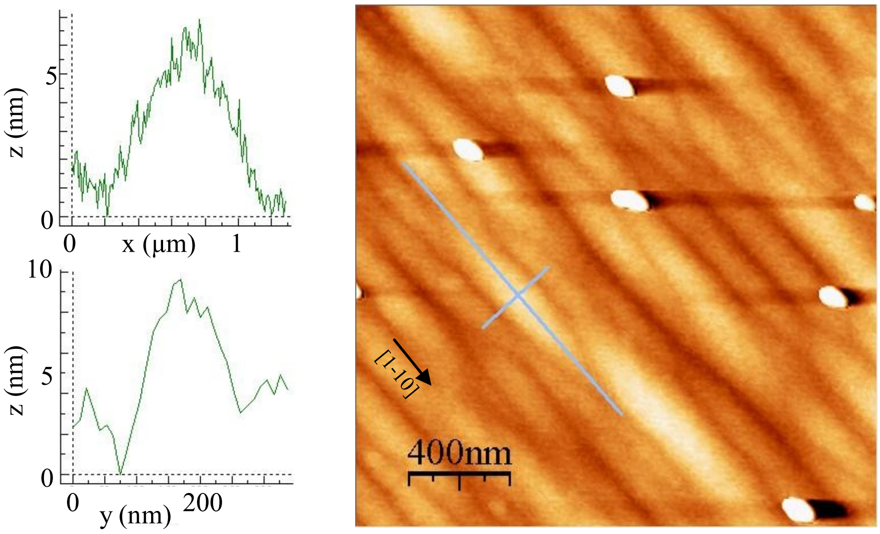

Figure 4.1: AFM image of the surface of a 40 nm thick ZnSe layer grown on GaAs(001).

The long-range mounds are frequently observed on MBE-grown epilayers of ZnSe and other zincblende semiconductors [106, 79]. They are clearly elongated in the $1\bar{1}0$ crystal direction. In [106] their emergence is attributed to island nucleation during MBE growth in conjunction with a potential barrier at step edges. The latter hinders mobile adatoms on top of an island from climbing down to a lower level, and thus promotes growth on top of already existing islands.

The resolution of the available ex-situ AFM is not sufficient to observe individual atomic steps. Apart from the mounds and the post-growth contamination the ZnSe surface thus appears flat, as expected for a high-quality MBE-grown epilayer.

4.1.2 Photoluminescence Spectrum

A very sensitive probe of the material quality and impurity content in a semiconductor is its luminescence spectrum. A high density of impurities or defects usually leads to a high density of non-radiative recombination channels, or to donor-acceptor pair recombination. Figure 4.2 depicts a near band-edge PL spectrum of a 100 nm thick, undoped ZnSe layer on GaAs, taken at 1.6 K. The sample is grown in the Compact 21 ZnSe MBE chamber. Several sharp luminescence lines with a FWHM between 0.9 meV and about 2.0 meV are observed at 2.800 eV, 2.807 eV, 2.811 eV, and 2.819 eV. The literature value of the low-temperature band gap of unstrained ZnSe is about 2.82 eV. The binding energy of free excitons is approximately 20 meV, that of biexcitons is about 4 meV [35]. The small biaxial strain due to pseudomorphic growth on GaAs increases the energy gap slightly (deformation potentials see e.g. [107]). The sharp lines at 2.800 eV and at higher energies are therefore attributed to various free excitons (e.g. excitons in the ground or excited states, biexcitons, charged excitons) and bound excitons. The broader, less intense line at 2.78 eV is attributed to donor-acceptor pair recombination. The high intensity of the exciton lines compared to the donor-acceptor pair recombination indicates good quality of the grown ZnSe material, and a low density of impurities or defects.

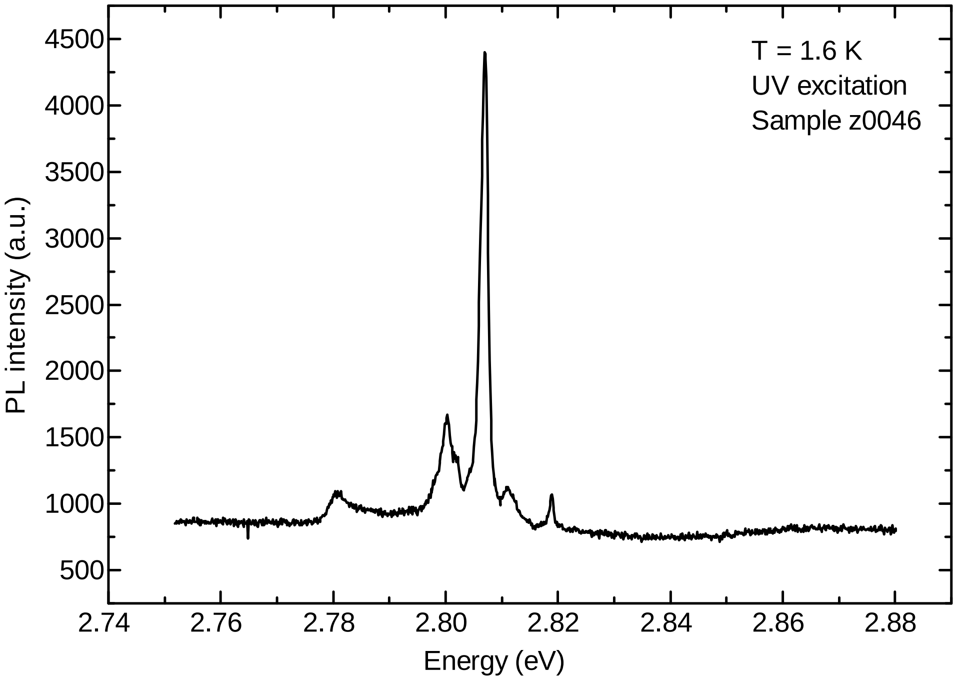

Figure 4.2: PL spectrum of a 100 nm thick ZnSe layer, taken at a temperature of 1.6 K with excitation in the UV. The sample is grown in the Compact 21 MBE chamber.

4.1.3 Hall Measurements

Hall measurements are an important electric characterization method for doped semiconductor layers, since they provide precise information on the carrier density, the type of conductivity (n- or p-type), and on the carrier mobility [101]. Figure 4.3 shows the Hall resistance R_{xy} and the longitudinal resistance R_{xx} of a 200 nm thick ZnSe layer as a function of the applied magnetic field. The layer is highly n-type doped with ZnI. It is grown on a thick multilayer buffer structure to shield it from the ZnSe / GaAs heterointerface below.

For Hall measurements, a constant voltage is applied longitudinally to a lithographically prepared Hall bar structure (depicted in the inset of figure 4.3) and a series resistor, and a magnetic field is applied perpendicular to the layer plane. The Hall resistance is obtained from the Hall voltage U_{xy} measured between opposing contact pads by $R_{xy} = U_{xy}/I$, and the longitudinal resistance is given by the voltage drop U_{xx} between two neighboring contact pads $R_{xx} = U_{xx}/I$.

With $R_{xy} = B/(d \cdot n \cdot e)$, where d is the layer thickness of 200 nm and e is the elementary charge, the carrier density $n = 1.60 \times 10^{19}$ cm^{-3} is obtained. This is in good agreement with the value of about 2 $\times$ 10^{19} cm^{-3} measured by ECV on calibration samples, and is close to the maximum achievable density of 3 $\times 10^{19}$ cm^{-3} Shibata et al. have reported for Iodine doped ZnSe in MOVPE [49]. The resistivity of the present layer is $\rho = 1.7$ m$\Omega \cdot$cm, which is also very close to the best value of 1.3 m$\Omega \cdot$cm reported by Shibata et al.

The mobility μ is given by $R_{xx} = l/(b \cdot d \cdot n \cdot e \cdot \mu)$. With $l = 160\ \mu m$, $b = 40\ \mu m$, $R_{xx} = 345\ \Omega$, and d and n as above, the mobility is $\mu = 226$ cm^2/Vs. Ruda et al. have calculated the electron mobility in bulk, n-type ZnSe as a function of the donor concentration up to 3×10^{18} cm^{-3} [108]. A linear extrapolation of their total mobility to 1.6×10^{19} cm^{-3} yields a value significantly below 1000 cm^2/V s at 77 K, limited by impurity scattering. The present value is slightly lower but is still considered to be in good agreement with this theoretical limit.

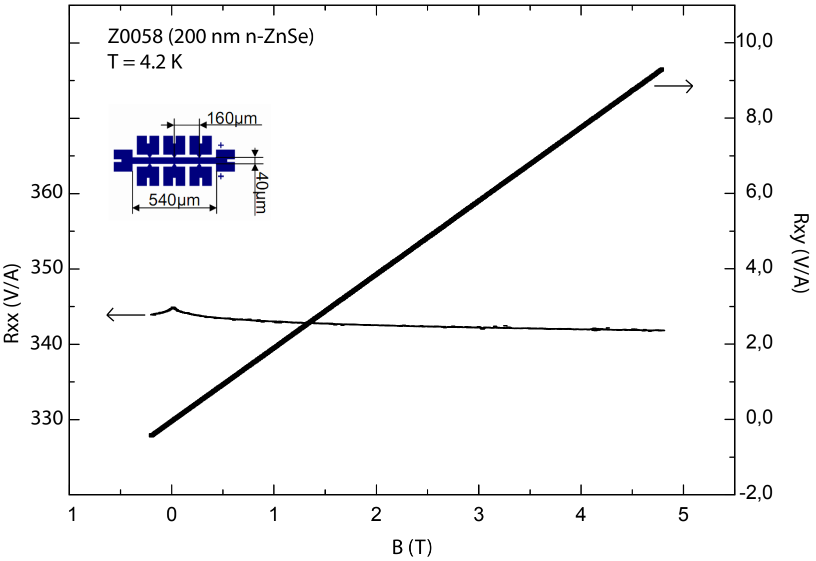

Figure 4.3: Longitudinal resistance R_{xx} and Hall resistance R_{xy} of a highly doped, 200 nm thick n-ZnSe layer. The inset shows the geometry of the Hall bar. The sample is grown in the Compact 21 MBE chamber.

4.2 Diluted Magnetic Semiconductor Layers

The giant Zeeman effect in II-VI diluted magnetic semiconductors is the main handle for electron spin manipulation in the heterostructures studied in the present work. In these structures, the giant Zeeman effect usually manifests itself in a change of device resistance in a magnetic field or in a variation of I-V characteristics. It can be directly observed in optical experiments such as magneto-PL, where the large splitting of the band edges and the relaxation of photo excited carriers to the respective lower spin state leads to a pronounced, Brillouin-like shift of the band-edge luminescence to lower energies.

Magneto-PL spectra of a 70 nm thick (Zn,Mn)Se layer fabricated in the Compact 21 MBE chamber are shown in figure 4.4. The nominal Mn concentration of the layer, according to XRD measurements on calibration samples, is 8 %. The spectra are measured at 1.6 K and in magnetic fields up to 6 T. At 0 T the luminescence spectrum shows one peak at 2.843 eV with a FWHM of 3.2 meV. The literature value for the band gap of unstrained $Zn_{0.92}Mn_{0.08}Se$ is 2.834 eV (see table 2.2), which is consistent with the measured PL energy considering that significant compressive strain in the layer slightly increases the band gap. In a magnetic field the luminescence line shifts to lower energies following a Brillouin function, as shown in the inset. Due to the high Mn concentration in this sample the shift is quite large, reaching - 60 meV for 6 T. At a small field of 0.25 T another luminescence peak appears at slightly higher energies than the 0 T peak. It may be attributed to recombination involving carriers from the energetically higher minority-spin level, which have not relaxed to the lower majority-spin level before recombination.

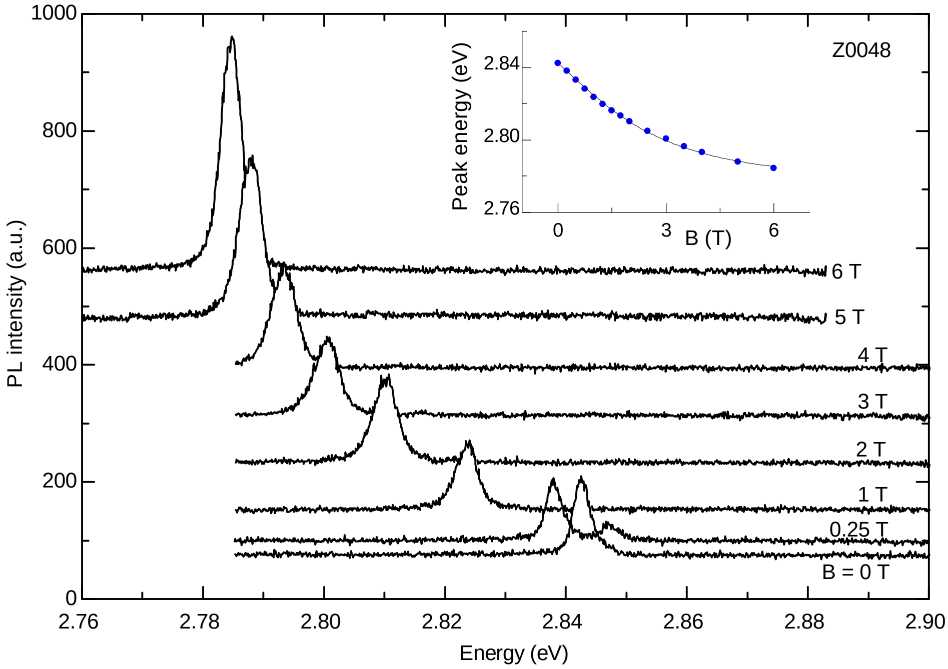

Figure 4.4: Near band edge magneto-PL spectra of a 70 nm thick (Zn,Mn)Se layer, measured at 1.6 K. The inset shows the peak position as a function of the magnetic field. The solid line is a fit to the data based on a modified Brillouin function (see section 2.2), yielding a Mn concentration of 6.2 %. The sample is grown in the Compact 21 MBE chamber.

4.3 Tunnel Barriers

Few nm thin layers of (Zn,Be)Se with a high Be content up to about 30 % serve as tunnel barriers in the fabricated resonant and spin-dependent tunneling heterostructures. The high Be concentration leads to high tensile strain, which poses the risk of plastic relaxation.

Figure 4.5 shows XRD $\omega - 2\Theta$ scans of two calibration samples containing thin, highly strained (Zn,Be)Se layers (black curves). The (Zn,Be)Se layers are embedded in thicker, nearly symmetric ZnSe cladding layers grown on GaAs (see inset), and the layer structure thus forms an x-ray interferometer, as described in section 3.2.1.

The highest peak at $\Delta\Theta = 0°$ is the GaAs 004 reflection. The double peak at lower angles around $\Delta\Theta = -0.25°$ originates from the ZnSe cladding layers. The ZnSe layer peak is split into two due to x-ray interference caused by the thin (Zn,Be)Se interlayer. The broad peak with a maximum at a high angle $\Delta\Theta = 1.43°$ for curve (a) and $\Delta\Theta = 1.86°$ for curve (b) is the direct 004 Bragg reflection of the (Zn,Be)Se interlayer. Since the interlayer is very thin, this peak is broad with a FWHM on the order of 1°, and is low in intensity. The high frequency oscillations observed over nearly the whole angular range in both scans are thickness oscillations from the ZnSe cladding layers. Their angular separation corresponds approximately to the thickness of one cladding layer (see equation 3.5). Since the layers are of slightly different thickness, oscillations with slightly different periodicity superimpose, resulting in a beating in their intensity.

The dynamic simulations in figure 4.5 (red curves) correspond to a 7.2 nm thin $Zn_{0.77}Be_{0.23}Se$ layer between 52 nm and 55 nm thick ZnSe cladding layers (a) and to a 5.7 nm thin $Zn_{0.71}Be_{0.29}Se$ layer between 66 nm and 69 nm thick ZnSe layers. Since both, x-ray interference and direct Bragg reflection of the (Zn,Be)Se interlayer, are observed, the simulations are unique with respect to the interlayer composition and thickness. If only x-ray interference were observed, only the phase shift due to the interlayer could be determined, resulting in an ambiguity in the composition and thickness of the interlayer (see section 3.2.1). With these structural parameters the simulations accurately reproduce all important features of the experimental scans, including the x-ray interference, thickness oscillations, and the direct, low intensity reflection from the (Zn,Be)Se interlayer.

The observation of thickness fringes and x-ray interference between ZnSe cladding layers, along with good agreement between simulations and measured scans, indicates that the layer structures are of high structural quality and are fully strained. Plastic relaxation due to the high tensile strain is negligible. The high density of dislocations associated with plastic relaxation would destroy coherence of the lattice, thus suppressing x-ray interference and thickness oscillations and leading to a discrepancy between simulations and measured scans. Apart from investigating the structural quality of potential tunnel barrier layers, such XRD measurements on test layer structures are used for the calibration of composition and growth rate of (Zn,Be)Se layers with a high Be content up to 30 %.

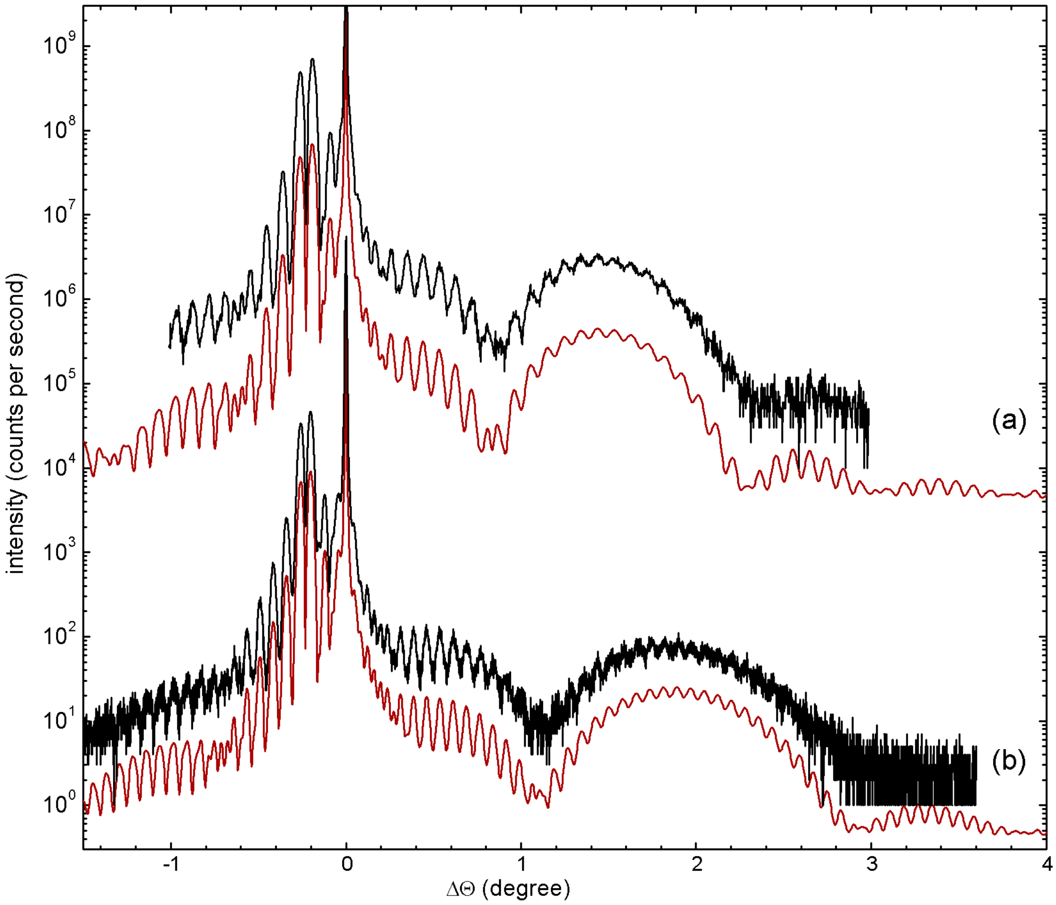

Figure 4.5: XRD $\omega - 2\Theta$ scans (black) and simulated diffraction patterns (red) around the GaAs 004 reflection of two layer structures containing a thin, highly tensile-strained (Zn,Be)Se layer between thicker ZnSe cladding layers (see inset).

4.4 Quantum Wells

An important building block for semiconductor quantum heterostructures is the finite quantum well, consisting of a thin layer of a low band gap material sandwiched between thick cladding layers of material with a higher band gap. Figure 4.6 shows the PL spectrum of such a quantum well structure fabricated in this work. The structure nominally consists of a 10 nm wide $Zn_{0.9}Cd_{0.1}Se$ quantum well embedded in 50 nm and 70 nm thick ZnSe cladding layers, grown on GaAs(001). Before and after the quantum well layer a 30 s growth interruption is inserted to smoothen the heterointerfaces.

The PL spectra in figure 4.6 are taken at a temperature of 1.6 K, with low power

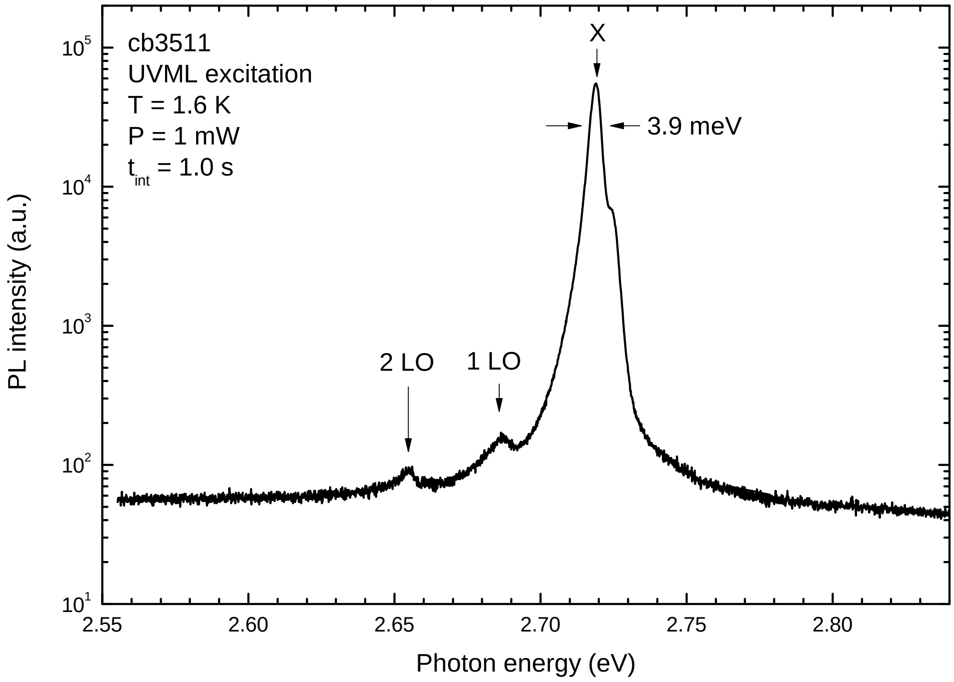

Figure 4.6: PL spectrum of a 10 nm wide $Zn_{0.9}Cd_{0.9}Se$ quantum well embedded in ZnSe.

optical excitation in the UV (above the ZnSe band gap). The main PL line is at 2.719 eV and there are two LO phonon replicas (1LO and 2LO) at lower energies. The main PL line is attributed to recombination of free or bound excitons in the quantum well. Its position is in good agreement with the effective quantum well band gap of 2.701 eV, calculated by adding the electron and hole quantization energy (42 meV and 8 meV, respectively[1]) to the band gap of $Zn_{0.9}Cd_{0.1}Se$ (2.682 eV), and subtracting 30 meV to account for the exciton binding energy in the 10 nm wide quantum well (see [42]). The remaining small energy difference may be due e.g. to compressive biaxial strain or to atomic interdiffusion, which both increase the QW band gap, or due to localization of excitons at impurities.

The low FWHM of the main PL line of 3.9 meV indicates a high lateral homogeneity of the quantum well width and composition. A near-band edge luminescence from the ZnSe barrier material is not observed. Together with the high intensity of the QW PL signal this indicates that the ZnSe material is of a high purity, since excitons generated in ZnSe have a long enough diffusion length to be localized in the quantum well before recombination. The shoulder about 4 meV above the main PL line may be due to excitons bound to different impurities or due to charged or excited excitons.

---

[1] Using an effective mass of 0.15 m_0 for electrons and 0.8 m_0 for holes, and assuming a conduction band offset of 84 %.

4.5 Self-Assembled CdSe QDs

The MBE growth and the structural and optical properties of self-assembled CdSe quantum dots (QDs) are described in this section. The focus is on the influence of diefferent barrier materials on CdSe island formation and on the quantized states in the QDs. The results have been obtained mostly by J. Henke in his diploma thesis and are discussed there in great detail [34].

A general overview over growth and properties of self-assembled, epitaxial semiconductor nanostructures in different material systems is given by Stangl [109]. For the self-assembly of CdSe islands and quantum dots, a variety of different MBE-based formation processes is compared by Mahapatra [79]. Variants of MBE, such as formation of islands by thermal activation during in-situ annealing of a CdSe epitaxial layer (see also [110, 111, 112]), as well as deposition and re-desorption of amorphous Se or Te layers (see also [113, 114, 115]), have been shown to yield islands of different size, density, and with different degrees of Cd / Zn interdiffusion. According to these investigations, the deposition of a few ML of CdSe on ZnSe by "normal" MBE (i.e. without additional process steps like in-situ annealing, capping / decapping with Se etc.) typically results in a rough (Zn,Cd)Se layer with shallow ($\approx$ 1 nm), abutting mounds and with local variations in Cd content (usually less than 50 % [116]). The potential fluctuations in such inhomogeneous quantum well layers act as QDs and confine excitons and individual carriers three-dimensionally. The QD density measured by μ-PL is typically in the range of $10^{11} - 10^{12}$ cm^{-2} [79].

The effect of Be or Mn in the ZnSe barrier material on CdSe QDs is the subject of only a few studies. Kim et al. found that the PL energy of CdSe QD ensembles embedded in $\mathrm{Zn}_{1-x}\mathrm{Mn}_x\mathrm{Se}$ is redshifted and narrowed with increasing x in the range from 0 % to 25 % [117]. It was concluded that the presence of Mn in the barriers increases the Cd content in the QDs, and has a positive effect on island homogeneity. Lee et al. also found evidence for Mn in the barriers influencing CdSe island growth [118, 119]. Be in the barrier material is reported to affect CdSe island formation even in low concentrations of 3 % [120]. By PL and Raman measurements it was found that the Cd concentration x in optically active QDs is increased from $x = 0.42 - 0.43$ for pure ZnSe barriers to $x = 0.47 - 0.52$ for $Zn_{0.97}\mathrm{Be}_{0.03}$Se barriers. Also the lateral size of the QDs is reduced by the addition of Be.

4.5.1 Growth of Self-Assembled CdSe QDs

As a part of this work, the structural and optical properties of self-assembled CdSe QDs embedded in (Zn,Be,Mn)Se barrier materials of different composition are investigated, with the prospect of utilizing such QDs in dilute magnetic 0D resonant tunneling diodes. For this purpose, several series of samples with CdSe layers of varied coverage and embedded either in ZnSe, in $\mathrm{Zn}_{0.8}\mathrm{Be}_{0.2}\mathrm{Se}$ or in $\mathrm{Zn}_{0.72}\mathrm{Be}_{0.2}\mathrm{Mn}_{0.08}\mathrm{Se}$ layers are fabricated. For the sake of simplicity the term "CdSe quantum dots" is used to refer to the fabricated samples, even though Cd / Zn interdiffusion can not be excluded.

Since the QDs are intended to be embedded in resonant tunneling diode structures, no prolonged annealing steps and capping / decapping procedures are used in their fabrication. As side effects such steps might cause enhanced interdiffusion or introduce additional impurities or defects, which is detrimental to the RTD structure. Instead, QDs are formed by plain MBE following the method described in [121]. After the growth of a ZnSe or (Zn,Be,Mn)Se layer at 300 °C, a 10 s growth interruption with the substrate under Se flux is introduced to smoothen the starting surface. Then CdSe is deposited by opening the Cd shutter. With a typical Cd BEP of 1.2×10^{-7} Torr the growth rate is about 20 s / ML [2] (1 ML CdSe $\approx$ 3.3 Å). A clear transition of the RHEED pattern from streaky to spotty upon reaching a critical CdSe coverage, as observed for Stranski-Krastanov island growth in other material systems [122], is not observed. A predominantly 2D 2 x 1 diffraction pattern is observed during and after CdSe growth. This is consistent with the observation of S. Mahapatra for CdSe QDs grown by MBE at 300 °C ([79], section 5.3). After CdSe deposition another 10 sec growth interruption is introduced, followed by growth of the capping layer. For samples intended for AFM no cap layer is grown, but the sample is cooled immediately and taken out of the chamber.

4.5.2 Morphology of CdSe QDs

Figure 4.7 shows AFM images of samples with 2 ML CdSe grown on (a) ZnSe and on (b) $Zn_{0.72}Be_{0.2}Mn_{0.08}Se$. For both samples clear islands can be discerned, which are not present on a pure ZnSe surface (compare figure 4.1). These CdSe islands have a typical base diameter of 30 nm, are about 1 nm high, and have a very high density in the range $10^{10} - 10^{11}$ cm^{-2}. Exemplary height profiles are shown in figure 4.8. The island morphology and density are similar to those frequently quoted for the CdSe / ZnSe material system [79, 123, 124]. Furthermore, the islands are slightly elongated along the [110] crystalline direction, perpendicular to the ZnSe surface undulations. Such an elongation of self-assembled CdSe islands has also been observed in TEM images [110] and by optical means [98, 125].

Comparing the images (a) and (b) in figure 4.7, a slight trend towards a smaller lateral size of CdSe islands for CdSe grown on (Zn,Be,Mn)Se can be presumed. This trend is in agreement with the findings in [120]. However, when evaluating the island morphology statistically for 20 islands on each sample, no significant differences between CdSe islands grown on ZnSe, on $Zn_{0.8}Be_{0.2}Se$, and on $Zn_{0.72}Be_{0.2}Mn_{0.08}Se$ are found [34].

---

[2] determined by XRI on reference samples (see section 3.2.1)

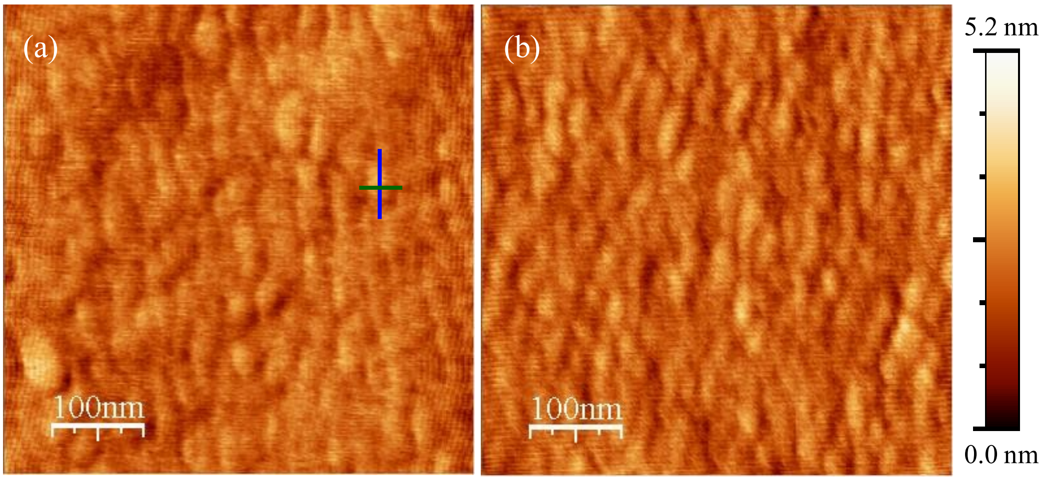

Figure 4.7: AFM images of a 2 ML thick CdSe layer grown on (a) ZnSe and on (b) $Zn_{0.72}Be_{0.2}Mn_{0.08}Se$. The color scale depicted on the right is the same for both images. Both images were recorded by J. Henke [34].

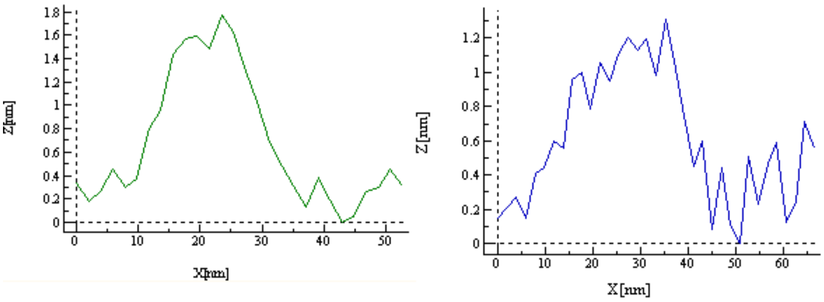

Figure 4.8: Height profiles of a typical CdSe island (highlighted in figure 4.7) in lateral and longitudinal direction.

4.5.3 PL of CdSe QDs Embedded in ZnSe and (Zn,Be)Se

To study the influence of the matrix material on the optical properties of CdSe quantum dots, two series of samples with CdSe QDs of varied coverage Θ, embedded in (a) pure ZnSe and in (b) thin layers of $Zn_{0.8}Be_{0.2}Se$ are fabricated. The latter corresponds to typical tunnel barrier layers in II-VI RTDs, with a nominal band gap of 3.22 eV (see table 2.2). The layer structures and band diagrams are depicted in figure 4.9.

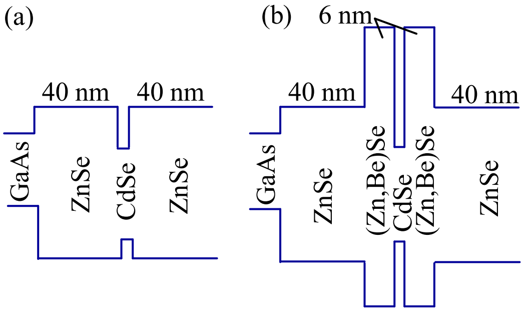

Figure 4.9: Sketch of the band profile of undoped CdSe / ZnSe (a) and CdSe / (Zn,Be)Se (b) heterostructures for PL.

Figure 4.10 depicts PL spectra of the two sample series. The spectra are taken at $T \leq 13\,\mathrm{K}$, $B = 0\,\mathrm{T}$, and with an excitation energy of $h\nu = 3.05\,\mathrm{eV}$ (i.e. above the band gap of ZnSe). They are normalized in intensity. For CdSe QDs embedded in ZnSe (panel (a)) a single, pronounced luminescence peak with a FWHM of several tens of meV is observed. Its energy depends on the CdSe coverage. It is attributed to excitonic recombination in the CdSe layer. As the coverage is increased from 0.6 ML to 3.4 ML, the peak energy continuously shifts from 2.73 eV down to 2.21 eV, reflecting the decreasing confinement energy of excitons in CdSe. At the same time the luminescence peak shape changes from a rather irregularly shaped, narrow peak with a FWHM of 21 meV and a low-energy tail, to a nearly Gaussian peak with a higher FWHM of 51 meV. The latter corresponds to an ensemble of CdSe quantum dots with a Gaussian distribution of islands size or Cd content. Luminescence from excitonic recombination in the ZnSe layers is not observed in the spectra in figure 4.10 (a). This is an indication for the high quality of the fabricated layers, since it implies that excitons have a long mean-free path before recombination.

PL spectra of CdSe QDs embedded in $Zn_{0.8}Be_{0.2}Se$ are shown in figure 4.10 (b). For small coverages $\Theta \leq 1$ ML the spectra are dominated by an about 15 meV wide luminescence line at 2.78 eV. This line is much weaker for samples with higher CdSe coverage, but its energetic position is nearly independent of the coverage. It is attributed to a recombination process in the ZnSe cladding layers, such as donor-acceptor pair transitions or recombination of bound excitons [35]. Apart from this ZnSe luminescence line, another peak is observed at different energies depending on CdSe coverage. For the lowest coverage of $\Theta = 0.75$ ML the peak is at a high energy of 2.92 eV, and is very low in intensity compared to the ZnSe luminescence line. With increasing CdSe

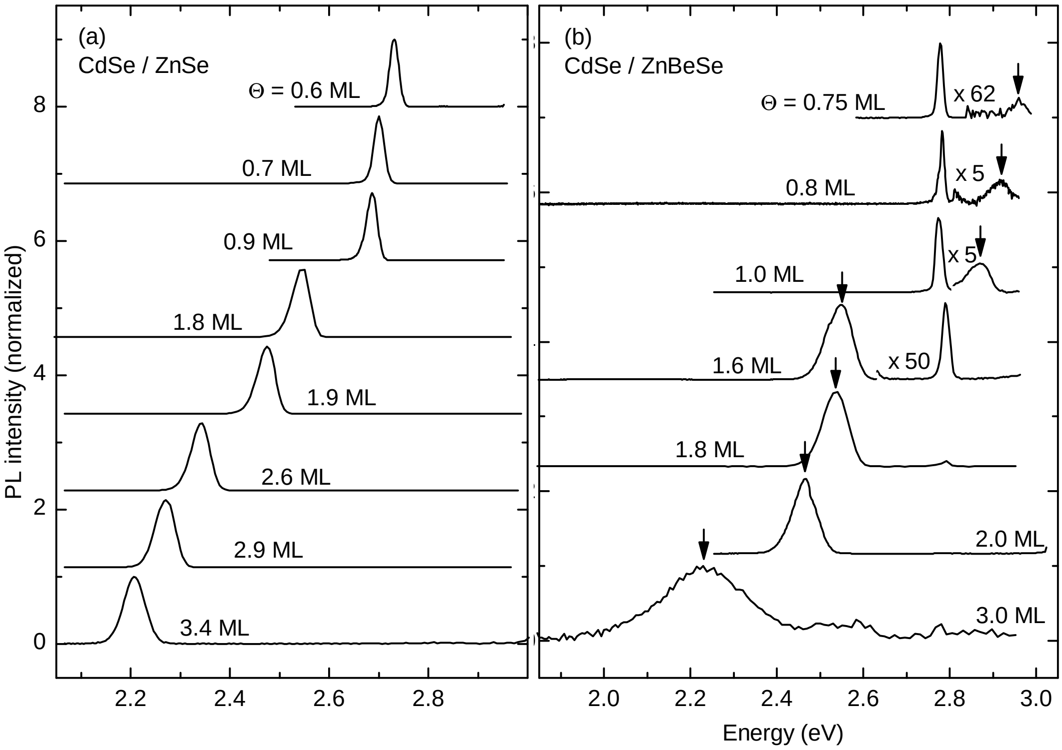

Figure 4.10: Photoluminescence spectra of ensembles of self-assembled CdSe QDs with different CdSe coverage Θ, embedded (a) in a ZnSe matrix and (b) in about 6 nm thin $Zn_{0.8}Be_{0.2}Se$ layers (structure see figure 4.9). The arrows in (b) indicate the luminescence band from the CdSe QD ensemble. The spectra are taken at $T \leq 13\,\mathrm{K}$, $B = 0\,\mathrm{T}$, and with an excitation energy of $h\nu = 3.05\,\mathrm{eV}$. Spectra are normalized and offset for clarity.

coverage it increases in intensity and monotonically shifts to lower energies. Between 1.0 and 1.6 ML it crosses the ZnSe PL line. Due to the clear dependence on the CdSe coverage and due to its relatively high FWHM, this peak is attributed to the CdSe QD ensemble. For higher coverages $\Theta \geq 1.6$ ML, when it is energetically below the ZnSe line, this CdSe QD luminescence dominates the spectrum, and the ZnSe line nearly vanishes for $\Theta \geq 2$ ML.

The strong variation of the ZnSe and the CdSe QD luminescence intensity for series (b) can be understood as follows: For both sample series, the excitation light ($h\nu =$ 3.05 eV) is absorbed in both, the ZnSe cladding layers and the CdSe layer. While for series (a) excitons generated in ZnSe may easily diffuse into the CdSe layer and contribute to the strong CdSe PL, this is hindered for series (b) by the presence of the tunnel barriers. Because fewer excitons are lost to the CdSe, the ZnSe luminescence in series (b) is stronger than in series (a), for $\Theta \leq 2.0$ ML. For low coverages $\Theta \leq 1.0$ ML, the effective band gap in the CdSe QDs in series (b) is larger than the ZnSe band gap, and the direction of exciton transfer is reversed. Excitons generated in the QD layer

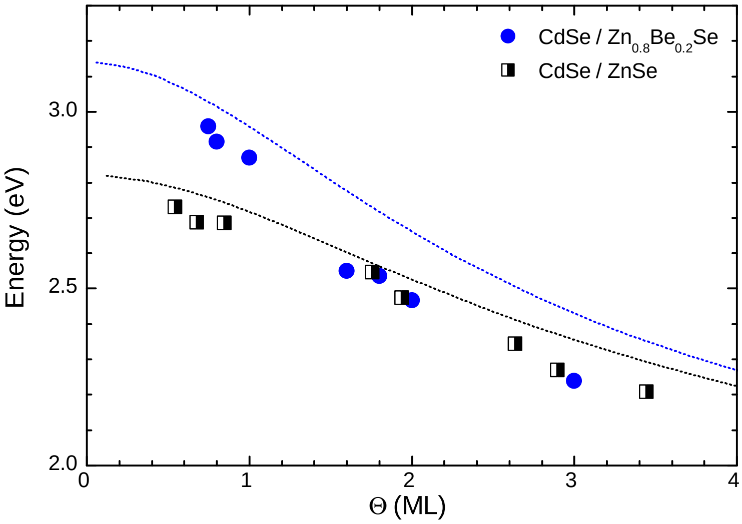

Figure 4.11: Measured PL energy of CdSe QD ensembles embedded in ZnSe and in $Zn_{0.8}Be_{0.2}Se$ as a function of the CdSe coverage Θ(symbols). The dotted lines are model calculations for finite quantum well of CdSe / ZnSe (black) and CdSe / $Zn_{0.8}Be_{0.2}Se$ (blue).

may tunnel through the $Zn_{0.8}Be_{0.2}Se$ barriers into ZnSe, which explains the rather low intensity of the QD PL compared to the ZnSe PL for these coverages.

The QD ensemble PL peak energy is shown in figure 4.11 as a function of the coverage for both sample series (a) and (b). While the PL peak energy of CdSe QDs embedded in (Zn,Be)Se is significantly larger at low coverages, it decreases more rapidly with coverage. For coverages $\Theta \geq 1.6$ ML virtually no difference can be found between the two sample series.

For both series the QD PL energy decreases continuously with CdSe coverage. An abrupt transition of the PL to lower energies at a certain critical coverage, a hallmark of island growth in the Stranski-Krastanow mode [126], is not observed. This is consistent with other studies on the MBE growth of CdSe islands, e.g. [79] and references therein. It is also consistent with the absence of a distinct 2-d to 3-d transition of the RHEED pattern in these samples.

Also shown in figure 4.11 are calculated PL energies of smooth CdSe quantum wells with ZnSe barriers (black dotted line) and with $Zn_{0.8}Be_{0.2}Se$ barriers (blue dotted line). The PL energies are obtained by calculating the single-particle electron and the heavy hole ground states (considering the respective effective masses in CdSe and in the barrier materials) in a finite CdSe quantum well with different barrier materials, adding them to the CdSe band gap, and introducing estimated corrections for lateral confinement (plus 50 meV) and exciton binding energy (minus 30 meV). For details of the calculations refer to [34]. This simple model can by no means be considered an accurate representation of self-assembled quantum dots, however, it is intended to capture the essential effects of the different barrier heights on the quantized levels in the dots. The calculations overestimate the PL energy over the whole range of coverages by several tens of meV. This may be due to an imperfect estimate of lateral confinement energy or exciton binding energy, or due to the fact that, for inhomogeneous confinement energies, PL preferentially probes the energetic minima since excitons thermalize and are localized there.

For small coverages the calculations show that the PL energy of CdSe QDs embedded in $Zn_{0.8}Be_{0.2}Se$ is blue-shifted relative to QDs embedded in ZnSe, by an amount corresponding to the difference in the band gap of the barriers. This blue-shift is in very good agreement with the measured values for small coverages $\Theta \leq 1$ ML. For these coverages the model of a smooth, finite quantum well may be more accurate than for higher coverages, judging from the relatively narrow PL lines (see figure 4.10). For higher coverages the model overestimates the effect of the barrier material. This can possibly be explained by a different intermixing behavior of CdSe depending on the barrier material, as reported in [120]. A higher Cd content for QD layers grown on (Zn,Be)Se compared to such on ZnSe would lower the band gap in the QDs and can thus partially compensate the higher band gap in the barrier. A lower tendency for Cd intermixing may also be supported by the reported lattice hardening effect of Be in ZnSe [127, 128].

Regarding the use of such QDs in resonant tunneling devices, where electron tunneling through an individual CdSe QD is desired, two recommendations can be given based on the results in this subsection: (1) If electron tunneling through the ground state of a single QD is desired, a low coverage $\Theta \lesssim 1$ ML should be used. In that case, the majority of QDs have an electron ground state well above the ZnSe conduction band edge, and only a small number of exceptionally large QDs are available for tunneling at low bias. (2) Reducing the QD density by the application of alternate QD fabrication techniques, such as those proposed in [79], may also help to distinguish individual QDs in resonant tunneling transport.

Chapter 5

Band Offsets and Carrier Distribution at the ZnSe / GaAs Heterointerface

This chapter contains a systematic study of the structural and electronic properties of n-ZnSe / n-GaAs heterointerfaces [17]. A new ZnSe growth start process is presented, which markedly improves electron transport across such interfaces and may thereby allow for higher spin-injection efficiency from ZnSe based DMS into GaAs. The results of temperature dependent electric transport, ECV, and Raman measurements for interface potential barrier height, depletion widths, and interface state density are modeled with a 1-d Poisson solver. It is concluded, that the proposed growth start method leads to a reduction of the conduction band offset at the ZnSe / GaAs heterointerface.

At isovalent semiconductor heterointerfaces, such as GaAs / AlAs or Si / Ge, the chemical band offsets, interface states and doping levels completely determine the alignment and bending of the band edges. The electronic properties of *heterovalent* heterointerfaces, such as GaAs / Ge or ZnSe / GaAs, however, are additionally influenced by acceptor- and donor-type bonds across the interface [129]. A prototypical heterovalent material system is the II-VI / III-V semiconductor combination of ZnSe / GaAs, which has the advantage of closely matching lattice constants allowing for high quality epilayers. At such an interface, Zn-As bonds lack 1/4 of an electron on average and act as acceptors, while Se-Ga bonds have 1/4 excess electron and act as donors. The effect of these bonds is twofold: on the one hand, an excess of one type of bond over the other corresponds to n- or p-type planar doping, which can potentially be as high as $3.1 \times 10^{14}\,\mathrm{cm}^{-2}$, see Ref. [130]. Density functional theory calculations show that such abrupt interfaces are thermodynamically unstable [16]. On the other hand, even if both are exactly balanced in number, their spatial arrangement on an atomic scale can lead to an electric dipole moment perpendicular to the heterointerface, which substantially affects and can even reverse the band offsets [16]. Applying photoelectron spectroscopy, Nicolini et al. observed a variation of the valence band offset (VBO) with the Zn / Se flux ratio employed during heteroepitaxy of ZnSe on GaAs (001) [131]. Furthermore, any atomic intermixing across a heterovalent interface implies doping of the adjacent layers, and thus affects the carrier distribution and band bending around the interface [132, 133, 134].

The heterovalent ZnSe / GaAs (001) heterointerface has been studied extensively as part of the efforts to develop ZnSe-based optoelectronic devices. There the emphasis was mostly on reducing the density of structural defects originating from the heterointerface, in order to increase device lifetime [135, 136]. It has been established [137, 138, 139] that avoiding the reaction of Se with the GaAs substrate surface by initiating ZnSe growth under Zn-rich conditions can yield defect densities as low as $10^3\,\mathrm{cm}^{-2}$. More recently, this heterointerface has played a role in spin injection from ZnSe based diluted magnetic semiconductors into GaAs [5, 15] and in optical studies of heterovalent coupled quantum wells in II-VI and III-V materials [140, 141]. The functionality of such structures is very sensitive to band bending and band offsets at the ZnSe / GaAs interface.

In this paper we present a comprehensive study of the electronic and structural properties of heterovalent semiconductor heterointerfaces, and of the influence of different atomic composition profiles at the interface. As a representative material system we studied n-ZnSe / n-GaAs heterointerfaces prepared by molecular beam epitaxy (MBE), and we varied the interface composition by predeposition of Zn or Se in the fractional monolayer (ML) range at ZnSe growth start. We find that the potential barrier height at the heterointerface can be changed over several hundred meV in a controllable fashion. We attribute this to a variation of the interface band offsets induced by electric dipole moments and of band bending induced by a redistribution of acceptors.

The growth start process is monitored by reflection high-energy electron diffraction (RHEED), and the structural quality of the epilayers is studied by high resolution X-ray diffraction (HRXRD). Temperature dependent current-voltage (I-V) measurements, electrochemical capacitance-voltage measurements (ECV), and Raman spectroscopy are used to characterize the potential barrier and carrier density at the heterointerface.

The paper is organized as follows: after listing details of sample fabrication and measurements in section 5.1 and describing the particular growth start procedures in section 5.2, the results of structural and electronic characterization are presented in sections 5.3 and 5.4, respectively. The results are discussed in section 5.5 in terms of a band bending model including a varied conduction band offset and different distributions of acceptor states at or close to the heterointerface.

5.1 Experimental Details

Samples are grown on epi-ready n-GaAs(001) ($N_\mathrm{d} = 1 - 5 \times 10^{18}\,\mathrm{cm}^{-3}$) substrates by MBE in a system of interconnected III-V and II-VI chambers of the type Riber 32. Wafers are glued with In onto Mo sample holders, and the substrate temperature is measured by a thermocouple in thermal contact with the Mo block. After growth of a

200 nm thick n-GaAs buffer layer ($N_{\mathrm{d,GaAs}} = 3 \times 10^{18}\,\mathrm{cm}^{-3}$) at 600 °C, the substrate is transferred to the II-VI chamber under ultra high vacuum, keeping an As-terminated, (2×4) reconstructed GaAs surface. In the II-VI chamber one of several growth start procedures is applied, as described in section 5.2. The II-VI part is grown at a substrate temperature of 300 °C and nominally consists of a 200 nm n-ZnSe ($N_{\mathrm{d,ZnSe}} = 5 \times 10^{18}$ cm^{-3}) layer and a 30 nm n^+-ZnSe ($2 \times 10^{19}\,\mathrm{cm}^{-3}$) top contact layer. Si and $\mathrm{ZnI_2}$ evaporated from effusion cells are used as n-type dopants in GaAs and ZnSe, respectively. Even though the total ZnSe layer thickness is close to the critical thickness for plastic relaxation in this material system, HRXRD confirms that all samples are pseudomorphic.

During ZnSe growth the Zn and Se beam equivalent pressures (BEP) are 8×10^{-7} Torr and 3×10^{-6} Torr, resulting in a growth rate of 1.2 Å/s and a (2×1) reconstructed surface. For Se predeposition a reduced Se BEP of 1×10^{-7} Torr is provided by opening the main shutter and leaving the Se cell shutter closed. Thereby the exposure time required for a Se coverage of 1 ML is increased from less than 1 s to about 18 s, allowing controllable submonolayer deposition by a meandering Se flux. The Se cell in our system is a valved cracker cell operated in the non-cracking mode. During growth the sample surface is monitored by RHEED, using an electron beam energy of 12 keV.

For I-V measurements across the interface, (500 μm)^2 sized mesas are fabricated lithographically. Ohmic contacts to the n$^+$-ZnSe are prepared by in-situ evaporated Al/Ti/Au, and to the n-GaAs substrate by alloyed In on the backside. Temperature dependent I-V curves are recorded using an HP 4145B parameter analyzer and a temperature controlled helium flow cryostat. The ohmic nature of the metal / n$^+$-ZnSe contact is confirmed at 300 K and cryogenic temperatures. ECV is carried out using a BioRAD Polaron semiconductor profiler on samples whose in-situ metalization was wet chemically removed before profiling. Raman investigations are performed utilizing an argon-ion laser (Coherent Innova 90, $h\nu = 2.6$ eV) as excitation source and a SPEX double monochromator equipped with a multichannel detector as analyzer. The samples are cooled to liquid nitrogen temperature in a coldfinger cryostat. HRXRD is done using a Panalytical X-Pert diffractometer equipped with a Cu-K$_{\alpha 1}$ source and a Ge analyzer crystal.

5.2 Growth Start

Five samples named A to E are fabricated using different ZnSe growth start procedures on As-terminated, (2×4) reconstructed GaAs(001) surfaces, as listed in table 5.1. The procedures differ in shutter sequences and substrate temperatures and aim at an increasing amount of Se at ZnSe growth start from sample A to E. In order to be able to detect any drift in growth conditions, the samples are grown in the sequence C, E, B, D, A.

For sample A the substrate is exposed to Zn flux for 20 s at a low substrate temperature

Sample	Growth start	t (nm)	A_d/A_l (%)	Φ_b (meV)	Σ ($10^{13}\,\mathrm{cm}^{-2}$)	$w_{d,\mathrm{ZnSe}}$ (nm)	$w_{d,\mathrm{GaAs}}$ (nm)
A	20 s Zn, ALE	200	70	550 ± 150	1.6	-	-
B	20 s Zn	242	23	470	1.1	20	26
C	7 s Se	232	9	300	1.9	50	15
D	11 s Se	219	5	280	1.4	41	16
E	15 s Se	207	24	73	1.3	37	16

Table 5.1: Summary of fabricated samples with different ZnSe growth start (see section 5.2) and the results of structural, electrical and Raman characterization. t is the ZnSe layer thickness obtained from HRXRD and A_d/A_l is the ratio of diffusely scattered X-ray intensity to that under the ZnSe 004 Bragg peak. Φ_b is the potential barrier in the conduction band at the n-ZnSe / n-GaAs heterointerface determined by temperature dependent I-V measurements, Σ is the areal electron deficit at the heterointerface obtained by integration of ECV profiles, $w_{d,\mathrm{ZnSe}}$ and $w_{d,\mathrm{GaAs}}$ are the individual depletion widths on the ZnSe and the GaAs side of the heterointerface, as determined by Raman spectroscopy.

of 230 °C, then ZnSe growth is commenced in an atomic layer epitaxy (ALE) mode by alternately supplying Zn and Se flux while the substrate is ramped to the final growth temperature of 300 °C. After approximately one minute this temperature is reached and growth is continued in MBE mode.

For sample B the substrate is exposed to Zn flux for 20 s as well, but the starting temperature is 300 °C and ZnSe growth is immediately commenced in MBE mode by opening the Se shutter. Due to the higher starting temperature and the consequently lower sticking coefficient of Zn, the ZnSe / GaAs interface formed by this growth start is expected to be slightly less Zn-rich than for sample A. The initial (2×4) RHEED pattern does not change during Zn irradiation, but a quick transition to a 2D (2×1) reconstructed surface is observed upon opening of the Se shutter.

For samples C, D and E the substrate at 300 °C is exposed to the reduced Se BEP of 1×10^{-7} Torr at closed Se cell and open main shutter for different durations. Then ZnSe MBE growth is initiated by simultaneously opening the Zn and Se shutter.

During Se exposure RHEED shows a gradual transition from the initial (2×4) surface to an unreconstructed one, which is helpful in controlling the Se coverage. The RHEED patterns observed with the electron beam parallel to the $[1\bar{1}0]$ crystal direction are depicted in figure 5.1.

The top panel shows the GaAs (2×4) surface kept at 300 °C in the II-VI chamber with closed main shutter. Since the 2/4 streaks have about the same intensity as the other fractional order streaks, the surface can be more specifically assigned to type $(2 \times 4) - \beta$, according to Ref. [142]. The sample can be kept in this state for several minutes. Upon opening the main shutter and thereby applying a Se BEP of 1×10^{-7} Torr, the 2/4 order streaks weaken and disappear after 7 s. Then the 1/4

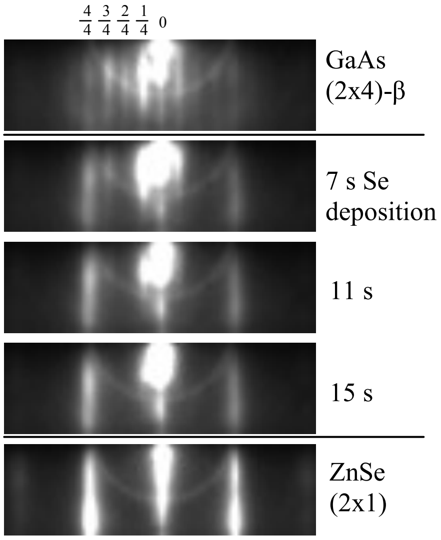

Figure 5.1: RHEED patterns observed in the $[1\bar{1}0]$ azimuth before (top panel) and during Se predeposition (7 s to 15 s). The bottom panel shows the pattern during ZnSe growth at about 15 nm layer thickness.

and 3/4 order streaks disappear after about 15 s, leaving an unreconstructed surface which does not change appreciably with further Se exposure. Samples C, D, and E are grown with Se predeposition for 7, 11 and 15 s, respectively.

A rough estimate of the Se coverage can be obtained from the deposition rate [75]

$$R = \frac{p}{\sqrt{2\pi m k_B T}}. \tag{5.1}$$

With $p = 10^{-7}$ Torr, $m = 4 \times 79$ amu for Se_4, a cell temperature of $T = 250\,^{\circ}\mathrm{C}$, the Boltzmann constant k_B and assuming unity sticking coefficient, we get $R_{\mathrm{Se4}} = 8.6 \times 10^{12}\,\mathrm{cm}^{-2} s^{-1}$ or 0.8 ML of Se atoms deposited within 15 s (neglecting element dependent pressure gauge sensitivity). We therefore ascribe the transition to an unreconstructed surface observed by RHEED to the deposition of Se in the fractional ML range. This is consistent with scanning tunneling microscopy results of Li and Pashley [143].

5.3 Structural Properties

HRXRD scans of all samples are measured in $\omega - 2\Theta$ and ω directions. Typical results are depicted in figure 5.2. For samples B to E HRXRD shows an 004 Bragg peak of a fully pseudomorphic ZnSe layer with more than 10 thickness fringes in $\omega - 2\Theta$ direction (figure 5.2 (a)). The ZnSe 004 Bragg peak of sample A is slightly broadened and thickness fringes are less pronounced than for the other samples. From a fit of a

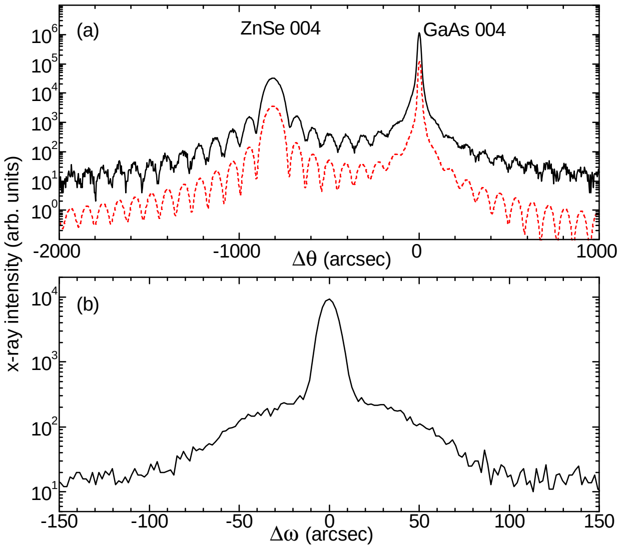

Figure 5.2: (a) HRXRD $\omega - 2\Theta$ scan in the vicinity of the 004 reflection of sample E (black solid line) and dynamic simulation (red dashed line). Curves are offset for clarity. (b) ω scan of the ZnSe 004 reflection of the same sample (x-ray beam is parallel to the 110 crystal direction), showing the narrow ZnSe Bragg peak and the broad, low intensity background peak which is attributed to diffuse scattering at dislocations.

calculated curve to the $\omega - 2\Theta$ scans we determined the ZnSe layer thickness as listed in table 5.1. We note that, although the growth duration and fluxes for all samples are identical, the ZnSe layer thickness decreases continuously with Se predeposition from 242 nm for sample B to 207 nm for sample E. The full width at half maximum (FWHM) of the ZnSe layer peak in ω direction (figure 5.2 (b)) is about 10 arcsec for samples B to E, which is close to the resolution limit, and there is no significant broadening relative to the substrate peak. Thus the structural quality of these layers is very good and we find no sign of plastic relaxation. For sample A the ω FWHM is 20 arcsec, which, together with the slightly inferior $\omega - 2\Theta$ scan data, indicates that this sample is of lower structural quality. This may be due to a non optimized ALE start procedure for this sample.

A more sensitive HRXRD based characterization of epitaxial layer quality is demonstrated in Refs. [95, 96]. The intensity of the broad peak forming the background of an epilayer Bragg peak in the ω direction (figure 5.2 (b)) is attributed to diffuse scattering from strained regions around dislocations. Thus, the ratio of integrated intensities of the diffusely scattered broad peak and the narrow Bragg peak from the epilayer is a sensitive measure of dislocation density. The intensity ratio is obtained by separately fitting Gaussian profiles to the diffuse and Bragg peak. The results for all samples are listed in table 5.1. Remarkably, samples with a moderate Se coverage at growth start have a lower dislocation density than those with Zn-rich growth start. For our highest Se coverage, however, the dislocation density increases sharply, as expected for growth on Se-rich surfaces [138].

5.4 Electronic Properties

5.4.1 I-V Characteristics

As a first measure of the electronic properties of the fabricated heterovalent heterointerfaces we analyze the room temperature I-V characteristics measured across the interface in $(500\,\mu m)^2$ mesas. The results are shown in figure 5.3. We first note that all I-V curves are non-ohmic, which indicates that electron transport is limited by a potential barrier. Second, the conductivity at a fixed bias voltage strongly depends on the ZnSe growth start procedure. There is a monotonic trend towards higher current density with increasing Se predeposition, which spans nearly five orders of magnitude. This indicates that the potential barrier limiting the current is situated at the heterointerface, and that its height and / or width are reduced by Se predeposition. However, the resistance even of the best conducting samples is rather high. The differential resistance of sample E is 83 kΩ at 0 V, while for purely diffusive transport the resistance would be $< 1\,\Omega$. Third, we note that the I-V characteristics are asymmetric: when ZnSe is on negative potential with respect to GaAs the current is higher than in the opposite direction. The former polarity is denoted as $V > 0$ (forward bias) in figure 5.3. This is consistent with a type I band line-up, in which the conduction band (CB) edge in ZnSe lies above that of GaAs (defined as positive CB offset). The asymmetry is very pronounced for samples A and B with a Zn-rich growth start, and becomes much weaker with increasing Se predeposition.

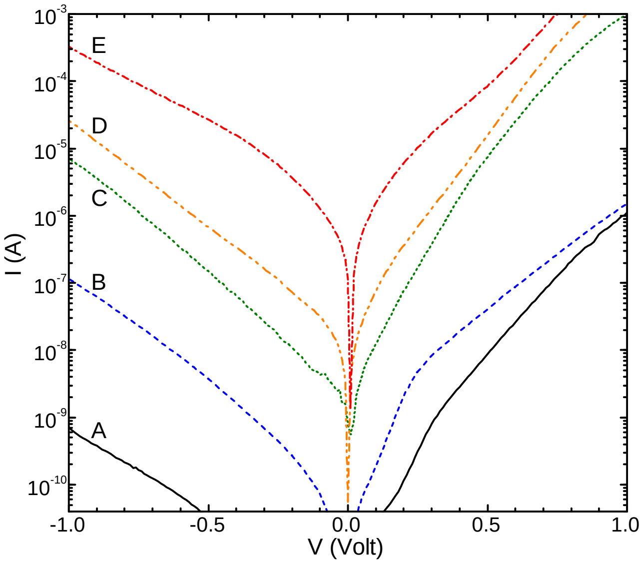

Figure 5.3: Room temperature I-V characteristics measured through the n-ZnSe / n-GaAs heterointerface for samples A to E in $(500\,\mu m)^2$ diodes. Positive bias corresponds to electron flow from ZnSe to GaAs.

For a quantitative measure of the heterointerface potential barrier, I-V curves are taken as a function of temperature in the thermionic emission regime. In this regime the following relationship between the "reduced current" I' and the applied bias voltage V holds for small bias voltages [101]:

$$I' = \frac{I}{T\left(\exp\left\{\frac{eV}{k_B T}\right\} - 1\right)} \propto \exp\left\{\frac{-\Phi_b}{k_B T}\right\}, \qquad (5.2)$$

with the current I, the temperature T, the elementary charge e and the Boltzmann constant k_B. In the model, which neglects tunneling, Φ_b is the potential barrier height in the conduction band measured from the Fermi energy. In the experiment, tunneling may reduce the energy needed for electrons to traverse the barrier, so Φ_b rather corresponds to the activation energy for thermally activated tunneling. It corresponds to the absolute height but is also slightly influenced by the shape of the heterointerface potential barrier.

Φ_b can be determined from the slope of $\ln(I')$ when plotted over $1/T$ in an Arrhenius plot [144, 145]. This is shown in figure 5.4 for sample D at different bias voltages. For $T > 250$ K I' in figure 5.4 varies exponentially with inverse temperature, indicating the thermionic emission regime, and it becomes temperature independent at low temperatures where tunneling conduction dominates. The barrier height extracted from the slope in the exponential region is shown in the inset of figure 5.4 as a function of the applied bias. For each sample Φ_b is extrapolated to zero bias and the mean value of the extrapolation from the positive and negative side is taken as the final barrier height. In sample A, due to its high resistance and possibly also due to fluctuating barrier properties caused by structural defects, the barrier height could only be determined at higher applied bias voltages and with a relatively large uncertainty. As listed in table 5.1 we find a high barrier of about 550 meV for the ALE growth start sample A, 470 meV for the conventionally grown Zn-rich sample B and a monotonic reduction with Se predeposition, down to 73 meV for sample E. One of our main results is thus that Se predeposition drastically and controllably reduces the potential barrier in the conduction band at the n-ZnSe / n-GaAs heterointerface. It is remarkable that the bias dependence of the barrier height $\phi_b(V)$ of samples C to E with low barrier is rather symmetric, as shown exemplary in the inset of figure 5.4.

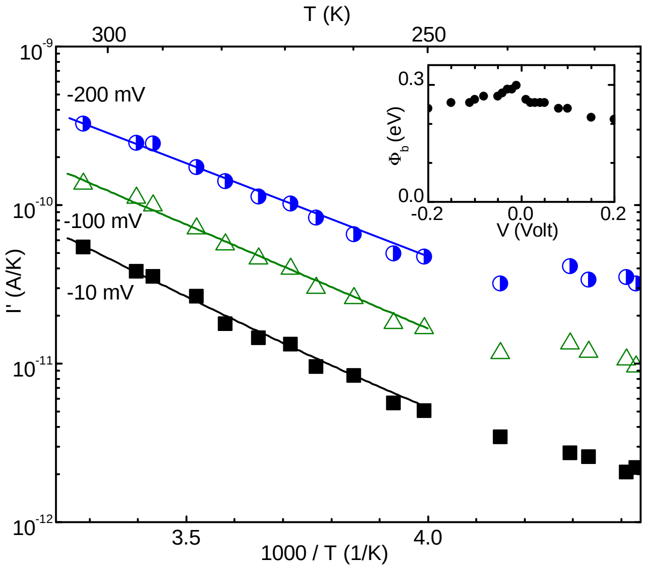

Figure 5.4: Arrhenius plot of the reduced current I' (definition see equation 5.2) versus inverse temperature at different bias voltages for sample D. The interface barrier height Φ_b determined from the slope of I' is plotted in the inset as a function of bias.

5.4.2 Carrier Density Distribution

In figure 5.5 we show the electron density profiles n(z) of all samples measured by ECV at room temperature. Close to the surface, the 30 nm thick, $2 \times 10^{19}\,\mathrm{cm}^{-3}$ doped n$^+$-ZnSe top contact layer can be seen, followed by the $5 \times 10^{18}\,\mathrm{cm}^{-3}$ doped "bulk" n-ZnSe. At a depth corresponding approximately to the ZnSe / GaAs heterointerface there is an about 40 - 60 nm wide depletion region, after which the carrier density increases to the value intended for the n-GaAs buffer. We note that there is no electron accumulation on the GaAs side of the heterointerface. The scattering of the depth of the depletion region is mainly attributed to inaccuracy of the ECV etch rate. Integrating the difference between the donor density $N_{\mathrm{d,i}}$ (i = ZnSe or GaAs), measured far away from the interface, and the electron density n(z) across the interface region gives an integrated electron deficit

$$\Sigma = \int N_{\mathrm{d,i}} - n(z)\,\mathrm{d}z. \tag{5.3}$$

Evaluating this integral in the range $100\,\mathrm{nm} \leq z \leq 300\,\mathrm{nm}$ for all measured profiles yields Σ in the range $1.1 - 1.9 \times 10^{13}\,\mathrm{cm}^{-2}$, as listed in table 5.1 for the individual samples. We estimate experimental error bars for Σ of $\pm 0.5 \times 10^{13}\,\mathrm{cm}^{-2}$ based on the reproducibility of the measurements and on the uncertainty of the heterointerface position in ECV profiles. We thus find an average electron deficit $\Sigma = (1.5 \pm 0.5) \times 10^{13}\,\mathrm{cm}^{-2}$ at the studied heterovalent ZnSe / GaAs heterointerfaces, with no significant variation with the growth start procedure. This electron deficit is often interpreted directly as the density of interface states [146]. In section 5.5 we will show that in these n-doped heterovalent samples it is not only due to interface states, but also to an extended distribution of acceptors or to a lack of donors (e.g. due to segregation) over several tens of nm around the interface. Our measured value for Σ is in remarkable agreement with the results of Kassel et al., who found an areal density $1.0 - 1.5 \times 10^{13}\,\mathrm{cm}^{-2}$ of interdiffused Zn-acceptors in GaAs at ZnSe / GaAs heterointerfaces [133].

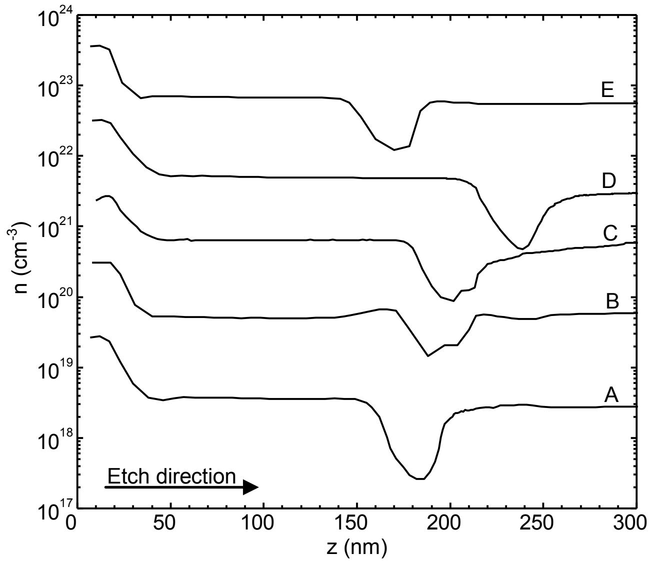

Figure 5.5: Profiles of the electron density n(z) obtained by ECV for samples A to E. The origin of the bottom axis corresponds to the ZnSe surface. Curves B to E are subsequently offset by one order of magnitude.

For the determination of the individual depletion layer width on each side of the ZnSe / GaAs interface, Raman spectroscopy is applied. As exemplary results, the spectra in figure 5.6 show the inelastic light scattering intensity of the samples B and E in the frequency range of the ZnSe and GaAs lattice vibrations. The peaks originate from the longitudinal optical (LO) phonon modes ($\tilde{\nu}_{\mathrm{LO,ZnSe}} = 256\,\mathrm{cm}^{-1}$, $\tilde{\nu}_{\mathrm{LO,GaAs}} = 294\,\mathrm{cm}^{-1}$) and from the coupled plasmon-LO-phonon modes (PLP), located at $\tilde{\nu}_{\mathrm{PLP,ZnSe}} = 207\,\mathrm{cm}^{-1}$ and $\tilde{\nu}_{\mathrm{PLP,GaAs}} = 272\,\mathrm{cm}^{-1}$. They allow the individual determination of the depletion layer widths $w_{\mathrm{d,ZnSe}}$ and $w_{\mathrm{d,GaAs}}$, since only the depletion layers give rise to the LO phonons. From the doped ZnSe epilayer and the doped GaAs behind the interface the shifted peaks $\mathrm{PLP}_{\mathrm{ZnSe}}$ and $\mathrm{PLP}_{\mathrm{GaAs}}$ arise [147]. Thus, the distinction between both depletion layers is enabled by the intensities of the $\mathrm{LO}_{\mathrm{ZnSe}}$ and $\mathrm{LO}_{\mathrm{GaAs}}$ peaks. In ZnSe, the LO intensity is directly proportional to the $w_{\mathrm{d,ZnSe}}$, since the regions with carriers instead emit coupled PLP modes at a different wavenumber. The ZnSe material is transparent for the laser light ($h\nu = 2.6\,\mathrm{eV} < E_g = 2.8\,\mathrm{eV}$). The value of $w_{\mathrm{d,ZnSe}}$ is obtained after intensity calibration with an undoped ZnSe layer of well-known thickness. In the opaque GaAs ($E_g = 1.5$ eV), light attenuation effects are considered because of the finite penetration depth $d_p = 70$ nm (see Ref. [148]). The straightforward procedure for the calculation of $w_{\mathrm{d,GaAs}}$ is described in great detail in Ref. [149].

The exemplary spectra of the samples B (Zn-start) and E (15 s Se predeposition) in figure 5.6 show clear differences. Sample B gives a strong $\mathrm{LO_{GaAs}}$ together with a rather weak $\mathrm{LO_{ZnSe}}$. In contrast, in sample E $\mathrm{LO_{GaAs}}$ is reduced, while $\mathrm{LO_{ZnSe}}$ and $\mathrm{PLP_{GaAs}}$ are enhanced. The fitting results, also shown in figure 5.6, yield an $\mathrm{LO_{ZnSe}}$ enhancement factor of 1.88 for sample E with respect to B. As explained above, the intensity of the $\mathrm{LO_{ZnSe}}$ peak is directly proportional to the width of the carrier depleted region in ZnSe. After intensity calibration we obtain for sample B and E the $w_{\mathrm{d,ZnSe}}$ values of 20 nm and 37 nm, respectively. Considering the GaAs signals, for the Se predeposited sample the ratio of the depletion-induced $\mathrm{LO_{GaAs}}$ intensity and the doping-induced $\mathrm{PLP_{GaAs}}$ intensity amounts to $I_{\mathrm{LO}}/I_{\mathrm{PLP}} = 0.20$, which means a considerable reduction with respect to the corresponding value for sample B, which is as high as 0.32. The evaluation of these results according to Ref. [149] yields $w_{\mathrm{d,GaAs}} = 26$ nm for sample B and $w_{\mathrm{d,GaAs}} = 16$ nm for sample E. For the other Se predeposited samples C and D we observe the same trend as for sample E. The corresponding depletion layer values are listed in table 5.1. Thus, throughout our sample series the determination of the individual depletion layer thicknesses $w_{\mathrm{d,ZnSe}}$ and $w_{\mathrm{d,GaAs}}$ by Raman spectroscopy reveals a partial shift of the depleted interface region from the GaAs side towards the ZnSe side with increasing Se predeposition.

As a third probe of the carrier density at the heterointerface we measured the capacitance of the mesa diodes already used for I-V measurements. Since, unlike in ECV measurements, the metal / semiconductor contacts in these samples are ohmic, their capacitance is determined only by the depletion region at the ZnSe / GaAs heterointerface. Accounting for possible parallel conductance of the mesas (especially for sample E), we measured capacitances in the range C = 289 - 348 pF for all samples. In the total depletion approximation the capacitance is $C = \epsilon\epsilon_0 A/w_{\mathrm{d,total}}$, with $A = (500\,\mu m)^2$ and $w_{\mathrm{d,total}}$ being the total width of the carrier depleted region. The dielectric constant ϵ should be the appropriately weighted, harmonic mean between the ZnSe value $\epsilon_{\mathrm{ZnSe}} = 8.6$ and the GaAs value $\epsilon_{\mathrm{GaAs}} = 12.9$, reflecting the distribution of the depletion region between the two materials. When assuming equal depletion on both sides, $\epsilon = 2/\left(1/\epsilon_{\mathrm{ZnSe}} + 1/\epsilon_{\mathrm{GaAs}}\right) = 10.3$, depletion widths $\mathrm{w_{d,total}} = 65 - 78$ nm are obtained for all samples. This range for $\mathrm{w_{d,total}}$ is in fair agreement with the sum of the individual depletion widths measured by Raman spectroscopy (table 5.1) and the depletion width in ECV profiles (figure 5.5). For the Se-start samples C to E the agreement of capacitance with Raman and ECV results is further improved when it is considered that the larger fraction of the depleted region is in ZnSe, and therefore ϵ is smaller. Differences between the depletion width results obtained by the three applied methods ECV, Raman and capacitance measurements, may be due to possible systematic errors and due to different limits to the electron density below which a layer appears as depleted.

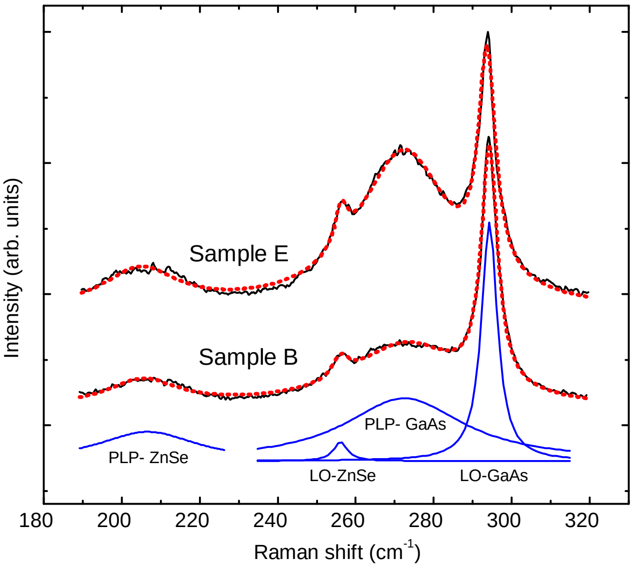

Figure 5.6: Exemplary Raman spectra of samples B and E, taken with an excitation wavelength of 477 nm (black solid curves). Each spectrum comprises the phonon peaks $\mathrm{LO}_{\mathrm{ZnSe}}$ and $\mathrm{LO}_{\mathrm{GaAs}}$, originating from the carrier-depleted near-interface region, and the corresponding coupled Plasmon-Phonon modes $\mathrm{PLP}_{\mathrm{ZnSe}}$ and $\mathrm{PLP}_{\mathrm{GaAs}}$, originating from the doped ZnSe epilayer and the underlying doped GaAs, respectively. Both spectra are fitted by a superposition of four Lorentz functions (red dotted curves). At the bottom, the Lorentz functions corresponding to the fit for sample B are shown individually.

5.5 Discussion and Model Calculations

Our detailed results on depletion widths, carrier compensation and potential barrier heights at the studied heterovalent interfaces obviously require a much more detailed description than merely determining the chemical band offset given by the materials. In order to develop a consistent picture of the electronic properties of the n-ZnSe / n-GaAs heterointerface, which accounts for the observed electronic properties and for their variation with predeposition of Zn or Se, we have considered band offsets as well as band bending and have calculated 1-D band and carrier density profiles for different models of the heterointerface using a Poisson solver [1]. Material data for ZnSe and GaAs are taken from the literature [35, 150], and the donor density in ZnSe is $N_{\mathrm{d,ZnSe}} = 5 \times 10^{18}\,\mathrm{cm}^{-3}$ and in GaAs $N_{\mathrm{d,GaAs}} = 3 \times 10^{18}\,\mathrm{cm}^{-3}$. Calculations are done for a temperature of 300 K. We assumed that all impurities are fully ionized, unless noted otherwise.

Each adequate description of heterovalent semiconductor interfaces requires the possibility of a variable band offset. This is in contrast to isovalent interfaces, whose elec-

---

[1] Nextnano 3, see [55] and www.nextnano.de

tronic properties are determined by fixed valence and conduction band offsets (VBO and CBO), and for which a low density of interface states and effects like interface roughness and atomic interdiffusion only smear out the band offset region, without changing the offset value. At *heterovalent* heterointerfaces such as ZnSe / GaAs, however, the band offsets can be varied significantly by an electric dipole moment perpendicular to the interface, which originates from the atomic arrangement of donor- and acceptor type bonds across the interface. For ZnSe/GaAs, this contrasting behavior is visualized by comparing the non-polar (110)-oriented interface with the polar one on (001) planes. While the VBO at a non-polar ZnSe / GaAs (110) heterointerface is close to 1.1 eV, effective VBOs between 0.72 eV and 1.75 eV have been calculated for polar ZnSe / GaAs (100) heterointerfaces with different interface dipole moments ([16] and Refs. therein). This range of VBOs implies CBOs between -0.45 eV and 0.58 eV, considering that the ZnSe band gap is $\Delta E_g = 1.3$ eV wider than that of GaAs. The possibility of variable band offsets is thus included in three heterointerface models with increasing degree of sophistication concerning the acceptor state distribution, which are described in the following subsections (a), (b) and (c).

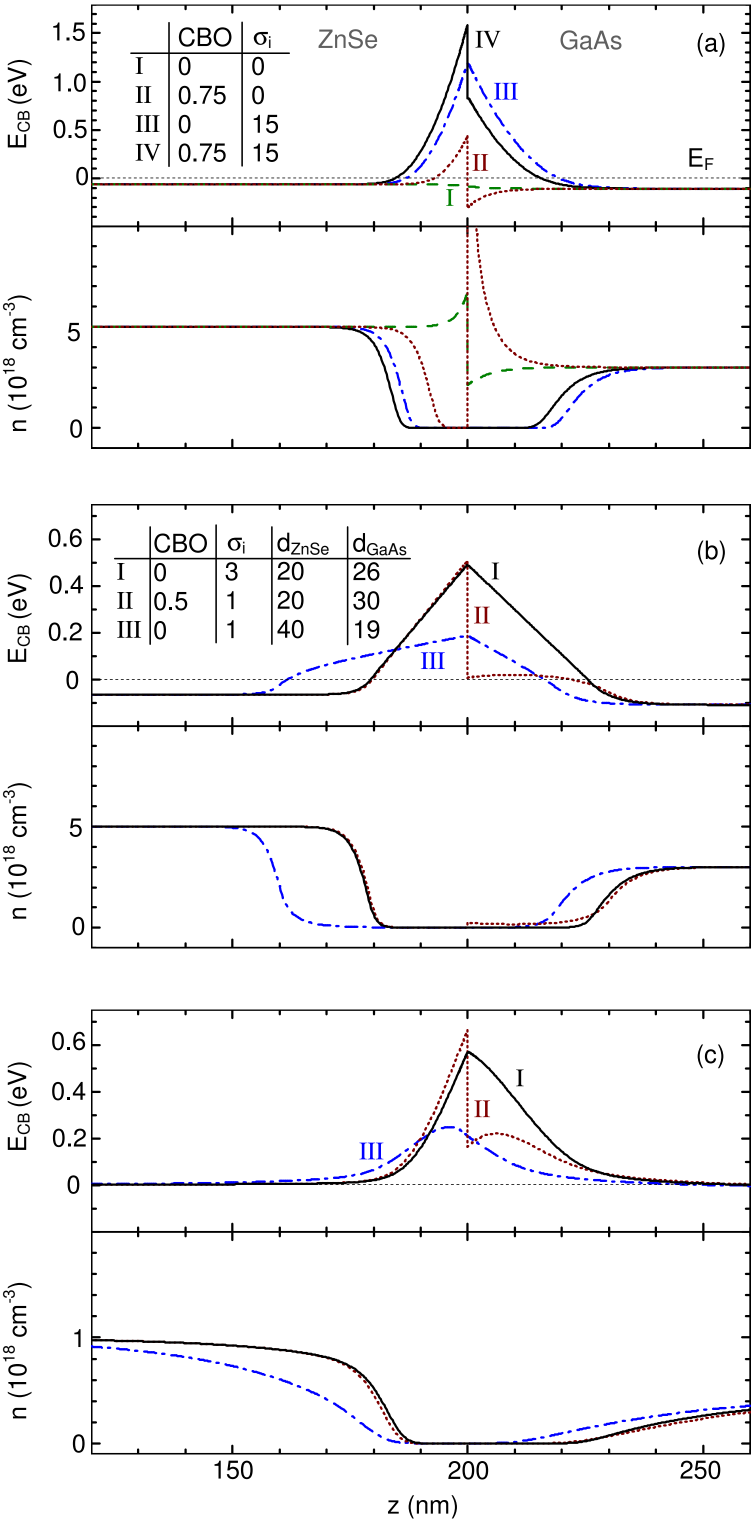

	CBO	σ_i
I	0	0
II	0.75	0
III	0	15
IV	0.75	15

	CBO	σ_i	d_{ZnSe}	d_{GaAs}
I	0	3	20	26
II	0.5	1	20	30
III	0	1	40	19

Figure 5.7: Calculated profiles of the CB edge E_{CB} and the electron density n in the conduction band for the three n-ZnSe / n-GaAs heterointerface models described in section 5.5. In (a) only a CBO and an interface state density σ_i are considered, the parameters corresponding to the individual curves are listed in the inset (CBO in eV and σ_i in $10^{12}\,\mathrm{cm}^{-2}$). In (b) the effects of atomic interdiffusion and segregation are included by assuming exactly compensated regions of width d_{ZnSe} and d_{GaAs} on the two sides of the heterointerface (both given in nm in the inset). In (c) such effects are modeled by an exponentially varying n- or p-type doping density at the interface, the parameters corresponding to the curves are listed in table 5.2. Incomplete ionization of impurities is allowed only in (c). The temperature is 300 K and the interface is situated at z_i = 200 nm. Note the different scale of E_{CB} in (a) compared to (b) and (c), and of n in (c) compared to (a) and (b).

5.5.1 Model (a): Variable Band Offset and Interface State Density

In panel (a) of figure 5.7 the calculated Γ_6 CB diagrams and electron density profiles are shown for n-ZnSe / n-GaAs heterointerfaces with CBO = 0 eV (curve I) and CBO = 0.75 eV (curve II). A finite CBO causes a barrier in the conduction band, electron depletion in ZnSe and accumulation in GaAs. Even though barrier heights comparable to those observed in this work can be easily caused by a CBO in the range predicted in the literature [16], the corresponding electron density profiles are in obvious disagreement with our results, as we observe no electron accumulation in GaAs but an integrated electron deficit $\Sigma = 1.5 \times 10^{13}\,\mathrm{cm}^{-2}$. Accounting for this deficit with an interface state density $\sigma_i = 1.5 \times 10^{13}\,\mathrm{cm}^{-2}$ together with CBO = 0 (curve III) or with CBO = 0.75 eV (curve IV) in both cases yields electron density profiles that are in better agreement with our measured profiles. Even for a CBO as large as 0.75 eV there is no electron accumulation on the GaAs side and the total width of the depleted region is in fair agreement with the experimental results. However, this model results in potential barriers of more than 1 eV, much larger than measured in this work. Lower barriers can only be explained by assuming that Σ is not only caused by a two-dimensional interface state density, but by acceptors distributed over several tens of nm around the interface. This is in agreement with our previous work, in which we have found evidence for an exceptionally large depletion region at n-ZnSe / GaAs heterointerfaces [134]. Effects leading to such a spatial extension of the depletion region are compensation of n-doping due to atomic interdiffusion across the heterointerface [132], dissolution and segregation of As atoms from the As-terminated GaAs surface at growth start, and segregation of iodine donors in ZnSe during MBE deposition.

		I	II	III
CBO	(eV)	0	0.5	0
σ_i	($10^{12}\,\mathrm{cm}^{-2}$)	3	1	0
$N_{0,\mathrm{GaAs}} \cdot \lambda_{\mathrm{GaAs}}$	($10^{12}\,\mathrm{cm}^{-2}$)	10	12.5	6.2
λ_{GaAs}	(nm)	20	20	20
$N_{0,\mathrm{ZnSe}} \cdot \lambda_{\mathrm{ZnSe}}$	($10^{12}\,\mathrm{cm}^{-2}$)	0	0	7.5
λ_{ZnSe}	(nm)	0	0	25
k	(nm)	25	25	25

Table 5.2: Parameter sets used for the three simulations depicted in panel (c) of figure 5.7.

5.5.2 Model (b): Interdiffusion and Segregation Modeled with Box-Shaped Doping Profiles

The simulations in panel (b) include such a spatially extended electron deficit by assuming exact compensation of donors with acceptors of the density $N_\mathrm{a} = N_\mathrm{d}$ in a region of width d_ZnSe in ZnSe and d_GaAs in GaAs at the heterointerface. The integrated electron deficit in the interface region is then

$$\Sigma = \sigma_i + d_\mathrm{ZnSe} \cdot N_\mathrm{d,ZnSe} + d_\mathrm{GaAs} \cdot N_\mathrm{d,GaAs}, \tag{5.4}$$

with the nominal bulk donor densities $N_\mathrm{d,ZnSe}$ and $N_\mathrm{d,GaAs}$. Outside this box-shaped region the donor density equals the bulk values in the two materials. This assumption of an exactly compensated region with abrupt transition to homogeneously doped bulk layers on both sides of the heterojunction may seem arbitrary, but the exact doping density profiles are not central to our discussion in this subsection. A more realistic model is described in the next subsection. Together with a variable CBO and σ_i the model thus includes four parameters, which are adjusted so that the resulting CB and carrier density profiles agree with the measured quantities Φ_b, $w_\mathrm{d,ZnSe}$, $w_\mathrm{d,GaAs}$ and Σ for samples B and E, representing Zn-rich and Se-rich growth start, respectively.

Curves I and II are both consistent with the experimental results for sample B. Curve I is calculated with a vanishing CBO and a relatively high $\sigma_i = 3\times10^{12}\,\mathrm{cm}^{-2}$, while curve II is calculated for a high CBO $= 0.5$ eV and a low $\sigma_i = 1\times10^{12}\,\mathrm{cm}^{-2}$. For curve I we use $d_\mathrm{ZnSe} = 20$ nm and $d_\mathrm{GaAs} = 26$ nm, and for curve II $d_\mathrm{ZnSe} = 20$ nm and $d_\mathrm{GaAs} = 30$ nm. Since both parameter sets equally well reproduce all four measured electronic interface properties within their respective uncertainties, answering the question of whether a high CBO or a high interface state density produces the observed potential barrier in the Zn-rich samples requires additional experimental information. We find such information in the asymmetry of the I-V curves (figure 5.3): a symmetric barrier is lowered nearly equally by an applied voltage independent of the polarity of the voltage, and thus the resulting I-V characteristics are nearly symmetric. An asymmetric barrier caused by a large CBO, on the other hand, is only lowered if the material with the higher lying CB edge is on negative potential, while for the other bias direction always a finite, nearly triangular barrier remains. The I-V characteristics of such a barrier is also asymmetric, with the forward bias direction corresponding to the material with the higher CB edge energy being on negative potential. Thus the markedly asymmetric I-V characteristics especially of samples A and B indicates that the observed high interface barrier for those samples is asymmetric and is caused by a substantial CBO.

Curve III is an adaptation to sample E and is calculated with CBO $= 0$ eV, $\sigma_i = 1 \times 10^{12}\,\mathrm{cm}^{-2}$, $d_\mathrm{ZnSe} = 40$ nm and $d_\mathrm{GaAs} = 19$ nm. In order to obtain a low potential barrier obviously both the CBO and σ_i need to be relatively low. The resulting potential barrier is rather symmetric and thus is consistent with the low asymmetry of I-V curves (figure 5.4) and of the bias-dependence of the barrier heights (inset of figure 5.4). For all simulations in panel (b) Σ is in the range $2 - 3 \times 10^{13}\,\mathrm{cm}^{-2}$, which is in fair agreement with the value derived from ECV profiles. Thus we have shown that the measured electronic interface properties Φ_b, $w_{\mathrm{d,ZnSe}}$, $w_{\mathrm{d,GaAs}}$, Σ and the degree of asymmetry in the I-V curves can be consistently explained with a model including a variable CBO and σ_i, and using box-shaped doping profiles to account for extended depletion regions at the interface. The reduction of the interface potential barrier with Se predeposition is ascribed mainly to a reduction of the CBO, based on a qualitative evaluation of the asymmetry of I-V curves.

5.5.3 Model (c): Interdiffusion and Segregation Modeled With Continuous Doping Profiles

In panel (c) we show calculated band and electron density profiles based on a physically more intuitive model, where we assume exponentially decaying acceptor and donor densities instead of the box-shaped ones in model (b), and allow for incomplete ionization of impurities at 300 K. Interdiffusion of acceptor type atoms in ZnSe and in GaAs is modeled as an exponentially decreasing acceptor density

$$N_{\mathrm{a,i}}(z) = N_{0,\mathrm{i}} \exp\left\{\frac{-|z-\hat{z}|}{\lambda_{\mathrm{i}}}\right\}, \tag{5.5}$$

where i=ZnSe or GaAs, $\hat{z}$ is the interface position and $N_{0,\mathrm{i}}$ and λ_{i} correspond to the saturation density and diffusion length of interdiffused atoms. Furthermore, delayed incorporation of iodine donors in ZnSe ($z < \hat{z}$) due to segregation is modeled as

$$N_{\mathrm{d}}(z) = N_{\mathrm{d,ZnSe}}\left(1 - \exp\left\{\frac{-|z-\hat{z}|}{k}\right\}\right), \tag{5.6}$$

with $N_{\mathrm{d,ZnSe}}$ being the nominal bulk donor density in ZnSe, and k corresponding to the segregation length. The integrated electron deficit is

$$\Sigma = \sigma_i + N_{0,\mathrm{ZnSe}} \cdot \lambda_{\mathrm{ZnSe}} + N_{0,\mathrm{GaAs}} \cdot \lambda_{\mathrm{GaAs}} + k \cdot N_{\mathrm{d,ZnSe}}. \tag{5.7}$$

As done for model (b), we adjust the model parameters to give band and electron density profiles which best fit the measured electrical interface properties. The resulting profiles for sample B and E are shown in panel (c) of figure 5.7 and the corresponding model parameters are listed in table 5.2. Due to incomplete ionization the electron density n in the conduction band is lower than the donor density $N_{\mathrm{d,i}}$. Such a lower electron density is in good agreement with the PLP mode frequencies observed by Raman and infrared spectroscopy (not shown here).

The Zn-rich sample B can be described by a vanishing CBO and a relatively large interface state density σ_i (curve I), resulting in a nearly symmetric barrier, as well as by a large CBO = 0.5 eV and a smaller σ_i (curve II), resulting in an asymmetric barrier. As explained in (b) only the latter is consistent with the shape of the I-V curves. Such a large CBO is predicted in Ref. [16] for an atomic interface configuration with a pure Zn plane and a subjacent mixed anionic plane with a composition of 50 % As and 50 % Se. It is depicted in figure 5.8 under the title “Mixed anionic plane”. This interface fulfills the charge neutrality condition (neglecting a small σ_i), and is the most stable of the configurations calculated in Ref. [16].

For the Se-rich growth start sample E (curve III), the CBO and σ_i both have to be small. A systematic parameter variation in our model calculations shows that the observed small potential barrier $\Phi_b = 73$ meV limits the possible values of model parameters to about CBO < 0.1 eV and $\sigma_i < 2 \times 10^{12}\,\mathrm{cm}^{-2}$. A small interface state density σ_i may be explained considering that predeposition of Se on GaAs leads to some donor-type Ga-Se bonds, which partially compensate acceptor-type interface states. A small CBO is related to the formation of a heterointerface with a vanishing electric dipole moment, as it is calculated in Ref. [16] for interfaces with two mixed atomic planes. Such a configuration is shown in figure 5.8 under the title “Two mixed planes”. The (2×2) interface containing a mixed anionic plane with 75 % Se and 25 % As on top of a cationic plane with 25 % Zn and 75 % Ga has a CBO as low as 80 meV, in agreement with our measurements, and a rather high stability [16]. It contains a high proportion of Se at the heterointerface and thus is reasonable for an interface formed by Se predeposition. This high Se concentration may stabilize Zn atoms incorporated in the cationic Ga plane underneath, and thereby ensure charge neutrality of the interface.

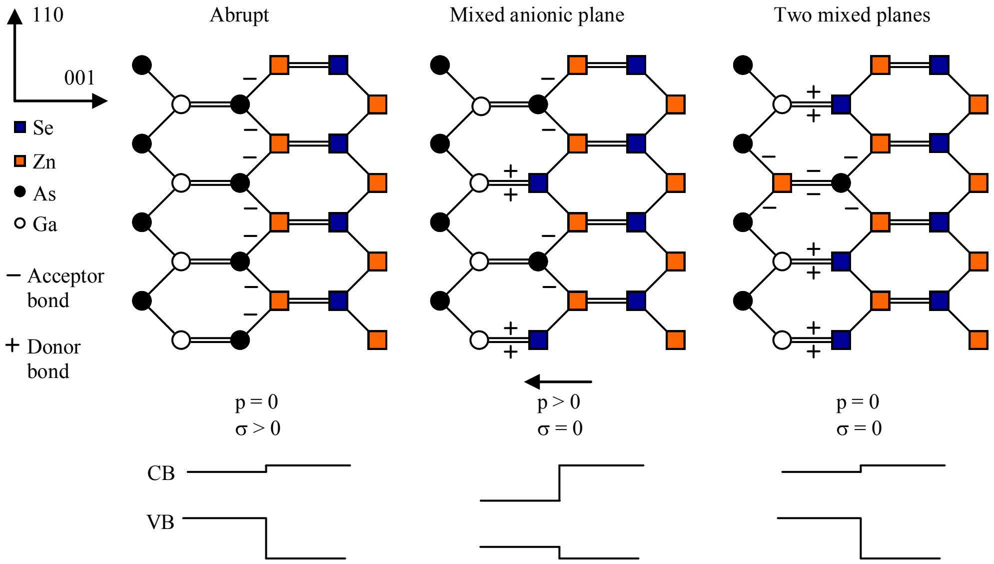

Figure 5.8: Atomic configurations of the ZnSe / GaAs heterointerface leading to different electric dipole moments p and interface charge densities σ, as calculated in [16].

The areal density $N_{0,\mathrm{GaAs}} \cdot \lambda_{\mathrm{GaAs}}$ of interdiffused Zn acceptors in GaAs is higher for I and II than for III, which is reasonable regarding that during a Zn-rich growth start Zn considerably diffuses into GaAs. λ_{GaAs} is 20 nm, in reasonable agreement with detailed studies on Zn diffusion in GaAs at higher temperatures [151]. For all three curves the segregation length k of iodine donors in ZnSe is taken as k = 25 nm, consistent with ECV measurements on reference samples. The areal density of acceptors in ZnSe is 0 in I and II and is finite in III. This can be understood in terms of a replacement of As atoms by predeposited Se at the GaAs surface, and their subsequent partial incorporation in the growing ZnSe layer as acceptors. In a Zn-rich growth start this As replacement is largely prevented. Such a complex growth start mechanism may also affect the MBE growth rate in the early stages of growth, and thereby cause the significantly reduced total layer thickness for longer Se predeposition (compare table 5.1). A reduced growth rate for several minutes after growth start is also directly observed by in-situ XRD studies of ZnSe / GaAs heteroepitaxy [152].

In this section we have shown that our experimental values for the potential barrier height, the individual depletion widths and the electron deficit at ZnSe / GaAs heterointerfaces can be consistently modeled using reasonable parameters for band offsets, interface state density, atomic interdiffusion and segregation of dopants.

Our observation of a reduction of the CBO with Se predeposition may seem in contrast to literature results. For ZnSe growth with a wide range of Zn/Se flux ratios, a reduction of the VBO with increasing Se flux was reported [131]. For comparing these studies with ours, it should be noted that two strongly different growth procedures were applied: (i) in our case ZnSe epilayer growth with a fixed Zn/Se flux ratio, optimized for structural quality and transport properties. Our only variable parameter is the amount of predeposited elementary Zn or Se at the interface prior to the ZnSe epilayer growth start; (ii) in Ref. [131] growth of interface and ZnSe epilayer with a constant Zn/Se beam pressure ratio (BPR), which was varied in a wide range ($0.1 < \mathrm{BPR} < 10$).

These different procedures with their specific growth kinetics in terms of e.g. interdiffusion and desorption may well lead to different atomic configurations at the interface. From theoretical modeling it was shown that different interface configurations with comparable formation energy exist, which have opposing electric dipole moments, i.e. different CBO values [16]. Furthermore, it should be noted that the VBO for close-to-stoichiometric ZnSe growth start conditions in Ref. [131] is 0.98 ± 0.14 eV, which corresponds to a CBO $= 0.32 \pm 0.14$ eV. This value fits well between our results for Zn predeposition (sample B) and the lowest Se predeposition (sample C).

A more detailed quantitative comparison of our results, derived essentially from transport experiments on doped "thick-layer" heterostructures, with literature VBO values, derived from photoemission spectroscopy on extremely thin epitaxial layers, is hampered by possible additional, process-dependent sample properties, such as densities of dopants and defects, or a reduced effective ZnSe band gap at the interface. The impact of these effects may be quite specific for the various experimental methods. Therefore, for this purpose a combined analysis of the same samples first by electron photoemission spectroscopy and subsequently by our characterization methods after ZnSe overgrowth would be required for the various growth start procedures.

5.6 Conclusion

We have studied the electronic and structural properties of MBE-grown n-type ZnSe / GaAs (001) heterointerfaces, a prototype of *heterovalent* semiconductor interfaces, and their variation with predeposition of Zn or Se in the fractional monolayer range at ZnSe growth start. Temperature dependent I-V measurements across the heterointerfaces show that the potential barrier in the conduction band is reduced from about 550 meV for a very Zn-rich growth start, to 73 meV for our highest Se coverage. Based on the increasing symmetry of I-V curves, we attribute this to a reduction of the ZnSe / GaAs conduction band offset by an electric interface dipole moment. The lower offset manifests itself in a drastically reduced resistivity of the interface. Independent of the growth start ECV shows a carrier depleted region of about 50 nm width at the heterointerface with a constant electron deficit of $1.5 \times 10^{13}\,\mathrm{cm}^{-2}$, while Raman spectroscopy measurements reveal that the depletion region is partially shifted from GaAs to ZnSe with Se predeposition.

Taking account of a variable band offset, interface state density, atomic interdiffusion and segregation is necessary to give a detailed description of the band bending and carrier distribution at heterovalent heterointerfaces. The effects of variable band offsets and interdiffusion leading to compensation or doping at the interface are general properties of heterovalent heterointerfaces. The extent of these effects depends on the material combination, epitaxial growth conditions and especially on the sequence of the molecular deposition.

Chapter 6

Single DMS Tunnel Barriers

In this chapter a new approach to spin filtering in diluted magnetic semiconductor heterostructures is described. It exploits the different tunnel probabilities of spin-up and spin-down electrons through a single (Zn,Be,Mn)Se DMS tunnel barrier, which is embedded in non-magnetic n-ZnSe contact layers. In contrast to resonant tunneling diodes, single tunnel barrier structures do not require a specific resonance voltage to be applied in order to act as a spin filter. Additionally it may be envisioned that such a structures can also serve as a spin detector, using the spin electromotive-force technique mentioned in [65].

J. C. Egues in 1998 proposed a spin-filter using a single, band gap matched (Zn,Mn)Se layer between n-type ZnSe contacts [153, 13]. While for B = 0 the conduction band in the treated structures is essentially flat, the paramagnetic (Zn,Mn)Se layer acts as a tunnel barrier for electrons of spin-up orientation and as a quantum well for electrons of the opposite orientation when a magnetic field is applied. The conductivity of spin-up electrons is then exponentially suppressed and oscillations occur in the conductivity of spin-down electrons. The same concept has been studied theoretically by A. Saffarzadeh, with an emphasis on the effect of different Mn concentrations and barrier thicknesses on the spin polarization of the tunneling current [14].

Even though spin filtering by resonant tunneling in II-VI DMS heterostructures has been demonstrated and studied extensively, no experimental realizations of spin filters utilizing a single DMS tunnel barrier have been published, to the best of the authors knowledge. As a part of this work such structures are fabricated, and their properties are described in this chapter. They show considerable negative magnetoresistance of up to -64 % at 4.2 K, in good agreement with calculations of spin-dependent tunneling conduction through a single DMS barrier.

Such structures are different from the widely studied magnetic tunnel junctions, in that they don't rely on ferromagnetic emitter- and collector layers [154]. As all-semiconductor devices they potentially allow spin injection into non-magnetic semiconductors. Spin filtering by tunneling through a DMS tunnel barrier also differs from the well known spin alignment by diffusive transport in thick DMS layers [5], in that it can be fully coherent and thus potentially useful for applications in spin-based quantum computing [28]. Additionally it may be envisioned that the spin-dependent tunneling probability can also be used to sense spin polarization in an electron reservoir adjacent to a DMS tunnel barrier, similar to the concept described in [65] as spin electro motive force.

6.1 Device Structure and Functional Principle

The layer stack and a self-consistently calculated band diagram of the fabricated single barrier structures are schematically depicted in figures 6.1 and 6.2, respectively. On a GaAs(001) substrate an about 200 nm thick GaAs layer and a partially doped, pseudomorphic (Zn,Be)Se multilayer buffer are grown. The latter serves the purpose of shielding the sensitive tunneling transport layers from the ZnSe / GaAs heterointerface, and is described in more detail in [134, 155]. On the (Zn,Be)Se multilayer buffer, a 100 nm thick, highly n-doped ($N_d = 2\times10^{19}\mathrm{cm}^{-3}$) ZnSe bottom contact layer is grown. It is followed by the active region, which consists of the (Zn,Be,Mn)Se DMS tunnel barrier embedded in a nearly symmetric emitter / collector structure with shallow, undoped ZnSe pre-wells and low doped ($N_d = 1 \times 10^{18}\mathrm{cm}^{-3}$) $\mathrm{Zn}_{0.97}\mathrm{Be}_{0.03}\mathrm{Se}$ barrier layers. It is capped with a 30 nm thick, highly n-doped ($N_d = 2 \times 10^{19}\mathrm{cm}^{-3}$) ZnSe top contact layer. Ohmic contact is made to the top layer by in-situ evaporation of Al, Ti and Au, as described in chapter 5. About $100 \times 100\,\mu m^2$ mesas are prepared by optical lithography, and the bottom contact is made to the lower 100 nm highly doped n-ZnSe layer by ex-situ evaporation of Au. Electric transport is then measured vertically through the structure by applying a voltage between the top and bottom contacts.

The emitter and collector in the fabricated structures incorporate a shallow, undoped quantum well, which has been developed previously for RTD structures in the same material system [121]. From self-consistent Poisson-Schrödinger calculations the lowest sub energy is estimated to be about 7 meV below the Fermi energy E_F (see green line in figure 6.1).

Several single DMS barrier samples are fabricated by MBE, with varied zero-field barrier height and thickness. Their main parameters are listed in table 6.1. The addition of Be to the DMS barrier layer increases its band gap, and thereby ensures a finite conduction band barrier height Φ_0 for both spins at zero field. Using literature values for the band offsets (see section 2.1), the barrier height measured from the ZnSe conduction band edge in the emitter is $\Phi_0 = 112\,meV$ for 7 % Be and 8 % Mn.

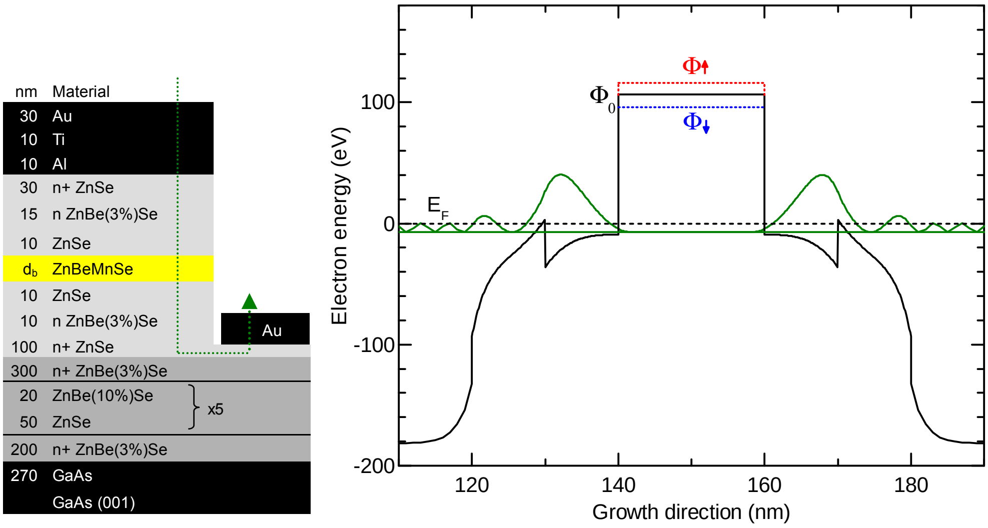

Figure 6.1: Left: Schematic of the layer and mesa structure of a single DMS tunnel barrier sample for vertical transport. The current path is indicated by the green dotted line. Right: self-consistently calculated conduction band profile (black line) of the structure on the left, and probability density function of the quasi-bound electron state in the emitter and collector pre-wells (green line). The energies are given relative to the Fermi level E_F. The DMS tunnel barrier height due to the conduction band offset is Φ_0 (measured from the emitter conduction band edge). In an external magnetic field and at low temperatures, the s-d exchange interaction in the DMS tunnel barrier causes a spin splitting of the barrier height of up to $2\Delta E_{CB} \approx 20$ meV (compare figure 2.3), leading to a spin-dependent tunnel probability.

Sample	Be %	Mn %	d_b (nm)
cb3475	7	8	11
cb3476	7	8	8
cb3502	7	8	20
cb3514	7	8	24
cb3515	4	8	26

Table 6.1: Summary of the fabricated single DMS tunnel barrier samples. The nominal concentration of Be and Mn in the tunnel barrier are denoted by 'Be %' and 'Mn %', respectively. d_b is the barrier thickness.

6.2 Model Calculations of Magnetoresistance and Spin Polarization

The composition of the tunnel barrier is chosen such that the band offset causes a finite barrier height Φ_0 of the order of about 100 meV in the conduction band. When an external magnetic field is applied, the s-d exchange interaction leads to gradual splitting gradual splitting in the conduction band $2\Delta E_{CB}$ of up to about 20 meV (see section 2.2). The barrier height is then spin-dependent

$$\Phi_{\uparrow\downarrow} = \Phi_0 - \frac{eV}{2} \pm \Delta E_{CB}, \tag{6.1}$$

causing a spin-dependent tunnel probability of electrons. The term $eV/2$ is included to account for the reduction the tunnel barrier height with bias voltage in the low bias regime $e \cdot V \ll \Phi_0$. The tunnel probability T obtained from transfer matrix calculations (see section 2.4.2) for typical values of the barrier heights $\Phi_0 = 80$ meV, $\Phi_\downarrow = 70$ meV, $\Phi_\uparrow = 90$ meV (estimated for a Mn content of 8 % and $B \approx 6$ T) and for a typical barrier thickness of 20 nm is plotted as a function of incident electron energy E_z in figure 6.2. For an incident electron energy of $E_z = 10$ meV the ratio of the tunnel probability for spin-up and spin-down electrons $T_\downarrow/T_\uparrow$ is about 25.

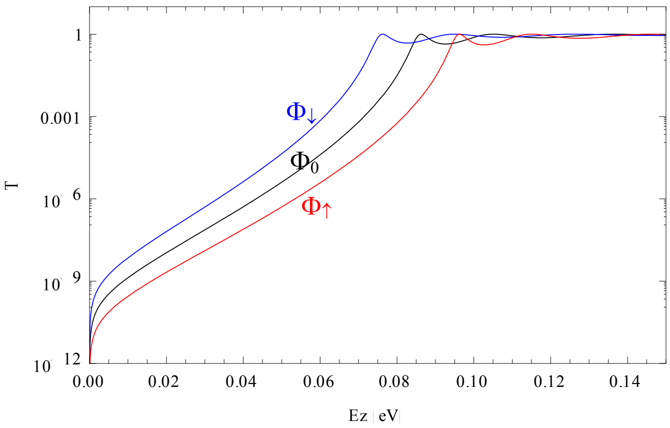

Figure 6.2: Calculated tunnel probability T as a function of the incident electron energy E_z for three different barrier heights of 70 meV ($\Phi_\downarrow$), 80 meV (Φ_0) and 90 meV ($\Phi_\uparrow$) . The calculations are done without bias and for a barrier thickness of 20 nm.

In section 2.4.2 the current-voltage characteristics of single semiconductor tunnel barriers are discussed theoretically. The spin-up and spin-down current densities $J_\uparrow$ and $J_\downarrow$ can be calculated from equation 2.28, using the spin-dependent barrier height in equation 6.1. The total current through a device of the cross-section A is then

$$I = A(J_\uparrow + J_\downarrow) \tag{6.2}$$

and its resistance is $R = \frac{V}{A(J_\uparrow + J_\downarrow)}$.

The magnetoresistance describes the change of the resistance with the magnetic field relative to the zero field resistance, and is given by

$$\begin{aligned} MR &= \frac{R(B) - R(0)}{R(0)} \\ &= \frac{2 \cdot J(\triangle E_{CB} = 0)}{J_{\uparrow +} J_\downarrow} - 1. \end{aligned} \tag{6.3}$$

It is plotted in figure 6.3 for different barriers, as a function of the conduction band shift $\triangle E_{CB}$. As a guideline, for B = 6 T and for a Mn concentration in the tunnel barrier of 8 %, ΔE_{CB} = 9.8 meV is calculated, using the appropriate parameters S_{eff} and T_0 (see section 2.2). Most importantly, MR is negative, i.e. the device resistance decreases with the magnetic field. For $\Phi_b = 85\, meV$ and a barrier thickness of $d_b = 20\, nm$, the magnetoresistance reaches -63 % at $\triangle E_{CB} = 10\, meV$, and about -93 % for $\triangle E_{CB} = 20\, meV$. For very small $\triangle E_{CB} < 1\, meV$ the magnetoresistance is close to 0, since the variations of $J_\uparrow$ and $J_\downarrow$ nearly compensate each other. For larger $\triangle E_{CB}$ MR is negative, and it approaches -100 % for very large $\triangle E_{CB}$. The effect is stronger for thicker and lower barriers, as long as $\triangle E_{CB}$ does not become larger than $(\Phi_0 - \frac{eV}{2})$.

Since the proposed devices are envisioned as spin-filters, the main quantity of interest is the spin polarization of the current

$$\alpha = \frac{J_\downarrow - J_\uparrow}{J_\downarrow + J_\uparrow}. \tag{6.4}$$

It is plotted in figure 6.4 as a function of $\triangle E_{CB}$. In contrast to the magnetoresistance, the spin polarization increases about linearly from $E_{CB} = 0$, and converges to +100 % for high $\triangle E_{CB}$. Again, the effect is stronger for thicker and for lower barriers.

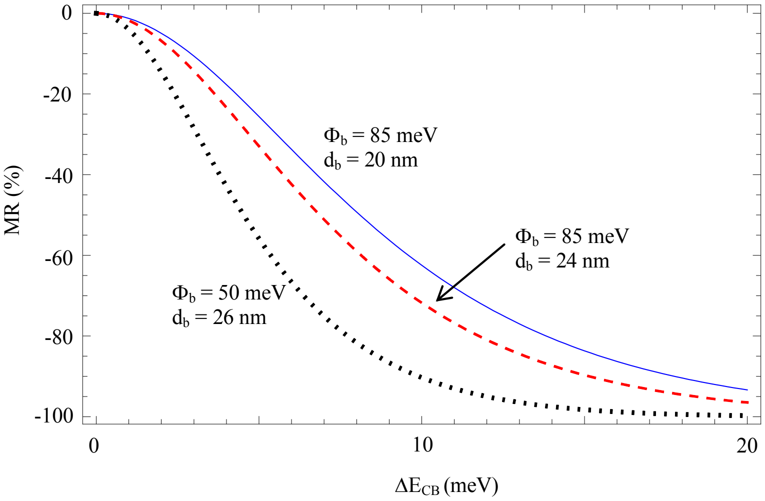

Figure 6.3: Magnetoresistance MR as a function of the spin splitting of the conduction band ΔE_{CB} , calculated for single DMS tunnel barriers of different height and width.

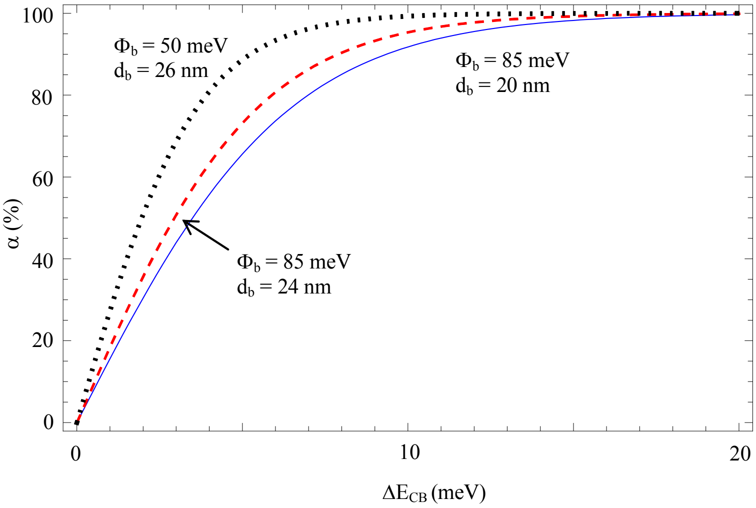

Figure 6.4: Spin polarization α as a function of the spin-splitting of the conduction band ΔE_{CB} , calculated for single DMS tunnel barriers of different height and width.

6.3 I-V Characteristics

Figure 6.5 depicts the I-V characteristics of the single DMS barrier sample cb3502, measured at 4.2 K and with a magnetic field between 0 and 6 T applied parallel to the growth direction.

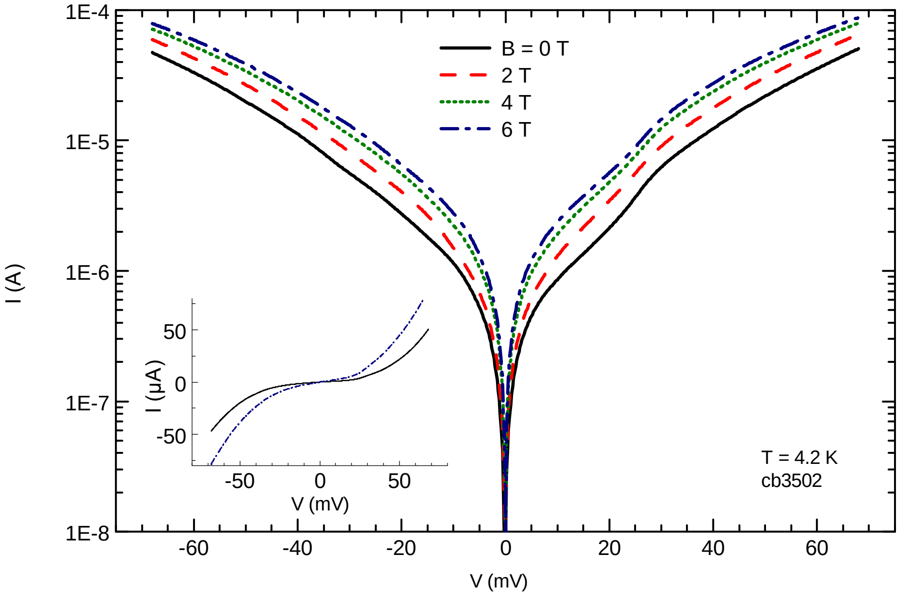

Figure 6.5: Left: I-V characteristics of a single DMS tunnel barrier sample (cb3502, contact 6 to D), measured at 4.2 K and in different magnetic fields with B || I. The inset shows the same data plotted on a linear scale.

First we note that the I-V characteristics are ohmic for very low bias $V \lesssim 10\, mV$, and that the current increases superlinearly for higher bias in the investigated range up to 70 mV. This general behavior is in good agreement with the theoretically expected characteristics discussed in section 2.4.2.

Secondly we note that the curves are very symmetric with respect to bias voltage, indicating that the potential barrier limiting the current is reduced by bias voltage irrespective of its polarity. This is consistent with the expected symmetric shape of the ideally rectangular DMS tunnel barrier and the n-type emitter / collector structure. If the current in the device were limited by an asymmetric potential barrier, e.g. a roughly triangular Schottky barrier at one of the contacts, this asymmetry would be reflected in the I-V curves.

Finally, and most importantly, the device shows strong negative magnetoresistance, as expected for spin-dependent tunneling through a DMS barrier. For $B = 6$ T the tunneling current at low bias is about a factor of three higher compared to $B = 0$ T. For higher bias the effect is reduced but still significant. A more detailed analysis of the magnetoresistance is given in the next section.

These characteristics are shared qualitatively by the samples cb3514 and cb3515, the zero-field I-V curves of which are shown in figure 6.6. For sample cb3414, which nominally has a 20 % thicker barrier than the above studied sample cb3502, the resistance is more than an order of magnitude higher than for cb3502. For sample cb3515, which has an even thicker but significantly lower barrier (due to much lower Be content), the resistance is slightly smaller than for sample cb3502. The first samples cb3475 and cb3476 have ohmic I-V characteristics with a very low resistance of less than $100\,\Omega$ at 4.2 K, and they show no change of resistance in a magnetic field. This is interpreted as the tunnel barrier being too thin, such that transport is limited by a series resistance (e.g. in the contact layers) and not by the tunnel barrier. The change of the barrier height then only has a negligible effect on the total resistance.

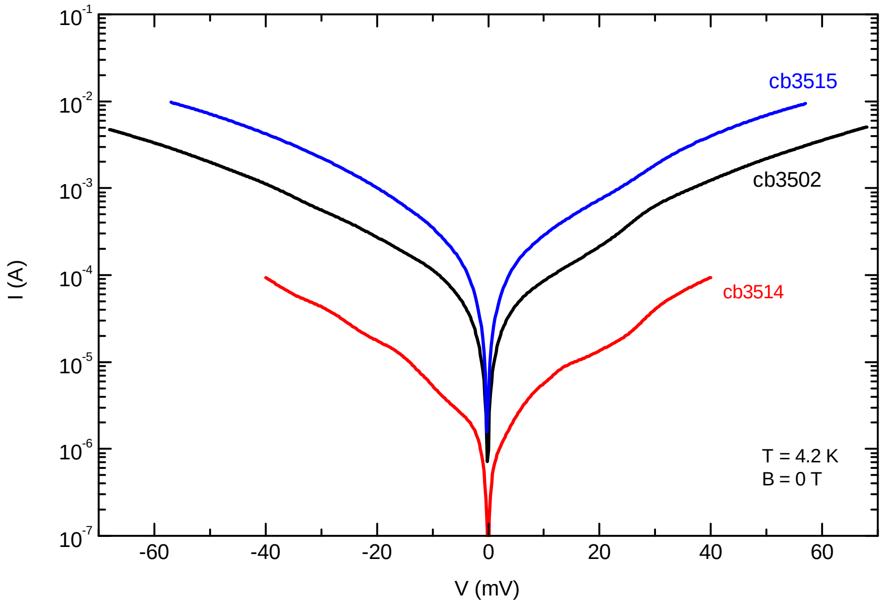

Figure 6.6: Comparison of I-V characteristics of different DMS tunnel barrier samples, measured at at 4.2 K and at 0 T (see table 6.1).

The experimental I-V curves can be reproduced to good accuracy with the theoretical model described in sections 2.4.2 and 6.2. The model is based on coherent intraband tunneling of electrons from an emitter Fermi sea with a constant density of states, through a tunnel barrier and into a collector Fermi sea. A finite, voltage-independent lever arm is allowed to account for partial bias voltage drop over the contact layers. It neglects electron scattering, band bending, and other forms of electron transport, such as hopping transport over impurities. Figure 6.7 shows I-V curves calculated from equations 2.28, 6.2 and 6.1, with parameters manually tuned to fit the experimental curves measured for sample cb3506 at B = 0 T and 6 T. Table 6.2 lists the parameter sets used for two I-V curves. Both curves are described very well by the model calculations up to a current of about $30\,\mu A\,(\approx 300\,A/cm^2)$. At higher currents the model overestimates the current through the device. This deviation may e.g. be due to a

Parameter	$B = 0\,T$	$B = 6\,T$
d_b	20 nm	20 nm
Φ_0	62 meV	62 meV
ΔE_{CB}	0	7.9 meV
r	1.45	1.45
E_F	15 meV	15 meV
T	4.2 K	4.2 K

Table 6.2: Parameters used for the calculation of the I-V curves shown in figure 6.7.

series resistance or due to band-bending, which both essentially influence the lever arm r, or due to heating of the Mn spin system [156], which reduces the spin-splitting of the barrier and thus increases the device resistance in a magnetic field.

The barrier thickness d_b and the temperature T used for the calculations (table 6.2) are set to the nominal experimental values. The Fermi energy in the emitter E_F is hard to measure independently, but the used $E_F = 15\,meV$ is close to the values obtained from self-consistent Poisson-Schrödinger calculations. The barrier height Φ_0 is lower than the value of 112 meV estimated from band-offsets. This may be due to confinement in the emitter pre-well (compare figure 6.1), to interdiffusion of Be into the surrounding layers, or even due to the image charge effect [62]. The lever arm r = 1.45 implies that a fraction 1 / r = 0.69 of the total voltage drops over the barrier. This is quite reasonable regarding the fact that, in the fabricated structures, the emitter and collector layers are relatively highly doped right up to the active region, and voltage drop especially over the depleted collector layer is relatively small.

The most important conclusion from the fits in figure 6.7 is that both the 0 T and the 6 T I-V curves can be approximated with the same set of parameters, differing only in the conduction band splitting ΔE_{CB}. The value $\Delta E_{CB} = 7.9\,meV$ is in good agreement with that expected for $Zn_{0.92}Mn_{0.08}Se$ in a magnetic field of 6 T and at a temperature of 4.2 K (see figure 2.3).

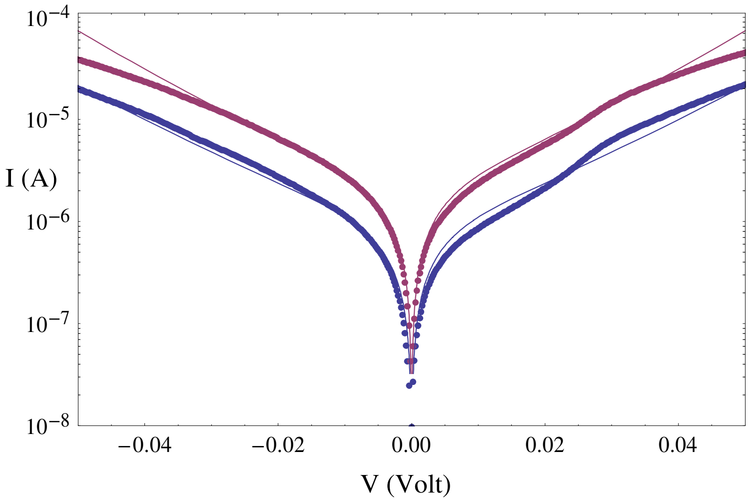

Figure 6.7: Comparison of measured I-V curves of sample cb3502 with calculated ones for magnetic fields of 0 T (blue) and 6 T (violet) at 4.2 K.

6.4 Magnetoresistance

The magnetoresistance (MR) at different bias voltages, obtained from a series of I-V curves taken in different magnetic fields with a step size of 0.25 T, is shown in figure 6.8 for sample cb3502. For 10 mV, 25 mV, and 50 mV, the MR is negative, and it decreases monotonically with B. It appears to saturate at very high fields, reaching up to -64 % at 6 T and at low bias. This general behavior is in good agreement with model calculations of the dependence of MR on the conduction band spin splitting ΔE_{CB} (figure 6.3), keeping in mind that ΔE_{CB} is related to B via a Brillouin function (section 2.2). At very low bias voltage the picture is more complex. For V = 1 mV MR is positive at low fields, it reaches a maximum at $B \approx 0.7T$ before decreasing into the negative range, with low-amplitude oscillations superimposed on the decrease. This behavior suggests that other MR effects, such as classical MR, weak localization, effects related to Landau quantization or the effects described in [157] specifically for DMS, may play a role as well. However, since vertical transport in thin, large-area layer structures is studied here, resistance effects related only to diffusive transport in the active region, are unlikely to be significant.

The simple model discussed in sections 2.4.2 and 6.2 predicts a stronger MR effect for lower barriers. In a first approximation, a bias voltage reduces the barrier height, and therefore it may be inferred that the magnitude of MR should generally increase with the bias voltage. This trend is seen in a limited range of $B \lesssim 2$ T, and for $V \lesssim 25$ mV. For higher fields and bias voltages, the magnitude of MR decreases with increasing bias voltage. One explanation for this opposite trend may be a reduction of ΔE_{CB} due to heating of the Mn spin system by the increased current at higher fields or bias voltages.

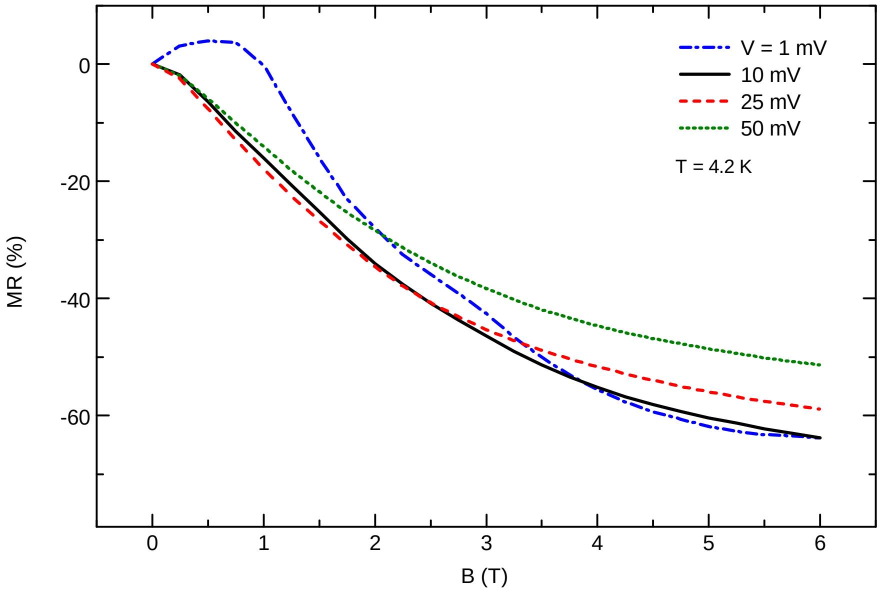

Figure 6.8: Magnetoresistance MR of sample cb3502 for different applied bias voltages.

Another fundamental effect that may play a role is a spin-dependent splitting of the Fermi level E_F in the emitter, similar to the effect causing a low efficiency of electron spin injection over interfaces with a large conductance mismatch [64, 65, 158]. If $J_\downarrow$ through the barrier is significantly larger than $J_\uparrow$, then the Fermi level of electrons of this spin orientation right before the barrier $E_{F,\downarrow}$ is lower than $E_{F,\uparrow}$. The opposite, $E_{F,\downarrow} > E_{F,\uparrow}$, is the case in the collector. This Fermi-level splitting is opposed to the spin splitting of the barrier heights, and can thus, in principle, pose an intrinsic limit to the magnetoresistance in these devices.

Assuming 1-d diffusive transport in the emitter, the local current density in one spin-channel $J_{\uparrow\downarrow}(z)$ in the emitter is linked to the gradient of the respective local Fermi level $E_{F,\uparrow\downarrow}(z)$ via the (spin-independent) conductivity σ

$$J_{\uparrow\downarrow}(z) = -\frac{\sigma}{e}\frac{\partial E_{F,\uparrow\downarrow}}{\partial z}. \tag{6.5}$$

The current densities in the emitter are related to the tunneling current through the barrier due to the continuity requirement. Similar to the discussion in [158], it is further assumed that the variation of the Fermi level in the emitter is given by a linear and an exponential component, governed by the spin flip time τ. The spin-splitting of the Fermi level right in front of the tunnel barrier (z $=$ 0) can then be derived as

$$\left[E_{F,\uparrow} - E_{F,\downarrow}\right]_{z=0} = -\frac{\pi\hbar^2\tau}{e\,m}\left[J_\uparrow - J_\downarrow\right]_{z=0}. \tag{6.6}$$

Since the current densities depend on the Fermi levels in front of the barrier in a non-trivial way (see dependence of J on E_F in equation 2.28), this is an implicit equation which can not be solved analytically. To get a rough estimate of the possible magnitude of the Fermi-level splitting in the present structures, we assume a spin-flip time of $\tau = 100$ ns and a current density difference of $[J_\uparrow - J_\downarrow]_{z=0} = 1\,\mathrm{A/cm}^2$ (compare I-V curves in figure 6.5 and consider the mesa size of $100 \times 100\ \mu m^2$). This yields a Fermi level splitting of about 10 meV, which is comparable to the s-d exchange interaction splitting of the barrier heights and may thus play an important role in the limitation of the MR. The estimate of 100 ns for the spin flip time has to be taken with care. Reliable data on the spin flip time of electrons in semiconductors is rare, and often the distinction between spin-flip time and the spin-coherence time in an ensemble of magnetic moments is not very clear. Dzhioev et al. have measured a spin-flip time of up to 100 ns in n-GaAs, with a non-monotonic dependence on the doping density [159]. Awschalom et al. also report spin lifetimes of 100 ns in GaAs and 60 ns in ZnSe [160, 161].

The I-V characteristics of sample cb3502 and its magnetoresistance at intermediate bias can thus at least be qualitatively understood in terms of the above described model. With a large, negative MR in moderate magnetic fields it shows the desired behavior of a single DMS tunnel barrier. As listed in table 6.1, samples cb3514 and cb3515 are grown with thicker and / or lower tunnel barriers, and should thus show even larger MR. However, even though the zero-field resistances of these samples (see I-V curves in figure 6.6) are in qualitative agreement with the nominal variations of the barrier height and thickness, their magnetoresistance is somewhat surprising. In figure 6.9 the MR of these samples is shown for a bias voltage of 10 mV and at 4.2 K. Apart from slightly stronger oscillations observed at low fields for sample cb3514, the three samples show only marginal differences in MR. The MR of sample cb3515, which has a 30 % thicker and a significantly lower barrier than cb3502, closely follows the MR of the latter sample in the whole range of magnetic fields studied. The highest value of MR reached at 6 T is thus about -64 %, independent of the height and width of the tunnel barrier.

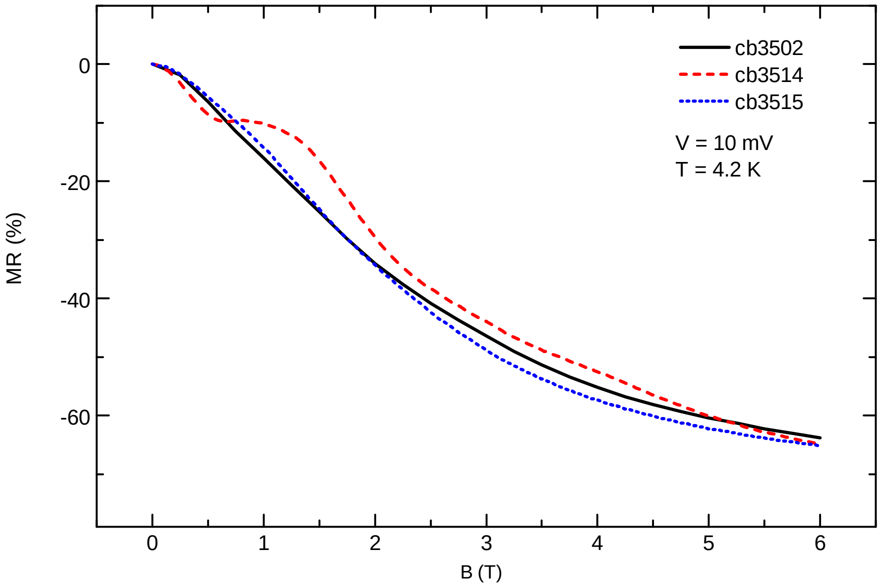

Figure 6.9: Magnetoresistance ratio R(B) / R(0T) for three single DMS tunnel barrier samples with different barrier height and width, measured at 4.2 K and at 10 mV bias.

Solving equation 6.6 numerically using reasonable parameters shows that the splitting is essentially proportional to the total current density $J_{\uparrow}+J_{\downarrow}$. It should thus be smaller for samples with a higher resistance, meaning that this model of a Fermi level spin splitting can not explain the limitation of MR for tunnel barrier samples with widely varying resistance (figures 6.6 and 6.9). The limitation of the MR to about 64 % independent of the barrier height and width thus remains an open question.

In contrast to the magnetoresistance, the spin polarization of tunneling electrons α can not be directly measured with the present experimental setup. From the measured magnetoresistance MR = -64 $ and from the calculations in figure 6.3, a high value $\alpha \approx 90$ % can be estimated. The spin polarization can potentially be probed directly in optical experiments relying on the rotation of the polarization direction of light by spin-polarized electrons, such as the Faraday-effect (in transmission) or the Kerr-effect (in reflection) [68]. Alternatively, the polarization of light emanating from the recombination of electrons transmitted through the DMS tunnel barrier with optically or electrically injected, unpolarized holes could be detected. The latter experiment would be similar to that described in [5].

Chapter 7

DMS Resonant Tunneling Diodes

This chapter explores several aspects of II-VI DMS RTDs. The complex diffraction pattern of tensile-strained, (Zn,Be)Se based RTDs in HRXRD is analyzed, and it is shown how such measurements can yield precise information about the quantum well and tunnel barrier thickness and composition [18]. Next, the influence of the variation of the quantum well thickness and composition on the position of resonances in the I-V characteristics of such RTDs is investigated. The chapter and the thesis close with the discussion of 0D resonant tunneling in RTDs with self-assembled CdSe quantum dots.

Resonant tunneling through double potential barriers in semiconductor heterostructures has been first reported by Chang, Esaki and Tsu in 1974 [162]. Since then a lot of progress has been made in optimizing the structures for high peak-to-valley current ratios (PVR) and high current density, and PVRs as high as 30 at room temperature [163]and current densities up to $10^6 A/cm^2$ have been reported [164]. Based on their unique property of negative differential resistance, the related multistability in the I-V curves, and the low dwell time of electrons in the tunneling state, RTDs have several potential applications in high frequency signal generation and high speed switching [57]. However, the high sensitivity of their I-V characteristics to layer thickness and composition fluctuations, as well as the still relatively low current densities and the lack of high frequency amplifiers, have hindered a widespread technological application of RTDs.

The above noted applications and effects have been realized mostly in the III-V material system of GaAs / AlGaAs. Other semiconductor material systems in which resonant tunneling has been reported include Si/SiGe [165], GaN/AlGaN [166], and the II-VI materials of HgTe/HgCdTe [167], CdTe/CdMgTe , ZnSe/BeTe [168], and ZnSe/(Zn,Be)Se [9].

From a fundamental physics perspective resonant tunneling in semiconductor heterostructures also allows to study a wealth of mesoscopic and spin-dependent transport effects. If the dimensionality of the resonant state is reduced from 2D (quantum well) to 0D (quantum dot) the RTD essentially constitutes an artificial atom with electric leads attached. Electrons are transported through such structures one-by-one due to the Coulomb-blockade effect [70]. In 0D III-V RTDs fundamental single-electron transport effects such as atomic-like shell filling and Hund's rules have been observed [19, 20]. Realizing such 0D RTDs in the II-VI dilute magnetic semiconductor material system allows to amplify the spin-dependent effects in such experiments by the s/p-d exchange interaction. This promises interesting spin-resolved single electron transport experiments and possibly new spintronic devices.

In II-VI semiconductors, the possibility of including of DMS layers in the tunneling heterostructure allows to exploit the large energy separation of spin states due to the s/p-d exchange interaction. This opens the possibility of different spin filtering and manipulation concepts based on a spin-dependent tunnel probability. Voltage controlled spin-filters based on II-VI DMS RTDs, which allow purely electrical switching of the spin orientation of an electron current, have been reported by Slobodskyy et al. in 2003 [9] and by Fang et al. in 2007 [10]. In 2006 Gould et al. reported resonant tunneling through a CdSe QD in a DMS RTD with clear splitting of the narrow resonance peak in a magnetic field [11]. Remarkably, the splitting remained finite even at zero field. This was interpreted as spin dependent tunneling through a single magnetic polaron, in which electrons in a QD mediate an effectively ferromagnetic interaction between adjacent Mn ions. In 2009 Rueth et al. found a Fermi edge singularity enhancement of resonant tunneling transport in a CdSe / (Zn,Be)Se QD RTD, a many particle effect related to the coulomb interaction between tunneling electrons and electrons in the emitter [21].

As a part of this work, II-VI semiconductor RTDs are fabricated and characterized with the focus on developing structures that allow to study 0D tunneling transport in magnetic environments. This goal is pursued on two routes:

On the one hand, quantum well RTDs suitable for fitting with a lateral gate to provide electrostatic confinement of the tunneling state from 2d to 0D are fabricated. An important requirement of such RTDs is that their intrinsic first resonance (without a gate voltage) is at very low energy, since a negative gate voltage required for lateral confinement drastically increases the resonance energy and therefore the required bias voltage. Different ways to reduce the resonance energy of II-VI RTDs are investigated, and it is found that resonances can be shifted from typically over 150 mV bias to close to 0 V by the admixture of Cd to the quantum well. Increasing the quantum well width also reduces resonance voltages, but only to a limit of about 100 mV.

On the other hand, II-VI RTDs including self-assembled CdSe QDs instead of a quantum well are fabricated, which allow to study 0D tunneling transport without the additional fabrication effort needed for electrostatic gates. As a prerequisite, the structural and optical properties of CdSe QDs embedded in (Zn,Be,Mn)Se tunnel barriers are investigated (see section 4.5). With the knowledge gained, self-assembled QD RTDs are fabricated, showing a rich variety of magneto transport effects, including 0D tunneling transport and possibly spin splitting of resonance peaks without a magnetic field.

Additionally, a method for non-destructive, XRD based characterization of the active region of (Zn,Be)Se based double-barrier RTDs is developed, which improves growth control of the sensitive structures.

In section 7.1 the basic structure and I-V characteristics of the fabricated (Zn,Be,Cd,Mn)Se RTDs are introduced. In section 7.2 XRD $\omega - 2\Theta$ diffractograms of such structures and the method to extract layer parameters of the active double-barrier region are presented. Sections 7.3 and 7.4 present the investigations on influencing the resonance energies in quantum well RTDs by varying the width and the depth of the quantum well, respectively. RTDs with self-assembled CdSe QDs and the structural and optical properties of such dots are treated in section 7.5 .

7.1 Basic Properties of II-VI DMS RTDs

Figure 7.1 depicts the nominal structure of a basic (Zn,Be,Mn)Se quantum well RTD fabricated at the beginning of this work. The basic layer sequence with III-V and II-VI buffer layers, contacts and emitter- and collector layers with a shallow pre-well, has been developed in previous works on DMS RTDs in Wuerzburg [169, 155, 66, 121].

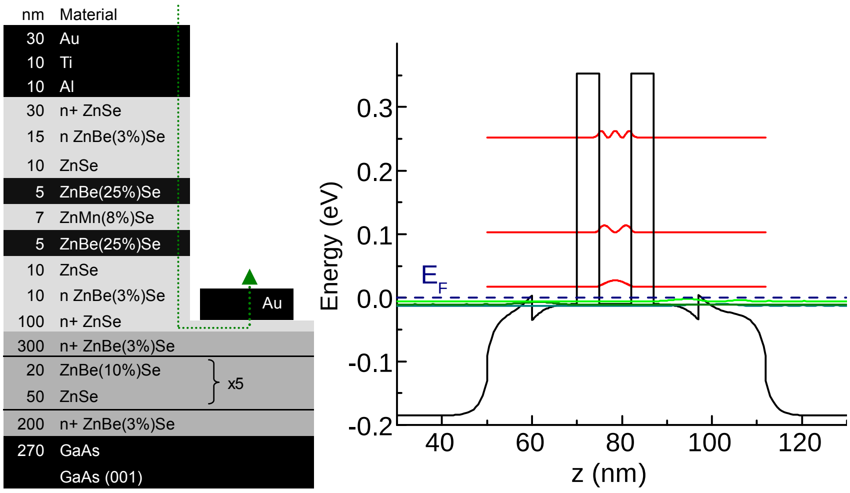

Figure 7.1: Left: Nominal layer structure of a typical II-VI DMS RTD. The nominal doping densities are $n = 10^{18}\text{cm}^{-3}$ and $n^{+} = 2 \times 10^{19}\text{cm}^{-3}$. Right: conduction band diagram obtained from self-consistent Poisson-Schrödinger calculations for the same structure, assuming fully ionized donors (black line). The squared wavefunctions of the quasi-bound states in the main quantum well (red lines) and in the emitter and collector pre-wells (green lines) are drawn at their respective energy levels. Energies are given relative to the calculated Fermi energy E_F.

On top of a GaAs(001) substrate a (Zn,Be)Se multilayer buffer is grown, as described in section 6.1. The RTD structure, grown on top of the buffer, consists of a 100 nm thick, highly doped ($N_d = 2 \times 10^{19} cm^{-3}$) ZnSe bottom contact layer, low doped ($N_d = 1 \times 10^{18} cm^{-3}$) emitter and collector layers forming a shallow quantum well ("pre-well"), the double barrier structure, and a 30 nm thick, highly doped ($N_d = 2 \times 10^{19} cm^{-3}$) ZnSe top contact layer. MBE growth of this structure is followed by in-situ deposition of 10 nm Al, providing good ohmic contact to n-ZnSe, 10 nm Ti as a diffusion barrier, and 30 nm Au to prevent oxidation. Square mesas of typically 100 µm lateral size and reaching down into the n-ZnSe bottom contact layer are processed lithographically, and a thick layer of Au is deposited ex-situ in a ring around the mesa for backside contacting. A basic double-barrier resonant tunneling structure, which was the starting point for the further investigations done in this work, consists of 6 nm thick (Zn,Be)Se tunnel barriers with a Be content of about 25% and a 7 nm wide (Zn,Mn)Se quantum well with 8 % Mn.

The conduction band profile of such an RTD structure, calculated by self-consistent solution of the Poisson and Schrödinger equations using *nextnano* [54, 55], is shown in figure 7.1. In the calculations it is assumed that all donors are fully ionized, leading to very high Fermi energy in highly doped regions. The effect of Mn on the band gap in the quantum well was neglected. Between about 350 meV high tunnel barriers three quasi-bound states are found at the energies of 16 meV, 102 meV and 251 meV above the Fermi level (indicated as red lines in figure 7.1). In the emitter and collector pre-wells the electron ground states (green lines) lie about 10 meV below the Fermi level. The pre-wells serve two purposes: first, they contribute to sharper resonances because they narrow the energy range of electrons available for tunneling. Secondly, the Fermi level in the pre-wells is given mainly by the well controlled height of the shallow $Zn_{0.97}Be_{0.03}Se$ barrier. It is relatively independent of the doping density in the contact layers, which may be subject to larger variations from sample to sample.

Figure 7.2 shows the I-V characteristics of such an RTD at 4.2 K without a magnetic field. Positive bias corresponds to electrons tunneling from the top to the bottom of the layer structure. For negative bias a first resonance with clear negative differential resistance occurs at about -0.15 V, and a second one around -0.5 V. For positive bias the resonances occur at slightly higher voltages and they are generally less expressed than for negative bias. This slight asymmetry may be caused by growth related effects like segregation of dopants or alloy materials, or by small differences in the emitter structure atop and below the double barrier structure.

The highest PVR achieved with the II-VI quantum well RTDs fabricated in this work was 2.4 at 4.2 K (sample cb3400). This is lower than the PVR of 6.0 at 4.2 K reported in Ref. [168], and even more so compared to PVR > 30 achieved in III-V systems even at room temperature [163]. However, an exceptionally high PVR was not of primary concern for this work.

At bias voltages several tens of mV above a resonance another weaker peak is often observed (see e.g. the shoulder at -0.24 V in figure 7.2), which is attributed to LO-

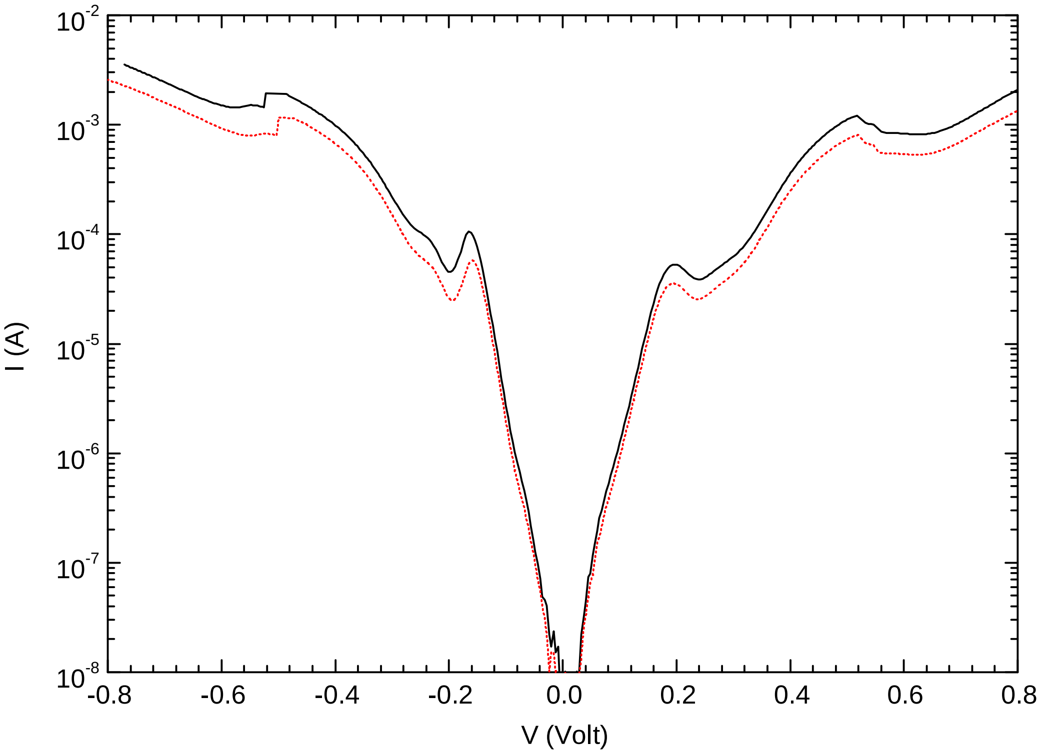

Figure 7.2: I-V characteristics of two mesas on a (Zn,Be,Mn)Se RTD wafer with the nominal structure depicted in figure 7.1, measured at 4.2 K and without a magnetic field .

phonon assisted resonant tunneling [170]. By comparing the voltage difference between the main resonance and the phonon replica to the LO-phonon energy (31 meV for ZnSe), a lever arm relating the voltage drop over the first tunnel barrier to the total applied voltage can be calculated. For an ideal symmetric RTD with no voltage drop over collector and emitter layers and contacts, the lever arm would be exactly 2. For most of the structures fabricated in this work it was usually in the range between 2 and 3.

Finally, figure 7.3 depicts the I-V characteristics of an RTD with a (Zn,Mn)Se quantum well at low temperature and with a magnetic field of 6 T applied parallel to the growth direction. The resonance, situated at 159 mV at 0T, is split into two peaks separated by several tens of mV by a high magnetic field. This clear splitting is attributed to resonant tunneling through the two spin sublevels in the DMS quantum well, which are split by tens of meV due to the s-d exchange interaction (see subsection 2.2 and [9, 66]). The current on the two peaks should therefore be spin-polarized. Since the polarization of the current can be switched by simply tuning the applied voltage, this is the central feature of DMS RTDs.

A question that is not treated in detail in this work is the shape and width of the resonance peaks. The intrinsic width of the resonances calculated by the transfer ma-

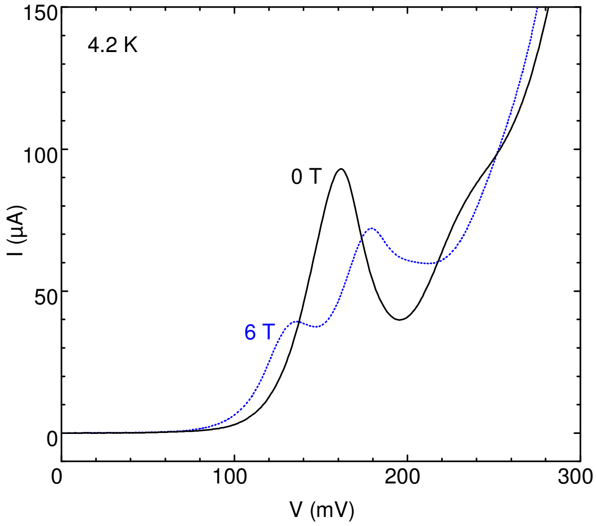

Figure 7.3: I-V curve of an RTD with a DMS quantum well at 4.2K, without and with an external magnetic field of 6 T applied parallel to the growth direction. The magnetic field splits the resonance into two peaks, which is interpreted as resonant tunneling through the two spin sublevels in the DMS quantum well .

trix method for typical parameters is on the μV scale, while the measured resonances have a width of several tens of mV. Effects contributing to such a broadening include inhomogeneity of the resonance energy due to well width or alloy fluctuations, the Fermi energy in the emitter, or scattering and breaking of k-conservation.

7.2 Determination of RTD Layer Parameters by High-Resolution X-Ray Diffraction

The current density in semiconductor tunnel devices generally depends exponentially on the barrier thickness and height, because of the corresponding dependence of the tunnel probability (see sections 2.4.2 and 2.4.3). In RTDs the quantum well layer thickness and composition also drastically influence the I-V characteristics, especially the resonance position. Good control over these parameters is therefore vital for reproducible sample fabrication, and the direct determination in final samples is very helpful.

The double barrier structure in an RTD wafer is typically less than 20 nm thick, and is usually embedded in an about 1 µm thick, complex buffer and contact layer structure. The scattering volume of the active layers is therefore comparatively small, and it seems unlikely that an experimental technique like XRD, which integrates over the complete layer structure, can yield useful information on the relevant double barrier parameters. However, the high lattice mismatch of (Zn,Be)Se tunnel barrier layers of

$(a_l - a_{sub})/a_{sub} = -1.6\%$ (for a Be content of 20 %), allows to obtain such information, since it separates the diffraction features of the tunnel barrier layers from those of all other layers (which have a Be content ≤ 10 %).

The procedure described below to extract barrier and quantum well layer parameters of strained RTDs from high-resolution x-ray diffractograms is similar to that presented in [171] for RTDs fabricated in the (In,Ga,Al)As material system on InP substrates.

$\omega - 2\Theta$ Diffractogram of a (Zn,Be)Se Double Barrier Structure

Figure 7.4 shows the $\omega - 2\Theta$ diffraction pattern of two II-VI heterostructures, which both contain few nm thin, highly strained (Zn,Be)Se layers. Curve (a) corresponds to a single, 7.2 nm thin $Zn_{0.77}Be_{0.23}Se$ interlayer, which is sandwiched between about 50 nm thick ZnSe layers (same data as in figure 4.5 (a)). Curve (b) results from a complete II-VI RTD structure with two (Zn,Be)Se tunnel barrier layers, which both have the same nominal composition and thickness as the interlayer in curve (a). In the range $0.8° \lesssim \Delta\Theta \lesssim 2.4°$ curve (a) clearly shows a broad Bragg peak resulting from the (Zn,Be)Se layer. In the same angular range, curve (b) shows a complex beating pattern consisting of at least three individual peaks of identical width. This beating pattern is the result of x-ray interference between the two (Zn,Be)Se tunnel barrier layers in the RTD structure. In the following it is shown that a detailed analysis of this beating pattern can yield accurate information on the tunnel barrier and quantum well thickness and composition in a finished II-VI RTD structure.

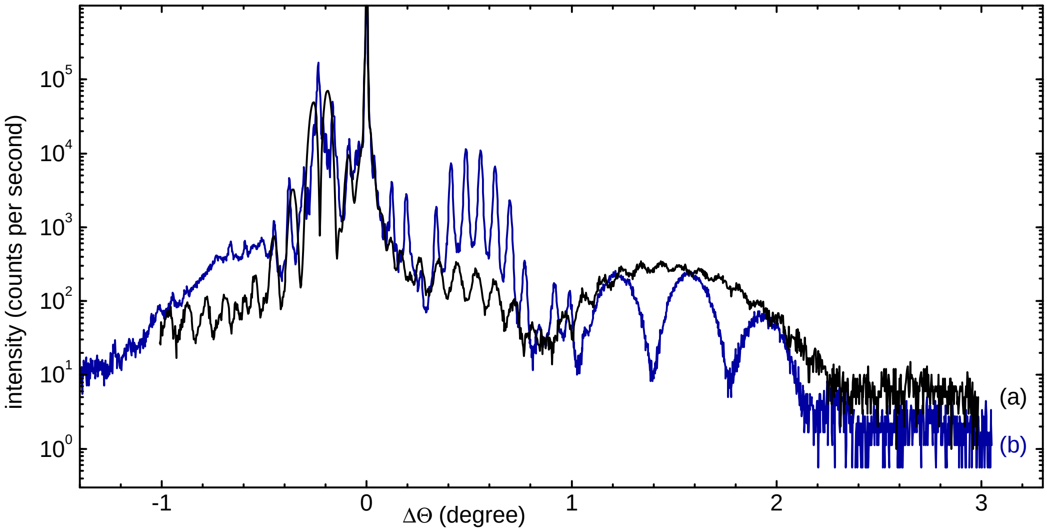

Figure 7.4: $\omega - 2\Theta$ scans of (a) a thin (Zn,Be)Se layer embedded in thick ZnSe cladding layers, and of (b) a complete II-VI RTD structure. The two tunnel barrier layers in (b) are nominally have the same composition and thickness as the single (Zn,Be)Se layer in (a).

Figure 7.5 shows simulated and measured XRD $\omega - 2\Theta$ diffractograms of several strained II-VI double barrier RTD structures. Curve (a1) is a simulated scan for a single, $d_b = 6.6$ nm thick (Zn,Be)Se tunnel barrier layer with a Be content of $x_b = 21\%$ on a GaAs(0 0 1) substrate. Curve (a2) is a simulated scan for a (Zn,Be)Se / (Zn,Mn)Se / (Zn,Be)Se double barrier structure, with the same parameters as (a1) for the (Zn,Be)Se layers.

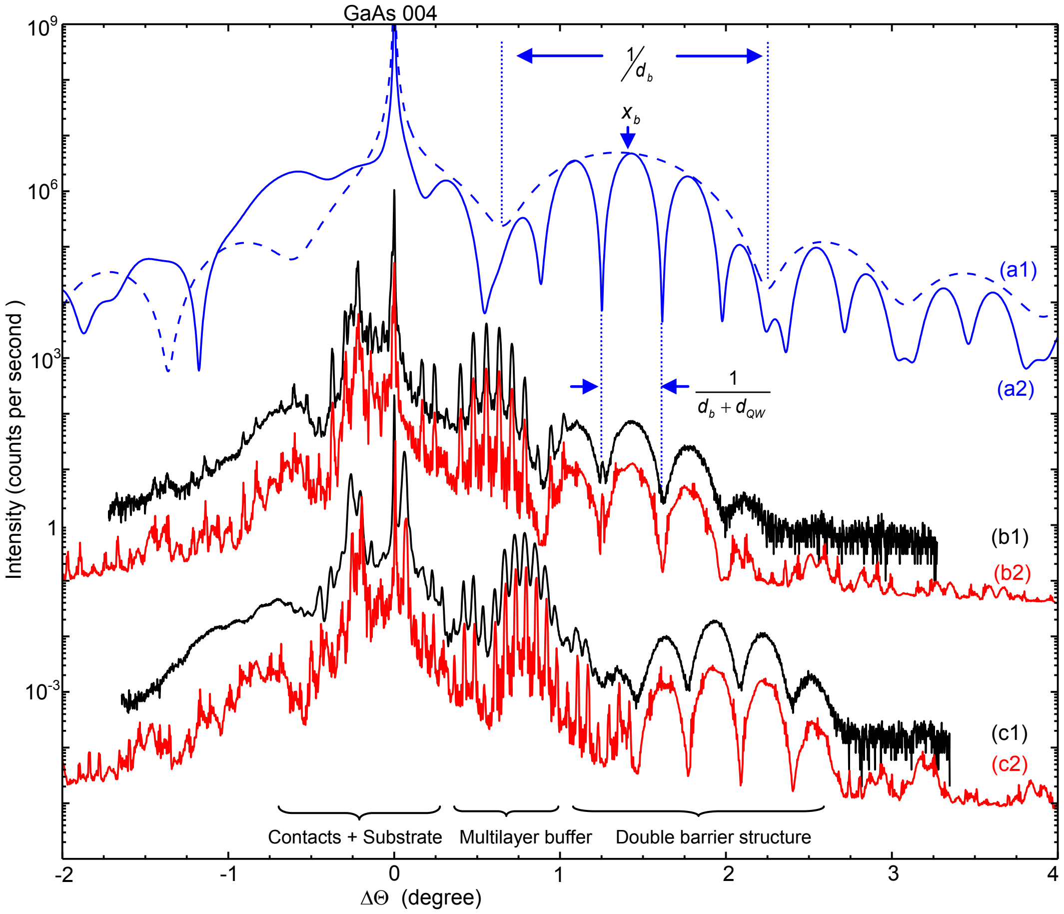

Figure 7.5: Measured and simulated HRXRD $\omega - 2\Theta$ scans of the 004 reflection of strained single and double-barrier II–VI structures. (a1) and (a2) are simulations of a single (Zn,Be)Se layer and a (Zn,Be)Se/(Zn,Mn)Se/(Zn,Be)Se double barrier structure, respectively. x_b and d_b denote the composition and thickness of the barrier layer, x_{QW} is the thickness of the quantum well layer. (b1) is the measured scan of a complete RTD structure including contact- and buffer layers, and (b2) is a fitted simulation. (c1) and (c2) are experimental and simulated scans of another RTD structure, where unintended variations in growth lead to higher x_b and d_b. The curves are shifted for clarity and the intensity scale is that of curve (b1). On the bottom, distinctive features in the diffraction patterns are assigned to different parts of the layer structure.

As is derived analytically by Haase et al. [171], the $\omega - 2\Theta$ diffractogram of a single tunnel barrier layer (a1) forms an envelope, under which that of a symmetric double barrier structure (a2) describes a beating pattern resulting from x-ray interference between the upper and the lower barrier layer. In contrast to the "conventional" x-ray interference described in section 3.2.1, where interference between thick cladding layers separated by a few nm thin spacer layer is observed, here the interfering layers themselves are only a few nm thin.

Since the envelope corresponds to the $\omega - 2\Theta$ diffraction pattern of a single tunnel barrier layer, its peak position and width are given only by the parameters of the tunnel barrier d_b and x_b, as described in section 3.2.1. They are not influenced by the quantum well layer.

The periodicity of the double-barrier beating, i.e. the angular spacing between two consecutive minima $\Theta_{\mathrm{min},i}$ and $\Theta_{\mathrm{min},i+1}$, is related to the sum of d_b and d_{QW} and the X-ray wavelength λ by [171]

$$d_b + d_{QW} = \frac{\lambda}{2\left(\sin\left(\Theta_{\mathrm{min},i+1}\right) - \sin\left(\Theta_{\mathrm{min},i}\right)\right)} \tag{7.1}$$

This relationship is identical to that for the angular spacing of superlattice satellite peaks (eq. 3.7), and in that sense a symmetric double barrier RTD can be thought of as a superlattice with a total thickness of only 1.5 periods. Finally, the angular position of the beating maxima and minima, or the phase of the beating, is influenced by all four double barrier parameters including the composition of the quantum well layer x_{QW}.

Curves (b1) and (c1) of figure 7.5 show $\omega - 2\Theta$ scans recorded on two complete II-VI RTD structures including contact and buffer layers, with nominal structures similar to that sketched in figure 7.1. At low angles $\Delta\Theta \lesssim 1°$ the diffraction patterns are dominated by the nearly lattice matched contact and buffer layers. Throughout the diffraction pattern, but mainly in the range $0.4° \lesssim \Delta\Theta \lesssim 1°$, superlattice reflections from the $5 \times (\mathrm{ZnSe/Zn_{0.9}Be_{0.1}Se})$ multilayer buffer are observed. At higher angles $\Delta\Theta \gtrsim 1°$ the beating from the thin double-barrier structure is clearly resolved. From this beating the layer parameters of the double barrier region can be deduced by the following procedure:

1. The $\omega - 2\Theta$ pattern of a single, strained (Zn,Be)Se layer on GaAs is simulated and is adjusted to the envelope of the recorded double-barrier beating, to obtain starting values for d_b and x_b.
2. From the beating period and from d_b the quantum well width d_{QW} is determined using equation 7.1.
3. The $\omega - 2\Theta$ pattern for a double barrier structure without contact layers is simulated, with the above determined values for d_b, x_b and d_{QW} as input parameters.

By varying also the last remaining parameter, x_{QW}, the simulation is adjusted for best agreement with the measured pattern.

4. The complete layer structure including all contact and buffer layers is simulated iteratively, and the agreement with the experimental pattern is optimized.

This procedure yields the parameters d_b, x_b, d_{QW} and x_{QW} with varying degrees of certainty. d_b and x_b can be considered rather hard parameters, since on the one hand they are deduced from the envelope independently of the quantum well properties, and on the other hand they enter the phase and periodicity of the beating. d_{QW} is less certain, since it is determined indirectly from the beating periodicity and the barrier thickness using eq. 7.1. Finally, x_{QW} cannot be determined unambiguously from HRXRD alone since it only influences the phase of the beating, which is determined only modulo 2π. A direct signal from the quantum well layer is hard to detect in these structures, since it is concealed by the similarly strained contact layers. However, in the low concentration range $x_{\mathrm{QW}} < 0.1$ the band gap of the (Zn,Mn)Se quantum well material is nearly constant due to bowing, and the resonance position and the I-V characteristics are only weakly influenced by the Mn concentration x_{QW}.

The curves (b2) and (c2) represent complete simulations of the two experimental curves (b1) and (c1). For sample (b) the obtained RTD parameters $d_b = 6.6$ nm, $x_b = 21$ %, $d_{\mathrm{QW}} = 8.1$ nm and $x_{\mathrm{QW}} = 8$ % agree well with the intended values. For sample (c) the analysis yields $d_b = 7.0$ nm, $x_b = 28.2$ %, $d_{\mathrm{QW}} = 10.0$ nm and $x_{\mathrm{QW}} = 8$ %. Due to accidental variations in growth conditions the barrier thickness and the beryllium content (corresponding the barrier height) for this sample are both about 20 % larger than intended, which lead to a drastic reduction of the tunneling current by about five orders of magnitude. This underlines the need for independent and direct determination of double barrier layer parameters for such sensitive devices.

As an example, the above analysis is applied to a series of RTDs where one parameter is systematically varied, while the others are kept constant. The series consists of five samples with the quantum well width d_{QW} varied between 5.0 nm and 13.0 nm in steps of 2.0 nm. The other parameters are nominally constant, with $d_b = 6.0$ nm, $x_b = 25\%$, $x_{QW} = 8\%$. In one sample (cb3388) the Be content is nominally lower, $x_b = 20\%$.

Figure 7.6 depicts $\omega - 2\Theta$ scans of the series. At low angles, where the nominally identical contact and buffer layers dominate the pattern, the scans are very similar. At higher angles, all scans show a clear double barrier beating pattern. As expected from eq. 7.1, the angular separation between successive beating maxima decreases with increasing d_{QW}. The position and the width of the beating pattern, however, are not influenced by the variation of the quantum well width. This is consistent with them being given only by the tunnel barrier properties.

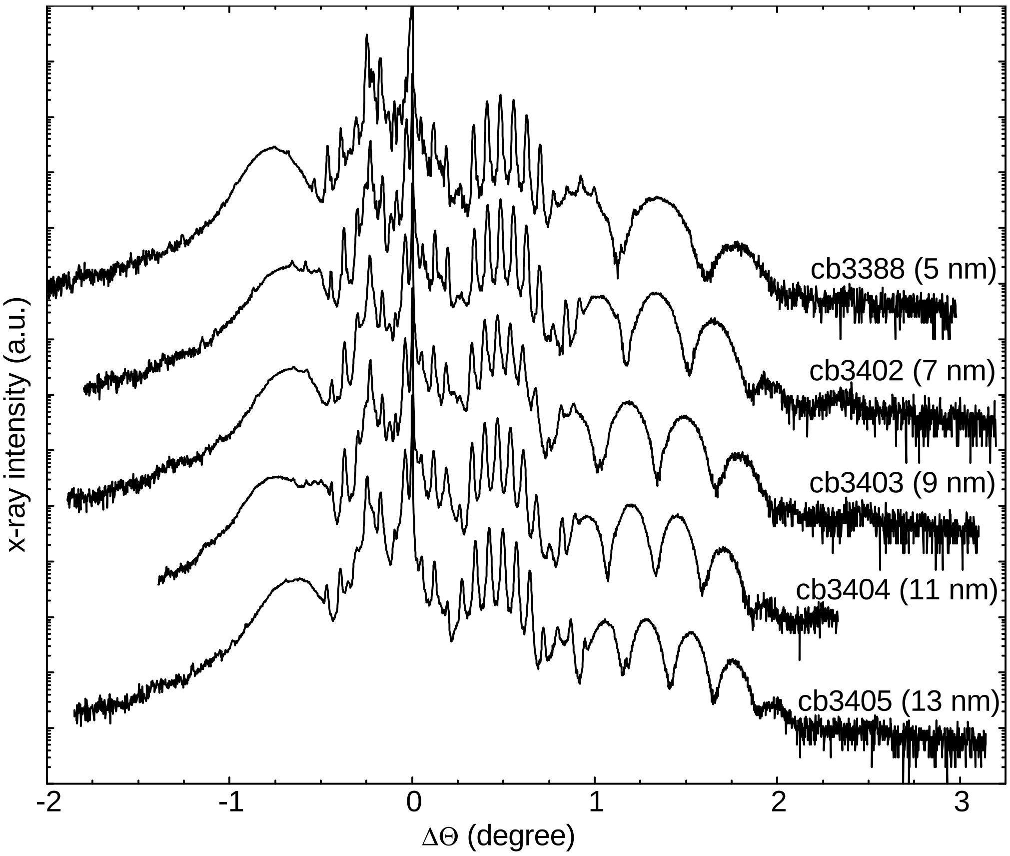

Figure 7.6: HRXRD O-2T scans of RTD wafers with nominal quantum well width between 5 and 13 nm, and nominally similar barrier thickness and barrier and quantum well composition. The QW width is indicated on the right. The curves are offset for clarity.

The results of complete simulations of these scans are summarized in table 7.1 and are compared to the respective nominal values. While there are slight deviations between the nominal and the measured values for d_b, x_b and x_{QW}, there is no systematic variation in these parameters in the series. The systematic increase in d_{QW}, however, is well reflected in the results. For the sample with the lowest d_{QW} the measured value of 5.3 nm is very close to the intended 5.0 nm. For samples with higher d_{QW} the measured values are consistently higher than the intended values by about 10 % to 21 %. Since the measured barrier thickness for these samples is also consistently higher than the intended values, and the Be and Mn concentrations are lower than intended, this suggests that the ZnSe growth rate in these later samples in this series was larger than the calibration value.

Sample	d_b(nm)		d_QW(nm)		x_b(% Be)		x_QW(% Mn)		$d_\mathrm{b} + d_\mathrm{QW}$(nm)	
	nom.	XRD	nom.	XRD	nom.	XRD	nom.	XRD	nom.	XRD
CB3388	6.0	6.0	5.0	5.3	20	18.0	8.0	6.0	11.0	11.2
CB3402	6.0	7.2	7.0	8.5	25	19.3	8.0	7.0	13.0	16.1
CB3403	6.0	6.8	9.0	9.9	25	19.3	8.0	7.0	15.0	16.8
CB3404	6.0	7.3	11.0	12.9	25	19.0	8.0	6.8	17.0	20.5
CB3405	6.0	6.8	13.0	15.2	25	19.3	8.0	6.0	19.0	23.1

Table 7.1: Comparison of the nominal active region parameters of a series of RTD wafers with the values obtained from XRD analysis of grown structures.

Reproducibility of Scans and Homogeneity of RTD Growth

The angular range $\Delta\Theta$ needed for an $\omega - 2\Theta$ scan of a II-VI RTD to cover the full double-barrier beating pattern as well as the contact layer signals, is typically about 4 - 5 °. At such high scan ranges, a small misalignment of the diffractometer at the center of the scan, and thereby a deviation of the scan direction from the $q_{||}$ direction, can have a strong effect at the higher angles. This poses the question of reproducibility of such $\omega 2 - \Theta$ scans.

Figure 7.7 shows three $\omega - 2\Theta$ scans taken at different positions on the same RTD wafer and under different azimuths. The diffractograms are nearly identical, indicating that (1) scans can be taken reproducibly even though a large angular range is scanned, and (2) that growth of double barrier structures is homogeneous in the sampled area. The good reproducibility of these scans indicates that the alignment is sufficiently good. It may also be helped by the relatively wide angle of acceptance of the rocking curve detector optics, which makes it relatively insensitive to small misalignment.

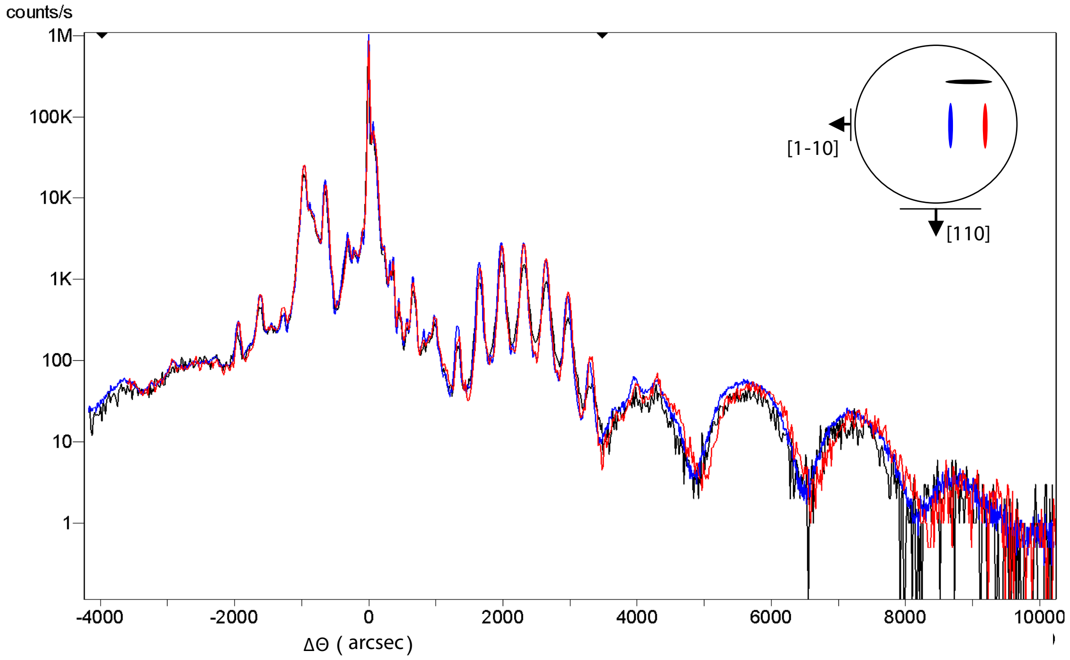

Figure 7.7: XRD $\Omega - 2\Theta$ scans taken at three positions of an RTD wafer (cb3448). The similarity of the scans indicates good homogeneity of the layer growth .

Correlation with Transport Measurements

To validate the above analysis the structural parameters obtained by XRD for different RTD structures are correlated with I-V characteristics. In a simple model describing the background tunneling current at low bias as proportional to the transmission probability in the WKB approximation (equation 2.23), the following dependence on the barrier thickness d_b and height Φ_b is derived

$$I_{V=\mathrm{const}} \propto \exp\left\{-2\sqrt{\frac{2m\Phi_b}{\hbar^2}}\cdot(2d_b)\right\}. \tag{7.2}$$

Here $m = 0.15\ m_0$ is the effective electron mass in ZnSe and $2d_b$ is the total barrier thickness for off-resonance tunneling. The barrier height Φ_b is calculated from x_b using literature values for the (Zn,Be)Se band gap at low temperature and a conduction band offset of $\Delta E_C = 0.7\Delta E_{gap}$

$$\Phi_b = 0.7(1.83x_b + 0.97x_b^2)\ \text{eV}. \tag{7.3}$$

The Fermi energy in the emitter (estimated 10 meV from self-consistent Poisson-Schrödinger calculations) and barrier lowering due to the applied voltage at 40 mV are neglected, since they are both small compared to the typical barrier height of 300 meV.

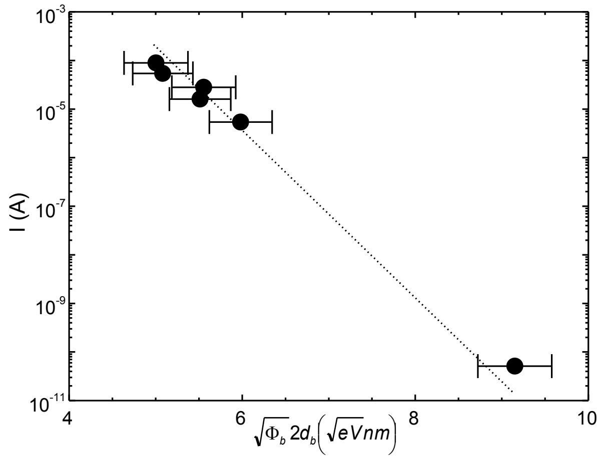

Figure 7.8: Plot of the current I at a fixed bias of 40 mV in the valley regime of several II-VI RTD structures versus the product $\sqrt{\Phi_b}2d_b$, which is calculated from the barrier thickness d_b and composition x_b obtained by HRXRD. The dotted line represents the exponential relationship in equation 7.2.

Figure 7.8 depicts the measured current at a fixed bias voltage of several RTD structures versus the product $\sqrt{\Phi_b}2d_b$, which is calculated from the parameters d_b and x_b obtained by HRXRD. The structures have nominally identical barrier parameters and a quantum well additionally alloyed with Cd to engineer the resonance position to low bias (see section 7.4). The resonance related to the first QW subband is at 15-30 mV in all samples. The background current shown in figure 7.8 is measured at about 40 mV in the valley above the first resonance. The error bars are calculated from estimated uncertainties $\Delta d_b = \pm 0.3$ nm and $\Delta x_b = \pm 1$ %. A grading of Be, Mn or Cd content at the interfaces strongly affects the electrical RTD characteristics but it is not detectable by HRXRD, as long as the depth scale of grading is small compared to the layer widths. A systematic error in the barrier height due to uncertainty in the literature data on the lattice constant, band gap, and band offset in the (Zn,Be)Se system is not included in the error bars, since it should affect all data points in a similar manner.

While most of the nominally identical structures indeed show similar barrier properties and current density, the data point at $\sqrt{\Phi_b}2d_b = 9.2\sqrt{\text{eV}}\text{nm}$ corresponds to a sample where unintentional growth variations lead to a drastic change in current density of six orders of magnitude. Within error bars all data points follow the exponential relationship of Eq. 7.2 (dotted line) and thus it is concluded that HRXRD of complete II–VI RTD structures can II–VI RTD structures can yield valid active region parameters, which determine the electrical and spin transport characteristics of such devices.

To illustrate the effectiveness of such analysis figure 7.9 shows the I–V characteristics of two RTD structures where HRXRD analysis has facilitated an improvement. Curve (a), showing no clear NDR and a large background current, is taken from a sample where the barriers are too thin and low, as determined from HR-XRD. The sample of

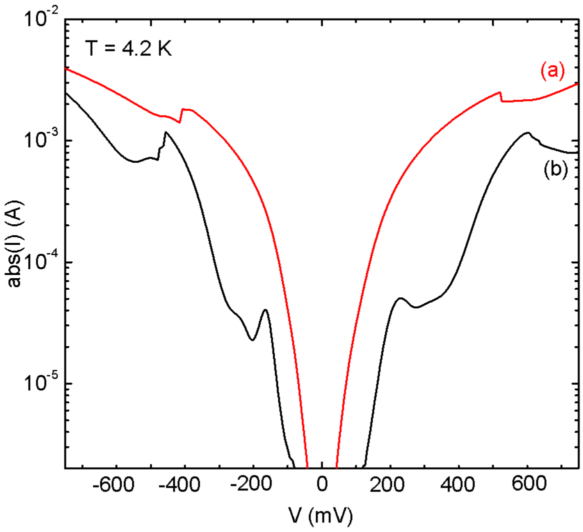

Figure 7.9: Current–voltage characteristics of RTDs with non optimized (a) and optimized (b) barrier parameters.

curve (b) has been fabricated subsequently with the Beryllium content increased by 3% and the barrier thickness increased by 1.6 nm, which leads to clear NDR and a reduced background current.

7.3 RTDs with Varied Quantum Well Width

One of the main characteristics of RTDs are the positions of resonances on the voltage scale. They are influenced by the energy of resonant levels in the quantum well, by the lever arm, i.e. the fraction of the applied voltage which effectively brings the quantized levels into resonance with the emitter, and by emitter properties, such as the doping level and the Fermi energy. The resonance voltage is an important parameter when RTDs are to be fitted with lateral gates to control resonant tunneling transport. Since the voltages which can be applied to such a gate are very limited, e.g. because of gate leakage, the resonant energy levels need to be at relatively low bias.

In this subsection the influence of a variation of the quantum well width d_{QW} on the resonance position of DMS II-VI RTDs is investigated. From simple QM considerations it is expected that a wider d_{QW} lowers the energy of quantized levels and moves them closer together (see section 2.4.3). For this purpose, a series of II-VI RTDs with a systematic variation of d_{QW} is fabricated. The general layer structure of buffer and contact layers is displayed in figure 7.1. The barrier and quantum well thickness and composition determined by HRXRD from the finished samples are listed in table 7.1.

I-V characteristics of the RTD series are shown in figure 7.10. The curves are survey measurements over a large voltage and current range. With the experimental setup

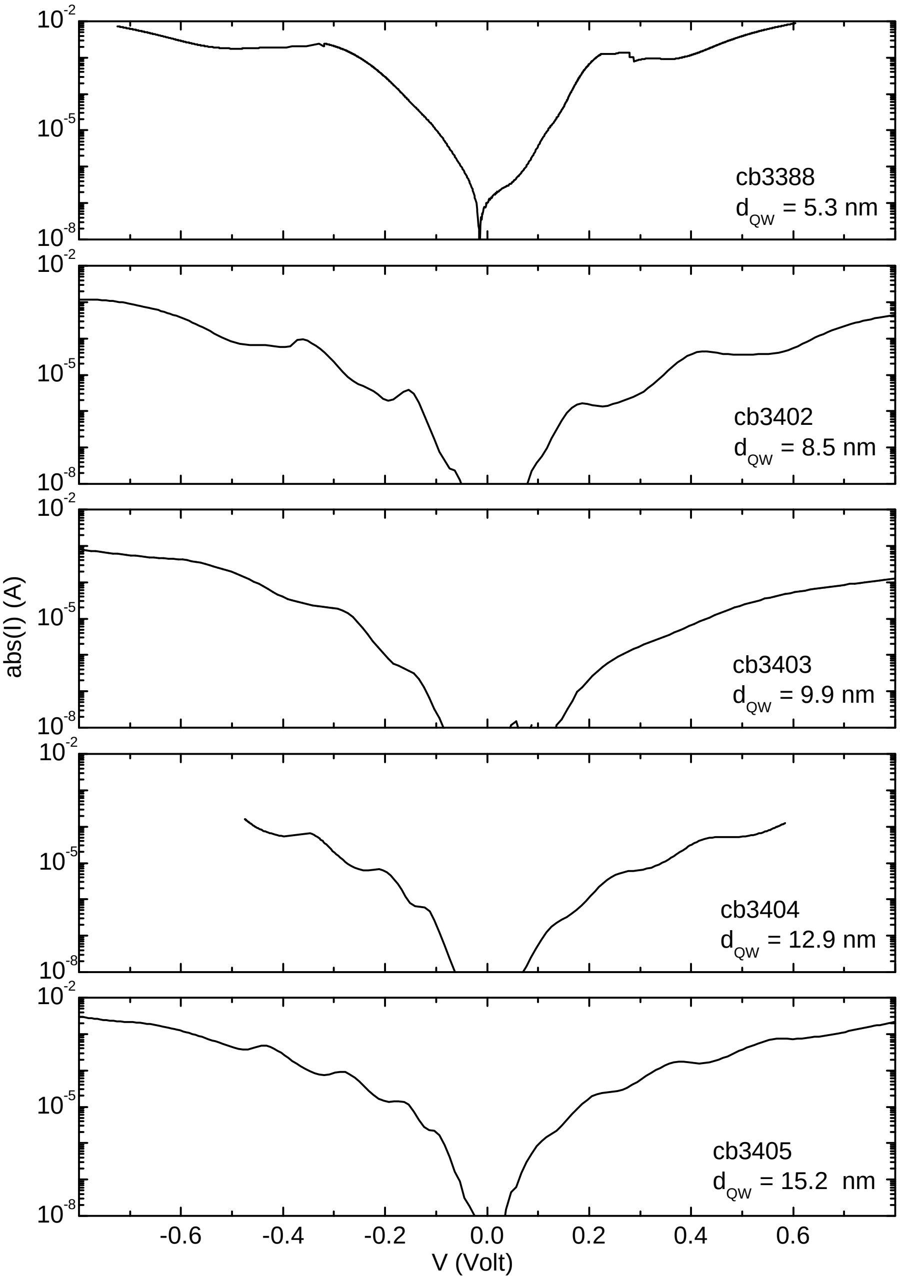

Figure 7.10: Low temperature (4.2K) I-V characteristics of a series of RTDs with varied QW width d_{QW}. The values for d_{QW} determined by XRD for the individual RTD wafers are listed on the right.

only currents higher than about 10nA can be measured with an acceptable signal-to-noise ratio. All RTDs show several resonances, with a PVR as high as 2.0 (sample cb3402). Since not all I-V curves show distinct resonance peaks and valleys, the curves are differentiated with respect to bias voltage to identify resonance positions. It is common practice to define the local minima (maxima) of the second derivative of the current with respect to voltage d^2I/dV^2, as the resonance position in positive (negative) bias direction [172, 173].

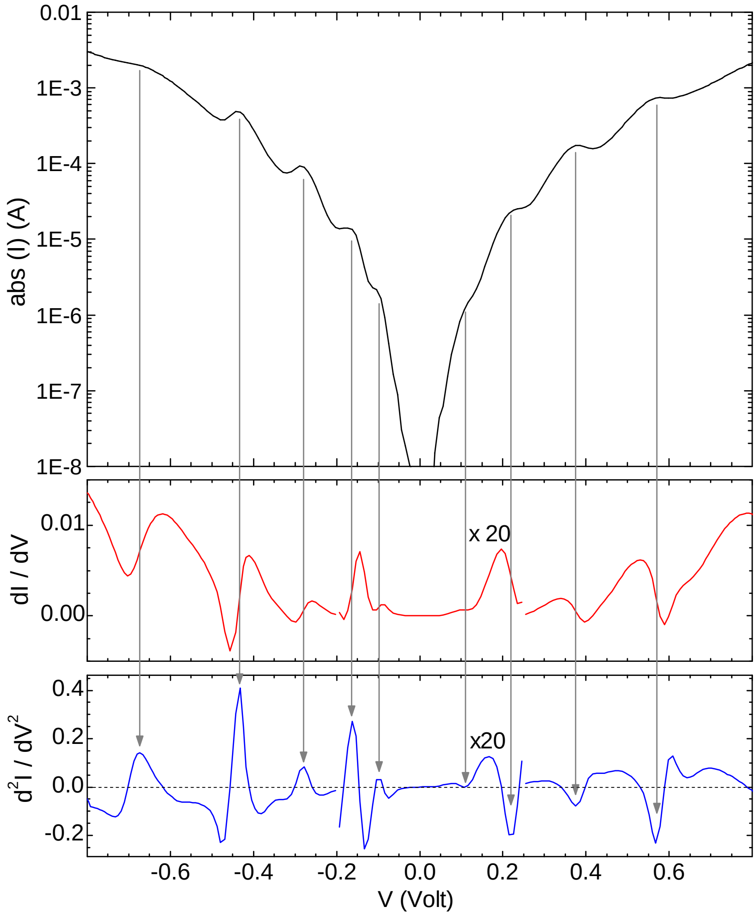

Figure 7.11: Low temperature (4.2 K) I-V characteristics (top), first derivative dI/dV (middle) and second derivative d^2I/dV^2(bottom) of RTD sample cb3405. The main resonances, obtained from the local minima (maxima) of the second derivative for $V > 0$ ($V < 0$), are indicated by arrows. Note that the top panel shows the absolute value of the current $abs(I)$, while the other two show the derivatives of the true current I. The maxima of $abs(I)$ at $V < 0$ correspond to minima of the true current (since $I < 0$), and therefore coincide with maxima of d^2I/dV^2 .

In figure 7.11 the I-V curve and its first two derivatives are shown for the RTD with the highest d_{QW} cb3405. For positive bias there are four distinct local minima in the second derivative d^2I/dV^2 at 0.107 V, 0.220 V, 0.374 V and 0.567 V. They are attributed to resonant electron tunneling through consecutive excited states in the 15.2 nm wide (Zn,Mn)Se quantum well. Another local minimum exists at 0.645 V, which is smaller in magnitude compared to the preceding minimum at 0.567 V. The voltage difference of 77 mV between them translates to an energy difference of 31.2 mV when a typical lever arm of 2.5 is assumed for the sample. This value closely matches the acoustic phonon energy at k=0 in ZnSe, and thus this minimum is attributed to a phonon replica of the preceding resonance.

For negative bias, five resonances are found at -0.098 V, -0.160 V, -0.280 V, and -0.435 V. Compared to the corresponding resonances in positive bias direction, they are at slightly lower bias voltages, and the I-V curve is therefore weakly asymmetric. Since the barrier / quantum well / barrier structure itself is nominally symmetric, this asymmetry has to be either due to the asymmetric emitter and contact structure (see figure 7.1), or to effects related to the MBE growth direction, such as segregation or interdiffusion of Be, Mn or I during growth. At bias voltages of about +0.04 and -0.06 V, features in the $I-V$ and the d^2I/dV^2 curves suggest that there might be further resonances at these voltages. However, the low currents $I \leq 10nA$ in this bias range make it hard to clearly distinguish resonance peaks from current noise with the given experimental setup. Thus at least four (five) resonances are identified in the bias range 0 V to +1 V (0 V to -1 V) for the II-VI RTD with the widest quantum well $d_{QW} = 15.2$ nm.

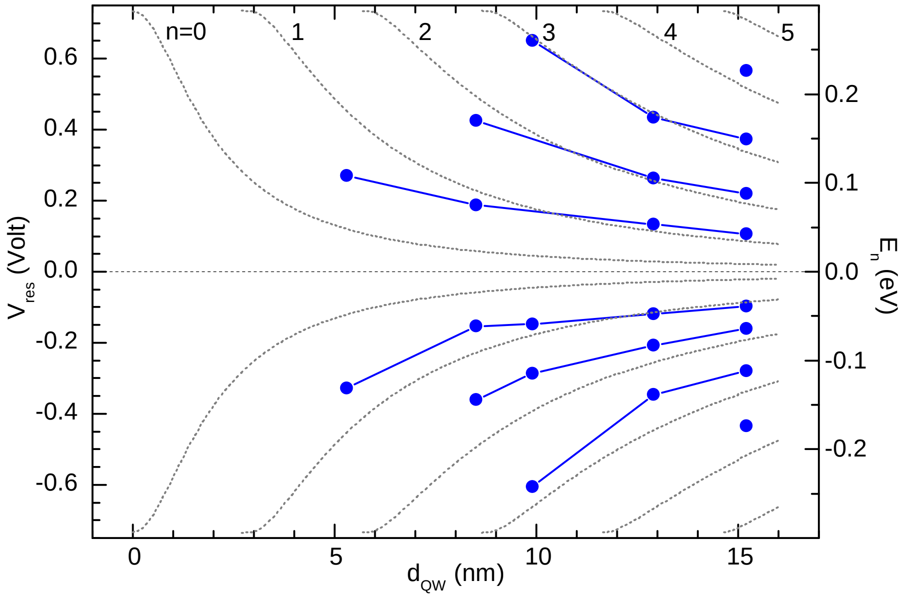

Figure 7.12: Measured resonance voltages V_{res} (dots) of a series of RTDs and calculated bound state energies E_n of a finite quantum well (dotted lines) as a function of the quantum well width d_{QW}. The quantum well width of the RTDs has been determined by XRD (see table 7.1). The energy levels have been calculated for a barrier height of $\Phi_b = 0.293\,eV$ (corresponding to a Be content of $x_{Be} = 19\,\%$), and an effective mass of $m = 0.15\,m_0$. A constant lever arm of 2.5 is assumed to connect the energy axis on the right to the voltage axis on the left. Lines between the symbols are guides to the eye.

The resonance voltages thus obtained from the d^2I/dV^2 characteristics for all RTDs of the series are plotted in figure 7.12 as a function of the quantum well width measured by

XRD. As expected, increasing d_{QW} decreases resonance voltages monotonically, and leads to a reduction of the voltage separation between subsequent resonance levels. The first resonance that could be clearly resolved for positive (negative) bias is shifted from +0.270 V (-0.329 V) down to +0.107 V (-0.098 V), as d_{QW} is increased from 5.2 nm to 15.2 nm. The number of resonances in the bias range 0 V to +1 V (0 V to -1 V) increases from 1 to four (five).

To compare this data to a simple quantum mechanical model, the energy levels $E_n$calculated for a finite quantum well with the barrier height $\Phi_b = 0.293\,eV$ and effective mass $m = 0.15\ m_0$are plotted as a function of the d_{QW} in the same graph (figure 7.12).

To relate the calculated bound-state energies E_n to the bias voltage V of the measured resonances, a constant lever arm $l = V/E_n = 2.5$ is assumed. Such a lever arm is typically measured for the fabricated RTDs from the voltage separation between main resonances and LO phonon replicas. The used barrier height corresponds to the conduction band barrier for (Zn,Be)Se tunnel barriers with a Be content $x_b 19\,\%$, which is measured by XRD for most of the structures (compare table 7.1). Band-bending and series resistance effects are included indirectly via the lever arm. The finite thickness of tunnel barriers is neglected in the calculations, since the barriers should be sufficiently high and thick that leakage of the wavefunctions does not influence the energetic position of the quantized levels (compare figure 2.8). Increasing inclination of the initially symmetric band profile with bias voltage, and the resulting variation of the transmission characteristics and energy levels of quasi-bound states is another effect which had to be neglected in this simple model.

The calculated QW energy levels for $n \geq 1$ agree fairly well with measured resonance positions. Considering the simplicity of the model, the agreement is surprisingly good. However, in the vicinity of the lowest calculated energy level $n = 0$ no clear resonances could be observed.

Close examination of the I-V characteristics in figure 7.10 shows small features in the voltage range below ±0.1V, especially for samples cb3388, cb3402 and cb3405. These features indicate that there may be possible further resonances corresponding to n = 0. However, since they do not show up as clear peaks in the d^2I/dV^2 curves, and since they are close to the current resolution of the used setup, they are not regarded as clear resonances in this work. A more precise measurement of the I-V characteristics in the positive and negative low bias range is required to clarify whether these features are resonances or noise, and thus whether the agreement between model and theory also includes the n = 0 states.

The assumption of the lever arm being constant over a large bias range may be an oversimplification, since the underlying effects of charge accumulation and depletion in the emitter and collector layers are not necessarily linear in their voltage dependence. However, even for the higher excited states even at bias voltages over 0.5 V, the agreement between measured and modeled resonance positions is surprisingly close.

In conclusion, in this section the dependence of resonance positions of II-VI RTDs on the quantum well width has been investigated. Increasing d_{QW} clearly shifts all resonances to lower bias voltage and moves them closer together. The resonance voltages can be modeled to surprising accuracy by a simple, finite quantum well model, including a lever arm $l = V/E_n = 2.5$ which is independent of bias voltage.

7.4 RTDs with Cd in the Quantum Well

In this section the fabrication and the electrical and optical properties of II-VI double barrier RTDs with Cd added to the central DMS quantum well are described. Cd reduces the band gap of the quantum well (see figure 2.2), and should thus shift quantized levels to lower energy, and consequentially, current resonances to lower bias voltage.

Table 7.2 summarizes the nominal and measured (XRD) structural parameters of four selected RTDs with a $Zn_{1-x-y}Mn_xCd_ySe$ quantum well. The general growth recipe, and the emitter and contact structure are the same as those used for other RTDs in this work (see figure 7.1). The barrier thickness d_b, its composition x_b, the quantum well thickness d_{QW} and and the Mn content in the quantum well x are kept constant. Since the composition of the quaternary quantum well cannot be uniquely determined by XRD alone, only the nominal Cd and Mn concentrations are given in table 7.2 . There is a minor deviation between the nominal values and the values determined by XRD for some parameters. Since there is no systematic trend within the series, these deviations are neglected in the following analysis.

To add different amounts of Cd to the quantum well, the Cd effusion cell temperature is varied to yield different Cd BEPs. The Cd concentration in the RTDs thus obtained is calibrated by comparing the employed BEP to reference samples containing thick $\mathrm{Zn}_{1-x-y}\mathrm{Mn}_x\mathrm{Cd}_y\mathrm{Se}$ epilayers, the composition of which is determined by XRD and PL.

The I-V characteristics of this series measured at 4.2 K are shown in figure 7.13. Limited electric transport data only allows to analyze the first resonance at negative

Sample	d_b (nm)		x_b (% Be)		d_{QW} (nm)		x (% Mn)	y (% Cd)
	nom.	XRD	nom.	XRD	nom.	XRD	nom.	nom.
cb3418	6.0	6.0	25	21.5	7.2	7.5	8	0.0
cb3437	6.0	5.9	25	21.5	7.2	8.1	8	2.9
cb3436	6.0	5.5	25	22.0	7.2	7.2	8	5.9
cb3461	6.0	5.6	25	21.1	7.2	7.5	8	7.1

Table 7.2: Nominal (nom.) and measured (XRD) structural parameters of a series of RTDs with varied concentrations of Cd in the $\mathrm{Zn}_{1-x-y}\mathrm{Mn}_x\mathrm{Cd}_y\mathrm{Se}$ quantum well.

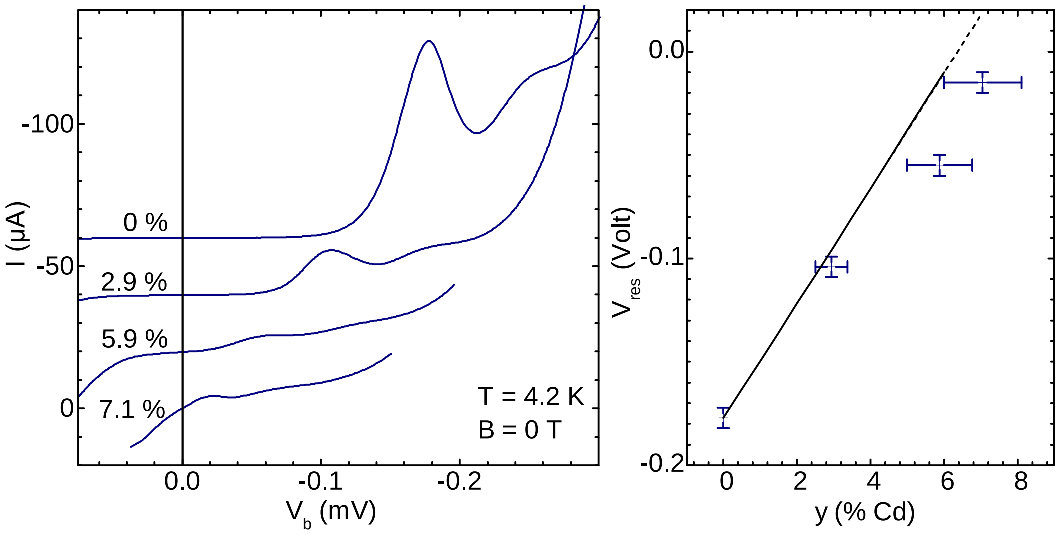

Figure 7.13: Left: low temperature (4.2 K) I-V curves of a series of RTDs with varied concentration of Cd in the quantum well. The curves are offset for clarity. Right: voltage V of the first current peak as a function of Cd concentration y (crosses), and the variation of the peak voltage with y calculated from equation 7.4 (black line). For $V_{res} < 0$ resonances can't be observed, hence the dashed extension.

bias in detail. Other resonances, as far as transport data is available, show similar behavior. For 0 % Cd a first resonance peak appears at 0.177 V, with a PVR of 1.88. A second peak attributed to an LO phonon replica of this resonance is seen at 0.248 V, yielding a lever arm of 2.3. The same lever arm is also obtained from the first resonance at 2.9 % Cd. With increasing Cd content the resonance is monotonically shifted to lower bias voltages, down to about 0.015 V for 7.1 % Cd. Concomitant to the reduction of the resonance voltage, the PVR as well as the peak current are reduced by the addition of Cd. Since the emitter and the double-barrier structure are optimized for a high PVR for resonances at high bias, their parameters are not necessarily optimal for the lower bias resonances. A lower PVR is thus not surprising.

The peak voltage V_{res} obtained from the extrema of the second derivative d^2I/dV^2 is plotted on the right in figure 7.13 as a function of the Cd concentration. The error bars are based on an estimated uncertainty of 15 % for the Cd concentration (mainly due to the BEP measurements) and 5 mV uncertainty of the peak position. For comparison, the variation of the peak voltage due to the variation of the band gap (black line) is calculated by the following semi-empirical model equation

$$V(y) = V_{\mathrm{res}}(0) - 0.84 \cdot l \cdot (E^{\Gamma}_{\mathrm{g,ZnSe}} - E^{\Gamma}_{\mathrm{g,ZnCdSe}}(y)). \tag{7.4}$$

Here $V_{\mathrm{res}}(0)$ is the measured resonance voltage for 0 % Cd, $l = 2.3$ is the lever arm measured for 0 % (and for 2.9 % Cd), the factor 0.84 corresponds to the fraction of the band offset between ZnSe and (Zn,Cd)Se occurring in the conduction band (see section

2.1), and $E^{\Gamma}_{\mathrm{g,ZnSe}}$ and $E^{\Gamma}_{\mathrm{g,ZnCdSe}}$ are the literature values for the band gaps of ZnSe and (Zn,Cd)Se, respectively (see section 2.1). This simple model neglects differences in the quantum confinement energy due to different barrier heights, effects of Cd on the effective mass in (Zn,Mn)Se, and a variation of the lever arm. Within error bars the model describes the peak voltage for these RTDs reasonably well, with a trend of underestimating the voltage for higher Cd concentrations. One possible explanation for this deviation shall be given in the following.

Since only the band gap in the quantum well is reduced and that of the emitter layers stays constant, the quasi bound states in the quantum well can drop below the Fermi level for high Cd concentrations. In that case electrons are permanently transferred from the emitter layers to the quantum well, leading to charge accumulation and increasing the potential energy of electrons in the quantum well. This potential increase partially compensates the energetic reduction of the quasi-bound levels caused by the addition of Cd. As a result, the variation of the quantum well subband energy with Cd content is smaller when the first level is below the Fermi level compared to above the Fermi level.

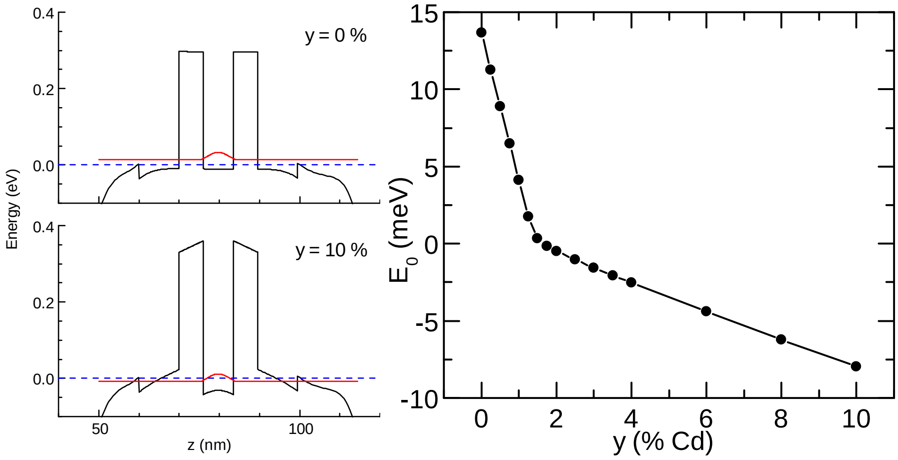

Figure 7.14: Left: Self-consistently calculated conduction band profiles (black solid line) and first quasi-bound state (squared wavefunction, red solid lines) for $\mathrm{Zn_{0.785}Be_{0.215}Se}$ / $\mathrm{Zn_{0.98-\mathit{y}}Mn_{0.08}Cd_{\mathit{x}}Se}$ /$\mathrm{Zn_{0.785}Be_{0.215}Se}$ RTDs with y = 0 % and 10 % Cd. The energy is given relative to the calculated Fermi energy E_F (blue dashed lines). Right: Energy E_0 of the first quasi-bound state as a function of the Cd content y. The energy is given relative to the Fermi energy E_F . Note the change in slope that occurs when E_0crosses the Fermi energy.

This effect is illustrated in figure 7.14, which shows the self-consistently calculated first quasi bound state in 6 nm $\mathrm{Zn_{0.785}Be_{0.215}Se}$ / 7 nm $\mathrm{Zn_{0.98-\mathit{y}}Mn_{0.08}Cd_{\mathit{x}}Se}$ / 6 nm $\mathrm{Zn_{0.785}Be_{0.215}Se}$ double barrier RTDs at zero bias as a function of the Cd content in the quantum well. For low Cd concentrations, when E_0 is above E_F, the variation of E_0 mainly follows the change of the band gap. When E_0 is below E_F, the slope is reduced by the partial compensation of the reduction of the band gap by charge accumulation. Such a change in slope in principle can explain the relatively high resonance voltages observed for y $>$ 2.9 %, but it can be hardly confirmed due to the limited number of data points (figure 7.13). Since the structures simulated in figure 7.14 contain heavily doped, degenerate layers, a quantitative evaluation of the results should be taken with care. They are shown here merely to qualitatively illustrate the effect of charge transfer into the QW.

Another characteristic of the I-V curves, which is related to the shift of the resonance, is the differential resistance $R_{\mathrm{diff}} = 1/(dI/dV)$ in the vicinity of 0 V bias. The values for R_{diff} obtained from a linear fit to the I-V curves in the range -5 mV to + 5 mV are listed in the following table.

y (% Cd)	R_{diff}
0	$> 2\ M\Omega$
2.9	435 $k\Omega$
5.9	36 $k\Omega$
7.1	3.6 $k\Omega$

While for the RTD without Cd only a lower limit of the resistance of 2 $M\Omega$ can be given, it decreases monotonically down to about 3.6 $k\Omega$ for the highest Cd content of 7.1 %. This low resistance, together with the ohmic nature of the I-V curve in a relatively broad voltage range nearly up to the first current peak, supports the claim that the resonant energy level for the highest Cd concentration is already below the Fermi energy.

Since the purpose of II-VI RTDs in the context of this work is their potential use as voltage controlled spin filters, figure 7.15 shows the I-V characteristics at external magnetic fields 0 T and 6 T of another RTD with 7.6 % Cd and 8 % Mn in the quantum well (sample cb3451). While for RTDs with higher resonance voltages the resonance usually splits into two peaks in an external magnetic field, as shown in figure 7.3, which are attributed to the two spin channels, the resonance in figure 7.15 appears to shift only to higher energies. This can be understood considering that the external magnetic field shifts the energetically lower spin level to below the bottom of the energy spectrum of electrons in the emitter. Thereby it removes its availability for resonant tunneling. The disappearance of one spin channel may also explain the slightly decreased background current at non-resonant bias voltages, as well as the reduction of R_{diff} around 0 V bias by more than a factor of 2.

As a complementary method of analysis, the RTDs of the present series have also been investigated by photoluminescence spectroscopy. The most interesting signal here is that of carrier recombination in the DMS quantum well, since on the one hand it allows to further characterize the electronic properties of the grown quantum well heterostructures, and on the other hand it may allow to access the resonant energy level optically also during electric transport experiments.

Figure 7.16 depicts low temperature (T $<$ 13 K) PL spectra taken of the RTDs of

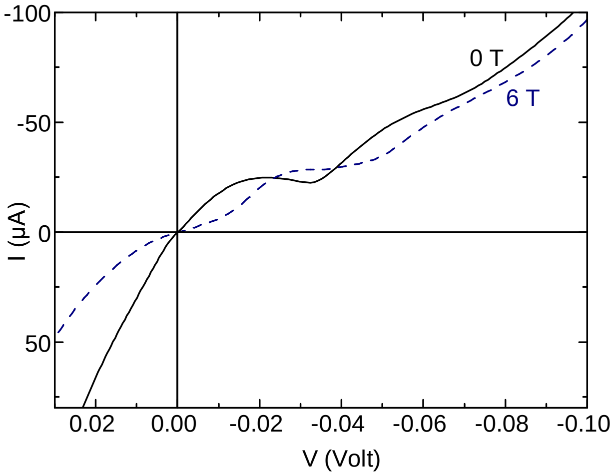

Figure 7.15: Low temperature (4.2K) I-V curves at B = 0 T (black solid line) and B = 6 T (blue dashed line) of an RTD with 7.6 % Cd in the quantum well (cb3451).

this series. They are measured on pieces of the RTD wafers different from those used for transport experiments, and from which the in-situ metal layer had been removed wet chemically. The excitation energy is either 3.05 eV or 2.88 eV - both are above the band gap of the ZnSe and $Zn_{0.97}Be_{0.03}Se$ contact layers and below that of the tunnel barrier material. In the range between 2.795 eV and 2.805 eV all spectra show a conglomerate of one or more, several meV wide luminescence peaks. Based on their energetic position and on the observation that they change only slightly in moderate magnetic fields (compare spectra of sample 7.1 % Cd), they are attributed to neutral or charged excitons bound to different impurities in ZnSe [35]. The distribution of spectral weight between these luminescence lines varies with the Cd content of the samples.

Besides this ZnSe related luminescence, most spectra show another luminescence line (marked by arrow) in the displayed energy range, which depends on the Cd content in the quantum well. For 0 % Cd a small peak at 2.840 eV is found, which is absent in the other spectra. For 5.9 % and 7.1 % Cd strong peaks appear at 2.759 eV and 2.729 eV, respectively. For the sample with 2.9 % Cd no additional luminescence peak is observed. The fact that these lines appear at successively lower energy with increasing Cd content suggests that they are related to carrier recombination in the (Zn,Mn,Cd)Se quantum well. To prove this, magneto-PL spectra are recorded for the samples with 0 % and 7.1 % Cd in magnetic fields up to 6 T. The magneto-PL spectra at 2 T, 4 T, and 6 T of the 7.1 % sample are shown in the lower part of figure 7.16. While the luminescence line previously attributed to ZnSe is only marginally influenced by the magnetic field, the additional line in question is clearly shifted to lower energies by the magnetic field. It follows a Brillouin-like function up to $\Delta E = -45\ meV$ for 6 T. For the 0 % sample a similar shift is observed for the peak at 2.840 eV. This large, Brillouin-like reduction of the luminescence energy is a clear indication that the peaks

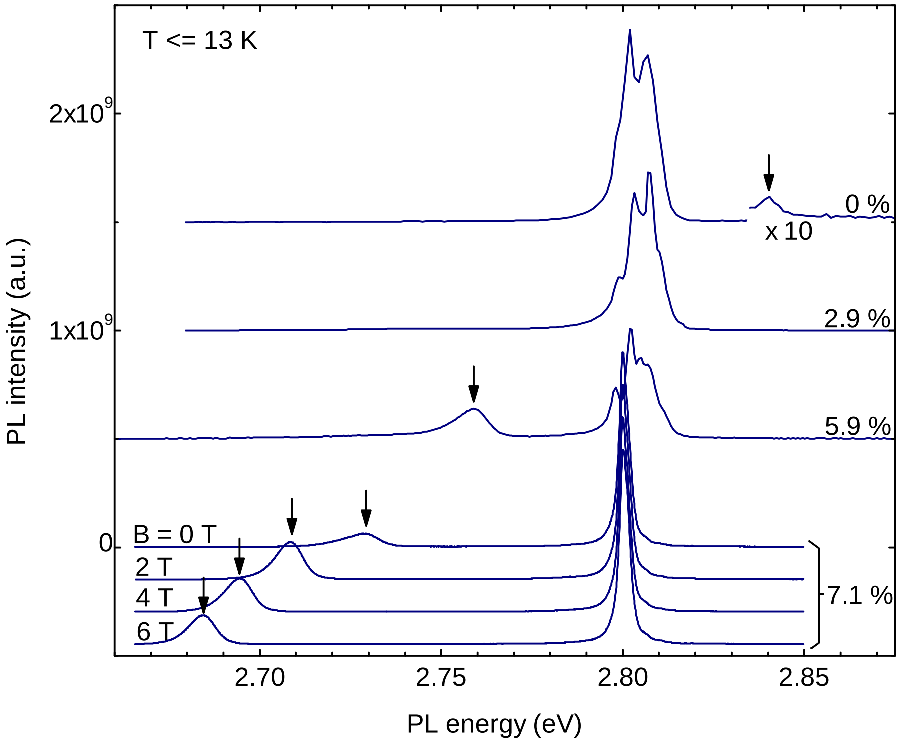

Figure 7.16: Low temperature PL spectra of a series of RTDs with a $Zn_{1-x-y}Mn_xCd_ySe$ quantum well with varied concentrations of Cd. The luminescence lines attributed to carrier recombination in the $Zn_{1-x-y}Mn_xCd_ySe$ quantum well are marked by arrows. Unless indicated otherwise on the left, the spectra are taken without an applied magnetic field. The excitation energy is 3.05 eV for the samples with 0 % to 5.9 % Cd, and 2.88 eV for the sample with 7.1 % Cd. The QW luminescence line of the latter is not influenced by this change of excitation energy.

result from carrier recombination in the DMS quantum well of the RTDs (compare subsection 2.2).

Figure 7.17 shows the energy of the quantum well luminescence as a function of the Cd content. The horizontal error bars are based on an estimated uncertainty of 15 % for the Cd content, and the vertical ones correspond to the FWHM of the PL peaks. For the sample with 2.9 % Cd the center of the ZnSe peak presumed to conceal the quantum well luminescence is taken as the peak position, and the error bar spans the FWHM of this broad luminescence line. Also plotted in figure 7.17 is the direct band gap E_g^Γ of $Zn_{0.92-y}Mn_{0.08}Cd_ySe$, which has been calculated from literature values for the (Zn,Mn)Se and the (Zn,Cd)Se band gap by linear interpolation (see table 2.2). To fully reproduce the measured data the exciton binding energy in the quantum well, quantum confinement of electrons and holes, strain effects and possible many-particle effects due to the presence of a 2DEG in the quantum well, would all have to be treated correctly, which goes beyond the scope of this work. However, it is clear that the PL

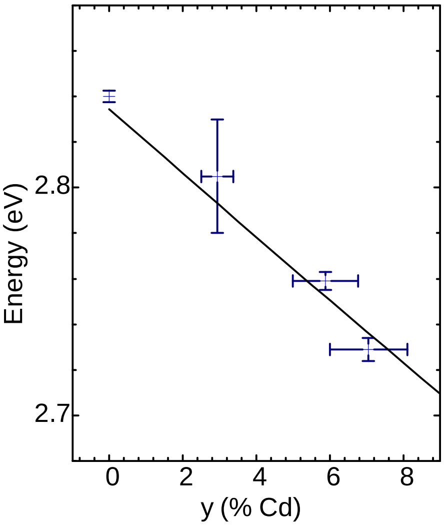

Figure 7.17: Peak energy of the quantum well luminescence line of RTDs with a $Zn_{0.92-y}Mn_{0.08}Cd_ySe$ quantum well as a function of the Cd concentration y (crosses). The solid black line represents the literature value of the band gap of $Zn_{0.92-y}Mn_{0.08}Cd_ySe$ (table 2.2).

peak energy goes parallel to the variation of the (Zn,Mn,Cd)Se band gap over a large energy range of over 0.1 eV. This substantiates the notion that the peak emanates from the (Zn,Mn,Cd)Se quantum well. The data points for 0 %, 2.9 % and 5.9 % Cd lie less than about 5 - 10 meV higher than the corresponding (Zn,Mn,Cd)Se band gap value. This can be due e.g. to quantum confinement (which is about 30 meV for electrons and heavy holes combined) or due to the compressive strain of the quantum well layer.

The observation of a photoluminescence signal emanating from the quantum well of a DMS RTD is quite interesting from several perspectives. First of all, the width of the PL peak allows to judge the quality and homogeneity of the quantum well. For 0 % Cd the QW PL linewidth is about 6.4 meV, while for 5.9 % it is 10 meV and for 7.1 % it is 11 meV. Thickness fluctuations of 1 ML of a finite quantum well corresponding to sample cb3461 can be calculated to lead to a minimal PL peak width of 4.6 meV (similar to [174]). Since the incorporation of Cd to the quantum well introduces additional inhomogeneity, a higher luminescence linewidth is expected for RTDs with Cd compared to the RTD without Cd. Altogether, a PL line width of up to 11 meV indicates very good homogeneity of layer thickness, composition and interface abruptness of the quaternary, diluted magnetic quantum wells.

Secondly, a luminescence signal from the quantum well opens up the possibility of optically influencing or probing the resonant energy level during resonant tunneling transport. Combined optical and electric transport experiments on the same sample, similar to Ref. [175], could yield information about the dynamics of charge and spin transport by resonant tunneling.

In summary, in this section MBE growth and the electrical and optical properties of II-VI DMS RTDs with up to 7.1 % Cd admixed to the quantum well has been discussed. The addition of Cd to the quantum well in the studied series results in a reduction of resonance position from 0.177 V for 0 % to about 15 meV for 7.1 %, and an accompanying reduction of the PVR. The reduction of resonance bias can be understood based on the variation of the quantum well band gap weighted with the conduction band offset and a constant lever arm of 2.3. A lower PVR can be explained since the emitter and barrier layers are not optimized for lower bias resonances. For Cd contents higher than 5.9 % in the quantum well, a clear photoluminescence signal could be observed due to carrier recombination in the main (Zn,Mn,Cd)Se quantum well. From the PL peak width good structural and compositional quality of the grown heterostructures can be inferred. Additionally, such RTDs may allow for simultaneous transport and optical experiments, in which spin and charge level in the QW are influenced optically.

7.5 Resonant Tunneling through Self-Assembled CdSe QDs

This section describes the growth and properties of II-VI RTDs which contain a layer of self-assembled CdSe quantum dots instead of a quantum well. The 0D quasi-bound states associated with self-assembled QDs are an alternative way to study 0D resonant tunneling in a DMS environment, which does not need an electrostatic gate for lateral confinement.

The layer structure of such a QD RTD is shown in figure 7.18. The buffer and contact layer structure is identical to that of the previously described quantum well RTDs, including the emitter and collector design with shallow pre-wells. Since the incorporation of Mn into self-assembled CdSe QDs is difficult to control, and since this work is intended to reproduce and further explore the results in [11], Mn is inserted in the tunnel barrier material.

The CdSe coverage is chosen with the aim of making the dots large enough to provide sufficient lateral localization, while at the same trying to keep the electron ground state energy in the majority of the QDs above the Fermi level. If the coverage is too small, the resulting layer is merely a relatively flat and homogeneous wetting layer, with only weak lateral localization. On the other hand, if the coverage is too high, many QDs will have energy levels at or below E_F. Many of those will then be in resonance at low bias voltages, making it hard to distinguish their resonance peaks in I-V curves. The PL studies of section 4.5 are used as a rough guide to judge the QD properties, and a coverage of 1 ML has been selected for the present structures. It was calibrated using x-ray interference measurements on ZnSe / CdSe / ZnSe calibration samples, as described (see section 3.2.1).

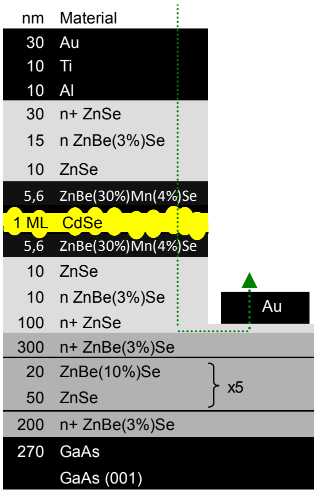

Figure 7.18: Typical layer structure of a dilute magnetic II-VI RTD with self assembled CdSe QDs.

The pillar size of a processed RTD is about $100 \times 100\ \mu m^2$. Using the island density of $10^{10} - 10^{11}$ cm^{-2} measured by AFM (section 4.5) for the density of QDs, about $10^6 - 10^7$ QDs are expected per RTD pillar. Even though there are many QDs in one RTD pillar, transport is still expected to be dominated by the largest QDs, since those are tuned into resonance first at low bias voltages and since they form weak spots in the tunnel barriers (see [21] and refs. therein).

In the following paragraphs the I-V characteristics of a nonmagnetic and a dilute magnetic QD RTD are shown and briefly discussed. Both show clear peaks due to 0D resonant tunneling. The magnetic RTD additionally shows a large splitting of the resonance peaks in an applied magnetic field, indicative of pronounced s-d interaction induced effects on the tunneling process.

Nonmagnetic QD RTD Figure 7.19 shows I-V characteristics of the nonmagnetic QD RTD. Its nominal structure is that depicted in figure 7.18, but no Mn is included in the tunnel barriers. The characteristics are measured at a temperature of 4.2 K and with magnetic fields $0\,\mathrm{T} \leq B \leq 6$ T applied parallel to the growth direction. Other mesa diodes processed from the same wafer show qualitatively similar characteristics, but the details of the curves are individual to each mesa.

First the I-V curve at 0 T shall be discussed. Around 0 V bias the current is negligible, which indicates that no quantized level is available for resonant tunneling at low bias. At 12 mV and 33 mV bias two distinct resonance peaks occur, with a peak current of about 200 pA and a FWHM of about 3 mV. Before and after the peaks the current is nearly constant (excluding some fine structure), with the current after the peak being about 100 pA higher than before. The current increase above 40 mV is probably due to further QDs coming into resonance, and possibly also due to tunneling through

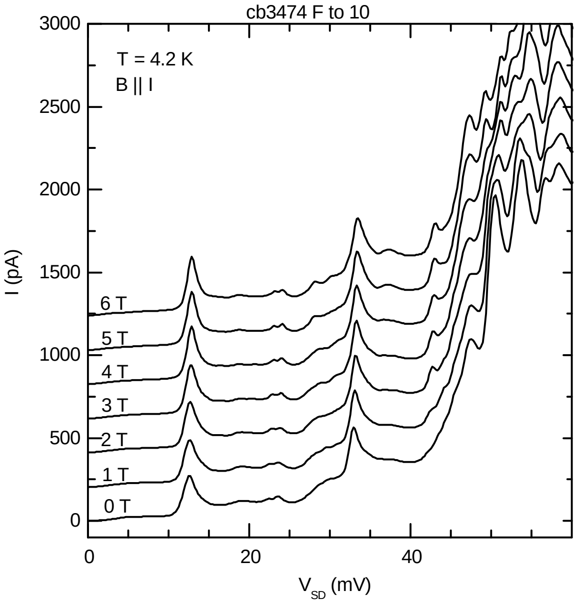

Figure 7.19: Low-temperature (4.2 K) I-V curves of an RTD with self-assembled CdSe QDs without Mn (sample cb3474) in magnetic fields from 0 to 6 Tesla.

excited states in the QDs already responsible for the lower bias resonances.

The peaks and the current plateaus can be understood qualitatively as described in section 2.4.3 (see page 32). Each peak marks the onset of resonant tunneling via a quasi-bound state in a single QD. When such a level becomes aligned with the Fermi energy E_F in the emitter, the current is strongly enhanced by a Fermi-edge-singularity, causing a sharp current peak [67, 21]. When the bias voltage is increased further, the resonant level is reduced, but as long as it is on the same energy level as occupied states in the emitter, electrons tunnel through the QD one at a time. The current is then approximately constant, with a slight increase possibly due to the deformation of the barrier by the applied voltage. In this single electron transport regime, the time it takes for one electron to travel through the double barrier structure can be calculated from the magnitude of the current step ΔI at a resonance. With $\tau = e/\Delta I$ and $\Delta I \approx 70$ pA we get a transit time of $\tau \approx 2.5$ ns. For comparison, Geim et al. calculate a transit time of 2 ns for single electron transport through their 0D RTD structure [67]. Assuming that transport is limited by the lifetime of an electron in the resonant state [1], Geim et al. estimate the intrinsic linewidth ΔE of the resonant state from the uncertainty principle $\Delta E \cdot \tau \approx \hbar$. Doing this for the present data yields a linewidth $\Delta E \approx 2.6 \times 10^{-7}$ eV, or 3 mK.

When the QD level drops below the lowest subband in the emitter, the current is expected to drop to zero. Such a drop is not observed here, probably since another

---

[1] Other effects, such as a finite attempt frequency of electrons in the emitter, are negelected

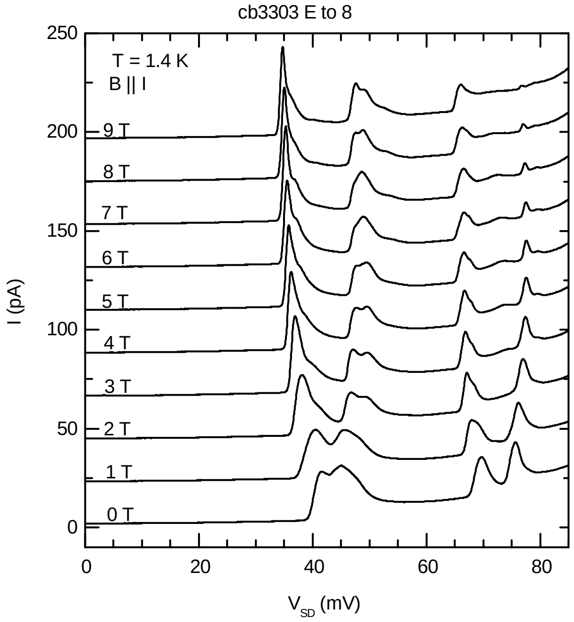

Figure 7.20: I-V curves of an RTD with 1 ML of self-assembled CdSe QDs and 4 % Mn in the tunnel barriers (sample cb3503) in magnetic fields from 0 to 14 Tesla.

state in the same or a different QD comes into resonance. Scattering of the tunneling electrons may also prevent the current from dropping to zero after a QD level is pulled below the emitter.

Additional fine structure can be seen in the current plateaus, e.g. small "wiggles" around 23 mV. Such fine structure may be related to variations in the local 2D density of states in the emitter, for which the 0D resonant energy level acts as an energy spectrometer [176].

The B-field dependence of the I-V curves of such non-magnetic II-VI QD RTDs is described by Rueth et al. [21]. Here we simply note that at 4.2 K the main resonant tunneling peaks, which are related to the Fermi-edge singularity, are only weakly affected by a magnetic field. The fine-structure on top of the current plateaus, as well as the features at higher bias $\geq$ 40 mV, however, show systematic variations in a magnetic field. A detailed analysis of this behavior goes beyond the scope of this thesis.

Magnetic QD RTD The I-V characteristics of a magnetic quantum dot RTD, with the structure depicted in figure 7.18, are shown in figure 7.20. The curves are taken at 1.4 K and in magnetic fields up to 9 T.

As for the nonmagnetic QD RTD, the I-V characteristics show negligible current around 0 V bias. At about 40 - 45 mV a clear resonance peak marks a step increase in the current, and more resonances are observed at higher bis voltages. The first resonance is split into two peaks, with a voltage separation of about 5 mV. When an external magnetic field is applied the peaks further separate, following (approximately) a Brillouin curve, and they saturate for fields higher than about 6 T. Increasing temperature counteracts the effect of a magnetic field and also reduces the separation of peaks at 0 T. This is consistent with the behavior expected for s-d exchange splitting of resonant levels (see figure 2.3).

The remarkably clear splitting of resonance peaks in an external field can be understood as Fermi-edge singularity enhanced tunneling through individual spin sublevels in a CdSe QD, which are split by several meV due to s-d exchange interaction with Mn ions in the barriers (see section 2.2). Even though Mn is not directly incorporated in the CdSe QDs, such an interaction is reasonable, considering that the wavefunctions of electrons, which are confined in the relatively small QDs, extend significantly into the barriers. The Brillouin-like shift of the two peaks with magnetic field and the reduction of the splitting by increasing temperature support the picture of tunneling through individual spin-sublevels. The remarkably clear separation of the very sharp resonance peaks suggests that the tunneling current through the spin sublevels has a high degree of spin polarization.

Even more remarkable than the clear spin separation achievable in this QD RTD is the fact that the two resonance peaks do not completely merge at zero magnetic field. In [11] a similar zero-field splitting is explained in terms of an effectively ferromagnetic interaction between the Mn ions on the outskirts of the QD and electrons in the QD. As an intriguing consequence, such dilute-magnetic QD RTDs act as voltage-controllable spin filters without the need for an external magnetic field.

To further substantiate the notion of zero-field splitting of resonance peaks, more I-V curves of other mesas on the same DMS QD RTD wafer are depicted in figure 7.21. The green curve corresponds to the mesa studied in detail previously. In the other two curves the current is negligible as well up to the point where the first QD comes into resonances. Two closely adjacent peaks are observed when the QD level is close to the Fermi level and transport is enhanced by FES. For the green and the black curved B-field dependent measurements show that the peaks move in opposite directions when a field is applied. Therefore, zero-field splitting of resonances is clearly observed in several DMS QD RTDs.

In principle, these structures should also exhibit spin splitting of the barrier height in a magnetic field, similar to that discussed in chapter 6. Since not only the energy level in the QD, but also the tunnel barrier is reduced (increased) for the lower (higher) spin-sublevel electrons, the corresponding resonance peak in the I-V curve should thus be enhanced (decreased) due to the higher (lower) transmission probability. However, the tunnel barriers in these RTD structures are on the order of 300 meV and are significantly higher than the s-d exchange interaction induced spin splitting (see figure 2.3). The effect is thus expected to be rather weak.

A third feature of tunneling magneto-transport in the magnetic QD RTD (figure 7.20) is the shape and height of resonance peaks at very high magnetic fields. The lower

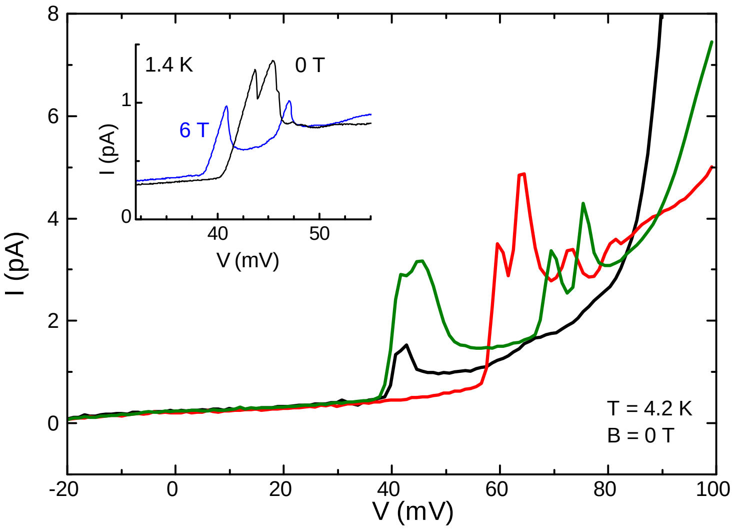

Figure 7.21: I-V curves of different mesa diodes on a QD RTD wafer with 4 % Mn in the barriers. No B-Field is applied and the temperature is 4.2 K. The inset shows a higher resolution I-V curve of the mesa represented by the black curve at a lower temperature and with a magnetic field of 6 T. For each mesa diode the onset of the first resonance consists of two close but separately resolved peaks, consistent with a zero-field spin splitting in all these mesas.

spin-sublevel resonance strongly increases in high fields $\geq 6\,\mathrm{T}$, while the upper spin-sublevel resonance further splits into two peaks. This high-field behavior is beyond the scope of this thesis.

Bibliography

[1] J. K. Furdyna, J. Appl. Phys. **64**, R29 (1988).

[2] S. A. Wolf, D. D. Awschalom, R. A. Buhrman, J. M. Daughton, S. von Molnar, M. L. Roukes, A. Y. Chtchelkanova, and D. M. Treger, Science **294**, 1488 (2001).

[3] I. Zutic, J. Fabian, and S. Das Sarma, Rev. Mod. Phys. **76**, 323 (2004).

[4] D. D. Awschalom and M. E. Flatte, Nature Physics **3**, 153 (2007).

[5] R. Fiederling, M. Keim, G. Reuscher, W. Ossau, G. Schmidt, A. Waag, and L. W. Molenkamp, Nature **402**, 787 (1999).

[6] B. T. Jonker, Y. D. Park, B. R. Bennett, H. D. Cheong, G. Kioseoglou, and A. Petrou, Phys. Rev. B **62**, 8180 (2000).

[7] N. Dai, H. Luo, F. C. Zhang, N. Samarth, M. Dobrowolska, and J. K. Furdyna, Phys. Rev. Lett. **67**, 3824 (1991).

[8] N. Dai, L. R. Ram Mohan, H. Luo, G. L. Yang, F. C. Zhang, M. Dobrowolska, and J. K. Furdyna, Phys. Rev. B **50**, 18153 (1994).

[9] A. Slobodskyy, C. Gould, T. Slobodskyy, C. R. Becker, G. Schmidt, and L. W. Molenkamp, Phys. Rev. Lett **90**, 246601 (2003).

[10] Z. L. Fang, P. Wu, N. Kundtz, A. M. Chang, X. Y. Liu, and J. K. Furdyna, Appl. Phys. Lett. **91**, 022101 (2007).

[11] C. Gould, A. Slobodskyy, D. Supp, T. Slobodskyy, P. Grabs, P. Hawrylak, F. Qu, G. Schmidt, and L. W. Molenkamp, Phys. Rev. Lett. **97**, 017202 (2006).

[12] A. Slobodskyy, C. Gould, T. Slobodskyy, G. Schmidt, L. W. Molenkamp, and D. Sanchez, Appl. Phys. Lett. **90**, 122109 (2007).

[13] J. C. Egues, C. Gould, G. Richter, and L. W. Molenkamp, Phys. Rev. B **64**, 195319 (2001).

[14] A. Saffarzadeh, Solid State Commun. **137**, 463 (2006).

[15] M. Ghali, R. Arians, T. Kümmell, G. Bacher, J. Wenisch, S. Mahapatra, and K. Brunner, Appl. Phys. Lett. **90**, 093110 (2007).

[16] A. Kley and J. Neugebauer, Phys. Rev. B **50**, 8616 (1994).

[17] A. Frey, U. Bass, S. Mahapatra, C. Schumacher, J. Geurts, and K. Brunner, Phys. Rev. B **82**, 195318 (2010).

[18] A. Frey, M. Rüth, R. Dengel, C. Schumacher, C. Gould, G. Schmidt, K. Brunner, and L. Molenkamp, J. Cryst. Growth **312**, 1036 (2010).

[19] S. Tarucha, D. G. Austing, T. Honda, R. J. van der Hage, and L. P. Kouwenhoven, Phys. Rev. Lett. **77**, 3613 (1996).

[20] S. M. Reimann and M. Manninen, Rev. Mod. Phys. **74**, 1283 (2002).

[21] M. Rüth, T. Slobodskyy, C. Gould, G. Schmidt, and L. W. Molenkamp, Appl. Phys. Lett. **93**, 182104 (2008).

[22] "International Technology Roadmap for Semiconductors," (2010), semiconductor Industry Organization, http://www.itrs.net/.

[23] M. N. Baibich, J. M. Broto, A. Fert, F. N. Van Dau, F. Petroff, P. Etienne, G. Creuzet, A. Friederich, and J. Chazelas, Phys. Rev. Lett. **61**, 2472 (1988).

[24] J. M. Kikkawa, I. P. Smorchkova, N. Samarth, and D. D. Awschalom, Science **277**, 1284 (1997).

[25] J. M. Kikkawa and D. D. Awschalom, Phys. Rev. Lett. **80**, 4313 (1998).

[26] J. Åkerman, Science **308**, 508 (2005).

[27] S. S. P. Parkin, M. Hayashi, and L. Thomas, Science **320**, 190 (2008).

[28] V. Cerletti, W. A. Coish, O. Gywat, and D. Loss, Nanotechnology **16**, R27 (2005).

[29] P. W. Shor, SIAM J. Sci. Stat. Comput. **26**, 1484 (1997).

[30] L. K. Grover, Phys. Rev. Lett. **79**, 325 (1997).

[31] H. Ohno, Science **291**, 840 (2001).

[32] T. Jungwirth, J. Sinova, J. Mašek, J. Kučera, and A. H. MacDonald, Rev. Mod. Phys. **78**, 809 (2006).

[33] A. H. MacDonald, P. Schiffer, and N. Samarth, Nature Materials **4**, 195 (2005).

[34] J. Henke, *ZnCdMnSe Quantenstrukturen in ZnBeSe Barriereschichten*, Master's thesis, Julius Maximilians Universität Würzburg (2009).

[35] U. Rössler, *Landolt-Börnstein, Vol. III, Semiconductors* (Springer, 1999).

[36] J. R. Chelikowsky and M. L. Cohen, Phys. Rev. B **14**, 556 (1976).

[37] S. Nakamura, T. Mukai, and M. Senoh, Appl. Phys. Lett. **64**, 1687 (1994).

[38] S. Strite, M. Lin, and H. Morkoc, Thin Solid Films **231**, 197 (1993).

[39] To the best of the authors knowledge, this figure has been created by a former student or faculty member at the chair of EP 3 at Physikalisches Institut, Universität Würzburg. Its precise authorship could not be determined, and it is regretted that due credit can not be given.

[40] C. Chauvet, E. Tournié, and J.-P. Faurie, Phys. Rev. B **61**, 5332 (2000).

[41] A. Waag, Th. Litz, F. Fischer, H. J. Lugauer, T. Baron, K. Schull, U. Zehnder, T. Gerhard, U. Lunz, M. Keim, G. Reuscher, and G. Landwehr, J. Cryst. Growth **184-185**, 1 (1998).

[42] G. V. Astakhov, D. R. Yakovlev, V. P. Kochereshko, W. Ossau, W. Faschinger, J. Puls, F. Henneberger, S. A. Crooker, Q. McCulloch, D. Wolverson, N. A. Gippius, and A. Waag, Phys. Rev. B **65**, 165335 (2002).

[43] K. Wilmers, T. Wethkamp, N. Esser, C. Cobet, W. Richter, M. Cardona, V. Wagner, H. Lugauer, F. Fischer, T. Gerhard, and M. Keim, Phys. Rev. B **59**, 10071 (1999).

[44] D. Keller, *Optische Eigenschaften ZnSe-basierter zweidimensionaler Elektronengase und ihreWechselwirkung mit magnetischen Ionen*, Ph.D. thesis, Julius Maximilians Universität Würzburg (2004).

[45] A. Twardowski, T. Dietl, and M. Demianiuk, Solid State Commun. **48**, 845 (1983).

[46] S. Lankes, T. Reisinger, B. Hahn, C. Meier, M. Meier, and W. Gebhardt, J. Cryst. Growth **159**, 480 (1996).

[47] S. Wei and A. Zunger, Appl. Phys. Lett. **72**, 2011 (1998).

[48] B. Koenig, U. Zehnder, D. R. Yakovlev, W. Ossau, T. Gerhard, M. Keim, A. Waag, and G. Landwehr, Phys. Rev. B **60**, 2653 (1999).

[49] N. Shibata, A. Ohki, and A. Katsui, J. Cryst. Growth **93**, 703 (1988).

[50] A. Twardowski, M. von Ortenberg, M. Demianiuk, and R. Pauthenet, Solid State Commun. **51**, 849 (1984).

[51] C. Kittel, *Introduction to solid state physics* (Wiley, 2005).

[52] P. Harrison, *Quantum Wells, Wires and Dots* (Wiley Interscience, 2005).

[53] F. Capasso, Science **235**, 172 (1987).

[54] A. Trellakis, T. Zibold, T. Andlauer, S. Birner, R. Kent Smith, Morschl R., and P. Vogl, J. Comput. Electron. **5**, 285 (2006).

[55] S. Birner, T. Zibold, T. Andlauer, T. Kubis, M. Sabathil, A. Trellakis, and P. Vogl, IEEE Trans. Electron Devices **54**, 2137 (2007).

[56] S. Birner, (2011), http://www.nextnano.de.

[57] H. Mizuta and T. Tanoue, *The physics and applications of resonant tunneling diodes*, edited by H. Ahmed, M. Pepper, and A. Broers (Cambridge university press, 1995).

[58] F. Schwabl, *Quantenmechanik* (Springer Verlag, 2002).

[59] E. Burstein and S. Lundqvist, eds., *Tunneling Phenomena In Solids* (Plenum Press, 1969).

[60] M. Rossmanith, J. Leo, and K. von Klitzing, J. Appl. Phys. **69**, 3641 (1991).

[61] M. Rossmanith, K. Syassen, E. Böckenhoff, K. Ploog, and K. von Klitzing, Phys. Rev. B **44**, 3168 (1991).

[62] A. Schenk and G. Heiser, J. Appl. Phys. **81**, 7900 (1997).

[63] A. M. Roy, D. E. Nikonov, and K. C. Saraswat, J. Appl. Phys. **107**, 064504 (2010).

[64] G. Schmidt, D. Ferrand, L. W. Molenkamp, A. T. Filip, and B. J. van Wees, Phys. Rev. B **62**, 4790 (2000).

[65] E. I. Rashba, Phys. Rev. B **62**, R16267 (2000).

[66] A. Slobodksyy, *Diluted magnetic semiconductor resonant tunneling structures for spin manipulation*, Ph.D. thesis, Julius Maximilians Universität Würzburg (2005).

[67] A. K. Geim, P. C. Main, N. La Scala, L. Eaves, T. J. Foster, P. H. Beton, J. W. Sakai, F. W. Sheard, M. Henini, G. Hill, and M. A. Pate, Phys. Rev. Lett. **72**, 2061 (1994).

[68] C. Klingshirn, *Semiconductor Optics* (Springer, Berlin, 2005).

[69] B. Jouault, M. Gryglas, M. Baj, A. Cavanna, U. Gennser, G. Faini, and D. K. Maude, Phys. Rev. B **79**, 041307 (2009).

[70] C. W. J. Beenakker, Phys. Rev. B **44**, 1646 (1991).

[71] R. Hanson, L. P. Kouwenhoven, J. R. Petta, S. Tarucha, and L. M. K. Vandersypen, Rev. Mod. Phys. **79**, 1217 (2007).

[72] M. W. Dellow, P. H. Beton, C. J. G. M. Langerak, T. J. Foster, P. C. Main, L. Eaves, M. Henini, S. P. Beaumont, and C. D. W. Wilkinson, Phys. Rev. Lett. **68**, 1754 (1992).

[73] I. E. Itskevich, T. Ihn, A. Thornton, M. Henini, T. J. Foster, P. Moriarty, A. Nogaret, P. H. Beton, L. Eaves, and P. C. Main, Phys. Rev. B **54**, 16401 (1996).

[74] M. A. Herman and H. Sitter, *Molecular Beam Epitaxy*, edited by U. Gonser, R. M. Osgood, M. B. Panish, and H. Sakaki (Springer, 1996).

[75] E. H. C. Parker, ed., *The technology and physics of molecular beam epitaxy* (Plenum Press, New York, 1985).

[76] B. A. Joyce, Rep. Prog. Phys. **48**, 1637 (1985).

[77] J. R. Arthur, Surface Science **500**, 189 (2002).

[78] T. Schallenberg, *Shadow Mask assistet Heteroepitaxy of Compound Semiconductor Nanostructures*, Ph.D. thesis, Julius Maximilians Universität Würzburg (2004).

[79] S. Mahapatra, *Formation and properties of epitaxial CdSe / ZnSe quantum dots.*, Ph.D. thesis, Julius Maximilians Universität Würzburg (2007).

[80] T. A. Flaim and P. D. Ownby, J. Vac. Sci. Tech. **8**, 661 (1971).

[81] W. Braun, *Applied RHEED* (Springer, 1999).

[82] D. A. Allwood, I. R. Grant, N. J. Mason, R. A. Palmer, and P. J. Walker, J. Cryst. Growth **221**, 160 (2000).

[83] D. Wolfframm, D. A. Evans, D. I. Westwood, and J. Riley, J. Cryst. Growth **216**, 119 (2000).

[84] L. H. Kuo, K. Kimura, S. Miwa, T. Yasuda, and T. Yao, Appl. Phys. Lett. **69**, 1408 (1996).

[85] J. Riley, D. Wolfframm, D. Westwood, and A. Evans, J. Cryst. Growth **160**, 193 (1996).

[86] J. Griesche, N. Hoffmann, and K. Jacobs, J. Cryst. Growth **138**, 55 (1994).

[87] M. Vos, F. Xu, S. G. Anderson, J. H. Weaver, and H. Cheng, Phys. Rev. B **39**, 10744 (1989).

[88] D. K. Bowen and B. K. Tanner, *High resolution x-ray diffractometry and topography* (Taylor and Francis Ltd., 1998).

[89] H. R. Ress, *Neue Messmethoden in der hochauflösenden Röntgendiffraktometrie*, Ph.D. thesis, Julius Maximilians Universität Würzburg (1998).

[90] S. N. G. Chu, A. T. Macrander, K. E. Strege, and J. W. D. Johnston, J. Appl. Phys. **57**, 249 (1985).

[91] L. Tapfer and K. Ploog, Phys. Rev. B **40**, 9802 (1989).

[92] H. Holloway, J. Appl. Phys. **67**, 6229 (1990).

[93] K. A. Prior, X. Tang, C. O'Donnell, C. Bradford, L. David, and B. C. Cavenett, J. Cryst. Growth **251**, 565 (2003).

[94] G. D. Uren, M. S. Goorsky, G. Meis Haugen, K. K. Law, T. J. Miller, and K. W. Haberern, Appl. Phys. Lett. **69**, 1089 (1996).

[95] P. Kidd, P. F. Fewster, and N. L. Andrew, J. Phys. D **28**, A133 (1995).

[96] H. R. Ress, W. Spahn, R. Ebel, J. Nürnberger, M. Keller, H. Schäfer, M. Korn, M. Ehinger, W. Faschinger, and G. Landwehr, J. Cryst. Growth **184/185**, 90 (1998).

[97] G. Bastard, E. E. Mendez, L. L. Chang, and L. Esaki, Phys. Rev. B **26**, 1974 (1982).

[98] G. V. Astakhov, T. Kiessling, A. V. Platonov, T. Slobodskyy, S. Mahapatra, W. Ossau, G. Schmidt, K. Brunner, and L. W. Molenkamp, Phys. Rev. Lett. **96**, 027402 (2006).

[99] L. F. Ebel, *Molekularstrahlepitaxie und Charakterisierung von (Ga,Mn)As-Schichtstrukturen und InAs Quantenpunkten*, Master's thesis, Julius Maximilians Universität Würzburg (2006).

[100] P. Blood, Semicond. Sci. Technol. **1**, 7 (1986).

[101] S. M. Sze and K. K. Ng, *Physics of semiconductor devices* (Wiley, 2007).

[102] S. Y. Wang, J. Simpson, K. A. Prior, and B. C. Cavenett, J. Appl. Phys. **72**, 5311 (1992).

[103] S. Y. Wang, F. Haran, J. Simpson, H. Stewart, J. M. Wallaceand K. A. Prior, and B. C. Cavenett, Appl. Phys. Lett. **60**, 344 (1992).

[104] G. Binnig, C. F. Quate, and Ch. Gerber, Phys. Rev. Lett **56**, 930 (1986).

[105] M. Endress, *Herstellung und Charakterisierung von Spininjektoren auf Basis von II-VI-Halbleiter-Schichten*, Master's thesis, Julius Maximilians Universität Würzburg (2011).

[106] C. Orme, M. D. Johnson, J. L. Sudijono, K. T. Leung, and B. G. Orr, Appl. Phys. Lett. **64**, 860 (1994).

[107] S.-H. Wei and A. Zunger, Phys. Rev. B **60**, 5404 (1999).

[108] H. E. Ruda, J. Appl. Phys. **59**, 1220 (1986).

[109] J. Stangl, V. Holy, and G. Bauer, Rev. Mod. Phys. **76**, 725 (2004).

[110] H. Kirmse, R. Schneider, M. Rabe, W. Neumann, , and F. Henneberger, Appl. Phys. Lett. **72**, 1329 (1998).

[111] E. Kurtz, J. Shen, M. Schmidt, M. Grün, S. K. Hong, D. Litvinov, D. Gerthsen, T. Oka, T. Yao, and C. Klingshirn, Thin Solid Films **367**, 68 (2000).

[112] S. Mahapatra, C. Schumacher, T. Kiessling, G. V. Astakhov, U. Bass, W. Ossau, J. Geurts, and K. Brunner, Act. Phys. Pol. A **108**, 769 (2005).

[113] T. Aichele, I.-C. Robin, C. Bougerol, R. Andre, S. Tatarenko, and G. Van Tendeloo, J. Cryst. Growth **301-302**, 281 (2007).

[114] S. Mahapatra, K. Brunner, and C. Bougerol, Appl. Phys. Lett. **91**, 153110 (2007).

[115] S. Mahapatra, T. Kiessling, E. Margapoti, G. V. Astakhov, J. Renner, U. Bass, C. Bougerol, T. Schmidt, A. Bendounan, F. Schmitt, C. Schumacher, L. Worschech, W. Ossau, J. Geurts, L. W. Molenkamp, F. Reinert, A. Forchel, and K. Brunner, Phys. Stat. Sol. (c) **4**, 3129 (2007).

[116] D. Litvinov, A. Rosenauer, D. Gerthsen, H. Preis, K. Fuchs, and S. Bauer, J. Appl. Phys. **89**, 3695 (2001).

[117] C. S. Kim, M. Kim, S. Lee, J. Kossut, J. K. Furdyna, and M. Dobrowolska, J. Cryst. Growth **214-215**, 395 (2000).

[118] S. Lee, M. Dobrowolska, and J. Furdyna, J. Cryst. Growth **301-302**, 781 (2007).

[119] S. Lee, M. Dobrowolska, and J. K. Furdyna, J. Cryst. Growth **292**, 311 (2006).

[120] Y. Gu, Igor L. Kuskovsky, R. Robinson, I. Herman, G. Neumark, X. Zhou, S. Guo, M. Munoz, and M. Tamargo, Solid State Commun. **134**, 677 (2005).

[121] T. Slobodskyy, *Semimagnetic heterostructures for spintronics*, Ph.D. thesis, Julius Maximilians Universität Würzburg (2006).

[122] Y. Nabetani, T. Ishikawa, S. Noda, and A. Sasaki, J. Appl. Phys. **76**, 347 (1994).

[123] T. Kummell, R. Weigand, G. Bacher, A. Forchel, K. Leonardi, D. Hommel, and H. Selke, Appl. Phys. Lett. **73**, 3105 (1998).

[124] D. Litvinov, A. Rosenauer, D. Gerthsen, P. Kratzert, M. Rabe, and F. Henneberger, Appl. Phys. Lett. **81**, 640 (2002).

[125] T. Kießling, *Symmetry and Optical Anisotropy in CdSe / ZnSe Quantum Dots*, Ph.D. thesis, Julius Maximilians Universität Würzburg (2009).

[126] W. Seifert, N. Carlsson, M. Miller, M.-E. Pistol, L. Samuelson, and L. Reine W., Progress in Crystal Growth and Characterization of Materials **33**, 423 (1996).

[127] A. Waag, F. Fischer, H. J. Lugauer, Th. Litz, J. Laubender, U. Lunz, U. Zehnder, W. Ossau, T. Gerhardt, M. Moller, and G. Landwehr, J. Appl. Phys. **80**, 792 (1996).

[128] C. Verie, J. Cryst. Growth **B43**, 60 (1997).

[129] A. Franciosi and C. G. van de Walle, Surf. Sci. Rep. **25**, 1 (1996).

[130] H. Farrell, M. C. Tamargo, J. L. de Miguel, F. S. Turco, D. M. Hwang, and R. E. Nahory, J. Appl. Phys. **69**, 7021 (1991).

[131] R. Nicolini, L. Vanzetti, G. Mula, G. Bratina, L. Sorba, A. Franciosi, M. Peressi, S. Baroni, R. Resta, A. Baldereschi, J. E. Angelo, and W. W. Gerberich, Phys. Rev. Lett. **72**, 294 (1994).

[132] A. Colli, E. Carlino, E. Pelucchi, V. Grillo, and A. Franciosi, J. Appl. Phys. **96**, 2592 (2004).

[133] L. Kassel, J. W. Garland, P. M. Raccah, M. A. Haase, and H. Cheng, Semicond. Sci. Technol. **6**, A146 (1991).

[134] A. Frey, F. Lehmann, P. Grabs, C. Gould, G. Schmidt, K. Brunner, and L. W. Molenkamp, Semicond. Sci. Technol. **24**, 035005 (2009).

[135] A. Ishibashi, J. Cryst. Growth **159**, 555 (1996).

[136] F. Fischer, M. Keller, T. Gerhard, T. Behr, T. Litz, H. J. Lugauer, M. Keim, G. Reuscher, T. Baron, A. Waag, and G. Landwehr, J. Appl. Phys. **84**, 1650 (1998).

[137] C. C. Chu, T. B. Ng, J. Han, G. C. Hua, R. L. Gunshor, E. Ho, E. L. Warlick, L. A. Kolodziejski, and A. V. Nurmikko, Appl. Phys. Lett. **69**, 602 (1996).

[138] T. Yao, F. Lu, M. Cho, K. Koh, Z. Zhu, L. Kuo, T. Yasuda, A. Ohtake, S. Miwa, K. Kimura, and K. Nakajima, Phys. Stat. Sol. (b) **202**, 657 (1997).

[139] A. Ohtake, S. Miwa, L. Kuo, T. Yasuda, K. Kimura, C. Jin, and T. Yao, J. Cryst. Growth **184/185**, 163 (1998).

[140] A. A. Toropov, I. V. Sedova, S. V. Sorokin, Ya. V. Terent'ev, E. L. Ivchenko, and S. V. Ivanov, Phys. Rev. B **71**, 195312 (2005).

[141] A. A. Toropov, I. V. Sedova, S. V. Sorokin, Ya. V. Terent'ev, E. L. Ivchenko, D. N. Lykov, S. V. Ivanov, J. P. Bergman, and B. Monemar, Phys. Stat. Sol. (b) **243**, 819 (2006).

[142] H. H. Farrell and C. J. Palmstrom, J. Vac. Sci. Technol. B **8**, 903 (1990).

[143] D. Li and M. D. Pashley, Phys. Rev. B **49**, 13643 (1994).

[144] A. C. Gossard, W. Brown, C. L. Allyn, and W. Wiegmann, J. Vac. Sci. Technol. B **20**, 694 (1982).

[145] O. Chretien, R. Apetz, A. Souif, and L. Vescan, Thin Solid Films **294**, 198 (1997).

[146] H. Kroemer, Wu-Yi Chien, J. S. Harris, and D. D. Edwall, Appl. Phys. Lett. **36**, 295 (1980).

[147] G. Abstreiter, M. Cardona, and A. Pinczuk, Topics in Applied Physics **54**, 5 (1983).

[148] D. E. Aspnes and A. A. Studna, Phys. Rev. B **27**, 985 (1983).

[149] J. Geurts, Surf. Sci. Rep. **18**, 1 (1993).

[150] I. Vurgaftman, J. R. Meyer, and L. R. Ram Mohan, J. Appl. Phys. **89**, 5815 (2001).

[151] H. C. Casey, "Atomic diffusion in semiconductors," (Plenum Press, 1973) Chap. Diffusion in the III-V compound semiconductors.

[152] A. Benkert, C. Schumacher, K. Brunner, and R. B. Neder, Appl. Phys. Lett. **90**, 162105 (2007).

[153] J. C. Egues, Phys. Rev. Lett. **80**, 4578 (1998).

[154] S. Yuasa, T. Nagahama, A. Fukushima, Y. Suzuki, and K. Ando, Nature **3**, 868 (2004).

[155] F. Lehmann, *Prozessierung und elektrische Charakterisierung von ZnSe Heterostrukturen in verschiedenen Messgeometrien zum eindeutigen Nachweis der elektrischen Spininjektion*, Ph.D. thesis, Julius Maximilians Universität Würzburg (2005).

[156] D. Keller, D. R. Yakovlev, B. König, W. Ossau, T. Gruber, A. Waag, L. W. Molenkamp, and A. V. Scherbakov, Phys. Rev. B **65**, 035313 (2001).

[157] Y. Shapira, N. F. Oliveira, D. H. Ridgley, R. Kershaw, K. Dwight, and A. Wold, Phys. Rev. B **34**, 4187 (1986).

[158] G. Schmidt and L. W. Molenkamp, Semicond. Sci. Technol. **17**, 310 (2002).

[159] R. I. Dzhioev, K. V. Kavokin, V. L. Korenev, M. V. Lazarev, B. Y. Meltser, M. N. Stepanova, B. P. Zakharchenya, D. Gammon, and D. S. Katzer, Phys. Rev. B **66**, 245204 (2002).

[160] I. Malajovich, J. M. Kikkawa, D. D. Awschalom, J. J. Berry, and N. Samarth, J. Appl. Phys. **87**, 5073 (2000).

[161] J. M. Kikkawa, J. A. Gupta, I. Malajovich, and D. D. Awschalom, Physica E **9**, 194 (2001).

[162] L. L. Chang, L. Esaki, and R. Tsu, Appl. Phys. Lett. **24**, 593 (1974).

[163] T. Broekaert, W. Lee, and C. Fonstad, Appl. Phys. Lett. **53**, 1545 (1988).

[164] H. Sugiyama, H. Yokoyama, A. Teranishi, S. Suzuki, and M. Asada, Jap. J. Appl. Phys. **49**, 051201 (2010).

[165] K. Ismail, B. S. Meyerson, and P. J. Wang, Appl. Phys. Lett. **59**, 973 (1991).

[166] A. Kikuchi, R. Bannai, K. Kishino, C.-M. Lee, and J.-I. Chyi, Appl. Phys. Lett. **81**, 1729 (2002).

[167] K. F. Brennan and C. J. Summers, J. Appl. Phys. **61**, 614 (1987).

[168] U. Lunz, M. Keim, G. Reuscher, F. Fischer, K. Schull, A. Waag, and G. Landwehr, J. Appl. Phys. **80**, 6329 (1996).

[169] P. Grabs, *Herstellung von Bauelementen für Spininjektionsexperimente mit semimagnetischen Halbleitern*, Ph.D. thesis, Julius Maximilians Universität Würzburg (2005).

[170] V. J. Goldman, D. C. Tsui, and J. E. Cunningham, Phys. Rev. B **36**, 7635 (1987).

[171] M. Haase, W. Prost, P. Velling, Q. Liu, and F. J. Tegude, Thin Solid Films **319**, 25 (1998).

[172] D. L. Smith and S. M. Kogan, Phys. Rev. B **54**, 10354 (1996).

[173] K. Yoh, H. Kazama, and T. Nakano, Physica B **249-251**, 243 (1998).

[174] H. Sakaki, M. Tanaka, and J. Yoshino, Jap. J. Appl. Phys. **24**, L417 (1985).

[175] A. Patane, A. Polimeni, L. Eaves, P. C. Main, M. Henini, Yu. V. Dubrovskii, A. E. Belyaev, P. N. Brounkov, E. E. Vdovin, Yu. N. Khanin, and G. Hill, J. Appl. Phys. **88**, 2005 (2000).

[176] B. Jouault, M. Gryglas, G. Faini, U. Gennser, A. Cavanna, M. Baj, and D. K. Maude, Phys. Rev. B **73**, 155415 (2006).

Own publications

1. F. Sotier, T. Thomay, T. Hanke, J. Korger, S. Mahapatra, A. Frey, K. Brunner, R. Bratschitsch, and A. Leitenstorfer, Nature Physics **5**, 352 (2009).
2. A. Frey, F. Lehmann, P. Grabs, C. Gould, G. Schmidt, K. Brunner, and L. W. Molenkamp, Semicond. Sci. Technol. **24**, 035005 (2009).
3. A. Frey, M. Rüth, R. Dengel, C. Schumacher, C. Gould, G. Schmidt, K. Brunner, and L. Molenkamp, J. Cryst. Growth **312**, 1036 (2010).
4. A. Frey, U. Bass, S. Mahapatra, C. Schumacher, J. Geurts, and K. Brunner, Phys.Rev. B **82**, 195318 (2010).

Acknowledgements

Many people have contributed in various ways to the work described in this thesis, be it through guidance, collaboration, assistance or motivation. I wish to express my sincere gratitude to

- Prof. Karl Brunner for advising me as a PhD student, for sharing his deep understanding of semiconductor physics in countless long and fruitful discussions, and for the freedom to work independently in this interesting field. I also thank him for the very timely reading of the manuscript and for many helpful remarks in the preparation of this thesis.
- Prof. Laurens Molenkamp for the opportunity to work at EP3, to make use of its first-rate technological infrastructure. The uncompromisingly high academic standards of his group are exemplary in this field.
- Prof. Georg Schmidt and Charles Gould for the interesting and challenging work in the spintronics group.
- my co-workers in the MBE group, including Suddhosatta Mahapatra, Jan Wenisch, Andreas Benkert, Lars Ebel, Christoph Pohl, Christopher Ames, and Steffen Schreyeck for a great working atmosphere and for mutual support during the often turbulent times in the laboratory. I wish to thank especially Lars Ebel for many enjoyable conference trips.
- the students who worked with me, namely Jürgen Henke, Joel Thomas, Karol Winkler and Martin Endress, for their numerous contributions to this work and for a very good collaboration.
- the spintronics group, the PL group, and the Raman spectroscopy group at EP3 for being patient in-house customers of a sometimes erratic MBE chamber. I wish to thank Michael Rüth, Gabriel Dengel and Philip Hartmann for the very close collaboration on the RTD and single barrier projects, and for the discussion of transport results. Many thanks to Tobias Kiessling, Jan-Henrik Quast, Steffen Bieker, Franz Münzhuber and Christoph Aulbach for countless PL spectra and for the excellent explanation of the physics behind them. To Prof. Jean Geurts and to Utz Bass I wish to express my appreciation for their constructive role

in the ZnSe / GaAs heterointerface project, to which they contributed Raman measurements and many hours of discussion.

- the researchers from outside EP3, with whom I have had the pleasure to collaborate during this work. These include Prof. Grzegorz Karczewski from the Polish Academy of Sciences, Prof. Christian Kumpf and Florian Meyer from BESSY, Prof. Lukas Worschech and Thomas Schmidt from Technical Physics in Wuerzburg, Florian Sotier from the University of Konstanz, and the group of Prof. Gerd Bacher from the University of Duisburg-Essen. I wish to express my special gratitude to Grzegorz 'Greg' Karczewski - I have benefited a lot from his deep understanding of semiconductor physics, and his entrepreneurship and enthusiasm have initiated many interesting projects.

- the technical staff at EP3, consisting Volkmar Hock, Petra Wolf-Müller, Alfred Schönteich, Anita Gebhardt and Martin Zipf, for expert technical support and wizardry in many UHV-related or organizational issues. The long-term experience of Volkmar Hock with ZnSe based semiconductors, as well as his hands-on approach to many characterization issues have helped me in many ways. I also wisth to thank Roland Ebert for his excelent cryogenic engineering and for providing liquid Helium when it was needed urgently.

- all members of EP3, especially to Charles Becker, Christian Kehl, Christoph Aulbach, Christoph Brüne, Fanny Greullet, Felicitas Gerhard, Florian Lochner, Georgy Astakhov, Prof. Hartmut Buhmann, Holger Thierschmann, Luis Maier, Mathias Mühlbauer, Petra Fries, Rebekka Pfeuffer, Stefan Mark, Sven Issing, Tanja Borzenko, Taras Slobodskyy, Tsvetelina Naydenova, Prof. Wolfgang Ossau for their contributions to this work and for a great working atmosphere.

Eidesstattliche Versicherung

gemäß §5 Abs. 2 Ziff. 2, 3 und 5 der Promotionsordnung vom 22. September 2003 der Fakultät für Physik und Astronomie der Universität Würzburg

Hiermit versichere ich an Eides statt, dass ich die vorliegende Dissertation selbständig verfasst habe und keine weiteren als die angegebenen Quellen und Hilfsmittel dazu benutzt habe.

Die Dissertation wurde bisher weder vollständig noch teilweise an einer anderen Hochschule oder in einem anderen Prüfungsfach mit dem Ziel, einen akademischen Grad zu erwerben, vorgelegt.

Am 09. August 2006 wurde mir vom College of William and Mary (USA) der Titel Master of Science verliehen. Weitere akademische Grade habe ich weder erworben noch versucht zu erwerben.

Alexander Frey
Würzburg, 27.07.2011

Curriculum Vitae

Alexander Frey
Geboren am 16.02.1982 in Künzelsau

09.1988 - 07.1992	Besuch der Grundschule Ingelfingen
09.1992 - 07.1994	Besuch der Georg-Wagner-Realschule Künzelsau
09.1994 - 07.1999	Besuch des Schlossgymnasiums Künzelsau
09.1999 - 06.2001	Besuch des Ganerben Gymnasiums Künzelsau Abschluss: Abitur
08.2001 - 05.2002	Zivildienst im Rettungsdienst des DRK Hohenlohe
10.2002 - 07.2005	Studium Physik (Diplom) mit Nebenfach Informatik Julius-Maximilians-Universität Würzburg
08.2005 - 08.2006	Studium Applied Science, College of William and Mary, Virginia, USA. Abschluss: Master of Science (Applied Science). Thema der Abschlussarbeit: "Time-resolved magnetooptical measurement of the current distribution in high-temperature superconductor thin films"
11.2006 - 07.2011	Promotionsstudium am Lehrstuhl EP3 des Physikalischen Instituts der Julius-Maximilians-Universität Würzburg. Betreuer: Prof. Dr. Karl Brunner
ab 08.2011	Osram Opto Semiconductors GmbH Entwicklung von High Brightness LEDs

Alexander Frey
Würzburg, 27.07.2011